THESIS

# INVESTIGATION OF LIQUID COOLING ON M9506A HIGH DENSITY KEYSIGHT AXIE CHASSIS

Submitted by

Zachary Howard Gilvey

Department of Mechanical Engineering

In partial fulfillment of the requirements

For the Degree of Master of Science

Colorado State University

Fort Collins, Colorado

Fall 2021

Master's Committee:

Advisor: Todd M. Bandhauer

Anthony Marchese
Steve Simske

Copyright Zachary Howard Gilvey 2021

All Rights Reserved

# ABSTRACT

INVESTIGATION OF LIQUID COOLING ON M9506A HIGH DENSITY KEYSIGHT AXIE CHASSIS

Forced convection air-cooled heat sinks are the dominant cooling method used in the electronics industry, accounting for 86% of high-density cooling in data centers. However, the continual performance increases of electronics equipment are pushing these air-cooled methods to their limit. Fundamental limitations such as acoustics, cooling power consumption, and heat transfer coefficient are being reached while processor power consumption is steadily rising. In this study, a 4U, 5-slot, high density computing box is studied to determine the maximum heat dissipation in its form factor while operating at an ambient air temperature of 50°C. Two liquid cooling technologies were analyzed in this effort and compared against current state-of-the-art air-cooled systems. A new configuration proposed using return jet impingement with dielectric fluid FC72 directly on the integrated circuit die shows up to a 44% reduction in thermal resistance as compared to current microchannel liquid cooled systems, 0.08 K $W^{-1}$, vs 0.144 K $W^{-1}$, respectively. In addition, at high ambient temperatures (~45°C), the radiator of the liquid cooled system accounts for two thirds of the thermal resistance from ambient to junction temperature, indicating that a larger heat exchanger outside the current form factor could increase performance further. The efficiency of the chips was modeled with efficiency predictions based on their junction temperature. On a system level, the model showed that by keeping the chassis at 25°C ambient, the overall power consumption was significantly lower by 500W. Furthermore, the failure rate was accounted for when the chip junction temperature was beyond 75°C. FC72 jet impingement on the

die showed the best performance to meet the system cooling requirements and kept the chips below 75°C for the highest ambient temperatures but consumed the most pumping power of all of the fluids and configurations investigated. The configuration with microchannels bypassing TIM 2 showed near the same performance as jet impingement with water on the lid and reduced the junction temperature difference by 5°C when compared to baseline. When the fluid was switched from water to a water glycol 50/50 mixture, an additional thermal resistance of 0.010 K $W^{-1}$ was recorded at the heat sink level and a higher mass flow rate was required for the GC50/50 heat exchanger to achieve its minimum thermal resistance.

# ACKNOWLEDGEMENTS

# TABLE OF CONTENTS

ABSTRACT......i

ACKNOWLEDGEMENTS ......iii
LIST OF TABLES ......vi
LIST OF FIGURES ...... vii
NOMENCLATURE ...... xi
CHAPTER 1. Introduction ...... 1
1.1. Motivation for Research ...... 1
1.2. Research Objectives...... 4
1.3. Thesis Organization ...... 6
CHAPTER 2. Literature Review ...... 7
2.1. Integrated Circuit Description...... 7
2.1.1. Medium Time to Failure ...... 16
2.2. Review of Technology Research ...... 18
2.2.1. Air cooling ...... 19
2.2.2. Microchannel Cooling ...... 25
2.2.3. Jet impingement...... 32
2.3. Research Needs for Integrated Circuit Cooling...... 43
2.4. Focus of Current Investigation...... 47
CHAPTER 3. System Architecture and Assumptions...... 49
3.1. AXIe Chassis ...... 49
3.1.1. Full system model...... 53
3.1.2. Cooling configurations...... 56
3.2. Overview of Modeling Approach ...... 59
3.3. Thermodynamic Model...... 61
3.4. Component Modeling ...... 63
3.4.1. Manifold...... 63
3.4.2. Microchannel cold plate...... 65
3.4.1. Return jet impingement architecture...... 71
3.4.2. Radiator...... 74
3.4.3. Pump ...... 84
3.5. Acoustic Considerations ...... 84
CHAPTER 4. Analysis and Discussion...... 88
4.1. Heat Exchanger Design...... 88
4.2. Heatsink Performance...... 100
4.2.1. Microchannel cooling results...... 102

4.2.2. Jet impingement results ........ 105
4.2.3. Overall heat sink results ........ 113
4.3. System Level Performance ........ 116
4.3.1. High ambient temperature operation ........ 117
4.3.2. Pressure drop summary ........ 121
4.3.3. Leakage current summary ........ 125
4.3.4. Failure rate results ........ 126
4.3.5. Acoustic results ........ 127
4.3.6. Further considerations ........ 128
CHAPTER 5. Conclusions and Recommendations ........ 132
5.1. Recommendations for Future Research ........ 135

# LIST OF TABLES

**Table 2-1** Microchannel literature review summary ........ 31

**Table 2-2** Jet impingement literature review summary ........ 42

**Table 3-1** AXIe blade chip characteristics ........ 50

**Table 3-2** AXIe manifold and tubing characteristics ........ 56

**Table 3-3** Representative package thermal resistance values ........ 58

**Table 3-4** Microchannel geometries performance at 0.020 kg $s^{-1}$ for Big Chip 1 ........ 70

**Table 3-5** Rattner k factor and Nusselt number coefficients ........ 72

**Table 3-6** Dielectric test data and fluid properties for Big Chip 1 configuration 3-5d ........ 74

**Table 3-7** Louver fin dependent variables relation to independent variables ........ 82

**Table 3-8** Noise levels referenced to real world sounds ........ 85

**Table 4-1** Optimized heat exchanger dimensions for primary fluids ........ 96

**Table 4-2** Radiator performance metrics ........ 98

**Table 4-3** Water microchannel pressure drop breakdown ........ 102

**Table 4-4** Pressure drop breakdown for constant 0.0080 K $W^{-1}$ varying nondimensional spacing and height Water ........ 105

**Table 4-5** Pressure drop breakdown for constant 0.0080 K $W^{-1}$ varying jet diameter Water ........ 106

**Table 4-6** Pressure drop breakdown for constant 0.080 K $W^{-1}$ varying nondimensional spacing and height FC72 ........ 108

**Table 4-7** Pressure drop breakdown for constant 0.080 K $W^{-1}$ varying jet diameter FC72 ........ 110

**Table 4-8** System level summary ........ 117

**Table 4-9** Maximum allowable ambient temperature ........ 119

**Table 4-10** Head and flow requirements for the pumps ........ 124

**Table A–1** Steady state solver inputs and geometry ……………………………….……………………..146

**Table A–2** Fluid properties ……………………………………………………………..151

**Table A-3** Chip power and leakage current specifications……………….……………………..…154

**Table A-4** System thermal variables and heat exchanger inlet air temperature……..………..…154

**Table A-5** Heat exchanger external Nusselt number and pressure drop………..……..……..…156

**Table A-6** Thermodynamic cycle……………………………………………………..……..…159

**Table A-7** Heat sink performance, FC72 configuration 3-5d…………………………….………..163

**Table A-8** Microchannel cooling heat transfer and thermodynamic calculations configuration 3-5a…………………………………………………………………………………………..167

**Table A-9** FC72 Pressure drop configuration 3-5d…………………………………..………169

**Table A-10** Microchannel cold plate pressure drop configuration 3-5a…………....…..………179

**Table A-11** Head and flow rate calculations for pumps…………………….……………..………180

# LIST OF FIGURES

**Figure 1-1** a) Microprocessor power dissipation vs year b) Clock speed vs year [4,5]................ 1

**Figure 1-2**, Thermal design power time in server CPUs and GPUs [3]...................................... 2

**Figure 1-3** a) Keysight PXIe chassis (M9018B) b) Keysight AXIe chassis (M9506A)................ 4

**Figure 2-1** Typical heat sink thermal pathway.................................................................... 8

**Figure 2-2** Leakage power consumption vs chip temperature [7] ............................................ 10

**Figure 2-3** Thermal interface material graphics a) Actual TIM in electronic packages b) No TIM in between two surfaces c) Ideal TIM in between two surfaces [26] ........................................ 12

**Figure 2-4** Thermal resistance relationship between TIM and contacting surfaces [31]............ 13

**Figure 2-5** Median time to failure vs junction temperature ...................................................... 17

**Figure 2-6** Flow diagram a) air cooled electronics b) liquid cooled electronics......................... 18

**Figure 2-7** Standard metal heat sink. ........................................................................... 19

**Figure 2-8** Cross-section of heat pipe wick structure ........................................................... 22

**Figure 2-9** Example chip array temperature distributions ......................................................... 24

**Figure 2-10** Schematic of an economizer loop ........................................................................ 27

**Figure 2-11** 12-Slot Gemini LRU ............................................................................................ 29

**Figure 2-12** Velocity contours of impinging jet on surface [63] ............................................... 32

**Figure 2-13** Flow regions of impinging jet [64] ....................................................................... 33

**Figure 2-14** Flow field of free submerged jet along flow path of jet [64] ................................. 34

**Figure 2-15** Supersonic jet flow pattern .................................................................................. 36

**Figure 2-16** a) Jet impingement without returns b) Jet impingement with returns [70] ............. 37

**Figure 2-17** Return jet impingement manifolding a) Capillary cell architecture with bf = 3 b) Cross section through layered chip c) 3D view of one inlet and one outlet tree d) Top view of capillary cell architecture [73] ......................................................................................................... 38

**Figure 2-18** Repeating return impingement unit cell ................................................................ 39

**Figure 2-19** Return jet-slot impingement array ......................................................................... 41

**Figure 2-20** Literature review gaps summary ........................................................................... 44

**Figure 2-21** Direct liquid cooling system pressure drop breakdown [83] ................................. 46

**Figure 3-1** Keysight M9506a front view ................................................................................... 50

**Figure 3-2** Power profile derived from leakage current for Big Chip 1 .................................... 52

**Figure 3-3** Schematic of liquid cooled AXIe system ................................................................ 53

**Figure 3-4** Rendered liquid cooled AXIe chassis a) Front view system b) Top view board ....... 54

**Figure 3-5** Cooling configurations a) Microchannel cold plate with TIM 2 b) Return jet impingement on the lid bypassing TIM 2 c) Microchannel cold plate bypassing TIM 2 d) Return jet impingement on the die bypassing TIM 1 ......................................................................... 57

**Figure 3-6** Required thermal resistance to achieve a temperature difference for a power input . 58

**Figure 3-7** Numerical model functioning principles ................................................................ 60

**Figure 3-8** Schematic of manifold 1 and 2 ............................................................................ 63

**Figure 3-9** OTS cold plate with 150 µm skived channels. ...................................................... 65

**Figure 3-10** Nusselt number distribution for 3-sided microchannel .......................................... 68

**Figure 3-11** Mass flow rate vs pressure drop and thermal resistance for OTS microchannels.... 70

**Figure 3-12** Return jet impingement architecture a) repeating cell b) labeled dimensions ......... 71

**Figure 3-13** Keysight M9506A AXIe chassis with heat exchanger ........................................... 75

**Figure 3-14** Air side radiator geometry: corrugated louver fins in triangular arrangement [100]77

**Figure 3-15** M9506A Keysight AXIe chassis fan curves .......................................................... 83

**Figure 3-16** Flow rate vs sound pressure level [103] ................................................................ 86

**Figure 4-1** Heat exchanger optimization for radiator outlet temperature: internal fin length vs internal fin thickness. Internal geometry: $mliq = 0.99$ kg $s^{-1}$. External geometry: total_rows = 19, $\theta$ = 28 degrees, LPI = 22, $F_{t,ext}$ = 0.10 mm, $F_{l,ext}$ = 12.70-10.80 mm and $FPI_{ext}$ = 19. ................. 89

**Figure 4-2** Heat exchanger optimization for radiator outlet temperature: internal fin thickness vs internal fin per inch. Internal geometry: $mliq$=0.99 kg $s^{-1}$. External geometry: total rows= 19, θ = 28 degrees, LPI = 22, $F_{t,ext}$ = 0.10 mm, $F_{l,ext}$ = 12.70 mm and $FPI_{ext}$ = 19. ................................. 91

**Figure 4-3** Heat exchanger optimization for radiator outlet temperature: internal fin length vs internal fin per inch. Internal geometry: $mliq$= 0.96-1.42 kg $s^{-1}$. External geometry: total rows = 19, θ = 28 degrees, LPI = 22, $F_{t,ext}$ = 0.10 mm, $F_{l,ext}$ = 12.70 mm and $FPI_{ext}$ = 19. ...................... 92

**Figure 4-4** Heat exchanger optimization for radiator outlet temperature: external fins per inch vs external fin length. Internal geometry: total rows = 25-11, $mliq = 0.96$ kg $s^{-1}$, $FPI_{int}$ = 25, $F_{l,int}$ =

1.0 mm, $F_{th,int}$ = 0.5 mm. External geometry: $FPI_{ext}$ = 15-25, $F_{l,ext}$ = 8.16 – 17.2 mm, LPI = 22, $\theta$ = 28 degrees. ........ 93

**Figure 4-5** Heat exchanger optimization for radiator outlet temperature: external fins thickness vs external fin length. Internal geometry: total rows = 11-25, $mliq$ = 0.96 kg $s^{-1}$, $FPI_{int}$ = 25, $F_{l,int}$ = 1.0 mm, $F_{th,int}$ = 0.5 mm. External geometry: $FPI_{ext}$ = 19, LPI = 22, $\theta = 28$ degrees. ........ 94

**Figure 4-6** Heat exchanger optimization for radiator outlet temperature: external louvers per inch vs theta (louver angle). Internal geometry: total rows = 19, $mliq$ = 0.96 kg $s^{-1}$, $F_{l,int}$ = 1.0 mm, $F_{th,int}$ = 0.5 mm. External geometry: $FPI_{ext}$ = 19, $F_{l,ext}$ = 12.7 mm. ........ 95

**Figure 4-7** M9506A temperature distribution ........ 99

**Figure 4-8** Total thermal resistance for all chips and heat sinks ........ 100

**Figure 4-9** Junction temperatures at 71°C fluid average temperature ........ 101

**Figure 4-10** Thermal resistance breakdown of water microchannels configuration 3-5a ........ 103

**Figure 4-11** Thermal resistance breakdown of water microchannels with TIM 2 configuration 3-5c ........ 104

**Figure 4-12** Thermal resistance breakdown of water jet impingement on the lid config 3-5b ........ 107

**Figure 4-13** Thermal resistance breakdown of FC72 jet impingement on the die configuration 3-5d ........ 111

**Figure 4-14** Thermal resistance breakdown of FC72 on the lid configuration 3-5b ........ 112

**Figure 4-15** Thermal resistance breakdown of different cooling configurations on Big Chip 1 ........ 113

**Figure 4-16** Microchannel cooling vs return jet impingement ........ 114

**Figure 4-17** Pumping power vs junction temperature for configurations 3-5a–d, water, GC50/50, FC72, and Jet fuel A-1 ........ 116

**Figure 4-18** Pumping power vs Big Chip 1 thermal resistance and heat exchanger total thermal resistance for Water, FC72, and Jet fuel A-1 ........................................................................ 120

**Figure 4-19** Pressure drop breakdown of FC72 return jet impingement on the die SD = 8, $D_j$ = 400 μm ........................................................................................................................ 121

**Figure 4-20** Pressure drop break down of Water return jet impingement on the lid SD = 10, $D_j$ = 300 μm ........................................................................................................................ 122

**Figure 4-21** Pressure drop breakdown of Water microchannel bypassing TIM 2 ..................... 123

**Figure 4-22** Pump curve Sta-Rite DPC 1/2 H.P. 1/115V, Medium Head Centrifugal Pump .... 124

**Figure 4-23** Ambient temperature vs total power consumption due to leakage current ............ 125

**Figure 4-24** Failure rate vs ambient operating temperature ...................................................... 127

**Figure 4-25** Acoustic limit vs power flux on the M9506A Keysight AXIE chassis ................ 128

**Figure 4-26** Heat exchanger length effect on maximum ambient temperature......................... 130

**Figure A-1** Ansys 2021 Steady State Solver boundary conditions……………………...……145

**Figure A-2** Ansys 2021 Steady State Solver results for junction to case thermal resistance.……146

**Figure A-3** Ansys 2021 design modeler inputs……………………….…………………...…147

**Figure A-4** PFD of state points used for hand calculations……………………………….…...148

# NOMENCLATURE

| Variable | Description | Units/Formula |
|---|---|---|
| $A_s$ | Surface area | $m^2$ |
| $\bar{A}$ | Manifold pressure drop constant | - |
| $a$ | Rattner a coefficient factor | - |
| $b$ | Rattner b coefficient factor | - |
| $Bi$ | Biot number | - |
| $c$ | Rattner c coefficient factor | - |
| $C$ | Heat capacity rate | $W\ K^{-1}$ |
| $c_p$ | Specific heat capacity | $J\ kg^{-1}\ K^{-1}$ |
| $C_l$ | Louvered fin geometric constant | - |
| $Cr$ | Heat capacity rate ratio | - |
| $COP$ | Coefficient of performance | - |
| $d$ | Rattner d coefficient factor | - |
| $D_h$ | Hydraulic diameter | m |
| $D_j$ | Jet diameter | m |
| $\bar{f}$ | Manifold pressure drop constant | - |
| $f$ | Friction factor | - |
| $H$ | Head | ft $lb_f$ $lb_m$ |
| $h$ | Enthalpy | $kg\ kJ^{-1}$ |
| $htc$ | Heat transfer coefficient | $W\ m^{-2}\ -K^{-1}$ |
| $HD$ | Nondimensional height | - |
| $j$ | Colburn factor | - |
| $k$ | Pressure drop k factor | - |
| $k_{eff}$ | Effective thermal conductivity | $W\ m^{-1}\ K^{-1}$ |
| $k_f$ | Fluid thermal conductivity | $W\ m^{-1}\ K^{-1}$ |
| $K$ | Rattner K factor | - |
| $L$ | Length | m |
| $L_l$ | Louver length | m |
| $L_p$ | Louver pitch | m |
| $L_{p,s}$ | Sound power level | dB |
| $LMTD$ | Log mean temperature difference | K |
| $\dot{m}$ | Mass flow rate | $kg\ s^{-1}$ |
| $Nu$ | Nusselt number | - |
| $NTU$ | Number of transfer units | - |
| $\Delta P$ | Pressure drop | kPa/psi |
| $Pr$ | Prandtl number | - |
| $p_{rms}$ | Root mean square of sound pressure level | Pa |
| $P_{wet}$ | Wetted perimeter | m |
| $Q_{chip}$ | Thermal dissipation power | W |
| $\dot{Q}$ | Heat transfer rate | W |
| $R$ | Required thermal resistance | $K\ W^{-1}$ |

| | | |
|---|---|---|
| *Re* | Reynolds number | - |
| *SD* | Nondimensional jet spacing | - |
| *SPL* | Sound pressure level | dBa |
| *T* | Temperature | °C |
| $T_j$ | Junction temperature | °C |
| *TDP* | Thermal dissipation power | W |
| $T_d$ | Tube depth | mm |
| $T_p$ | Tube pitch | mm |
| *UA* | Overall heat transfer coefficient | W $m^{-2}$ $K^{-1}$ |
| $v$ | Velocity | m $s^{-1}$ |
| $\dot{V}$ | Volumetric flow rate | $m^3$ $s^{-1}$ |
| $\dot{W}$ | Power | W |
| $x$ | Fans volumetric flow rate | $m^3$ $s^{-1}$ |
| $z$ | Microchannel position | m |

**Greek and Latin**

| | | |
|---|---|---|
| $\alpha$ | Aspect ratio | - |
| $\beta$ | Ratio of diameters | - |
| $\lambda$ | Eigen value | - |
| ε | Heat exchanger effectiveness | - |
| η | Efficiency | - |
| μ | Dynamic viscosity | kPa s |
| ν | Kinematic viscosity | $m^2$ $s^{-1}$ |
| Ψ | Constriction resistance | - |
| $\theta$ | Louver fin angle | degrees |
| $\tau$ | Dimensionless plate thickness | - |
| $\zeta$ | Resistance coefficient | - |

**Subscripts and Superscripts**

| | | |
|---|---|---|
| a | air | NA |
| ai | Air inlet | °C |
| ao | Air outlet PCB | °C |
| ao2 | Air outlet heat exchanger | °C |
| Contact | Contact resistance | K $W^{-1}$ |
| f | fluid | NA |
| j | Junction temperature | °C |
| j,max | Maximum junction temperature | °C |
| th,req | Requires thermal resistance | |
| PTP | Primary thermal pathway | W |
| STP | Secondary thermal pathway | W |

# CHAPTER 1. Introduction

## 1.1. Motivation for Research

As the world continues to grow digitally, the strain on electronic equipment continues to increase. For instance, each Google search consumes enough power to run a 60W light bulb for 17 seconds [1], and there are 3.5 billion google searches every day [2]. Moore's law has enabled this growth in the internet by doubling the number of transistors every two years on the IC (integrated circuit); but has stalled for power dissipation, clock frequency, and heat flux (Figure 1-1) [3,4]. Since 1985, there was a power law relationship between the TDP (thermal design power) and clock speed, relating to the years, until about 2004 when the 100W, and 3.0 GHz limit, were reached. Beyond this point, thermal dissipation powers and the clock speeds have stalled. Comparing a 2004 Pentium processor to a 2020 EPYC processor, the transistor size has shrunk from 90 nm to 7 nm, and the clock speed has lowered from 3.8 GHz to 3.3 GHz. The total number of transistors has remarkably increased from 125M to 41.6B, and the available surface area on the die has increased (112 $mm^2$ vs 1008 $mm^2$). The Pentium 4 processor thermal dissipation power clocked in

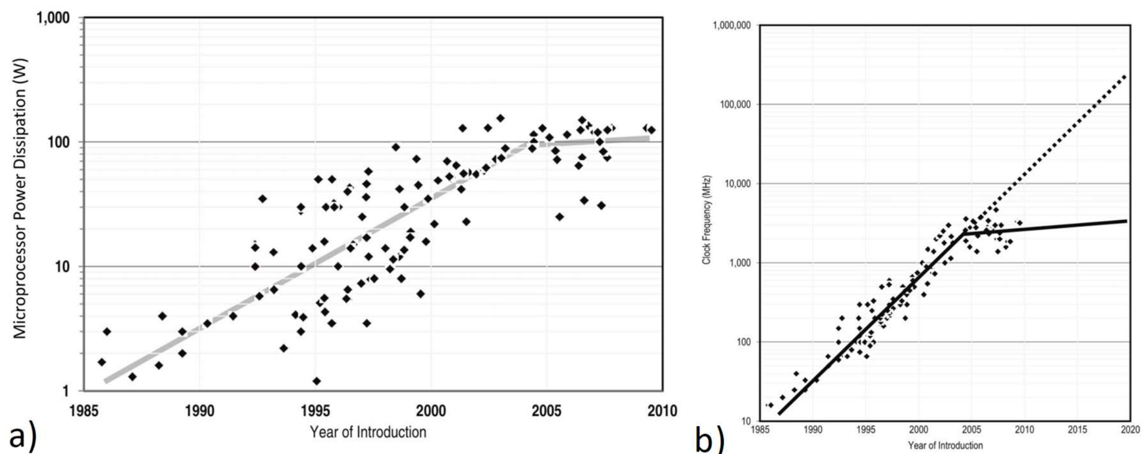


**Figure 1-1** a) Microprocessor power dissipation vs year b) Clock speed vs year [4,5]

at 89W but the new 2020 EPYC is 220W. This increase in heat load has partially been accommodated by increasing the die size but also has pushed air heat sinks to grow vertically, inhibiting densely packed printed circuit boards. Since 2004, to continue doubling transistors, the number of cores on a microprocessor has been increasing. Typical single-core, two-thread processors of 2004 such as the Pentium 4 extreme edition [5] can be compared to a modern AMD 7H12 64 core, 128-hyperthreaded processor of today. These smaller, higher density transistors are more efficient thus allowing Moore's law to continue [3]. Transistors have increased 333x but clock speed is actually lower as they utilize more parallel processing and spread the work out over 64 cores. TDP has less than tripled because it is so hard cool a 3000W chip that small. Heat fluxes have had to decrease to accommodate higher heat loads from 79.4 W $cm^{-2}$ down to 21.8 W $cm^{-2}$. Chip manufactures have been able to maintain the transistor trend without blowing through the roof on TDP because of advancements in fabrication methods allowing us to make smaller transistors. But as we now are at 7nm with plans for 5nm and 3nm, pretty soon, the atomic scale will be reached and reducing transistor size won't be an option anymore. As a result, other techniques, such as liquid cooling, must be employed in order to combat the growing thermal load.

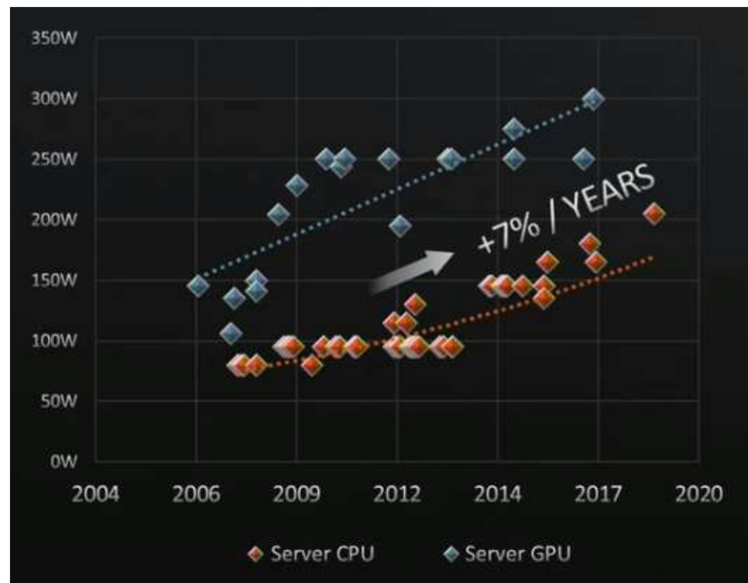


**Figure 1-2**, Thermal design power time in server CPUs and GPUs [3].

Figure 1-2 shows the past 15 years of server CPUs (central processing units) and GPUs

(graphic processing units) vs TDP. This trend has significantly slowed down compared to the 1980s to early 2000s that was shown in Figure 1-1 a). As these chips reach higher TDPs of 200W for CPUs, companies are switching towards liquid cooling solutions to handle higher density racks. The biggest challenge from the increasing TDP has been increased IC failures (approximately 50% of failures) [6,7]. The requirement to dissipate large heat fluxes and maintain low operating die or junction temperatures is critical for the longevity of the product and makes having a reliable cooling system extremely important [8]. These failures become particularly costly in various computationally intensive applications, which now includes manufacturing, AI, IoT, and test and measurement. In continuously operating manufacturing environments, component failures can result in significant losses in revenue. For this reason, thermal management is one of the top priorities when engineers are designing new products.

Significant research has focused on cooling techniques for high performance ICs such as microchannel cooling. Microchannel cooling solutions typically use higher thermal conductivity materials (e.g. silicon, aluminum, and copper) and have high heat transfer areas and coefficients. Another high heat flux cooling method that potentially enables a high heat transfer coefficients is return jet impingement but prior approaches are limited because they use high thermal conductivity materials. Return jet impingement conversely benefits from the material having a low thermal conductivity. One of the most common low thermal conductivity materials are plastics. Plastics are cheap and lightweight compared to silicon and copper. Additive manufacturing processes like DLP (Digital Light Projector) and SLA (Stereolithography Apparatus) are common methods for manufacturing return jet impingement systems cheaply out of different types of plastics. Temperature limits for Intel chips are typically either 75℃ or 85℃ [9] but are increasing towards 100℃ [10]. Beyond these temperatures, the failure rate exponentially increases. Operating

electronics at higher temperatures can degrade their life as well. Return jet impingement also does not require area enhancement like microchannels. This allows for the potential to change the packaging configuration and explore other cooling methods.

## 1.2. Research Objectives

One prominent electronics chassis of the past 20 years has been the Keysight PXIe. The PXIe chassis was first invented in the 1990s as a modular form factor chassis, but as computing power has increased, the thermal energy removal capability has been limited by the airpath of the PXIe. Figure 1-3a shows a picture of a 2020 18-slot Keysight PXIe chassis and its flow path in black. The flow path is not ideal because the air is ducted through large, empty volumes which

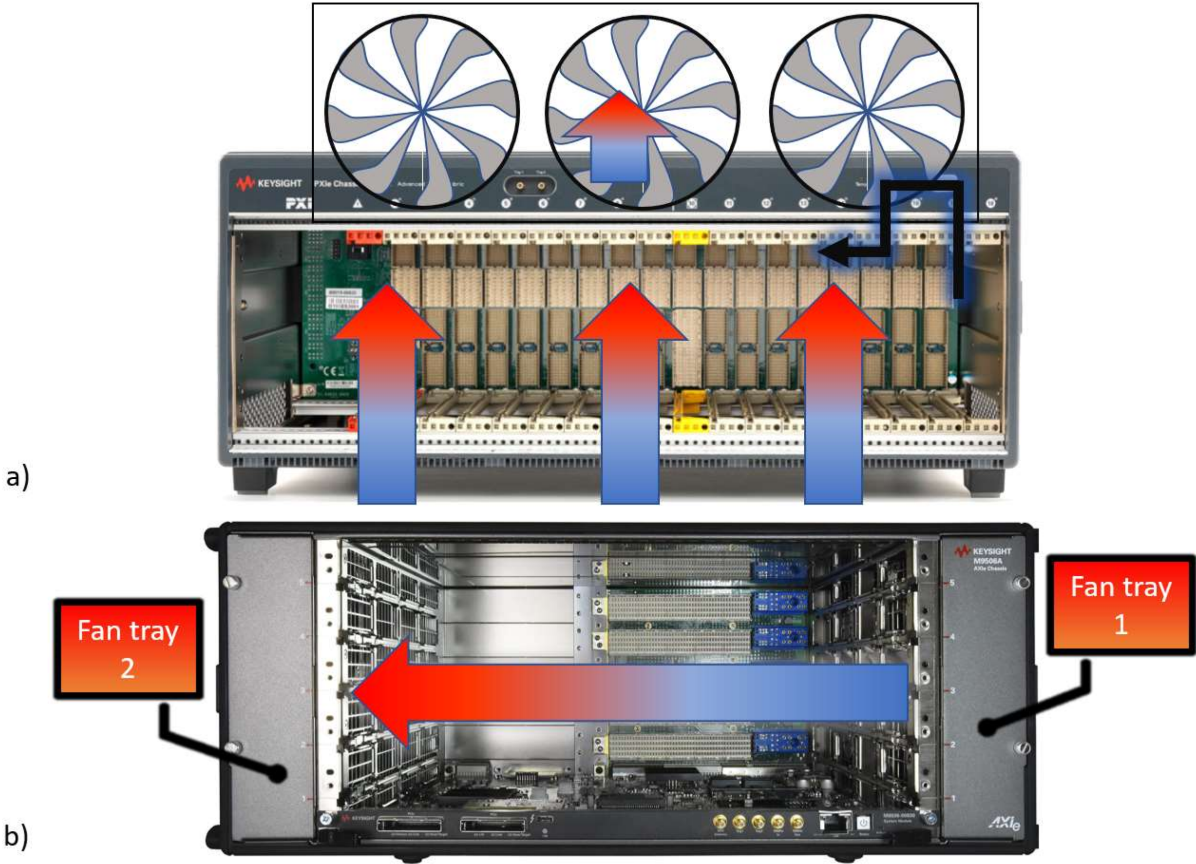


**Figure 1-3** a) Keysight PXIe chassis (M9018B) b) Keysight AXIe chassis (M9506A)

reduce computational density and there are many turns. The inlet air is sucked through the bottom of the chassis and up to cool the cards, then turns 90 degrees to move to the rear of the chassis where it is pulled out the back. Newer installations have used the next generation AXIe chassis shown in Figure 1-3b [11]. The AXIe chassis has a much better flow path and has less duct volume, utilizing more space for heat sinks, however, the fundamental limitations of air cooling are still being reached. When inadequate cooling is provided to 1 slot, relative to the particular board, in either chassis, the metal heat sinks are forced to grow their area vertically, expanding into multiple slots. This misaligns with the goal of densely packed printed circuit boards and thus requires other solutions.

It is clear that if computational power is to continue increasing, better cooling methods need to be established. The main objective of this effort is to investigate alternate cooling methods that will maximize the connector limit of a Keysight AXIe chassis. Currently, the Keysight AXIe chassis can supply 300 W/slot of cooling but has a maximum connector limit of 625 W/slot. The connector limit is based off the circuit the power is coming from. This is typically the standard 120V 30A outlet resulting in a maximum power draw of 3.6 kW. The chassis will be designed at 3.125 kW with a 475W clearance for other electronics on the circuit. The cooling methods investigated for this research will be microchannel cooling and return jet impingement cooling. These two liquid cooling methods will be modeled, and the results will be compared to determine which solution provides the most cooling capacity, energy efficiency, and the least convection thermal resistance. Based off the required flow characteristics, a pump will be sized and selected to investigate integration feasibility on the M9506A AXIe chassis. To summarize, this work will:

- Design a 3.125 kW liquid cooling system for the M9506A Keysight AXIE chassis

- Determine the best cooling configuration by looking at the benefits of removing a layer of TIM (Thermal interface material)
- Outline the benefits of keeping the chips cooler
- Optimize the energy efficiency of the system
- Determine the equivalent acoustic limit the system would produce using air cooling
- Size a pump that will fit into the system

## 1.3. Thesis Organization

This paper includes five additional chapters that detail the design of a high-performance electronic cooling system. Chapter two reviews literature on cooling methods for electronic systems on the micro and macro scales. Chapter three thoroughly describes the system architecture and assumptions for modeling both cooling systems. Chapter four presents a detailed discussion on the system results and performance of each component. The two cooling systems are compared based on their cooling capacity and feasibility of installation. Chapter five discusses the conclusions and recommendations. Finally, Appendix A provides simulation data confirming the junction to case thermal resistance and Appendix B provides sample calculations for the thermal resistance calculation of the electronic package, leakage current, heat exchanger modeling and the pump that will be required.

# CHAPTER 2. Literature Review

Miniaturization of high performance electronics is driving the market need for cost effective cooling solutions that are able to dissipate large heat fluxes [12]. To increase the computational performance of ICs, the number of transistors on such devices have more than doubled every two years and clock speeds have increased. This has resulted in an increasing TDP which needs to be rejected as heat. Significant research has been aimed at advanced and innovative methods for addressing this through microchannel cooling, jet impingement, hybrid microchannel jet impingement, and spray cooling among other techniques. This study will investigate channel dimensions used in literature and channel dimensions used in commercial applications to determine a realistic geometry for a scalable design for both microchannel and return jet impingement cooling. This chapter presents a review on cooling technologies focused for ICs. First, a description of ICs construction will be provided with detailed physics of the TIM followed by typical air-cooling methods from the literature and their performance. Then, liquid cooling studies for cooling similar packages will be reviewed. Finally, literature on the physics and relevant correlations of jet impingement heat transfer will be discussed. At the end of the chapter the research needs will be discussed based off the gaps in literature.

## 2.1. Integrated Circuit Description

In this section, an overview of the electronics package will be discussed. Primarily, the importance of the TIM (thermal interface material), the efficiency of the IC as it changes at various temperatures and the medium time to failure of ICs. The TIM is used to enhance the overall thermal conduction by reducing contact resistance. Figure 2-1 shows a typical electronics package for an air-cooled IC. The primary thermal path of heat rejection occurs through the finned heat sink and

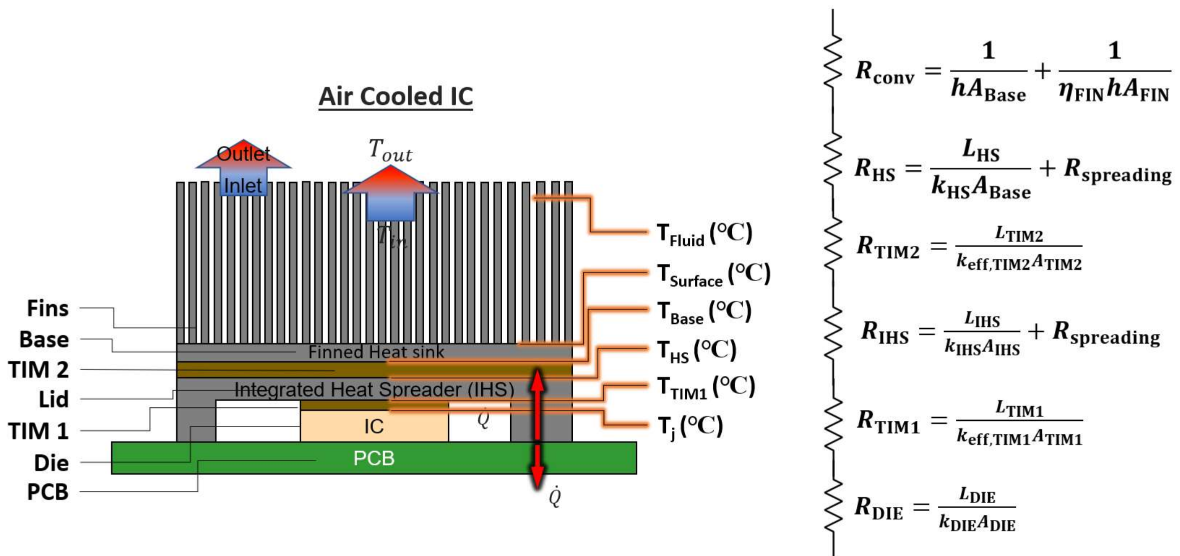


**Figure 2-1** Typical heat sink thermal pathway

some of the heat is rejected out of the bottom through the PCB (secondary thermal pathway). Neglecting contact resistances, the thermal resistance in the primary thermal pathway is conduction through the die, TIM 1, the IHS (integrated heat spreader), TIM 2, the finned heat sink and finally the heat is rejected to the air via convection. TIM 1 is typically a higher thermal conductivity TIM that the IC manufacture provides, and TIM 2 is a lower thermal conductivity TIM but typically has less thermal resistance due to its increased surface area. Depending on the TIM, air voids can arise between the TIM and the die causing localized areas of high thermal resistance (hotspots). Without a TIM, these air voids can cause up to 99% of the interfacial layer to be blocked [13]. In addition to using TIM, a certain amount of pressure is required to be applied to reduce the contact resistance further from the TIM. Any substance or material that fills the gap between the two contacting surfaces that has a thermal conductivity higher than that of air will decrease the contact resistance and should be used. TIM 1 and the lid are generally required to improve the reliability of the device by the IC manufacture to ensure there are not air voids between the die and the TIM.

As IC sizes scale to smaller dimensions, they become more efficient, using less power per switch; this is shown by the TDP not doubling when the total number of transistors do. The actual efficiency profile of the IC changes with junction temperature which is governed by its leakage current. The leakage current is an inefficiency of the IC and scales exponentially with junction temperature ($T_j$). As the transistor sizes decrease, the leakage current rises [14]. At 100 nm, it was 20% but expected to be 30-40% with smaller sizes. Without confronting this problem in the early 2000s, it could have accounted for 70% of the cache power at 70 nm. In Kim et al. [15] the cache on a microprocessor was investigated. In the study, it was determined that the cache consumed a majority of the power and it produced very high leakage rates on standby. Methods were used to reduce the leakage by 63%. This was done by identifying hotspots and putting global masks on them, predicting transitions by transitioning the cache line to the normal mode and tracking access moves by letting it periodically be in sleep mode. Wei [16] investigated a Ultra SPARC64 V max processor at the 90 nm manufacturing level. When the processor was operating at a power of 65W, 25W (38%) was lost due to leakage. When it was operating at maximum power of 120W, there was 65W (54%) leakage. In Krishnan et al. [17], when the chip temperature was lowered from 100°C to 70°C, the leakage power was reduced by 50%. At the lower manufacturing levels 45-nm to 28-nm, it was predicted that the leakage would amount for 40-50% of the total dissipation power [18].

Very high portions of power consumption can be accounted for by leakage at high temperatures. Figure 2-2 shows an example of leakage power of an IC at 100 nm with 0.7 V supply voltage [6]. The leakage power is based off multiple factors such as the input voltage and transistor size. If this voltage is too high or too low for a particular sized microprocessor, this leakage current will increase [19]. When the chip temperatures reach higher temperatures, further uncontrollable

temperature increases, or thermal runaway, can occur [19]. Thermal runaway is caused by the leakage current.

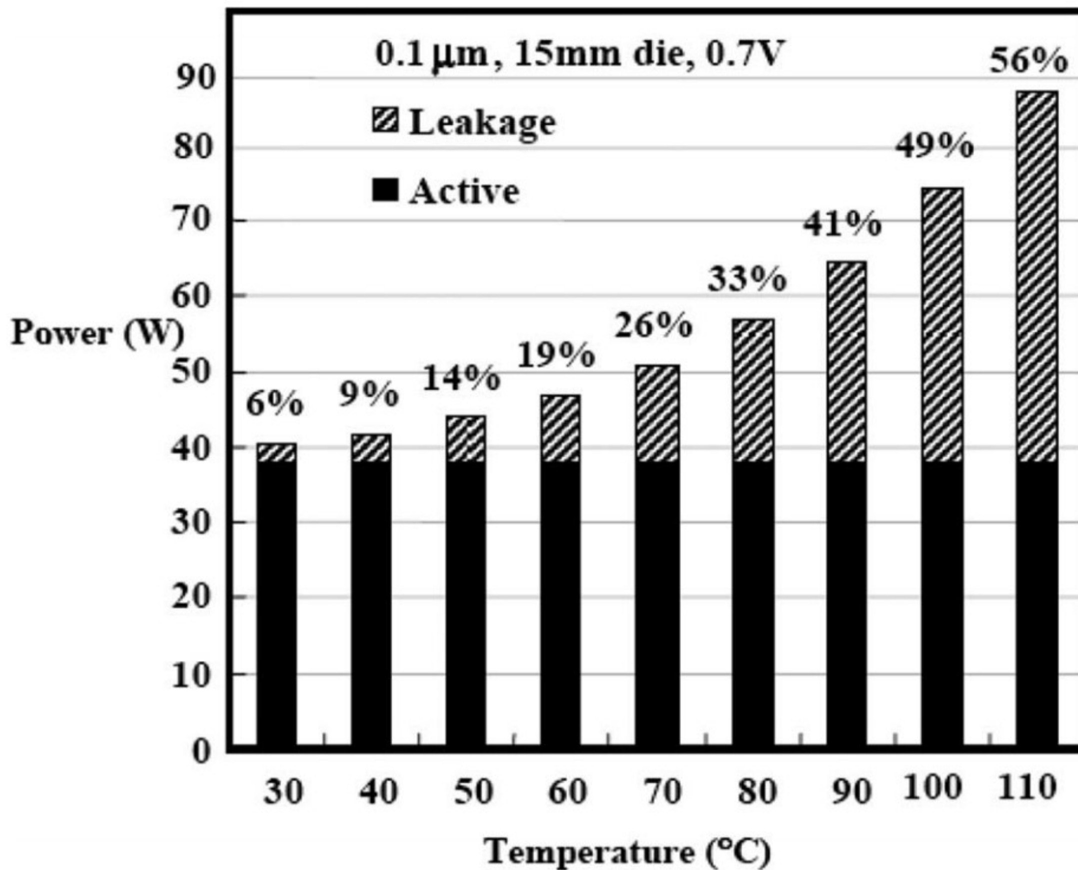


**Figure 2-2** Leakage power consumption vs chip temperature [7]

The 2004 Pentium 4 processor which had a thermal dissipation power of 89W and the new 2020 EPYC processor at 220W have a much different thermal resistance profile (from figure 2-1). For example, the die resistance would be $1/9^{th}$ for the modern processor compared to the generation of 2004 (1008 $mm^2$ vs 112 $mm^2$), assuming the same thickness and thermal conductivity. Similarly, the area of TIM 1 will be roughly 9x larger, decreasing the resistance of that to $1/9^{th}$, assuming the same properties. The larger area also decreases the spreading thermal resistance of the integrated heat spreader and the heat sink. These characteristics make the total heatsink thermal

resistance of the 2020 EYPC processor much lower than that of a 2004 generation, irrelevant of increased TIM thermal conductivity. This lower thermal resistance can accommodate higher power for the same temperature difference however, heat sinks still have had to grow vertically to accommodate today's heat loads, increasing $A_{fin}$, inhibiting densely packed PCBs (printed circuit boards). To accommodate the rises in heat loads of recent years, the packaging design has been optimized by increasing areas, reducing length scales, and changing materials to increase thermal conductivities. Extensive research has been accomplished focusing on increasing thermal conductivity of TIM's and will be reviewed as followed.

Chung [20] reviewed thermal fluids, pastes, solder and PCM's for use as TIMs. PCM's offered a high potential but further research was needed to investigate the contact resistance associated with them. Potential risks of PCM's include thermal instabilities and supercooling (cooling below the solidification point). Properties of good PCM's for TIMs are a melting temperature ($T_m$) slightly above room temperature, large heat of fusion, low viscosity, small or negative supercooling, good thermal cycling stability, and high thermal conductivity. Similarly, for thermal pastes, low viscosity and high thermal conductivity are desirable. Solder generally has a low melting temperature ($T_m$) and allows it to easily flow to create a thin sheet of good contact. In addition, solder tends to react with copper and form intermetallic compounds that further reduces thermal contact resistance. Of the three, solders showed highest thermal conductance. Solder's main disadvantage is that the manufacturing is more complex and requires heat to bond. Also, once attached, solder is difficult to rebond if it needs to be removed and re attached. This can be accomplished by reflow heating in an oven. Solders are also more rigid which could be problematic if unallowable thermal stresses arise as a result of a mismatched thermal expansion coefficient with silicon.

Figure 2-3 highlights the importance of TIM and contact pressure. A TIM without sufficient contact pressure is not an ideal TIM and looks like the TIM in Figure 2-2a. Figure 2-2b, and Figure 2-2c, show two surfaces without TIM, and with an ideal TIM, respectively. Real world TIMs are somewhere in between the non-ideal and ideal TIMs, as they are not perfect, but more pressure can shift this towards more ideal TIMs. The amount that the TIM can fill in the gaps depends on the material and on the pressure applied. Gwinn et al. [13] reviewed start-of-the art TIMs and split up conduction, and contact resistances to determine the means of heat transport. This was investigated by studying the optimal TIM for two high thermally conductive solids. There are two strategies for minimizing the contact resistance, the first being the use of TIM. Ensuring a high thermal conductivity TIM that can adapt to the imperfect surface features of the mating

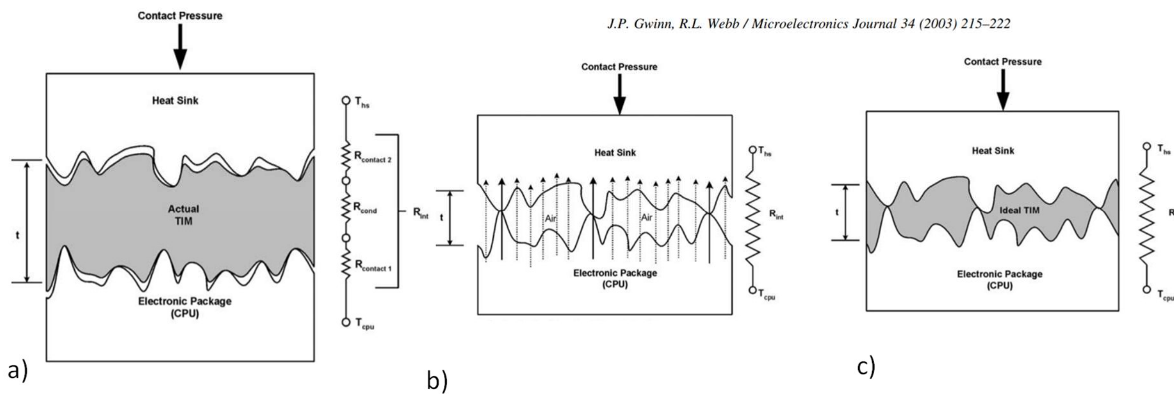


**Figure 2-3** Thermal interface material graphics a) Actual TIM in electronic packages b) No TIM in between two surfaces c) Ideal TIM in between two surfaces [26]

surfaces is crucial. The second is increasing the area in contact. This can be done by two methods. The first method for increasing contact area is applying sufficient contact pressure to flatten microroughness peaks on the material surface. The second for increasing contact area, without TIM, is smoothing the surface and minimizing roughness. Increasing pressure and smoothing the surface cannot be easily accomplished due limited allowable pressure on the PCB (printed circuit

board), and cost constraints. If these techniques are not employed, air voids can form as previously discussed.

Gwinn et al. [13] gave an example of the allowable pressure to be used on ICs. A copper plate and a copper lid are to be linked thermally as a CPU package and a heat sink. The CPU to be used is an Intel P4 processor. On the lid, there are a combination of surface roughness and surface non-flatness. The maximum pressure that can be applied for the 423-pin package is 25 lbf. This clip force results in 16.8 psi on the 961 mm$^2$ integrated heat spreader [21]. The reference heat sink clip commercial used only applies 5-16 psi [22]. Figure 2-4 shows thermal resistance of two different types of TIMs for varying thickness [23]. As the thickness increases so does the thermal resistance in a linear manner. This $R_{\mathrm{TIM}} = \frac{L}{k_{TIM}A_s} + R_c$ relationship is defined where L is the TIM

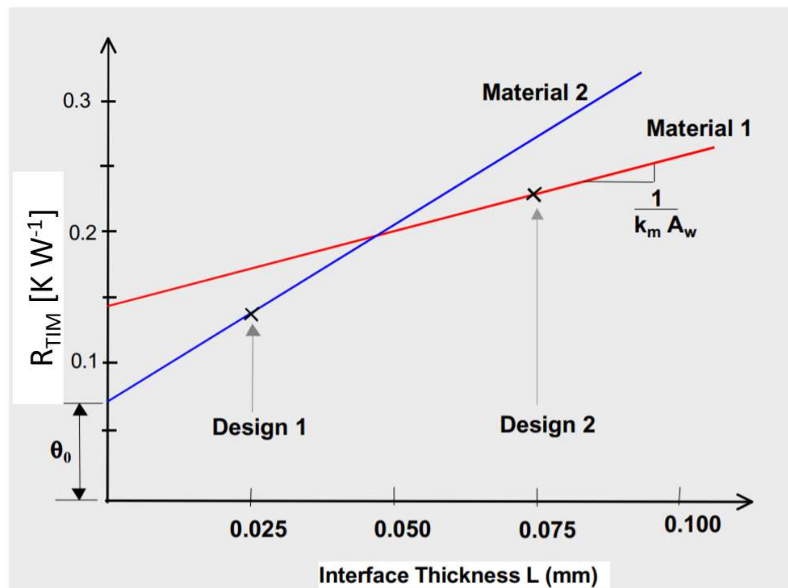


**Figure 2-4** Thermal resistance relationship between TIM and contacting surfaces [31]

thickness and $R_c$ is the contact resistance of surface 1 and 2. The slope here is a constant and inversely proportional to the thermal conductivity and area [24]. Certain materials can have better contact resistance but worse performance because their thickness is too great and thermal

conductivity isn't very high. Thus, for any material, the minimum thickness achievable from that material should be used.

Sim et al. [25] studied the effects of filling silicone rubber with thermally conductive, but electrically insulating, $Al_2O_3$ or ZnO fillers. Thermal gravimetry analysis (TGA) showed that filling silicone rubber with these materials increased thermal stability and thermal conductivity while decreasing the coefficient of thermal expansion (CTE). Using a filler loading of 10% by volume, thermal conductivity could be almost doubled from 0.145 W $m^{-1}$ $K^{-1}$ to 0.26 W $m^{-1}$ $K^{-1}$. This isn't very high as graphite pads can have thermal conductivities of 30 W $m^{-1}$ $K^{-1}$ but shows potential for modifying the coefficient of thermal expansions for metal TIMs. This is important because one primary physical attribute of TIM 1 is that the thermal expansion coefficient needs to closely match that of silicon to account for temperature changes without causing damage to the package.

Wei [16] studied high performance liquid metal TIMs to be used as TIM 1 in electronic packaging. These liquid metals need a thermal expansion coefficient near that of silicon to account for shrinkage/expansion at different operating temperatures. In his study, TIM 1 and TIM 2's dimensions were 18 x 18 x 0.2 mm and 40 x 40 x 0.06 mm respectively, with 48 W $m^{-1}$ $K^{-1}$ and 5.5 W $m^{-1}$ $K^{-1}$ thermal conductivities respectively. Thermal resistances of 0.013 K $W^{-1}$ and 0.0068 K $W^{-1}$ can be calculated without including contact resistance. Liquid metal TIMs such as In-10Ag (90% Indium and 10% silver) have been shown to have thermal conductivities up to 70 W $m^{-1}$ $K^{-1}$ [26]. In Koide et al. [26], In-10Ag with thickness of 0.2 mm achieved a thermal resistance of 0.0383 K $W^{-1}$. The contact resistance accounted for 77% for this liquid metal. The properties of In-10Ag required operating temperatures of 160-260°C to operate in the liquid phase; as this is above the temperature of the CPU, the liquid metal can stay in the solid phase during operation.

TIM 1 generally has higher thermal conductivity than TIM 2. TIM 1 needs a thermal expansion coefficient like that of silicon. Liquid metals pose the highest performance opportunity due to having low bulk thermal resistance and low thermal interface resistance. The risk of liquid metal leakage has been solved, but ultimately it comes down to cost for implementation. In high performance cases, CPU lids can be soldered directly to the cold plate to bypass TIM 2 [16]. Intel's eight generation processors that came out in 2017, codename Coffee Lake, solved these barriers and soldered the integrated heat spreader to the die to avoid thermal problems [27]. This can also allow higher ambient temperatures for the same performance, increase cooling efficiency, and accommodate increased TDP (thermal design power). A critical development in TIM technology for ICs.

Hanson et al. [28] extensively reviewed the recent advancements in thermal interface materials. The best materials for thermal interface resistances are liquid metals corresponding to around 2-5 $mm^2$ K $W^{-1}$. Graphene-based TIMs 100 μm thick were 10-20 $mm^2$ K $W^{-1}$. Graphite pads commonly used commercially are 52 $mm^2$ K $W^{-1}$ although most thermal pads contact resistance is in the range 100-300 $mm^2$ K $W^{-1}$. This can always be reduced by adding contact pressure. In Kempers et al. [29] the effective thermal conductivity of the graphite pad studied was 2 W $m^{-1}$ $K^{-1}$ at 15-29 psi. The properties of graphite pads can also be changed as well, such as to optimize it for a particular surface roughness and hardness. In Zhao et al. [30] a solder ratio of 1 was used on a graphite pad with Ag-Sn solder. The thermal conductivity in the vertical direction was 10 W $m^{-1}$ $K^{-1}$ and horizontal 1000 W $m^{-1}$ $K^{-1}$. The thermal resistance for a 150 μm sheet was 0.035 $cm^2$ K $W^{-1}$ at 30 psi. Graphite thermal conductivity reports up to 3000 W $m^{-1}$ $K^{-1}$ but this is along the graphite sheet plane and not in the direction of heat transfer [31]. This is because there are strong covalent bonds within the layers but weak van der Vaal's bonds connecting the layers

[32]. Faltstrom [32] extensively studied graphite pads and sheets for thermal interface materials. It was determined that the maximum thermal conductivity was 8 W $m^{-1}$ $K^{-1}$ at 3 MPa. As only 15 psi of clipping force is available, the thermal resistance relationship by Kempers et al will be used. The following summarizes the ideal TIM characteristics [13]:

1. High thermal conductivity
2. Easily deformed by small contact pressure to fill potential voids
3. Minimal thickness
4. Does not leak
5. Performance will not degrade with lifetime
6. Non-toxic
7. Manufacturing friendly (minimal complexity and user-friendly application)
8. Cost

### 2.1.1. Medium Time to Failure

There is a limited number of correlations relating electronic failure rates to junction temperatures, but a few have been developed and will be named here. Black [33] developed a well-known correlation relating the MTF (median time to failure) for individual transistors of semiconductors in hours, which has the exponential form:

$$MTF = \frac{1}{AJ^2} \exp\left( \frac{E_A}{K_B T} \right) \tag{2-1}$$

where $A$ is a constant that contains a factor involving the cross-sectional area, $J$ is the current density (per $cm^2$), $E_A$ is the activation energy (eV) which is approximately 0.68 eV for typical silicon, $K_B$ is the Boltzmann constant (eV/K) and $T$ is the absolute temperature (Kelvin) [33]. The U.S. Department of Defense also developed a correlation for the failure rate  as is expressed below [34]:

$$\lambda_p = \lambda_{BD} \pi_{MFG} \pi_T \pi_{CD} + \lambda_{BP} \pi_E \pi_Q \pi_{PT} + \lambda_{EOS} \tag{2-2}$$

where $\lambda_{\mathrm{BD}}$ depends on the part type, $\pi_{\mathrm{MFG}}$ depends on the manufacturing process, $\pi_{\mathrm{T}}$ is the temperature factor, $\pi_{\mathrm{CD}}$ is the die complexity factor which is a function of feature size and chip area, $\lambda_{\mathrm{BP}}$ is the package base failure rate, $\pi_{\mathrm{E}}$ is environment factor, $\pi_{\mathrm{Q}}$ is the quality factor, $\pi_{\mathrm{PT}}$ is the package type and $\lambda_{\mathrm{EOS}}$ is electrical overstress failure rate. This correlation was mentioned in Murshed and Castro [35] where they depict the failure rate exponentially rising beyond 75°C. The $\pi_{\mathrm{cd}}$ for this correlation was developed for a range of chip areas and feature sizes. Figure 2-5 plots the failure rate for different chip areas at 800 nm feature size where the orange line represents die size $0.70 < A_{\mathrm{s}} \leq 1.0$ cm$^2$, grey is $1.0 < A_{\mathrm{s}} \leq 2.0$ cm$^2$, gold is $2.0 < A_{\mathrm{s}} \leq 3.0$ cm$^2$, and red is the failure rate at 75°C. This correlation is highly dependent upon the chip surface area and feature size. The

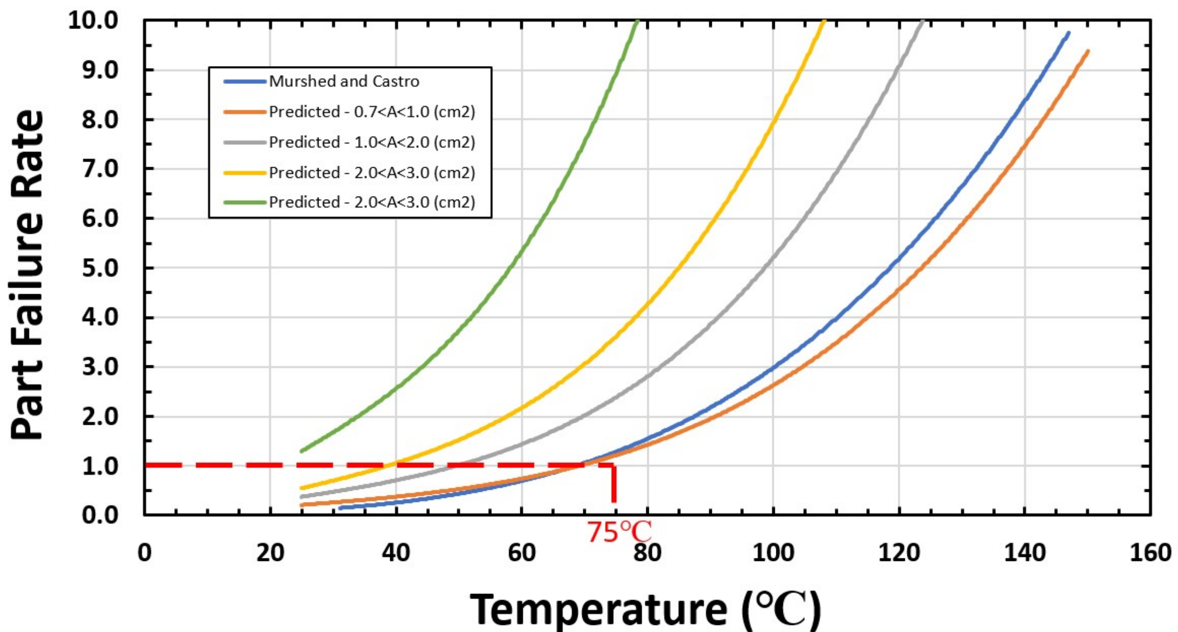


**Figure 2-5** Median time to failure vs junction temperature

line in green shows if one were to extrapolate the die size of $2.0 < A_{\mathrm{s}} \leq 3.0$ cm$^2$ down to 100 nm feature size as currently feature sizes have shrunk to 7 nm. By doing this the failure rate would be $2.5/10^6$ hrs at a 40°C junction temperature. This is clearly not the case as the IC would be failing when junction and ambient temperatures are equal although higher transistor densities could be

undergoing more stress and thermal management issues. The error of the correlation could be due to that when the correlation was developed it wasn't made to go down to the feature sizes that are currently possible today and doesn't account for transistor efficiency innovations. It is widely believed that the failure rate exponentially increases beyond 1 when the temperature passes beyond 75°C. Cengel's Heat Transfer textbook [36] notes that a rule of thumb is that the failure rate can be halved for each 10°C reduction of junction temperature. For this reason, when modeling the failure rates for the integrated circuits, the blue line will be used which is the same failure rate data that was published in Murshed and Castro [35].

## 2.2. Review of Technology Research

A vast majority of air and single-phase liquid cooling systems used in power electronics can be categorized into two overall cycles illustrated in Figure 2-6a, and Figure 2-6b, respectively. Performance of these systems in literature will be reviewed in subsequent sub sections and a table

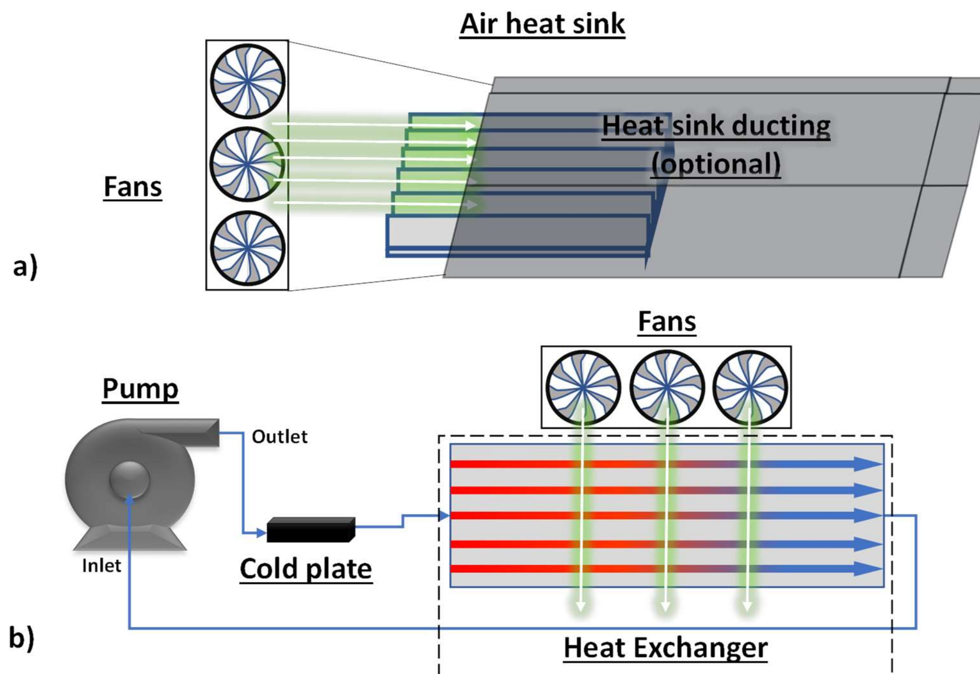


**Figure 2-6** Flow diagram a) air cooled electronics b) liquid cooled electronics

will be provided at the end of each to summarize. In Figure 2-6a, fans are used to blow air through the fins of the heat sink creating a velocity gradient along the wall. In order to increase this velocity gradient, and fix maldistribution, an air duct can be used to force airflow over the heat sink and increase flow resistance where the heat sink is not. This velocity gradient is directly proportional to the Nusselt number, and effectively, the heat transfer coefficient. Having a high wall velocity is key but it has fundamental limits due to the maximum pressure that fans can provide. Due to the mechanical nature of fans, the maximum pressure ratio for this type of machine ranges from 1.01-1.10 [37]. In Figure 2-6b, liquid is pumped into the cold plate where the fluid absorbs the chips heat. This heat then is transferred along with the cooling fluid into the heat exchanger where it is rejected to the ambient from the fans and then the cycle repeats.

### 2.2.1. Air cooling

Air cooling is the most common form of cooling ICs. In commercial settings, air cooling accounts for 86% of data centers highest density rack (n=431) [38] and is categorized into heat sink with or without a heat pipe. Depending on the application, a duct in between the fans and the

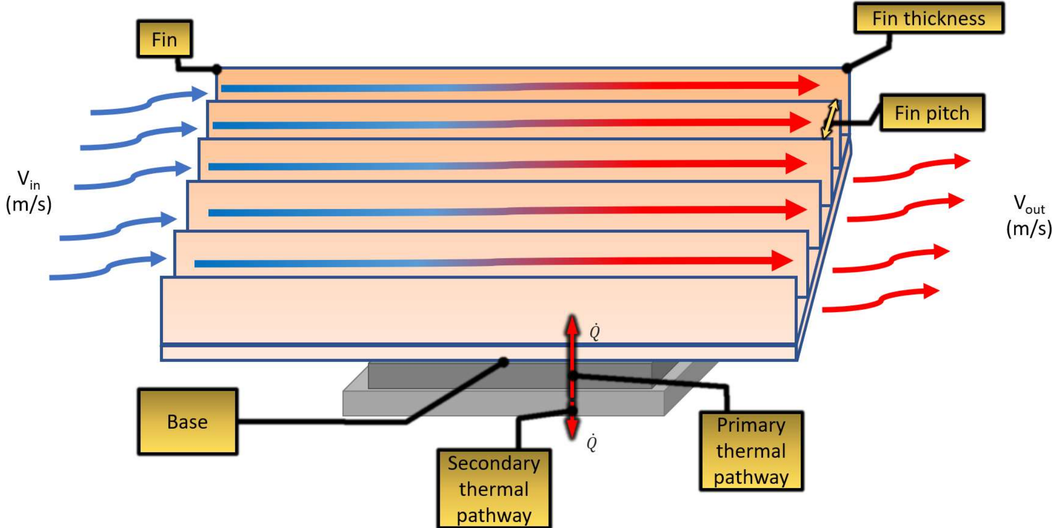


**Figure 2-7** Standard metal heat sink.

heat sink can be added to increase air flow and velocity gradients at the heat sink. The most basic form of air cooling is a heat sink shown in Figure 2-7. Here, a metal heatsink with fins is used to dissipate heat. Heat is conducted from the source through the base and spreads laterally and vertically up the fins. Air flows in-between the fins and picks up the heat which is removed and transferred out of the building via a facility HVAC system. The number of fins is optimized based on the heat transfer area and the flow rate of air over the fins. As the number of fins per inch is increased, the flow resistance of the air increases which causes an increased pressure drop. At a certain limit of pressure drop, the power required to drive the air through the fins will outweigh the benefits from the increase in heat transfer area. Numerical modeling is used with fan curves to determine an optimal number of fins/inch for a heat sink geometry. Research in air cooling technology is primarily focused on unprecedented structures that are difficult or impossible to create in regular manufacturing methods. Recent innovations in additive manufacturing have opened potential for scalability of these products.

Copeland [39] performed an analytical study to determine the optimum geometry for a 1U (rack slot height) server with forced convection over parallel plate fin heat sinks. It was shown that low fin pitch and high thickness resulted in the lowest thermal resistance, but a high pressure drop that was unreasonable for fans to provide. Next, they set the thermal resistance constant, calculated the air velocity, and determined that a medium fin pitch and reduced fin thickness minimized pressure drop. A modification of this geometry was studied in CFD by Freegah et al. [40] where these plate fin heatsinks had a fillet profile. Addition of these fillets resulted in superior performance compared to conventional by enhancing surface area and heat transfer coefficient. The best fillet profile was corrugated half-round pins and symmetric half round pins resulting in

25.1% and 29% reduction in thermal resistance respectively, with a 34.5% increase in heat transfer coefficient.

Plate fin heat sinks are commonly manufactured by bonding, folding, modified die-casting, forging, skiving and machining [41]. Folding, modified die casting and skiving can reach fin thicknesses as low as 200-300 microns. These manufacturing methods limit the possible manufacturable geometries especially depending on the scalability of the desired heat sink. Modular additive manufacturing could innovate new solutions further reducing costs of making custom metal heat sinks.

Al-damook and Alkasmoul [42] studied the thermal resistances of five different compact (plate-pin) air cooled heat sink configurations and compared them to conventional regular plate fins. These pin fin heat sinks had circular, square, elliptic, drop form and NACA 0050 turbulators in between conventional rectangular extruded fins. These heat sinks showed lower thermal resistance compared to conventional. Utilizing NACA airfoils as turbulators showed the best performance for thermal resistance and pressure drop. The splitter plate pin-fin heat sink showed the best thermal resistance at the cost of the highest pressure drop. This is an alternative method to expand the cooling envelope of air heat sinks; however, higher cost and increased manufacturing complexity is associated.

The second air-cooling method is one with an embedded heat pipe. Heat pipes are a highly efficient transportation mechanism for spreading heat from the package to the heat sink because it reduces spreading resistance compared to conduction of high thermal conductivity materials such as aluminum and copper. The heat pipe has a two-phase vapor-liquid mixture inside that flows back and forth from the condenser to the evaporator as shown in Figure 2-8 [43]. A wick is located inside to transport the fluid via capillary action and does not require a pump. Heat pipes allow

localized heat sources to be spread with extremely high effective thermal conductivities >100,000 W m$^{-1}$ K$^{-1}$ [44]. Another benefit to heat pipes is that the fluid is isolated in a closed system, minimizing spill risk and eliminating moving components which increases reliability.

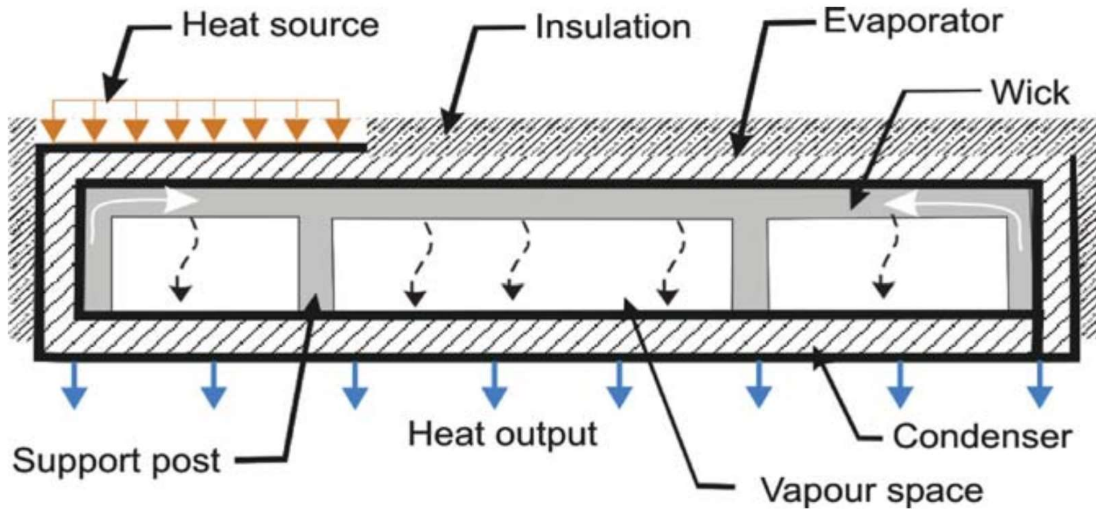


**Figure 2-8** Cross-section of heat pipe wick structure

Chang et al. [45] studied the performance improvement of two U shaped embedded heat pipes for electronics cooling. First, the heat pipes were investigated for their best point of efficiency which was 25W. At this point, the fluid flow in the heat pipe achieved the lowest thermal resistance. Beyond this point, the heat pipe thermal resistance increased as the temperature and pressure rose, causing increased vapor at the condenser inlet which decreases performance. The maximum heat allowed by these heat pipes was 55W. Beyond this point, the heat pipe burned out as the outside temperature reached 100°C. When the two heat pipes were embedded in the heat sink, the conduction resistance decreased from 0.15 K W$^{-1}$ to 0.10 K W$^{-1}$. In this investigation, the heat pipes transported 33-37% of the total TDP, where the rest was transported by conduction through the aluminum heat sink. The total thermal resistance of the heat sink was at its minimum of 0.27 K W$^{-1}$ at 140W load in the 1U form factor.

Xie et al. [46] performed experimental investigations on a newly designed heat pipe-heat sink with a modified condenser and wick structure. Results determined that the heat sink could effectively transfer 420W at a thermal resistance of only 0.118 K $W^{-1}$. The flow rate and pressure drop were 71 $m^3$ $h^{-1}$, and 30 Pa, respectively. At 200W, the heat sink thermal resistance was 0.13 K $W^{-1}$ and at 160W was approximately 0.16 K $W^{-1}$.

Wang et al. [47] studied the energy saving potential by adding embedded heat pipes to metal heat sinks. They determined that a 50% reduction in energy can be made by using a flat plate heat pipe heat sink compared to a plate fin heat sink with no heat pipes and 65% can be saved by 5 embedded heat pipes. This energy savings was due to the thermal resistance of the heat pipe heat sink being less than conventional heat sink thus, allowing higher inlet temperatures or reduced fan power to achieve the same required cooling affect. In another study by Boukhanouf et al. [43], the spreading resistance was reduced from 0.0278 K $W^{-1}$ to 0.0007 K $W^{-1}$ by using a flat plate heat pipe vs copper plate fined heat sink. Flat plate heat pipes present a significant decrease in spreading resistance however, there is an increased cost by adding these, of which is greater than embedded heat pipes.

In any case, the air-cooling envelope is hitting fundamental limits. The minimum thermal resistance for a 1U heat sink is approximately 0.16 K $W^{-1}$, and the height dimensions in this study are smaller than that. Another challenge is that the air temperature profile may be non-uniform, depending on the thermal load and distribution in the rack. This temperature non-uniformity can be significant as the air absorbs heat from high powered chips. An example can be seen in Figure 2-9 where 20 sCFM is used on each chip to cool an array of 140W chips, the air heats up by 12℃ before reaching the next chip, thus reducing cooling performance. This increase can be significant as 50℃ inlet air can quickly heat up to 62-74℃. In order to avoid large temperature differences

between front and rear chips, a large heat spreader is normally attached to both chips which reduces the temperature difference in the flow direction at the chip level. This problem is not as evident or severe with liquid cooling because fluids such as water have three orders of magnitude higher density and four times the heat capacity compared to air. This higher thermal mass fluid can absorb more heat for the same temperature difference (i.e. 1 LPM for the same conditions will only rise 2°C).

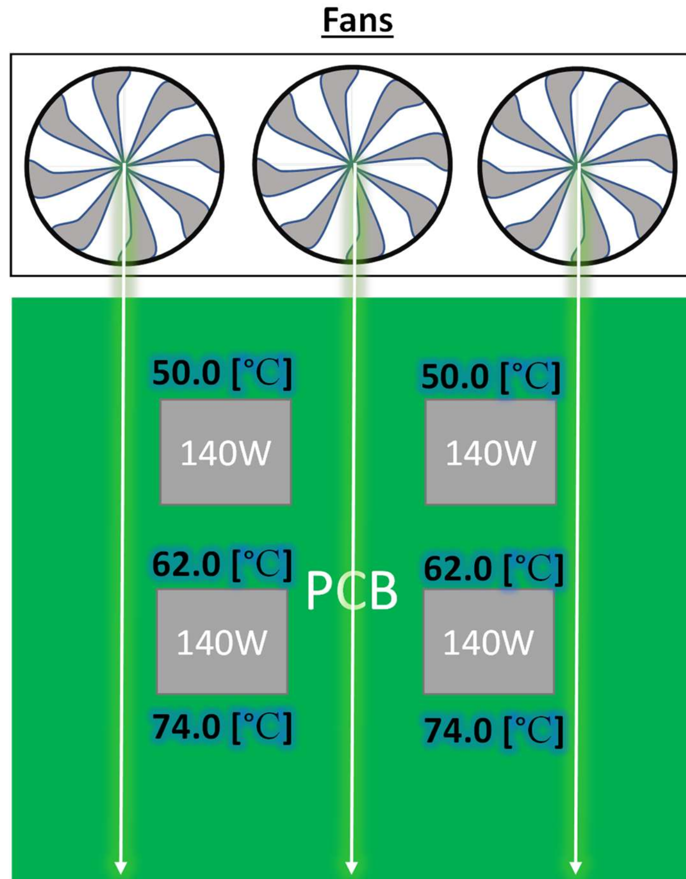


**Figure 2-9** Example chip array temperature distributions

Further cooling capabilities with air can be reached by increasing fan speed, heat transfer coefficient, surface area, junction temperature ($T_j$), or reducing spreading resistance and thermal resistance of the TIMs [42]. All of these are already at their limits though. The fan speed cannot be increased because there are already acoustic limits being reached and increased fan speed will exacerbate this. Furthermore, increase of fan speed also comes at the cost of reduced reliability of the fan and increased power consumption [42]. Increasing surface area is limited due to the space constraints of the application and reducing spreading resistance is already being incorporated by means of heat pipes. The cooling performance for convection heat transfer is based off Newton's Law of Cooling:

$$Q_{\text{chip,i}} = htc \cdot A_s \cdot \Delta T \tag{2-3}$$

where $htc$ is the heat transfer coefficient, $A_s$ is the surface area and $\Delta T$ is the temperature difference between the average fluid temperature and the surface temperature. The inlet fluid temperature rises however for higher powered chips because it is the average inlet temperature minus the surface temperature, making the same heat transfer and surface area perform worse by resulting in high junction temperatures. There are two ways to increase the heat rejected, $Q$, without changing the inlet fluid temperature: increase surface area or increase heat transfer coefficient. Microchannels employ both of these techniques. Increasing the heat transfer coefficient generally requires increased velocity gradients, smaller hydraulic diameters or increasing turbulence. This is dependent on the fluid delivery device and the manufacturing capabilities. Similarly, the ability to increase surface area is limited. In a confined space, the only option is to increase the fins per inch but benefits are dependent on the fluid delivery devise. With air, this means higher flow rate fans. However, if the product is to operate in an office environment, it needs to meet office environment acoustic regulations.

### 2.2.2. Microchannel Cooling

Microchannel cooling is the most common form of liquid cooling for integrated circuits because it can generate high heat fluxes. In one study, by Mudawar and Bowers [48], a heat flux of 27,600 W $cm^{-2}$ was reported, however, the pressure drop of 153.4 bar (2225 psi) was also extremely high and would require unreasonable pumping power. These results demonstrate that, similar to air cooling, a balance between heat transfer coefficient and pressure drop is critical in microchannel cooling applications. Countless research examinations and case studies have been performed to describe the performance of microchannel cooling on high heat flux devices. Key results on the optimal dimensions to minimize the microchannel thermal resistance will be

reviewed along with the die and package dimensions to aim the die sizes of this study. Lastly, liquid cooling system level designs with microchannels will be reviewed.

A microchannel cooling device was first investigated in a seminal 1981 paper by Tuckerman and Pease [49]. In their experiment, a heat flux of 790 W $cm^{-2}$ was rejected at a thermal resistance 0.09 K $W^{-1}$. At the time, this presented a 40-fold improvement in heat flux dissipation of an integrated circuit. This was accomplished with 50 μm wide channels, 50 μm thick walls, and 300 μm deep channels. It was concluded that the heat transfer coefficient scales inversely to channel width and that minimizing channel width will minimize thermal resistance.

Zhang et al. [50] performed experimental tests on a single-phase microchannel heat sink for two die sizes: 12 mm x 12 mm and 10 mm x 10 mm. The cold plate base finned dimensions were 15 mm x 12.2 mm, closely covering the die package area of each separate die studied. The channel width and depth were 210 μm and 2 mm, respectively. The TIM used was an Aavid Sil-free 1020 thermal grease with thermal conductivity of 0.79 W $m^{-1}$ $K^{-1}$. These resulted in thermal resistances ranging from 0.32-0.44 K $W^{-1}$ for the large die and 0.44-0.59 K $W^{-1}$ for smaller die. This 25-30% difference in thermal resistance is attributed to the increase spreader resistance of the smaller package as larger dice are significantly easier to cool. In both cases, these thermal resistances are relatively high due to the small package sizes and poor thermal interface material which have since significantly increased making it easier to cool higher TDPs. Modern FPGA die packages can be 25 mm x 25 mm, greater than 4x improvement in surface area from the previous study.

Hung et al. [51] numerically studied the effect of increasing outlet channel width and height of a porous microchannel heat sink. They determined that by increasing the outlet channel width, the thermal resistance and pressure drop decreased, however, the pressure drop was still greater

than non-porous microchannel heat sinks. They concluded that it was unclear if the performance increased by adding a porous material because the overall performance also depends on whether the fluid delivery device can overcome the additional pressure drop.

Ramakrishnan et al. [52], performed experimental simulations with a microchannel cold plate directly mounted onto a mock chip in the form of a two-die package. Here, the cold plate was attached in a new proposed configuration by removing TIM 2 and using one TIM between the dice (two die) and the cold plate. The die packages being cooled were a 90W FPGA (field-programable gate array) and a 210W Intel SKX (Skylake) with total footprint 26.49 $cm^2$. The study determined that by removing a layer of thermal resistance in the conduction path, higher allowable coolant temperatures were available for the same junction temperature. In a data center, this allows the possibility for only an economizer to be used with ambient temperatures and significantly reduces the chiller power consumption by raising the ambient temperature in data centers or raising coolant temperature. Dissimilar to the vapor compression cooling cycle, an economizer replaces the

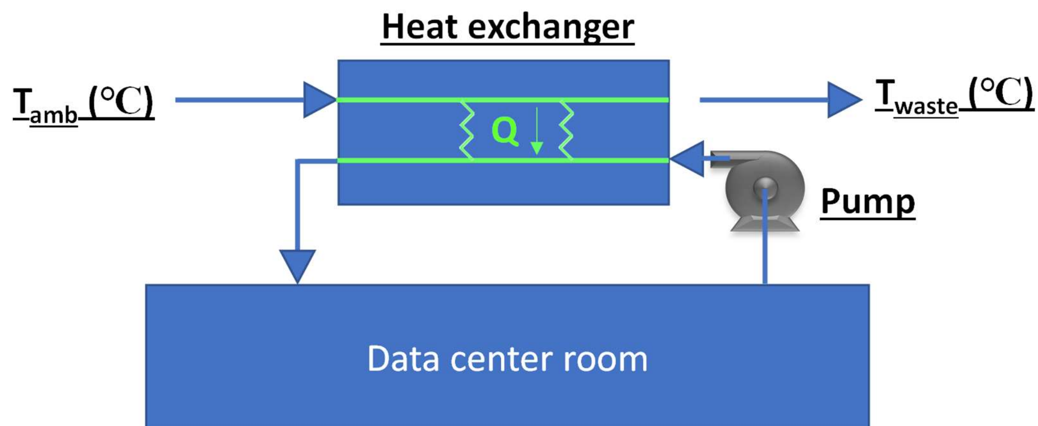


**Figure 2-10** Schematic of an economizer loop

compressor and expansion valve with a pump and refrigerant with fluids like water or glycol. The cycle for this can be seen in Figure 2-10 where heat is rejected to the ambient and cooling can be brought back from the outside when ambient temperatures are low enough. The lowest thermal

resistance of 0.0367 K $W^{-1}$ was obtained at a flow rate and pressure drop of 1 lpm and 5.51 kPa, respectively. The TIM in these experiments was a thermal grease, HT-C3200, with thermal conductivity of 6.0 W $m^{-1}$-$K^{-1}$. Comparisons were made to a compressible graphite sheet TIM with thermal conductivity 7.8 W $m^{-1}$-$K^{-1}$. A further improvement in performance was made by the new novel graphite TIM.

In further investigation by Ramakrishnan et al. [53], a single die package was cooled in the same configuration by removing TIM 2, and using one TIM in between the die and the cold plate. The effective heat transfer area of this chip was 6.45 $cm^2$ and a heat flux of 31 W $cm^{-2}$ was dissipated at a maximum power of 200W. The minimum thermal resistance of the cold plate was achieved at 0.03 K $W^{-1}$ at a flow rate and pressure drop of 0.75 lpm and 4.21 kPa, respectively. The pressure drop lowered to 2.76 kPa when the operating temperature increased to 45°C, increasing the COP (coefficient of performance) as calculated by dividing the heat removed by the work to remove that heat. The pumping power decreased due to the decreased dynamic viscosity at elevated temperatures. The TIM used was a silicone-free super thermal grease from Shin Etsu [54]. The thermal conductivity was 6 W $m^{-1}$ $K^{-1}$ and thermal resistance measured to be 0.0519 K $W^{-1}$. An OTS (off the shelf) cold plate was used with fin thickness of 100.6 μm, channel width of 154.3 μm, and fin height of 2.02 mm.

Wei et al. [55] performed experimental and numerical simulations to determine the effect of stacked microchannel heat sinks for microelectronics applications. They determined that parallel flow had the lowest thermal resistance while counter flow had the best temperature uniformity. The worst thermal resistance of 0.09 K $W^{-1}$ was in the counter flow configuration while the parallel flow configuration achieved 0.05 K $W^{-1}$. These low thermal resistances were accomplished by small channel dimensions of approximately 50 μm manufactured via DRIE (deep

reactive ion etching) in silicon. This solution is not currently a scalable cost-effective design even though it produced the lowest thermal resistance of the microchannels studied.

Chainer et al. [56] investigated a microchannel configuration with embedded microchannels in the 20 mm x 20 mm silicon die with a two-phase dielectric. The newly proposed configuration with embedded cooling on the die consisted of 20 channels that expanded radially, with a pin fin array 80 µm diameter with 200 µm pitch. The two-phase dielectric attained a thermal resistance of 0.038 K $W^{-1}$ at roughly 300 kPa of pressure drop.

Fusiara et al. [57] performed analysis for Xilinx and designed a cooling system for a densely packed array of 12 printed circuit board assemblies (PCBA), containing an FPGA and various other heat loads resulting in a height density of 777.2 W $U^{-1}$. The liquid cooling system housed a 12-slot Gemini LRU with 200W boards, of which 121W was consumed by the FPGA. Shown in Figure 2-11, this system is very similar to the system being designed and resembles the

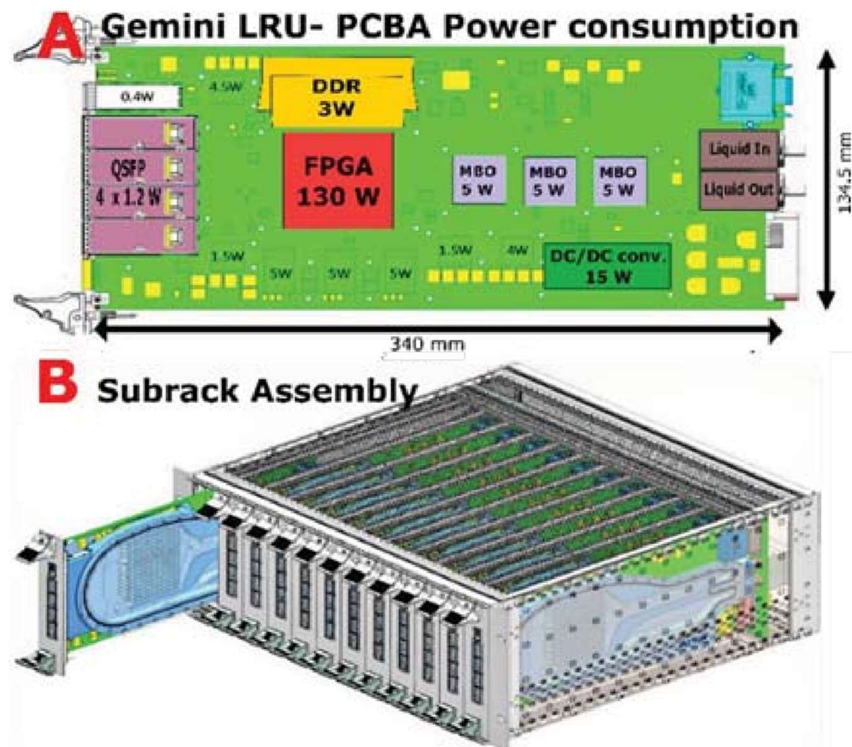


**Figure 2-11** 12-Slot Gemini LRU

form factor of the PXIe chassis. The cold plates investigated were rectangular pin fins, meandering channels and straight fins. Meandering mini-channels had the lowest thermal resistance for the same pressure drop. Die temperature was maintained at 60°C with 33°C inlet resulting in a thermal resistance of 0.27 K $W^{-1}$. This high thermal resistance comes from the mini-channel thickness being set to 2 mm due to manufacturing and cost limitations. This relatively high channel thickness was selected due to scalability and manufacturing capabilities. The estimated cost of these cold plates at 288 units was roughly 300 euros each. If a higher allowable cost was tolerable, smaller channel dimensions could be used to further decrease the thermal resistance of this microchannel cold plate.

Lucchese et al. [58] performed analysis on a 1.5U Facebook Open Compute Windmill V2 server with direct liquid cooling to determine the potential for waste heat recovery. While maintaining the junction temperature within safe operating limits, they investigated the lowest flow rates to maximize outlet temperature. At a flow rate of 1.9 g $s^{-1}$, the water outlet temperature rose from 30°C to 60°C. The waste heat availability from the OTS microchannels was increased from two sources: a) the reduction of thermal resistance between junction and fluid, and b) decreased mass flow rate due to more efficient cooling. David et al. [59] investigated a chiller-less data center of warm water cooled IBM System X volume servers with a height density of 345 W $U^{-1}$, where liquid microchannel cooling was implemented. The lowest ambient to fluid temperature recorded here was 18.5 °C. Kadhim et al. [60] analyzed a rack of thirty 1U Sun Fire V20z with direct-to-chip liquid cooling and two coolant pumping configurations. They found that by locating the pump in a central location resulted in the lowest mal distributions.

One of the above microchannel designs had a minimum thermal resistance of 0.03 K $W^{-1}$ however, as this approaches zero, the minimum attainable thermal resistance will be that of the

conduction resistance through the package. In order to reach maximum cooling, embedded microchannels have been investigated as well. Jung et al. [61] performed experiential simulations on an embedded silicon microchannel cold plate with 25 parallel channels with fin thickness of 50 µm, channel width of 150 µm and fin height of 75 µm. The results showed a thermal resistance of 0.68 K $W^{-1}$ at 0.1 lpm due to the small area selected. Anjali et al [62] investigated embedded microchannels in 3D stacking with fin thickness of 100 µm, channel width of 100 µm and fin height of 200 µm. The results showed a thermal resistance of 0.36 K $W^{-1}$ at 13.79 kPa of pressure drop.

The above microchannel literature review shows that the key parameters from microchannel heat exchangers include the lowest attainable channel thicknesses while maintaining large fin heights, of which both are dependent on the manufacturing method used. These articles

**Table 2-1** Microchannel literature review summary

| Name | Working Fluid | $\Delta P$ (kPa) | $q''$ (W $cm^{-2}$) | $R_{th,cp}$ (K $W^{-1}$) | $D_h$ (µm) | $F_{th}$ (µm) | $Ch_{th}$ (µm) | $F_{hieght}$ (µm) | $L$ (mm) |
|---|---|---|---|---|---|---|---|---|---|
| Tuckerman and Pease [49] | Water | 213.7 | 790 | 0.09 | 85.8 | 50 | 50 | 302 | N/A |
| Zhang et al. [50] | Water | 10.0 | 85 | 0.05 | 380 | 200 | 210 | 2000 | 15 |
| Ramakrishnan et al. [52] | Water | 5.5 | 31 | 0.037 | N/A | 150 | 200 | <3500 | 72 |
| Ramakrishnan et al. [53] | Water | 4.2 | 31 | 0.030 | 298.1 | 100.6 | 154.3 | 2020 | 31.5 |
| Fusiara et al. [57] | Water | 50.0 | N/A | N/A | 3652 | 2000 | 2000 | 10500 | N/A |
| Wei et al. [55] | Water | N/A | 71 | 0.05 | 106.1 | 94 | 56 | 500 | 10 |
| Jung et al. [61] | Water | 2.48 | 250 | 0.68 | 100 | 50 | 150 | 75 | 5 |
| Lucchese et al. [58] | Water | N/A | 3.76 | N/A | 490 | N/A | N/A | N/A | 30 |
| Chauhan et al [62] | Water | 13.8 | 4.74 | 0.36 | 133 | 100 | 100 | 200 | 12.5 |
| Chainer et al [56] | R1234 ze | 300 | 75 | 0.038 | N/A | N/A | N/A | 150 | N/A |

have been summarized in Table 2-1. Some of the literature reviewed is aimed towards future manufacturing capabilities and is not scalable for the modern consumer. In Chapter 3, OTF (off the shelf) microchannel heat exchanger dimensions will be reviewed and compared with dimensions studied in this literature review. Also, in this review, die sizes were studied and have increased since the early 2000s (based on the reference years), making larger TDPs easier to cool. Common package sizes for FPGAs have been determined to be around 25 x 25 mm. Furthermore, innovations in TIM technology have decreased the magnitude of thermal resistance that the TIM accounts for resulting in further inherent decreases in the overall thermal resistance. The one study of a custom designed cold plate for a Gemini LRU showed the barriers of cost and microchannel dimensions when the economy of scale is not present. The literature reviewed here will be used as a benchmark for the designed cold plate in this study.

### 2.2.3. Jet impingement

Jet impingement cooling is a promising technology due to its high heat and mass transfer rates which are achieved by forcing fluid through nozzles at high speed onto a surface as shown by the velocity contours in Figure 2-12 [63]. When the jets impinge on the surface, the fluid boundary layer is decreased, and extremely high heat transfer coefficients are achieved. The biggest challenge which has limited jet impingement adoption has been the heat transfer losses which occur from jet interference. In this section, the physics of

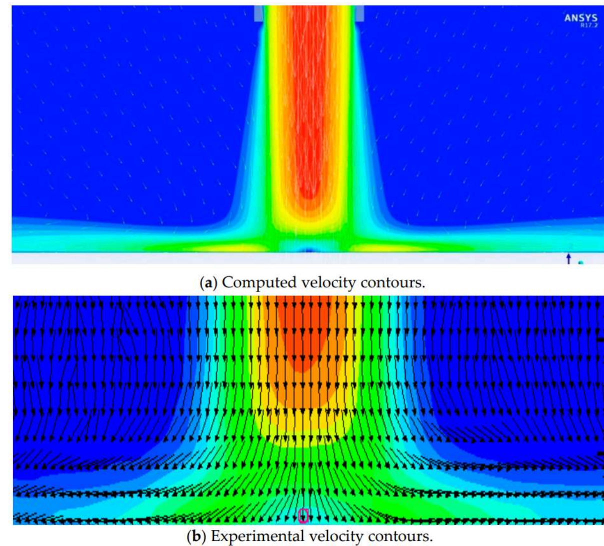


**Figure 2-12** Velocity contours of impinging jet on surface [63]

impinging jets will be discussed followed by jet-jet interference studies and return jet impingement models to solve this issue.

Geometrical characteristics that effect the heat transfer of the impinging jet are $D_j$ (jet diameter), $H/D_{jet}$ (nondimensionalized jet height), and $S/D_j$ (nondimensionalized jet spacing). The effect of these parameters will be discussed in detail in subsequent sections along with the micro scale physics of the jet. Figure 2-13 shows the velocity contours for the four main regions of jet impingement: initial free jet, decaying jet, the stagnation point and the wall jet [64]. If the nozzle is within a $D_j$ of 2, the free jet region may not exist because the stagnation region of high pressure is too close to the initial free jet. If the jet is too far from the impingement surface however, a decaying region forms. This decaying region forms at a length 4-8 jet diameters from the nozzle. The following region, defined as the location where the dynamic pressure is 95% of the original value, is called the stagnation region. Figure 2-13 and 2-14 show how the velocity profile changes as it approaches this decaying region. Initially, the velocity distribution is long and narrow, and the jet velocity is at a maximum. As the jet transitions, a high lateral velocity gradient is developed

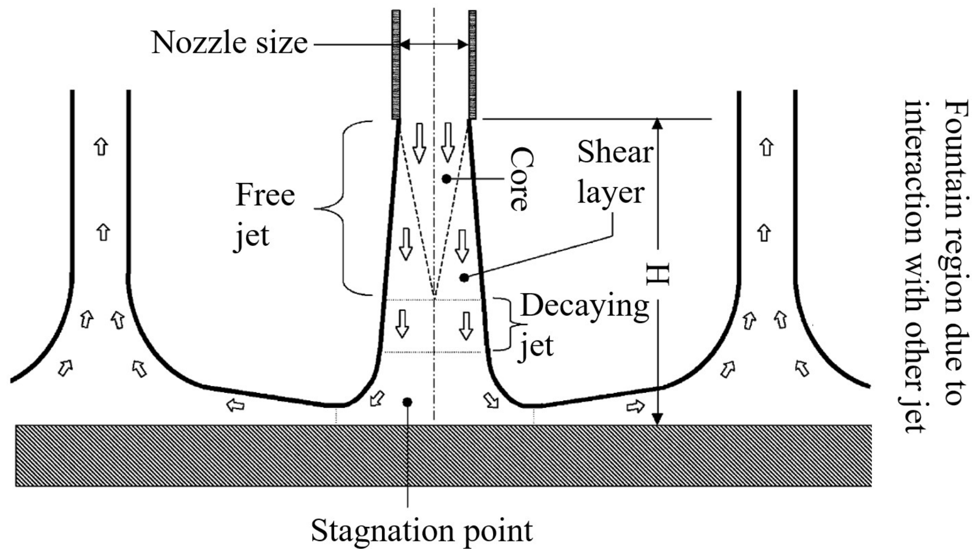


**Figure 2-13** Flow regions of impinging jet [64]

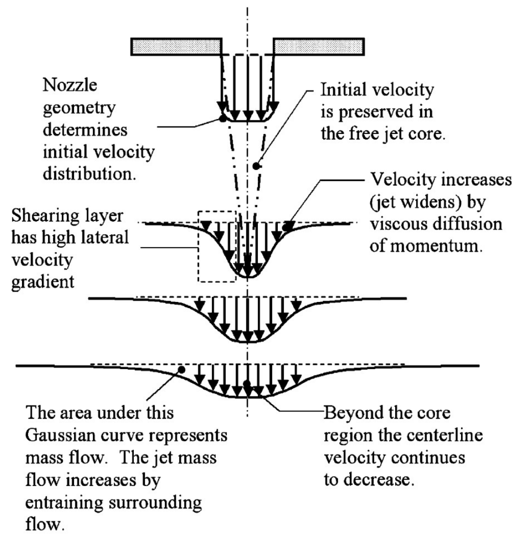


**Figure 2-14** Flow field of free submerged jet along flow path of jet [64]

through viscous diffusion of momentum. As the jet traverses axially, a Gaussian velocity profile develops and the maximum velocity decreases, but the overall mass flow increases as it picks up surrounding fluid. When the fluid hits the stagnation region, the momentum shifts laterally, and the no slip condition makes the shear stress on the surface very high and greatly effects the heat transport. The stagnation region extends approximately 1.2 $D_j$ from the surface for round jets [65]. Numerically, this can be characterized by $\overline{uv} < 0$, where this represents the mean velocity downward and laterally being less than zero, with bounds within 13% of nozzle height H. In Maurel and Solliec studies, this did not vary with Re or H/D [66].

After leaving the stagnation region, the fluid traverses laterally as a wall jet. The wall jet is a minimum thickness 0.75-3 $D_j$ from the centerline of the jet axis. The boundary layer thickness is no more than 1% of the jet diameter [65]. Since the thermal boundary layer is directly proportional to the fluid boundary layer the heat transfer is very high for small jet diameters. The wall jet has two shear layers. One is caused by the velocity gradient at the no slip condition between the wall and the fluid, and the other is the velocity gradient between the stagnant fluid defined by 5% of the wall jet's maximum speed. Similarly, to the decaying region, as the wall jet traverses

laterally, the mass flow rate increases due to the velocity gradient triggered by the stagnant fluid. The axial location of maximum velocity moves vertically from the impingement surface as it traverses laterally because the wall jet transfers stagnation pressure to dynamic pressure. Due to this shift, the maximum velocity can increase as it moves laterally but eventually will decelerate.

Different styles other than circular jets are possible. Nuntadusit et al. [67] studied heat transfer performance of elongated and circular jets for 6x4 array with no returns. A diameter of 13.2 mm, constant area of 136.8 $mm^2$ and Re=13,400 were studied. Non staggered elongated jets with an aspect ratio of 4 performed the best. At a Reynolds number of 13400, the Nusselt number was 6% and 12.5% higher than circular diameters for non-staggered and staggered respectively jet arrangements. The author mentioned that this is likely due to the decrease in crossflow interference. Nuntadusit et al. [68] later studied the heat transfer performance of jets with a swirl pattern for 3x3 array with no returns. The diameter studied was 16.5 mm at Re=20,000. They determined that for $S/D$= 2, 4, 6, 8, the heat transfer was 19.6%, 7.3%, 12.8% and 10.2% higher respectively, for multiple swirl impinging jets than conventional. This was accounted for by the additional fluid mixing around the impingement area.

Inefficiencies can be caused by the jet when the velocity is too high. One example by Kim et al. [69] studied extreme cases of jet velocities at Reynolds numbers up to 500,000. Supersonic jet speeds with air up to Mach 1.8 were characterized. Recirculation bubbles can form at these jet velocities which degrades heat transfer performance. Figure 2-15 shows an example of these recirculation bubbles forming in the stagnation region. This inefficiency needs to be considered when designing systems with high Reynolds/Mach numbers.

After a jet strikes the surface and transitions to lateral movement, the heat transfer coefficient decreases dramatically, so an array of jets is often used to cool a heat source. However,

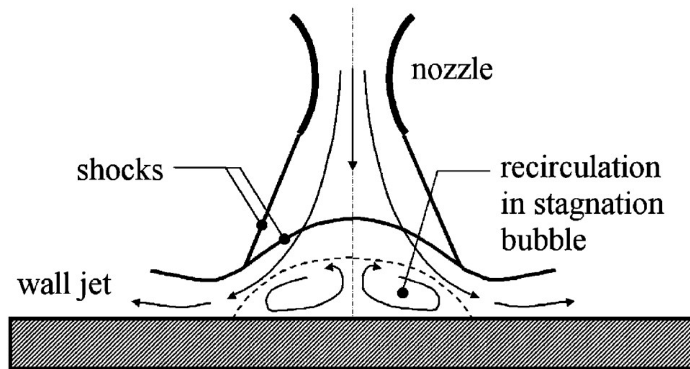


**Figure 2-15** Supersonic jet flow pattern

the exhausting fluid tends to interfere with other jets striking the surface and decreases the heat transfer coefficient. The first jet impingement array with interspersed fluid extraction was fabricated in 1994 by Huber and Viskanta [70]. They attempted to quantify the amount of jet-jet interaction for air Reynolds numbers between 3500 to 24000 and built a 3x3 array of jets starting with the geometry shown in Figure 2-16a-b. Nondimensional height and spacings of $H/D$ = 1, 6, and $S/D$ = 4, 6, 8, respectively, were tested and it was concluded that while $H/D$ = 1 and $SD$ = 4 obtained the highest Nusselt number, it also required the highest mass flow rate per unit area. The mass flow rate was four times greater than $H/D$ = 1 and $S/D$ = 8. Furthermore, they found that in architecture a, with the same Reynolds number, the surrounding jets' Nusselt number was 14-21% less at the stagnation point compared to a single jet with no interference. This proved that there is significant jet-jet interaction that degrades heat transfer performance with arrays of jets with no return ports. While this was a breakthrough in 1994, the manufacturing capabilities to build an array of jets with returns were not yet obtained. Hence, studies of arrays of jets without returns continued for years.

Fechter et al. [71] also studied the effects of cross-flow interference for jet vanes through numerical and experimental simulations. He found that the numerical simulation (Ansys CFX

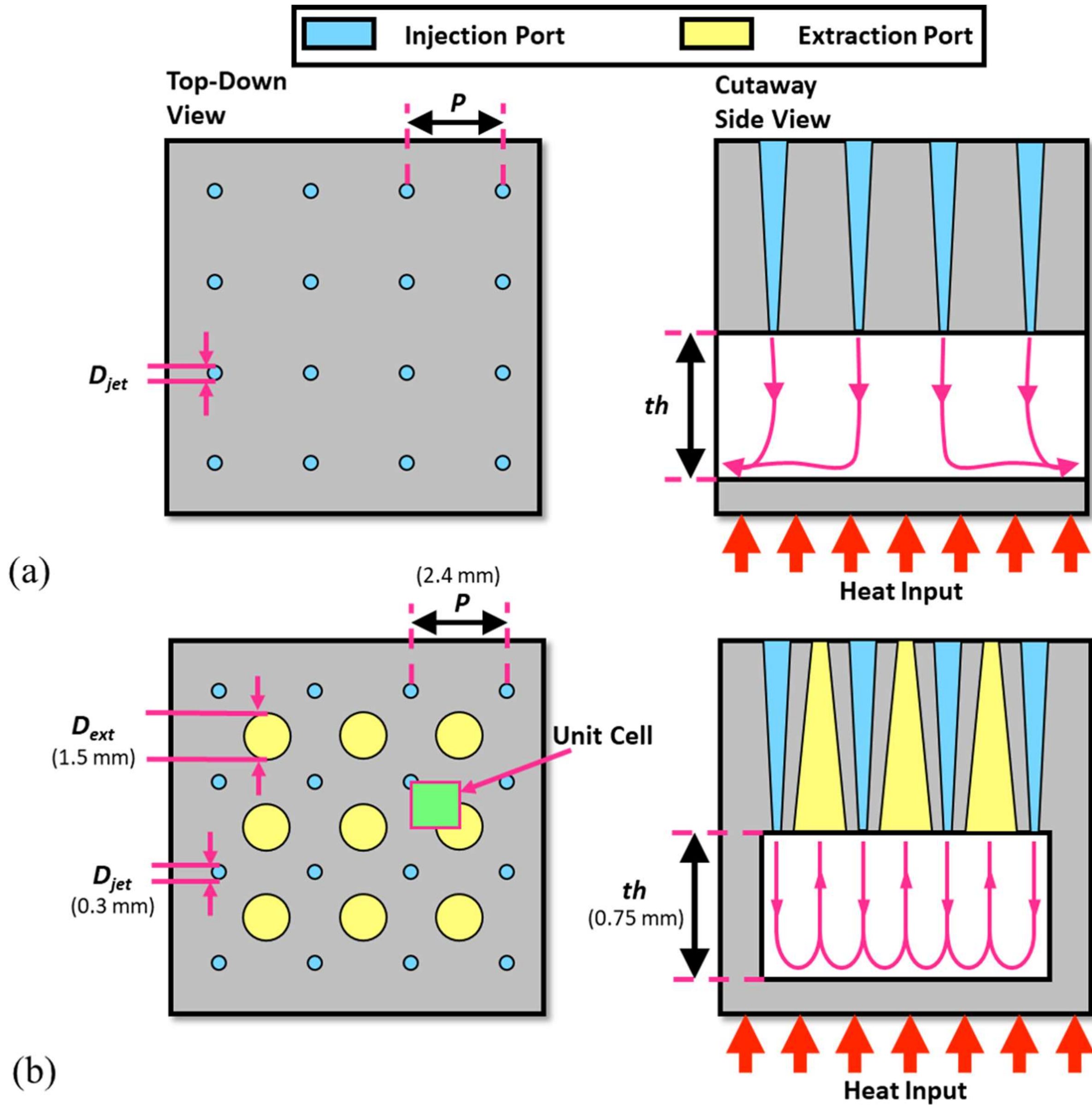


**Figure 2-16** a) Jet impingement without returns b) Jet impingement with returns [70]

12.1) significantly over predicted the Nusselt number at stagnation zone for turbulent flows (Re=10,000-40,000). Also, that jet-jet interference was greater at lower *H*/*D* values due to the channel cross-sectional area being lower. Robinson et al. [72] attempted to reduce the cross flow effects by utilizing a staggered 10 x 11 array with no returns. This was printed out of metal and

had a hybrid microchannel design to avoid crossflow effects. Jet diameters were 30 μm and COPs were as high as 100+ at flow rates below 0.45 lpm for a $q$" = 1000 W cm$^{-2}$ with ΔT = 35°C.

The next return jet impingement array was not developed until 2006 by Brunschwiler et al. [73]. The return jet impingement architecture with a branching manifold structure is shown in Figure 2-17a-d. Features were etched in silicon with $D_j$ = 30-126 μm and 45,000 jets. Silicon however is conductive material and caused the return jets to act as heat exchangers which degrade performance via preheating the inlet fluid before it becomes a jet. Nevertheless, a measured junction to fluid thermal resistance of 0.17 cm$^2$ K W$^{-1}$ was obtained at a flow rate and pressure drop of 2.5 lpm and 35.2 kPa, respectively. Results showed uniform heat transfer was achieved on the macro level due to injection and extraction ports being repeating cells even though the Nusselt

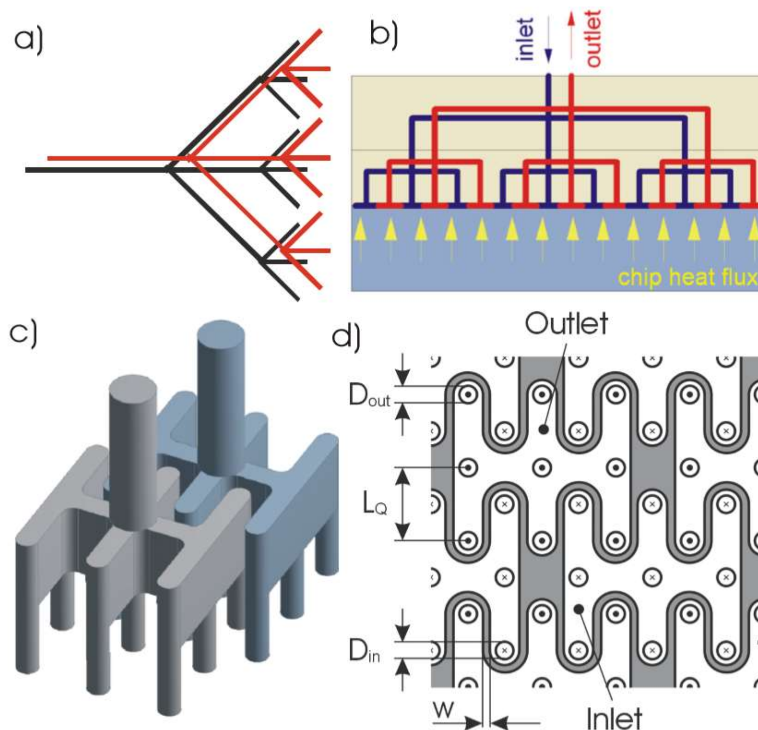


**Figure 2-17** Return jet impingement manifolding a) Capillary cell architecture with bf = 3 b) Cross section through layered chip c) 3D view of one inlet and one outlet tree d) Top view of capillary cell architecture [73]

number rapidly degrades laterally from the stagnation region. Thus, uniform heat transfer can be attained by utilizing a heat spreader.

Onstad et al. [74] developed the next type of array with extraction ports. Rather than four extraction ports showed in the above configurations, six extraction ports surrounded the jet inlet nozzle. On the three geometries tested, it was determined that the smaller extraction area to injection jet area obtained higher Nusselt number on average by 9%. The authors noted this was likely due to the extraction ports having velocities two times greater when area was halved. These results conflicted with the results from Rhee et al. [75] where the opposite trend was shown.

Rattner [76] performed computational simulations on a jet array with fluid extraction ports. The geometry modeled was a repeating unit cell of jets with fluid extraction ports shown in Figure 2-18 where fluid jets onto the surface and returns up the adjacent extraction port. Since there are no crossflow effects, just one-unit cell needs to be modeled to determine the performance of the whole array. Over 1000 randomized scenarios of Re: 20-500, Pr: 1-100, $S/D$=1.8-7.1 and $H/D$: = 0.1-4.0 were simulated to develop a correlation relating these parameters. The author then used jet impingement with edge removal, and microchannel heat transfer correlations to compare four cooling geometries on a 5 x 5 mm cooling surface. Microchannel's of 200 µm and 100 µm sidewalls were compared with jet diameters of 200 µm against interspersed fluid extraction holes 200 µm and edge removal thicknesses of 100 and 200 µm. The results showed that jet arrays with interspersed extraction ports obtained the lowest average temperature, 62℃, and improved temperature uniformity at this size compared to jet arrays with edge removal 100, and 200 µm, resulting

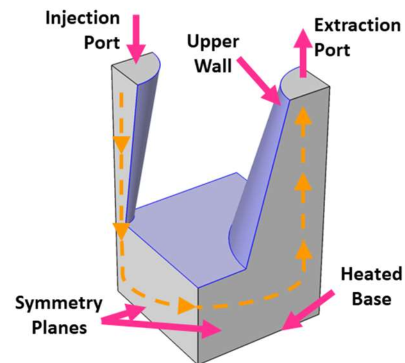


**Figure 2-18** Repeating return impingement unit cell

in 65°C, and 69°C, respectively. Microchannel cooling resulted in the highest temperature of 100°C likely due to the small flow rate and fin surface area causing the heat transfer to plateau for laminar flow.

Hobby et al. [77] performed experimental simulations and tested the accuracy of a number of heat transfer correlations found in literature for the return jet impingement geometry. A low cost 8x8 array with extraction ports was developed and made from a 3D printed photopolymer. Key geometry characteristics used were $D_j$=300 μm, $H/D$=2.5 and $S/D$=8. Reynolds numbers tested were 300-1500 with water as the working fluid. At a Reynolds number of 1500, a thermal resistance of 0.08 K $W^{-1}$ was obtained. Hubber and Viskanta [70], and Rattner's[76] correlations were close (within 10%) but began to diverge and over predict around Re = 1000 and predicted values were 25% higher. The correlation developed by Hoberg et al. [78] was not very accurate for this geometry, potentially due to maldistributions from their manifold system used. In further work by Hobby et al. [79], computational and experimental simulations were performed for Pr = 7, $Re_j$ = 300-1500, $SD$ = 8, and $HD$ = 2.5. The simulation results followed good agreement up to Re = 1000, but then over-predicted the Nusselt number for higher Reynolds numbers. This overprediction from simulation results could be because of neglecting viscous dissipation effects and/or the laminar to turbulent transition region for a jet at Re=1000-3000 [80].

Wei et al. [81] performed experimental and numerical simulations on a high spatial resolution and programable test chip. A single jet cooler with a 2000 μm jet diameter and six extraction ports of 2000 μm diameter was studied. Good agreement was found between experimental and numerical data showing the center and edge jet thermal resistance to be 0.55, and 1.65 K $W^{-1}$, vs 0.41, and 1.70, respectively. A 4x4 jet array with a diameter of 500 μm and a 5x5 return configuration (also 500 μm) was also studied. The 4x4 array had better heat transfer

performance due to smaller jet diameters, but both showed high efficiency for cooling hot spots with cheap 3D printed plastic. Wei et al. [82] then studied pressure drop through the device to determine the required pumping power. It was determined that the inlet/outlet accounted for 21% and 57% of the total pressure drop and that improving manifolding is more important than optimizing jet level.

Han et al. [83] studied a silicon based return jet-slot impingement array under experimental and computational simulations as shown in Figure 2-19. The die and lid size of the chip under investigation were 6.25 $cm^2$ and 25.0 $cm^2$, respectively. The maximum heat flux was 24 W $cm^{-2}$ at a temperature difference of 15°C. The dimensions of the cooler are 150 μm inlet channel width, 100 μm outlet channel width, 250 μm slot height, 400 μm fin thickness drainage trench width of 120 μm and 550 μm length [84]. The TIM properties were left out. The results of the study were an overall thermal resistance of 0.0667 K $W^{-1}$ at 1 lpm.

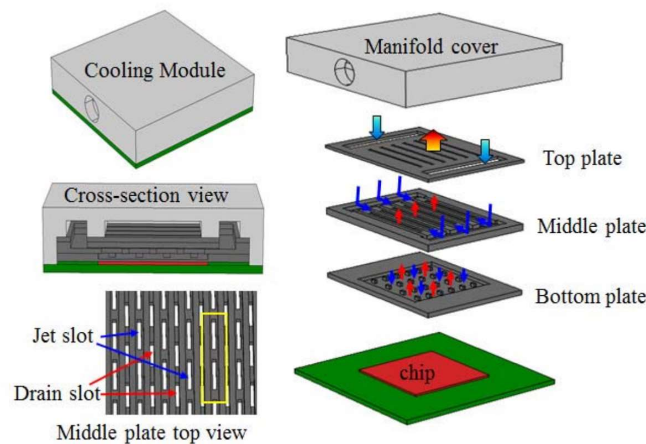

**Figure 2-19** Return jet-slot impingement array

To further increase heat transfer from the heat source, surface enhancements are possible as well for return jet impingement cooling. El-Sheikh and Garimella [85] showed that a 3.2-3.8x increase in effectiveness can be made by incorporating pin fins into the surface for a single air jet. Ndao et al. [86] studied heat transfer enhancements of circular, square, hydrofoil and elliptical pin

fins with single phase R134a as the impinging fluid for a single jet. They found that circular and square pin fins performed the best and that the larger diameter pin fins had higher heat transfer coefficients due to smaller flow area and thus higher velocity gradients. Along with these higher velocity gradients comes increased pressure drop. Based on the same pressure drop, the exact effects were not determined as the manifolding needs to be considered as well.

A summary of jet impingement literature is shown in Table 2-2. These jet impingement studies cover advancements in jet impingement over the years but limited general correlations for jet impingement with interspersed fluid extraction ports remain. Hydraulic diameters ranged from 40 μm up to 13,200 μm with jet arrays ranging from single jet studies to arrays greater than 40,000. Studies found smaller jet diameters correlate to higher heat transfer coefficients and that the optimal jet spacing varied by the jet height. Studies suggest the optimal nondimensional jet spacing (*SD*) is in the range (4-8) and lower nondimensional jet heights (*HD*) will provide the best

**Table 2-2** Jet impingement literature review summary

| **Name** | **Working Fluid** | **Array size** | **Returns** | **Reynolds number** | **ΔP (psi)** | **q" (W cm$^{-2}$)** | **$R_{th}$ (K W$^{-1}$)** | **$D_h$ (mm)** |
|---|---|---|---|---|---|---|---|---|
| Huber and Viskanta [70] | Air | 3 x 3 | Yes/No | 3,500-24,000 | N/A | N/A | 0.876 | 6.35 |
| Nuntadusit et al. [67] | Air | 6 x 4 | No | 13,400 | N/A | N/A | N/A | 13.20 |
| Fechter et al. [71] | Air | 5 x 1 | No | 10,000-40,000 | N/A | N/A | N/A | N/A |
| Robinson et al. [72] | Water | 10 x 11 | No | 860-4,300 | 23 | 1000 | 0.258 | 0.030 |
| Brunschwiler et al. [73] | Water | 150 x 150 | Yes | 5-900 | 5.1 | 370 | 0.043 | 0.030-0.126 |
| Onstad et al. [74] | Air | 6 x 6 | Yes | 500-10,000 | N/A | 1.33 | 0.018 | 8.46, 2.82 |
| Rattner [76] | Pr = 1-200 | 10 x 10 | Yes | 20-500 | 1.0 | 5 | 0.42 | 0.200 |
| Hobby et al. [79] | Water | 8 x 8 | Yes | 300-1,500 | 3.77 | 41 | 0.066 | 0.300 |
| Wei et al. [81] | Water | 4 x 4 | Yes | 340-1,000 | 5.80 | 78.1 | 0.25 | 0.500 |

performance in the range (1-3) but at the cost of increasing pressure drop. The fluid studied most was either water or air. Research highlights include Rattner [76] performing 1000 randomized computational simulations over a large range of fluids, and geometries, developing a non-geometry specific correlation. Bandhauer et al. [77] performed experimental studies and tested correlations in literature with a novel 3D printed return jet impingement device overcoming the jet-jet interference faced many years prior.

## 2.3. Research Needs for Integrated Circuit Cooling

The primary goal for an integrated circuit cooling solution is to limit the temperature of the junction. Beyond temperatures of 75°C, the medium time to failure for the IC exponentially increases for previous generations of processors. The literature reviewed air, microchannel and jet impingement for electronics cooling. Air cooling has had to expand into multiple slots to cool increasing heat loads, inhibiting densely packed PCBs. With the continuation of rising TDP, expanding into another slot will not be an option. Thus, there is a need for alternative solutions. The gaps for the liquid cooling studies can be summarized (Figure 2-20):

- Up to 90% of the total thermal resistance is accounted for by the junction to case and TIM 2 thermal resistance in liquid cooling studies. Investigation of *different electronics packaging configurations* has been limited but those that remove TIM 2 show an improvement in reducing the total thermal resistance. One study is by Ramakrishnan et al. [53] where $R_{\text{TIM},1}$ = 0.052 K W$^{-1}$ and the $R_{\text{cold plate}}$ 0.03 K W$^{-1}$. However, there have been no studies that investigate jet impingement cooling with all TIM layers removed and comparing this approach with microchannel.
- Several studies have considered waste heat potential at higher junction temperature but do not account for the added power consumption through increased leakage current rates.

| | a | b | c | d | e | f | g | h | i | j | k | l | m | n | p | q | r | s | This Study |
|---|---|---|---|---|---|---|---|---|---|---|---|---|---|---|---|---|---|---|---|
| Microchannel Modeling | ✓ | ✓ | ✓ | ✓ | ✓ | ✓ | ✓ | ✓ | ✗ | ✗ | ✗ | ✗ | ✗ | ✗ | ✗ | ✓ | ✗ | ✗ | ✓ |
| Jet Impingement Modeling | ✗ | ✗ | ✗ | ✗ | ✗ | ✗ | ✗ | ✗ | ✓ | ✓ | ✓ | ✓ | ✓ | ✓ | ✓ | ✓ | ✓ | ✓ | ✓ |
| Electronics Packaging | ✗ | ✓ | ✓ | ✓ | ✓ | ✓ | ✓ | ✓ | ✓ | ✓ | ✓ | ✗ | ✗ | ✓ | ✗ | ✓ | ✓ | ✓ | ✓ |
| Return Jet Impingement Modeling | ✗ | ✗ | ✗ | ✗ | ✗ | ✗ | ✗ | ✗ | ✓ | ✓ | ✓ | ✗ | ✗ | ✓ | ✓ | ✓ | ✓ | ✓ | ✓ |
| Leakage Current | ✗ | ✗ | ✗ | ✓ | ✗ | ✗ | ✗ | ✗ | ✗ | ✗ | ✗ | ✗ | ✗ | ✗ | ✗ | ✗ | ✗ | ✗ | ✓ |
| Failure Rates | ✗ | ✗ | ✗ | ✗ | ✗ | ✗ | ✗ | ✗ | ✗ | ✗ | ✗ | ✗ | ✗ | ✗ | ✗ | ✗ | ✗ | ✗ | ✓ |
| Removing Layers of TIM | ✗ | ✓ | ✗ | ✗ | ✗ | ✓ | ✗ | ✗ | ✗ | ✗ | ✗ | ✗ | ✗ | ✗ | ✗ | ✗ | ✓ | ✓ | ✓ |
| System Level Study | ✗ | ✗ | ✗ | ✗ | ✓ | ✗ | ✓ | ✓ | ✗ | ✗ | ✗ | ✗ | ✗ | ✗ | ✗ | ✗ | ✗ | ✗ | ✓ |
| Comparison of Microchannel And Return Jet Impingement | ✗ | ✗ | ✗ | ✗ | ✗ | ✗ | ✗ | ✗ | ✗ | ✗ | ✗ | ✗ | ✗ | ✗ | ✗ | ✓ | ✗ | ✗ | ✓ |

**Comprehensive study:** Combines all major aspects from literature, applied to electronics packaging

**a**: Tuckerman and Pease [45]
**b**: Zhang et al. [46]
**c**: Wei et al. [51]
**d**: Chainer et al. [56]
**e**: Alkharabsheh et al. [87]
**f**: Ramakrishnan et al. [48]
**g** : Fusiara et al. [52]
**h** : Lucchese et al. [53]
**i** : Huber and Viskanta [66]
**j** : Brunschwiler et al. [69]
**k**: Onstad et al. [70]
**l** : Nuntadusit et al. [63]
**m** : Fechter et al. [67]
**n** : Robinson et al. [68]
**p** : Huber and Viskanta [6
**q** : Rattner [71]
**r** : Hobby et al. [74]
**s** : Wei et al. [81]

**Figure 2-20** Literature review gaps summary

There is a need to quantify the increased power consumption at high junction temperatures when evaluating different cooling strategies at elevated temperatures, including in a high temperature ambient.

- Return jet impingement studies have been primarily limited to developing correlations for jet impingement heat transfer without jet-jet interference. There is a need to evaluate the performance of return jet impingement at a system level for electronics cooling applications.
- The system level tradeoff between non-dimensional jet spacing (SD) for return jet impingement has not been investigated, but it is known that lower SD result in higher mass flux required to achieve a thermal resistance. Increasing the SD will result in a lower overall mass flow rate which could reduce the system pressure drop, and this warrants further investigation.

- The system level liquid cooling studies available in literature do not incorporate an onboard heat exchanger. The effect of the heat exchanger in a fixed package volume for the system remains unknown.
- None of the studies investigate electronics cooling at high ambient temperatures (50°C) and often focus on the device scale or the rack scale environment in data centers. There is a need to determine the limiting factors at high ambient temperatures for closed loop liquid cooling systems.

The use of the TIM is to enhance thermal conduction between two surfaces. However, the redundancy of the second TIM has inhibited performance improvements of liquid cooling methods. Liquid cooling with microchannel and jet impingement offers low convection thermal resistance when compared to air. Many system level studies have used microchannel coolers as jet impingement has had limited success due to thermal short circuiting and jet-jet interference, but advancements in 3-D printing have enabled improved performance. There have been no studies which have developed a liquid cooling system comparing the two methods with the potential configurations that they can offer, especially at high ambient temperatures often experienced in the test and measurement market. For instance, in industry, microchannel cooling may only be attached to the lid of an IC via a TIM and cold plate. Jet impingement offers potential for attaching directly to the lid, bypassing TIM 2 and the cold plate, or attaching to the die bypassing all other thermal resistances.

Furthermore, the research will aid to fill gaps in improving pumping power efficiency, defined by the amount of overall system pressure drop required multiplied by the overall system flow rate required. Limited system level designs are available in literature as most focus on individual components themselves to give engineers the tools to design a system but one is by

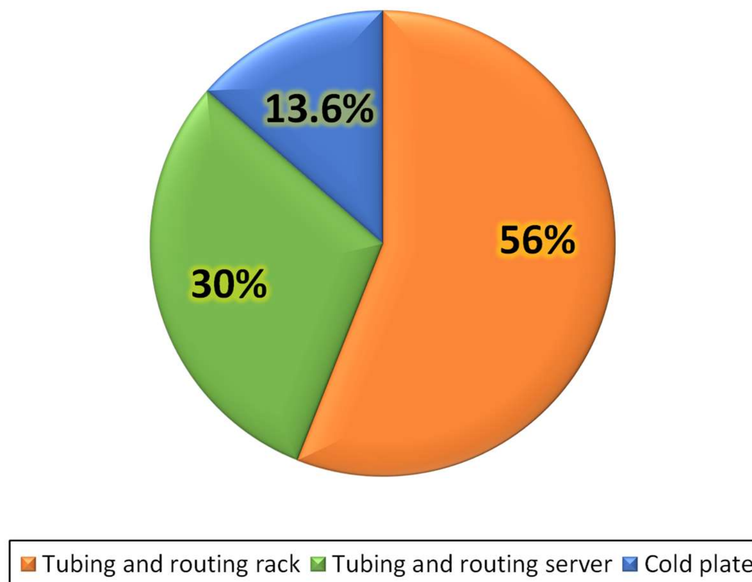


**Figure 2-21** Direct liquid cooling system pressure drop breakdown [83]

Alkharabsheh et al. [87]. A DLC (direct liquid cooling) system was designed and implemented in a data center rack and Figure 2-21 shows the pressure drop break down of the system. The server module only accounted 44% of the pressure drop for the total system and only 13.6% of the total system pressure drop was used for the cold plate and the rest of the pumping power was wasted on fluid routing by means of tubing and fittings. This is astonishing that 84.4% of the power consumed by the pump is wasted getting the fluid to and from the cold plate. If possible, it is desirable for the engineer to design the cold plate to be at an optimal ratio of flow rate and pressure drop to decrease the total required pumping power.Equation Chapter (Next) Section 1

The needs for integrated circuit cooling can be summarized as follows:

- Determine which thermal packaging profile can attain the lowest total thermal resistance.
- Address limiting factors on high ambient temperature operation for liquid cooling (50°C).

- Compare microchannel and return jet impingement cooling at the system level.
- Determine the leakage current effects on system power consumption at low and high ambient temperatures.
- Expand on the system level pressure drop for various cooling methods and the optimization potential for return jet impingement.

## 2.4. Focus of Current Investigation

The current study aims to utilize new developments in microchannel and return jet impingement cooling technologies to design a scalable liquid cooling system while minimizing junction temperature. The goal of this study will be to increase the rack density via more compact liquid cooling solutions, investigate the failure rate at high ambient temperatures, and predict the acoustic output of the air-cooling equivalent for the proposed system designed at 50°C ambient. Many studies have neglected the effect of IC efficiency with respect to junction temperature and this work will aim to fill this void, while aiming to reduce overall system power consumption. Furthermore, the designed systems will be investigated for pumping power efficiency defined by the product of pressure drop and mass flow rate, with respect to the total system power consumption. Finally, the systems will be evaluated based off the minimum overall thermal resistance attainable. To summarize, the investigation will:

- Utilize new developed correlations to compare microchannel and jet impingement cooling on a 4U scale.
- Determine whether microchannel or jet impingement cooling requires less pumping power.
- Investigate different cooling configurations by bypassing TIM 2 and/or TIM 1.
- Investigate energy saving potential by maintaining lower chip temperatures.

- Determine acoustic limit of the system with air cooling compared to liquid cooling.

# CHAPTER 3. System Architecture and Assumptions

The system designed in this thesis is a liquid-cooled 3.125 kW AXIe chassis comparing two cooling methods: microchannel cooling and return jet impingement. Both cooling techniques have three primary components: the pump, radiator, and chip level cold plate/cooling device. The third generation Keysight AXIe chassis was designed for future generation cooling architecture and has an allotted spot for a pump or other components on the backplane as well as high connector and power supply limits of 3.125 kW and 3.3 kW, respectively. These features make the AXIe chassis a platform for high-performance cooling and ideal for maximizing its power limits.

In the following sections of this chapter, the AXIe system will be described. The system diagram and the flow path considerations will be discussed. Then, modeling assumptions will be presented. Relevant heat transfer and fluid correlations will be discussed to determine system performance of each component. The change in power consumption over a range of temperature rises will be discussed and then, finally, acoustic considerations for the system will be evaluated.

## 3.1. AXIe Chassis

The Keysight M9506A AXIe chassis is a 5-slot/4U high performance computing box that can cool up to 300W/slot of current generation blades, but has an electrical connector limit of 625 W/slot [88]. Figure 3-1 shows a picture of the AXIe chassis where the cooling is accomplished by 6 fans on each side pushing and pulling the air from right to left. These two fan trays currently operate at an acoustic limit of 72 dBa, twice as loud as the previous generation with 1 fan tray. If the cooling is to increase to the maximum connector limit, acoustic limits must be breached, or liquid cooling needs to be deployed. Keysight currently uses high performance heat sinks with embedded heat pipes that reduce thermal resistances such as spreading, conduction, and convection but leave few options for improvement. The primary means of increasing performance

**Figure 3-1** Keysight M9506a front view

are increasing the velocity gradients on the heatsink, employing more advanced TIMs, and increasing surface area. Increased surface area results in increased volume, typically occupying more than one slot which reduces component density. Velocity cannot be increased either because acoustic limits have been reached. Higher flow can be achieved at the same acoustic limit with larger fans, however, the current form factor is inadequate.

The thermal loads of the various components assumed in this modeling effort are shown in Table 3-1 where L and A represent the components needing to be liquid or air cooled. The component specifications were developed by scaling the specifications on a representative current generation blade and the chip dimensions were selected based off previous studies die dimensions. The main processing chips were categorized into Big Chip 1, 2, and 3, respectively. Chips that can

**Table 3-1** AXIe blade chip characteristics

| Category | TDP (W) | $TDP_{PTP}$ (W) | $N_{chips}$ | $Area_{lid}$ ($cm^2$) | $Area_{die}$ ($cm^2$) | q" (W $cm^{-2}$) | $R_{jc}$ (K $W^{-1}$) | $T_j$ Max (°C) | $R_{req}$ (K $W^{-1}$) |
|---|---|---|---|---|---|---|---|---|---|
| **Big Chip 1 (L)** | 160 | 128 | 2 | 28.16 | 5.06 | 25.28 | 0.1 | 85 | 0.27 |
| **Big Chip 2 (L)** | 60 | 48 | 1 | 20.48 | 3.69 | 13.01 | 0.1 | 90 | 0.83 |
| **Big Chip 3 (A)** | 20 | 16 | 1 | 25.60 | 4.62 | 3.48 | 0.1 | 75 | 1.56 |
| **Regulators (L)** | 150 | 120 | 1 | 25.60 | N/A | N/A | 0.2 | 120 | 0.58 |
| **Memory (A)** | 31.25 | 25 | 1 | 16.00 | N/A | N/A | 0.2 | 85 | 1.4 |
| **Misc (A)** | 6.25 | 5 | 2 | 8.00 | N/A | N/A | 0.2 | 85 | 7 |
| **Total** | **625** | **500** | | | | | | | |

go into the Big Chip 1 category are FPGA, ASIC, CPU, and GPU. The die area for this type of chip was selected at 22.5 mm x 22.5 mm based off the literature review die dimensions. The other die areas (Big Chip 2 & 3) were scaled off the lid areas provided by Keysight. Big Chip 2 and 3 are lower level chips that don't do the main processing work load. The two high powered Big Chip 1's (FPGA's) account for 51.2% of the total blade power and are placed next to each other on the board. The regulators account for 24% of the power. The thermal resistance from die to lid has been given a value of 0.10 K $W^{-1}$ for the ICs and 0.20 K $W^{-1}$ for the non ICs given from typical thermal resistance values at Keysight. The die heat fluxes could not be calculated for the regulators because they do not have dies. The highest die heat flux is on Big Chip 1 at 25.3 W $cm^{-2}$ which is low compared to those common in literature (e,g,, $q$"=1000 W $cm^{-2}$ [72] and $q$" = 150-200 W $cm^{-2}$ [89]) which generally focus on a heat source without two layers of TIM to isolate heat sink performance. Comparing this to the 220W modern processor of today, the AMD 7H12 has a die heat flux of 21.8 W $cm^{-2}$, 3.5 W $cm^{-2}$ lower than that of Big Chip 1. Heat is dissipated via two pathways: the primary thermal pathway (top) and the secondary thermal pathway (bottom of PCB). The primarily thermal pathway heat load is shown by $TDP_{PTP}$ which has been given a value of 80% the TDP. This assumption has been validated by Gao's [90] experimental results which show that the heat dissipation out of the back of the PCB is between 18 and 25% but decreases as the liquid cooling solution flow rate is increased. The required thermal resistance in Table 3-1 has been calculated with the $TDP_{PTP}$ from an ambient temperature of 50°C. Big Chip 1 will be the most difficult to cool and require the least thermal resistance. The regulators will be the second most difficult to cool followed by Big Chip 2 and 3. The very high required thermal resistance by the memory and miscellaneous components (1.4 and 7 K $W^{-1}$) will mean that they will be air cooled because of the ease to meet these values. Big Chip 3 having the lowest maximum junction

temperature and high thermal resistance will mean this chip will be air cooled as well. Big Chip 2 will require further investigation. As previously mentioned, 50°C inlet air can quickly heat up to 62-74°C depending on the location on the board. As the reference temperature increases, Big Chip 2 becomes more difficult to cool than the regulators and requires a similar thermal resistance

Leakage current is an inefficiency of the processor which can consume significant portions of the overall power. Pedram et al. [6] developed a correlation for leakage current based on temperature for an 100 nm feature size Intel processor with 0.7 V supply voltage. The values for this correlation were plugged in and the leakage current was related only to temperature for the ICs being modeled:

$$\textit{Leakage current} = \frac{1}{1-(3.2251e\text{-}05 \cdot T_j^2 + 1.9515e\text{-}03 \cdot T_j - 3.5026e\text{-}02)} \tag{3-1}$$

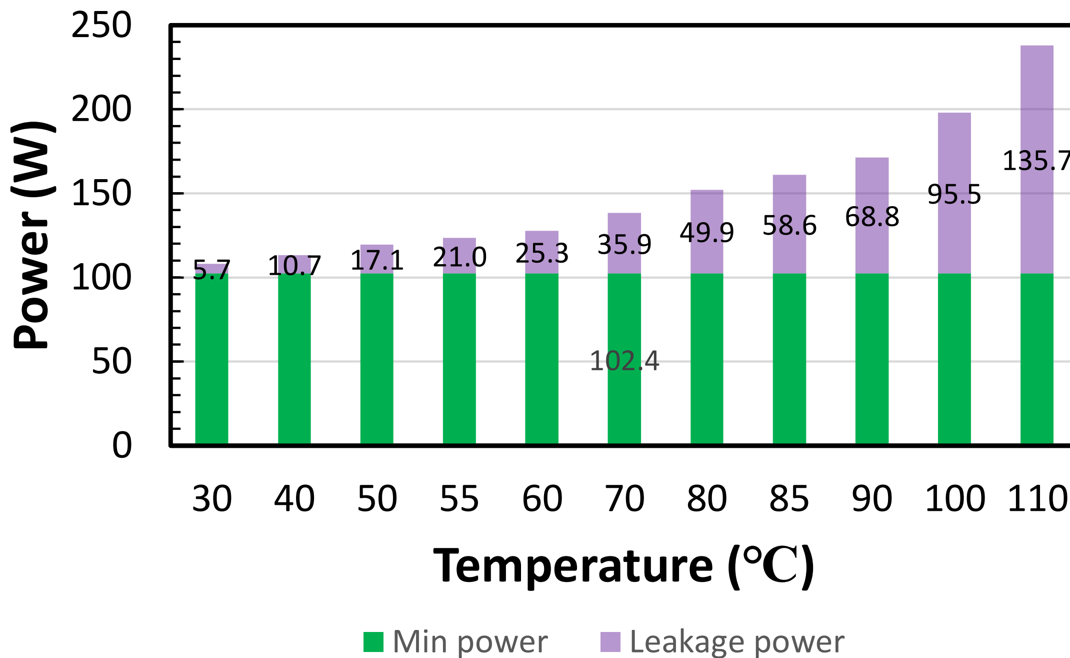


**Figure 3-2** Power profile derived from leakage current for Big Chip 1

where $T_j$ is the junction temperature in Celsius and leakage current is dimensionless. This leakage current was then multiplied by the minimum chip power at 85°C to obtain the actual power for a

particular temperature. For Big Chip 1 this was 102.4W. By using equation (3-1) across a variety of temperatures, Figure 3-2 was generated. Equation (3-1) is used in the present study to determine the TDP of Big Chip 1 through 3 and the memory when they are operating at various temperatures. For instance, when Big Chip 1 is operating at 85°C, the TDP will be 160W at a leakage of 36%, but when the chip is operating at 50°C, the TDP will be only 120W at a leakage of 14%. An important note is that the leakage current is exponentially related to temperature so that as the power increases, thermal runaway can occur in which the cooling mode will not be capable of dissipating the heat and the temperature continues to increase.

### 3.1.1. Full system model

A schematic of the flow loop is provided in Figure 3-3. The loop starts at the pump where the pressure is increased, and fluid is sent into upstream manifold 1 & 2. The first manifold is the chassis level manifold that distributes fluid to N number of slots, and the second manifold is the

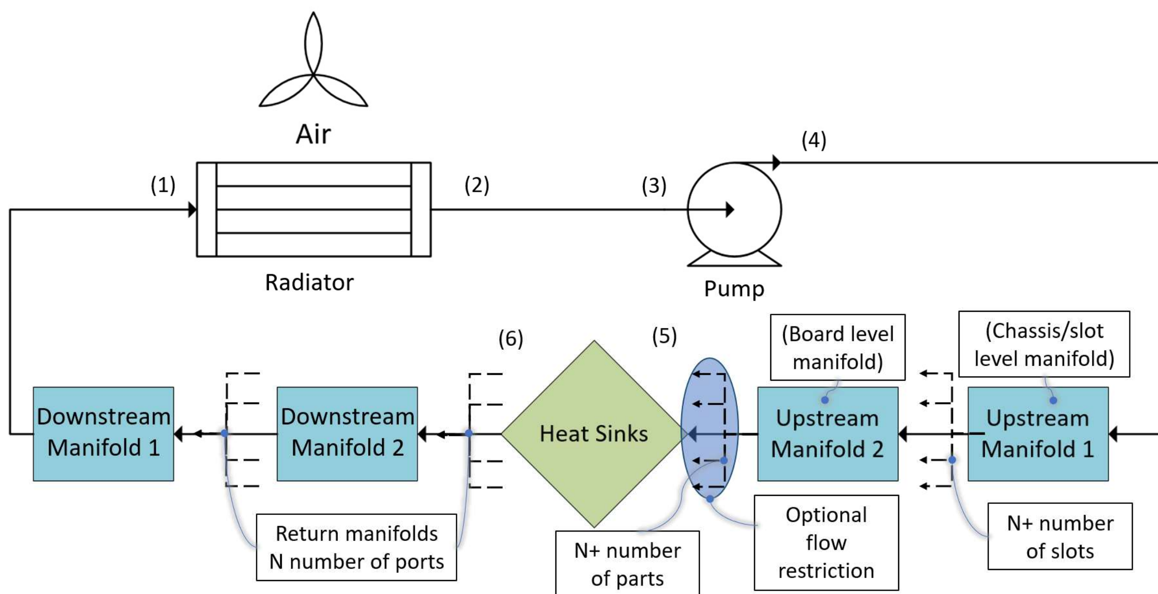


**Figure 3-3** Schematic of liquid cooled AXIe system

board level manifold that distributes the fluid to N number of chips. The board level manifold is the location for optional flow restrictions where a pressure element can be placed. After passing

into each cooling device, the fluid re-combines into the downstream manifolds and then into the radiator where the heat is rejected to ambient. The fan and radiator fit into fan trays 1 and 2, respectively. Although the dimensions of this slot are 2.1 in x 6.85 in x 11.5 in, the radiator height was reduced to 6.77 in to allow clearance. The flow path is such that the inner chassis load is cooled first and as a result, the air is slightly heated before cooling the radiator. This hybrid/modular design allows the chassis to be adaptable to any board because it can accommodate both liquid and air-cooling boards.

A CAD model was generated of the M9506A AXIe chassis with the proposed cooling system shown in Figure 3-4a-b with relevant dimensions in Table 3-2. There are two primary manifold

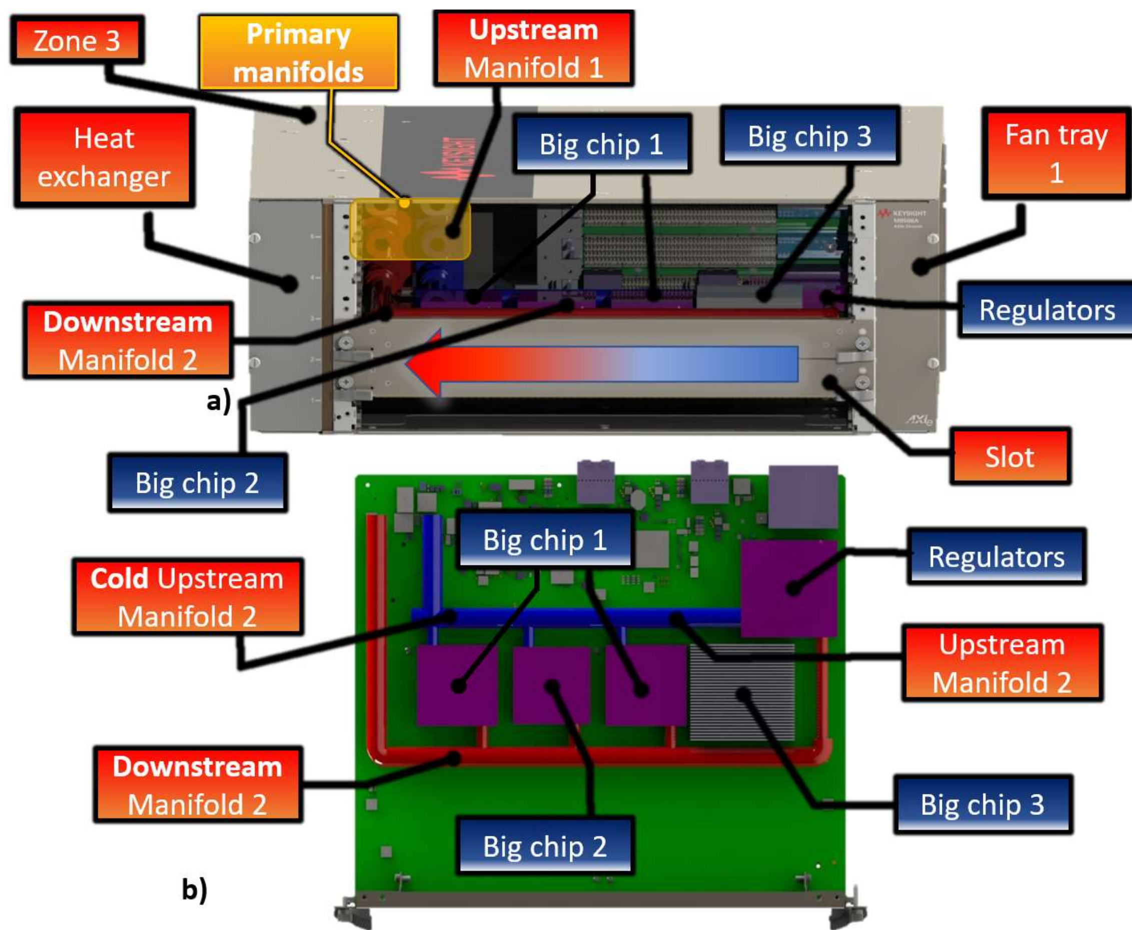


**Figure 3-4** Rendered liquid cooled AXIe chassis a) Front view system b) Top view board

distribution systems needed for the AXIe form factor: (1) dispersing fluid to each of the five slots from the radiator, and (2) dispersing fluid to each of the four primary heat sources. These two manifolds can be shown in red where the first manifold is shown vertically, and the second is horizontal in front of the chips. One key concern with traditional air-cooled systems has been the orientation and dimensions of the chips. Figure 3-4b shows the 12.7 in x 11.1 in board layout. The transparent squares above the heat sources represent the size of the cold plate with respect to the chip. The two highest powered chips (accounting for 52% of the cooling load) are placed next to each other. As mentioned previously, cooling this energy dense pair with air is difficult because the air heats up significantly as it moves along the flow path. Liquid cooling avoids this challenge by distributing fresh liquid at each chip. The maximum allowable height for the heat sink is 18.7 mm ± 0.05 mm. The return jet impingement heat sinks can utilize more space because they are 3D printed, however, the microchannel cold plates will be chosen from off the shelf components, which will limit their height and channel dimensions.

The components on the board from left to right are as follows: Big Chip 1, Big Chip 2, Big Chip 1, Big Chip 3, and the regulators, respectively. The relatively low junction temperature (75°C) for Big Chip 3 means that the chip should be air cooled because in the preliminary modeling, the temperature difference between the steady state liquid (75°C) and the junction temperature would be inadequate to provide cooling. By assuming an inlet air temperature of 55℃, Big Chip 3 requires a total thermal resistance of 1 K $W^{-1}$ which, with the area provided, can be achieved with a heat transfer coefficient of 12.3 W m $K^{-1}$.

The cold inlet supply manifold can be seen in blue and hot discharge in red, where a custom 3/8" quick connect is used to mate the cards to the chassis. The tubing has been selected based off the available space and pressure drop through each component. The main tubing consists of 1"

aluminum tubing connecting the manifold systems to the radiator and pump. The primary manifold is a one square inch box which provides the most volume and lowest pressure drop. The board level tubing/manifold is 3/8" ID and disperses fluid to the four heat sources. Connecting the board level manifold to each cooling device is a small portion of quarter inch tubing. The heat exchanger is located in fan tray 2 on the left and the pump is in zone 3 (not shown).

**Table 3-2** AXIe manifold and tubing characteristics

| Category | $D_h$ (in) | $L$ (in) |
|---|---|---|
| **Main tube** | 1.00 | 7.82 |
| **Board level tube** | 0.364 | 0.88 |
| **Chip tube 1** | 0.25 | 0.88 |
| **Chip tube 2** | 0.25 | 0.88 |
| **Chip tube 4** | 0.25 | 2.55 |
| **Mani 1** | 1.00 | 5.64 |
| **Mani 2** | 0.364 | 15.125 |

### 3.1.2. Cooling configurations

The different cooling configurations are shown in Figure 3-5a-d. In configuration 3-5a, water and water glycol pass through microchannels on a cold plate attached to the lid with a graphite pad TIM. The thermal correlation for the TIM developed in Kempers et al. [29] had an effective thermal conductivity of 2 W $m^{-1}$ $K^{-1}$ at 15-29 psi and will be used. In the second configuration 3-5b, water, water glycol, and a dielectric will be used with return jet impingement on the lid of the package. In configuration 3-5c, a microchannel cold plate will be used bypassing the thermal resistances of TIM 2 and the lid with the same fluids as configuration 3-5c. Finally, in configuration 3-5d, return jet impingement is used directly on the die with a dielectric. The dielectrics that will be investigated are Honeywell Fluorinert FC72, FC77, FC770, FC40, FC43, FC70, FC80, FC104, and jet fuel A-1. The first three and second to the last one are some of the most common dielectrics [35].

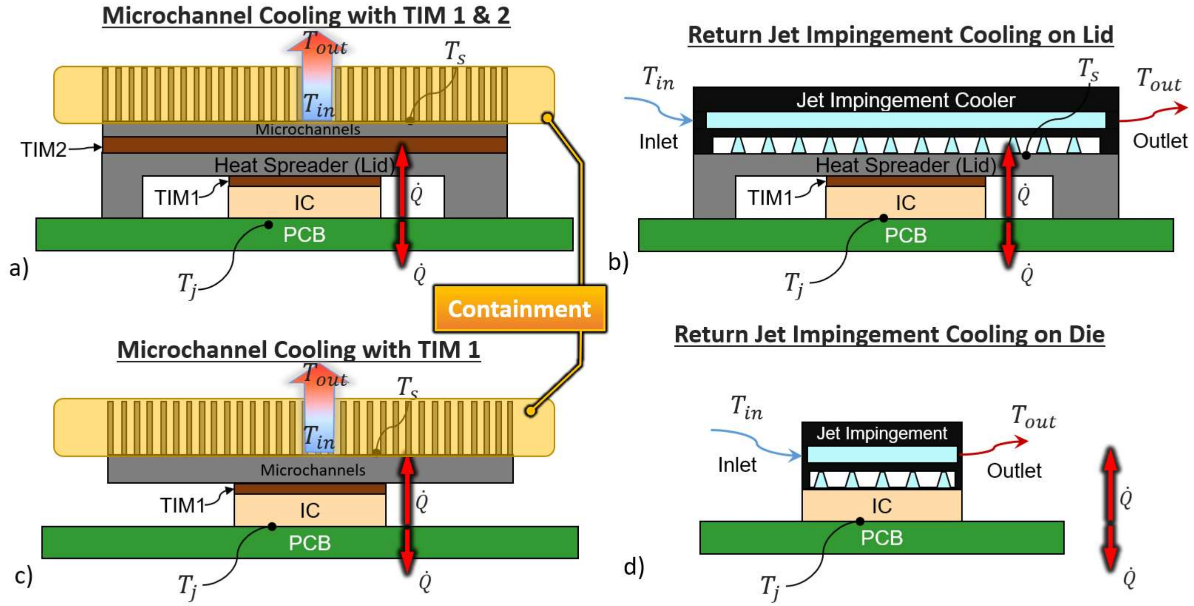


**Figure 3-5** Cooling configurations a) Microchannel cold plate with TIM 2 b) Return jet impingement on the lid bypassing TIM 2 c) Microchannel cold plate bypassing TIM 2 d) Return jet impingement on the die bypassing TIM 1

The primary benefit of cooling directly on the die is that convection is the only heat transfer mode:

$$R_{\text{cooling}} = R_{\text{conv}} \tag{3-2}$$

The return jet impingement on the lid adds contact and conductive thermal resistances as is shown below:

$$R_{\text{cooling}} = R_{\text{contact1/2}} + R_{\text{TIM1,ideal}} + R_{\text{IHS}} + R_{\text{conv}} \tag{3-3}$$

where $R_{\text{contact1/2}}$ are the contact resistances between the die and TIM 1 and TIM 1 and the lid, $R_{\text{TIM,ideal}}$ is the ideal conduction thermal resistance of the thermal interface material $\left(\frac{L_{\text{TIM}}}{k_{\text{TIM}}A_{\text{TIM}}}\right)$ and $R_{\text{IHS}}$ is the thermal resistance of the integrated heat spreader (lid). Lasty, by using microchannels, the thermal resistances are:

$$R_{\text{cooling}} = R_{\text{contact1/2}} + R_{\text{TIM1,ideal}} + R_{\text{IHS}} + R_{\text{contact3/4}} + R_{\text{TIM2,ideal}} + R_{\text{cold plate}} + R_{\text{conv}} \tag{3-4}$$

where $R_{contact3/4}$ is the contact resistance between the lid and TIM 2 and TIM 2 and the cold plate, $R_{TIM2}$ is the second TIMs thermal resistance, and $R_{cold\ plate}$ is the thermal resistance of the cold plate. The contact resistance and the ideal conduction resistance can be bundled into one term:

$$R_{TIM} = \frac{L_{TIM}}{k_{eff} A_{TIM}} \quad (3\text{-}5)$$

where $L_{TIM}$ is the thickness of the TIM, $k_{eff}$ is the effective thermal conductivity of the TIM at a particular pressure, and $A_{TIM}$ is the surface area of the TIM.

The thermal resistances that can be reduced or changed from the above equations are $R_{conv}$, $R_{TIM}$, and $R_{contact}$. $R_{TIM}$ and $R_{contact}$ can be reduced by increasing pressure, but the upper limit of pressure is relatively low at 29 psi and is already being reached. $R_{conv}$, however, can be changed

**Table 3-3** Representative package thermal resistance values

| Region | $k_{effective}$ (W m$^{-1}$ K$^{-1}$) | Thermal Resistance (K W$^{-1}$) |
|---|---|---|
| $R_{TIM\ 1}$ | 7.8 | 0.076 |
| IHS | 394.9 | 0.026 |
| $R_{TIM\ 2}$ | 2 | 0.022 |

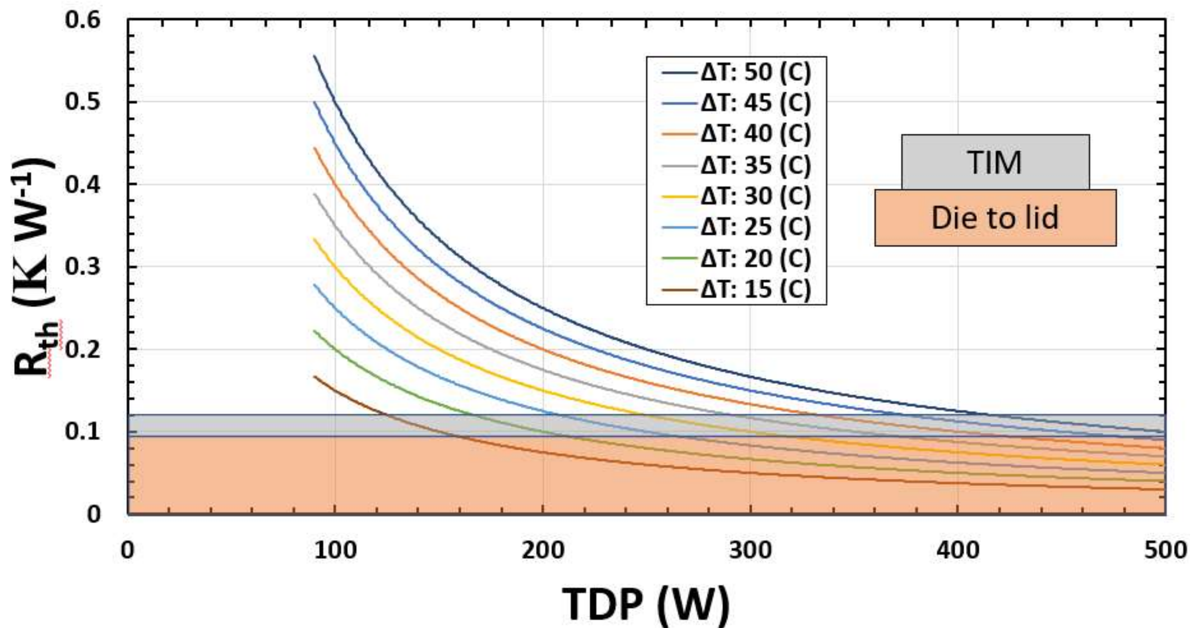


**Figure 3-6** Required thermal resistance to achieve a temperature difference for a power input

by varying the mass flow rate and varying geometry. The other thermal resistances are fixed and cannot be changed to lower the chip temperature. The thermal resistances of TIM 1, the IHS and TIM 2 are shown in Table 3-3 for this modeling effort. This first layer of TIM presents the largest thermal resistance due to its small surface area. The microchannel cooling configuration with cold plates (3-5a and 3-5c) have a higher area compared to return jet impingement for reducing $R_{conv}$, but the thermal resistance of the added TIMs and cold plate cannot be reduced. Figure 3-6 shows the representative breakdown of the typical heat sink thermal resistance from TIM 1, the lid, and TIM 2. This thermal resistance corresponds to the temperature difference between junction and the base of the cold plate. The thermal resistance for these typically adds a minimum of 0.12 K $W^{-1}$. For a 160W chip with 0 heat sink thermal resistance, the temperature difference between junction and the base of the cold plate will be at least 19°C.

## 3.2. Overview of Modeling Approach

The functioning principles for the modeling approach in this effort are shown in Figure 3-7 where a number of fluids and packing configurations will be input to the thermodynamic model. The goal of the thermodynamic model is to minimize the fluid and junction temperature. The heat exchangers for the primary fluids investigated will be optimized for their internal and external fin geometries at 50°C ambient temperature while varying the liquid mass flow rate. With the optimized heat exchangers, the heat sinks will be optimized for each packing configuration and fluid. The maximum allowable isentropic pumping power for the system will be limited at 0.25 hp. The jet impingement optimization will perform a sensitivity analysis on the geometry described in Hobby et al. [79] and investigate several non-dimensional spacing and heights as well as jet diameters for these optimal non-dimensional numbers. For water jet impingement on the lid, the convection thermal resistance will be set at 0.008 K $W^{-1}$ for Big Chip 1, while minimizing the

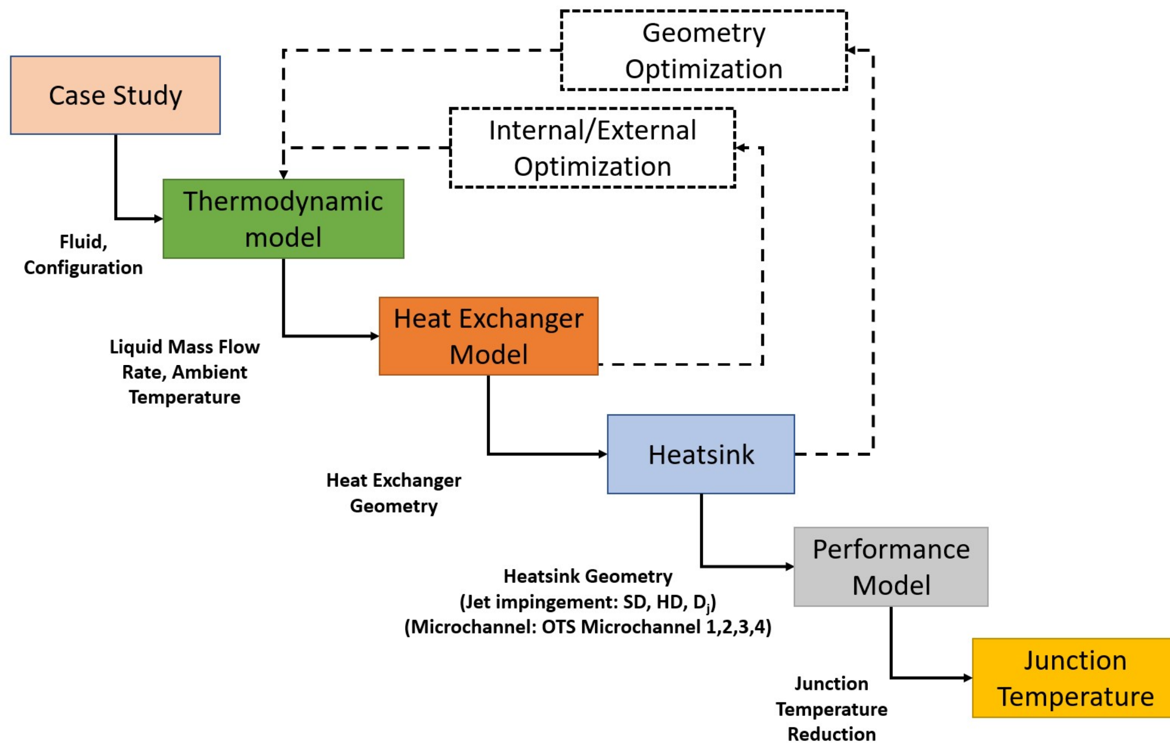


**Figure 3-7** Numerical model functioning principles

system pumping power. Several dielectrics (FC72, FC77, FC770, FC40, FC43, FC70, FC104 and Jet Fuel A-1) will be investigated for configuration 3-5d, jet impingement on the die, at a total thermal resistance of 0.10 K $W^{-1}$ with the geometry described in Hobby et al. [79]. The best dielectric fluid will be selected, and the geometry for this fluid will be optimized at 0.080 K $W^{-1}$. The microchannel optimization will input the dimensions of four OTS (off the shelf) microchannels that are less than $100 US and determine their performance based off the available flow rates for the system. The optimized heat exchanger and heatsink geometries for each respective fluid and configuration will be input to the performance model where different ambient temperatures are investigated and junction temperature, system power, and failure rates are minimized. Each configuration will be evaluated based off which can provide the necessary cooling to keep the junction temperatures below their maximum value. Finally, the performance

of each configuration will be investigated based off the failure rate, leakage current, and acoustic outputs.

## 3.3. Thermodynamic Model

Assumptions for the thermodynamic model will be stated in this section. The first is that 20% of the heat dissipates through the secondary thermal pathway via air fans and 80% is dissipated by the cooling solution based on proprietary information provided by Keysight. This assumption has been validated by Gao's [90] experimental results which show that the heat dissipation out of the back of the PCB is between 18 and 25%. The heat dissipated out the back of the PCB will be picked up by the air before passing through the radiator. Calculations are performed while the system is running at maximum power with all 5 slots full of identical representative blades, and the steady state fluid operating temperature will be calculated at the radiator outlet. In addition, the entire system is assumed to be running at a maximum power of 3.125 kW. The power map is as follows: 64% chip power, 24% regulators, 10% memory and 2% miscellaneous. The pump total-total efficiency, which is the product of all the loses multiplied by each other, is assumed to be 50%. Furthermore, the isentropic inefficiency of the pump is assumed not to be absorbed by the fluid and cooled by the power supply fan. Fan efficiencies are assumed to be 20%. Thermal resistance from the junction (die) to lid has been given a value of 0.10 $K\ W^{-1}$ for the Big Chips which is consistent with published values and was confirmed with computational simulation in Ansys as shown in Appendix A.4. Finally, a pressure drop element will be used for the cold plates to accommodate if certain chips do not require as much flow rate. This element would be in the form of restriction by either valve, bend, expansion/contraction, or extra tubing.

The form of the governing equations will be elaborated based on the assumptions of the thermodynamic model to solve the system as shown in Figure 3-3. These equations (3-6) - (3-10)

were solved by using an energy balance over the heat exchanger. The first equation represents the heat transferred to the air side of the heat exchanger:

$$Q_{\mathrm{rad}} = \dot{m}_{\mathrm{air}} c_{\mathrm{p,a}} (T_{\mathrm{ao,2}} - T_{\mathrm{ao,1}}) \tag{3-6}$$

where $T_{\mathrm{ao,2}}$ and $T_{\mathrm{ao,1}}$ represent outlet and inlet temperatures of the air to the heat exchanger and $c_{\mathrm{p,a}}$ is the specific heat of the air. $T_{\mathrm{ao,1}}$ is solved for:

$$Q_{\mathrm{chip,liq}} \cdot 20\% + Q_{\mathrm{chip,air}} = m_{\mathrm{air}} c_{\mathrm{p,a}} (T_{\mathrm{ao,1}} - T_{\mathrm{ai}}) \tag{3-7}$$

where $Q_{\mathrm{chip,liq}}$ is the total heat load that is liquid cooled, $Q_{\mathrm{chip,air}}$ is the total heat load that is air cooled, and $T_{\mathrm{ai}}$ is the inlet air to the chassis. Equation (3-8) represents the heat duty of the heat exchanger:

$$Q_{\mathrm{rad}} = \varepsilon_{\mathrm{rad}} C_{\mathrm{min}} (T_{\mathrm{h,rad,i}} - T_{\mathrm{ao,1}}) \tag{3-8}$$

where $\varepsilon_{\mathrm{rad}}$ is the effectiveness of the heat exchanger, $C_{\mathrm{min}}$ is the minimum heat capacity rate, $T_{\mathrm{h,rad,i}}$ is the hot fluid temperature, and $T_{\mathrm{ao2}}$ is the cold fluid inlet temperature. Equation (3-9) represents the heat transferred to the coolant stream for the chips:

$$Q_{\mathrm{rad}} = \dot{m}_{\mathrm{liq}} c_{\mathrm{p,l}} (h_{\mathrm{h,rad,i}} - h_{\mathrm{h,rad,o}}) \tag{3-9}$$

where $h_{\mathrm{h,rad,i}}$ and $h_{\mathrm{c,rad,o}}$ represents the inlet and outlet enthalpies of the working fluid. Alternatively, Equation (3-10) will be used with the enthalpy approximation for constant specific heats on dielectrics tested with minimal enthalpy data:

$$Q_{\mathrm{rad}} = \dot{m}_{\mathrm{liq}} c_{\mathrm{p,l}} (T_{\mathrm{h,rad,i}} - T_{\mathrm{h,rad,o}}) \tag{3-10}$$

where $T_{\mathrm{h,rad,i}}$ and $T_{\mathrm{h,rad,o}}$ represent inlet and outlet temperatures of the single-phase fluid and $\mathrm{c_{p,l}}$ is its specific heat.

The coefficient of performance of the liquid cooling system is calculated as follows:

$$COP = \frac{Q_{\mathrm{cool}}}{W_{\mathrm{pump}} + W_{\mathrm{fan}}} \tag{3-11}$$

where $Q_{cool}$ is the total chip power that has been cooled by the system, $W_{pump}$ is the pumping power and $W_{fan}$ is the power that the fans use. The power consumed by the fan and pump were modeled with equation (3-12):

$$W_{fan} = \Delta P_{air} \cdot \dot{V}_{air} / \eta_{t\text{-}t,fan} \tag{3-12}$$

where $\Delta P_{fan}$ is the total pressure drop of the fans, $\dot{V}_{air}$ is the volumetric flow rate and $\eta_{t-t,fan}$ is the total-to-total efficiency of the device.

## 3.4. Component Modeling

In this section the thermodynamic modeling of the heat transfer and pressure drop for each component will be discussed. The optimized heat sink, primary dielectric fluids and heat exchanger parameters will be presented. Finally, the fundamental equations for selecting a pump will be laid out.

### 3.4.1. Manifold

Figure 3-8 shows a schematic of the inlet and outlet manifolds which can be broken into four sections: inlet manifold 1, inlet manifold 2, outlet manifold 1, and outlet manifold 2. The purpose of manifold 1 is to distribute the flow to the five slots of the AXIe chassis. Once the flow is distributed, the second manifold disperses the fluid to each chip to be cooled. The outlet manifolds mirror the inlet manifolds functionally.

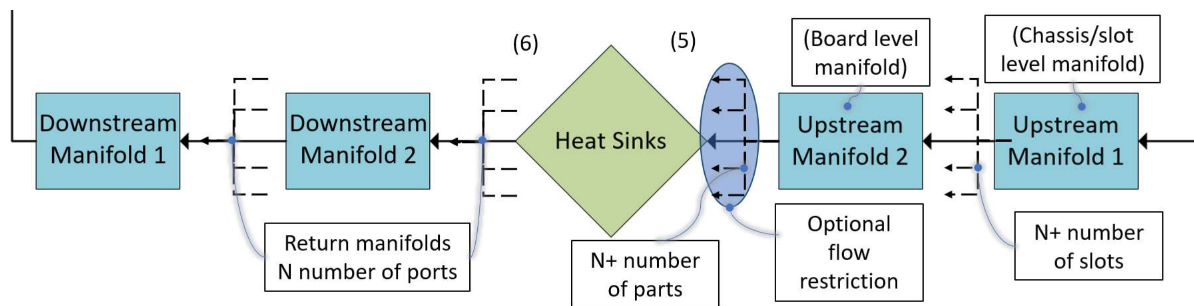


**Figure 3-8** Schematic of manifold 1 and 2

The manifold pressure drop correlations are from *Idelchik's Handbook of Hydraulic Resistances: second edition* [91] and are calculated as:

$$\Delta P_{\text{manifold}} = \zeta_{\text{manifold}} \cdot \frac{1}{2}\rho \cdot v_{\text{header,in}}^{2} \tag{3-13}$$

where $\zeta_{\text{manifold}}$ is the resistance coefficient and $v_{\text{header,in}}$ is the fluid velocity at the header inlet. The form of the resistance coefficient is calculated based on the $k_{\text{manifold}}$ value. The $k$-factor for the manifold can be calculated:

$$k_{\text{manifold}} = 1 - \frac{A_{\text{final,manifold}}}{A_{\text{inlet,manifold}}} \tag{3-14}$$

where $A_{\text{final,manifold}}$ is the area at the end of the manifold and $A_{\text{inlet,manifold}}$ is the area at the inlet of the manifold. For ease of manufacturing, these two areas are set equal, resulting in $K$=0. For $k_{\text{manifold}}$ between 0-0.3, the resistance coefficient takes the form:

$$\zeta_{\text{manifold}} = 2.63 - 0.54\bar{A} \tag{3-15}$$

where $\bar{A}$ is a constant. This constant can be calculated:

$$\bar{A} = \bar{f}\left(0.6 + \left(\frac{A_{\text{side,branch,inlet}}}{A_{\text{side,branch,outlet}}}\right)^{2} + \zeta_{\text{app}}\right)^{0.5} \tag{3-16}$$

where $\bar{f}$ is a constant, $A_{\text{side branch inlet}}$ is the area of the side branch inlet, $A_{\text{side branch outlet}}$ is the area of the side branch outlet, and $\zeta_{\text{app}}$ is the resistance coefficient of the non manifold sections. The first constant can be calculated:

$$\bar{f} = n_{\text{s}} \frac{f_{\text{s}}}{f_{\text{in}}} \tag{3-17}$$

where this represents the ratio of cross-sectional areas out and in the header respectively, multiplied by the number of side branches. Next, the resistance coefficient through all the areas besides the header (apparatus, piping, bends, baffles, etc.) is calculated:

$$\zeta_{\text{app}} = \frac{2 \cdot \Delta P_{\text{app,section}}}{\rho(\bar{f} \cdot v_{\text{header,in}})} \quad (3\text{-}18)$$

where $\Delta P_{\text{app section}}$ is the pressure drop through all of those areas. The next important thing to calculate is the maldistribution in manifold based on correlations from Perry's Chemical Handbook 6-32 [92] as follow:

$$\textit{Percent Maldistribution} = 100 \cdot \left(1 - \sqrt{\frac{\Delta P_{\text{o}} - \left|\Delta P_{\text{manifold}}\right|}{\Delta P_{\text{o}}}}\right) \quad (3\text{-}19)$$

where $\Delta P_{\text{o}}$ is the pressure drop from upstream factors and $\Delta P_{\text{manifold}}$ is the pressure drop through the manifold. These calculations will be performed four times for the four manifolds used in the AXIe design.

### 3.4.2. Microchannel cold plate

In microchannel cooling, a cold plate is used which has two parts: the base, and the microchannels, as shown in Figure 3-9. The cold plate acts to increase the heat transfer coefficient as well as the surface area. This section will first cover the conduction thermal resistance model of the cold plate, then the heat transfer and pressure drop through the microchannels.

**Figure 3-9** OTS cold plate with 150 µm skived channels.

The thermal resistance of the cold plate via conduction is accounted for by the conduction and spreading resistance:

$$R_{sp} = \frac{\psi_{max}}{k_{cp} \cdot r_1 \sqrt{\pi}} \tag{3-20}$$

where $\Psi_{max}$ is the dimensionless constriction resistance, $k_{cp}$ is the material thermal conductivity (394.9 W m$^{-1}$ K$^{-1}$ for copper), and $r_1$ is the equivalent radius of the square heat spreader. The dimensionless constriction resistance is calculated based on the following equation:

$$\Psi_{max} = \frac{\varepsilon \cdot \tau}{\sqrt{\pi}} + \frac{1}{\sqrt{\pi}}(1-\varepsilon)\phi_n \tag{3-21}$$

where $\varepsilon$ is a dimensionless parameter which is the ratio of heat source to heat spreader's equivalent radii ($r_1/r_2$), $\tau$ is the dimensionless plate thickness which is the ratio of plate thickness to heat spreader's equivalent radii ($th_{cp}/r_2$) and $\phi_n$ is a dimensionless parameter calculated by the equation below:

$$\phi_n = \frac{\tanh(\lambda_n \cdot \tau) + \frac{\lambda_n}{Bi}}{1 + \frac{\lambda_n}{Bi}\tanh(\lambda_n \cdot \tau)} \tag{3-22}$$

where $\lambda_n$ is an eigenvalue and Bi is the biot number calculated by the following two equations:

$$\lambda_n = \pi + \frac{1}{\varepsilon\sqrt{\pi}} \tag{3-23}$$

$$Bi = \frac{htc \cdot r_2}{k_{cp}} \tag{3-24}$$

where *htc* is the heat transfer coefficient. The biot number is the ratio of convection to conduction resistance and determines which one is the dominant mode of heat transfer. If $Bi \ll 1$, then convection resistance is dominant and vice versa. This number is primarily used in heat transfer to assume the lumped capacitance method if $Bi < 0.1$ in transient applications [93], and if it's not less

than 0.1, it may not be assumed. However, in this application, the correlation is valid for all values of Biot numbers, as it was developed for steady state heat spreading.

The heat transfer coefficient and pressure drop for the microchannels is calculated with correlations related to the Nusselt number:

$$htc = \frac{Nu \cdot k_f}{D_h} \tag{3-25}$$

where $htc$ is the heat transfer coefficient, $Nu$ is the Nusselt number, and $D_h$ is the hydraulic diameter of the channel. The Nusselt number is the ratio of convection to conduction heat transfer. If the Nusselt number is 1 then the convection heat transfer is not better than the conduction heat transfer. If Nu > 1, then convective effects become more influential. The hydraulic diameter used in the Nusselt number equation for 3 sided microchannels is:

$$D_h = \frac{4A}{P_{wet}} = \frac{4 \cdot (W_{ch} \cdot H_{ch})}{2 \cdot H_{ch} + W_{ch}} \tag{3-26}$$

where $W_{ch}$ is the channel width and $H_{ch}$ is the channel height. The Nusselt number correlation for 3-wall heated fully developed laminar flow in microchannels [94] is defined by the equation below:

$$Nu_3 = 8.235(1 - 1.883\alpha + 3.767\alpha^2 - 5.814\alpha^3 + 5.361\alpha^4 - 2.0\alpha^5) \tag{3-27}$$

Equation (3-27) is only dependent on alpha, the aspect ratio $(W_{ch}/H_{ch})$ which must be less than 1. The Nusselt number is calculated differently for the developing region at the inlet of the channel as is shown in the following equation:

$$Nu_3(z) = Nu_3 + 8.68\left(1000\frac{z}{\operatorname{Re} D_h \operatorname{Pr}}\right)^{-0.506} \exp\left[\left(-9.427\alpha^{-1} - 23.472\right) \cdot \frac{z}{\operatorname{Re} D_h \operatorname{Pr}}\right] \tag{3-28}$$

where z is the position into the channel, the Reynolds number (Re) is the ratio of inertial forces to viscous forces and the Prandtl number (Pr) is the ratio of momentum diffusivity to thermal

diffusivity. The first of these two dimensionless parameters, the Reynolds number, is used for determining whether the fluid is laminar or turbulent and is commonly involved in heat transfer correlations. The Reynolds number is defined below:

$$\mathrm{Re} = \frac{\rho v D_\mathrm{h}}{\mu} \tag{3-29}$$

where $\rho$ is the fluids density, $v$ is the mean velocity in the channel, $D_\mathrm{h}$ is the hydraulic diameter and $\mu$ is the dynamic visocisity. The second dimensionless number, the Prandtl number is calculated as follows:

$$\mathrm{Pr} = \frac{\mu c_\mathrm{p}}{k_\mathrm{f}} \tag{3-30}$$

where $c_\mathrm{p}$ is the specific heat and $k_\mathrm{f}$ is the fluids thermal conductivity. If the Prandtl number is significantly greater than 1, then the fluid will have high pressure losses for that same heat transport compared to fluids with lower Prandtl numbers. The pressure drop for the microchannel heat exchanger is calculated the same as the microchannels for the radiator and will be described in the radiator section.

For microchannel heat sinks, the flow is commonly laminar due to the small hydraulic diameter of the microchannels and because it is laminar, the Nusselt number is a fixed number once the flow is fully developed. Figure 3-10 plots the Nusselt number distributions for different aspect ratio microchannels as a function of nondimensional axial location where $z^* = \frac{z}{Re D_\mathrm{h} Pr}$ and z is the axial location in

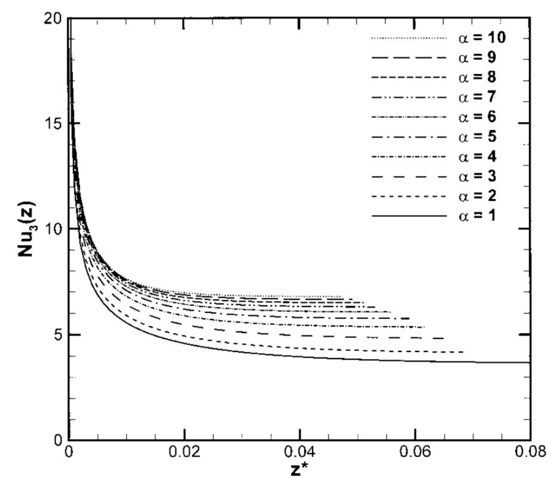


**Figure 3-10** Nusselt number distribution for 3-sided microchannel

the developing region from the previously mentioned correlation. For a fixed microchannel length (z), as the flow is increased, the developing region will increase as well and cause the Nusselt number and effectively heat transfer to increase. Furthermore, it can be seen that higher microchannel aspect ratio will result in higher Nusselt numbers.

A number of real-world microchannel heat sinks were obtained, and the dimensions were measured as shown in Table 3-4. These microchannel dimensions were then tested numerically to determine which has the lowest convection thermal resistance with water by varying the mass flow rate from 0-0.10 kg $s^{-1}$. The convection thermal resistance was calculated from the LMTD of the base temperature of the cold plate and the fluid temperatures in and out. Cold plate 1 had superior performance compared to the others due to its low channel width, high height, high aspect ratio, and high heat transfer coefficient and will be selected as the best cold plate for the Chapter 4 analysis. Cold plate 2 and 4 performed second best followed by cold plate 3. It is clear that cold plate 1 performs significantly better as the microchannel width was decreased to 150 μm and the fin thickness was held thicker than the microchannel width at 254 μm. The thermal performance and pressure drop of cold plate 1-4 vs mass flow rate is shown in Figure 3-11. As the mass flow rate increases, minimal effect in increased performance can be seen for cold plate 1 due to the small hydraulic diameter and laminar flow (Re= 5-530). This performance increase in convection heat transfer is from 0.0103 K $W^{-1}$ to 0.00959 K $W^{-1}$ while the pressure drop increases by a factor of 6. Cold plate 2 and 4 align similarly for convection resistance vs flow rate but cold plate 4 maintains significantly lower pressure drop due to the larger channel widths used. The flow rate for cold plate 2 and 4 reach the

**Table 3-4** Microchannel geometries performance at 0.020 kg s$^{-1}$ for Big Chip 1

| Cold Plate | Channel length (mm) | Channel Width (mm) | Fin Thickness (mm) | Fin Height (mm) | $R_{conv}$ (K W$^{-1}$) |
|---|---|---|---|---|---|
| 1 | 25.41 | 0.150 | 0.254 | 4.953 | 0.00959 |
| 2 | 36.63 | 0.524 | 0.385 | 1.721 | 0.0160 |
| 3 | 38.10 | 0.523 | 0.474 | 3.099 | 0.0127 |
| 4 | 40.64 | 0.673 | 0.334 | 4.547 | 0.0126 |

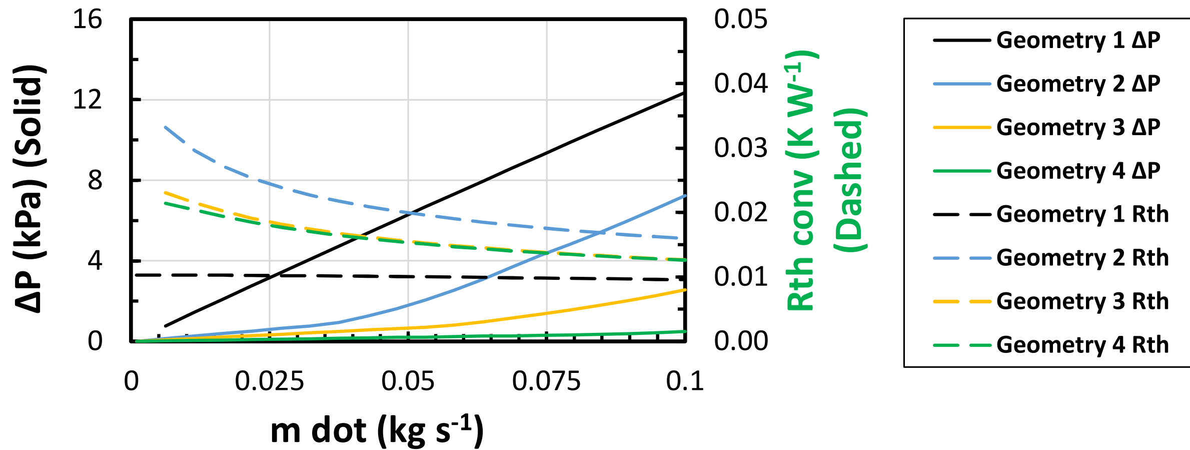


**Figure 3-11** Mass flow rate vs pressure drop and thermal resistance for OTS microchannels

transitional region with Re = 360-5667, and Re = 149-2369, respectively. This allowed the thermal resistance to further reduce as the developing region increased. Cold plate 3 performed worst with the second highest pressure drop and the worst convection thermal resistance due to its thick channels and fins. Thus, it can be seen that cold plate 1 is the best microchannel cold plate and that the optimal flow rate for forced single phase convection heat transfer with small channel widths is the minimum, as no noticeable effect in increased performance can be seen for increased mass flow rates. This is assuming the minimal mass flow rate can successfully absorb the heat load without significant temperature rise. In this modeling effort, the LMTD method was used to account for this.

### 3.4.1. Return jet impingement architecture

This section will outline the return jet impingement heat sink modeling. The modeling assumed a repeating unit cell within an array as shown in Figure 3-12a-b. In Figure 3-12a, the

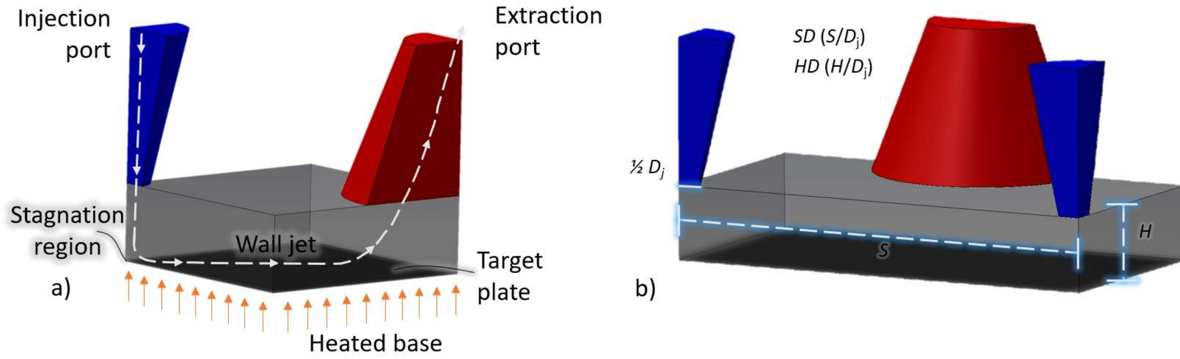


**Figure 3-12** Return jet impingement architecture a) repeating cell b) labeled dimensions

white arrows represents the flow path of the jet impingement fluid as it enters through the injection port and returns through the adjacent extraction port. The key dimensions in this unit cell are shown in Figure 3-12b. In a similar method as discussed previously, Nusselt number correlations will be used to calculate the heat transfer coefficient of the impinging jets.

$$Nu = \frac{htc \cdot D_{\mathrm{j}}}{k_{\mathrm{f}}} \tag{3-31}$$

where $htc$ is the heat transfer coefficient, $D_{\mathrm{j}}$ is the jet diameter, and $k_{\mathrm{f}}$ is the fluid's thermal conductivity. The Nusselt number correlation by Rattner [76] was selected and is shown below:

$$Nu = \mathrm{Pr}^{0.29} \cdot 10 \left\{ \sum_{j=1}^{20} a_{\mathrm{j}} \, \mathrm{Re}_{\mathrm{j}}^{b_{\mathrm{j}}} (SD)^{c_{\mathrm{j}}} (HD)^{d_{\mathrm{j}}} \right\} \tag{3-32}$$

where $SD$ is the nondimensional spacing between jets, $HD$ is the nondimensional height between the jet and the impingement surface, and $a_{\mathrm{j}}$, $b_{\mathrm{j}}$, $c_{\mathrm{j}}$, $d_{\mathrm{j}}$ are all constants shown in Table 3-5. The Rattner correlations were generated by performing over 1,000 randomized simulations of geometry and fluid properties ranging from: $SD$ = 1.8-7.1, $HD$ = 0.1-4.0, Pr = 1-200, and $\mathrm{Re}_{\mathrm{j}}$ = 20-

500. Hobby et al. [77] performed experimental simulations and tested the accuracy of a number of heat transfer correlations found in literature for this geometry as discussed in the jet impingement section in Chapter 2. Hubber and Viskanta [70], and Rattner's [76] correlations were close but began to diverge and over predict around Re = 1000. The correlation developed by Hoberg et al.

**Table 3-5** Rattner k factor and Nusselt number coefficients

| **k-factor coefficients** | | | | **Nusselt number coefficients** | | | |
|---|---|---|---|---|---|---|---|
| a | b | c | d | a | b | c | d |
| -0.0091 | 0 | 0 | -2.7 | -0.4262 | 0 | 0 | 1.5 |
| -0.0141 | 0 | 0.3 | -1.8 | -1.243 | 0 | -1 | 1 |
| -0.4498 | -0.7 | 0 | -1.8 | 0.7859 | -0.2 | 0 | 1 |
| 0.1548 | 0 | 0 | -1.8 | 1.807 | 0 | 0 | 1 |
| 0.0115 | 0 | 0.6 | -0.9 | -2.028 | 0 | -2 | 0.5 |
| 1.556 | -0.7 | 0.3 | -0.9 | -2.178 | -0.2 | -1 | 0.5 |
| 0.1025 | 0 | 0.3 | -0.9 | 5.203 | 0 | -1 | 0.5 |
| -21.99 | -1.4 | 0 | -0.9 | -5.989 | -0.4 | 0 | 0.5 |
| 5.374 | -0.7 | 0 | -0.9 | 2.252 | -0.2 | 0 | 0.5 |
| -0.5824 | 0 | 0 | -0.9 | -3.406 | 0 | 0 | 0.5 |
| 3.243 | 0 | 0.9 | 0 | 2.09 | 0 | -3 | 0.5 |
| 10.02 | -0.7 | 0.6 | 0 | -0.2111 | -0.2 | -2 | 0 |
| -16.22 | 0 | 0.6 | 0 | -2.827 | 0 | -2 | 0 |
| 25.38 | -1.4 | 0.3 | 0 | -14.44 | -0.4 | -1 | 0 |
| -37.73 | -0.7 | 0.3 | 0 | 11.79 | -0.2 | -1 | 0 |
| 27.13 | 0 | 0.3 | 0 | -1.623 | 0 | -1 | 0 |
| 412.1 | -2.1 | 0 | 0 | -37.66 | -0.6 | 0 | 0 |
| -103.8 | -1.4 | 0 | 0 | 61.32 | -0.4 | 0 | 0 |
| 35.65 | -0.7 | 0 | 0 | -31.21 | -0.2 | 0 | 0 |
| -15.09 | 0 | 0 | 0 | 6.782 | 0 | 0 | 0 |

[78] was not very accurate for this geometry, potentially due to maldistributions from their manifold system used. In further work by Hobby et al. [79], computational and experimental simulations were performed for Pr = 7, $Re_j$ = 300-1500, *SD* = 8, and *HD* = 2.5. The simulation results followed good agreement up to Re = 1000, but then over-predicted the Nusselt number for higher Reynolds numbers. This overprediction from simulation results could be because of neglecting viscous dissipation effects and/or the laminar to turbulent transition region for a jet at

Re=1000-3000 [80]. The model will use Rattner's correlation for Re = 20-500. By solving Equation (3-32), the heat transfer coefficient is found with Equation (3-31) and the convective thermal resistance is calculated as follows:

$$R_{\text{conv}} = \frac{1}{htc \cdot A_{\text{s}}} \tag{3-33}$$

where $A_s$ is the surface area of the lid.

The pressure drop is calculated with Equation (3-34). In Hobby et al. [79,95] the heat sink level manifold pressure drop accounted for 67% of the total pressure drop from the impingement part. If not designed well this can be up to 78% [96]. Rather than attempting to accurately model a complex heat sink level manifold distribution system, the percentage of pressure drop will be accounted for by 70% of the total part pressure drop. The return jet impingement heat sink pressure drop is calculated as follows:

$$\Delta P_{\text{jet,i}} = \frac{1}{2} K \cdot \rho \cdot v_{\text{jet,i}}^{\ 2} / Manifold_jet \tag{3-34}$$

where $K$ is the jet friction factor, $\rho$ is the fluid density, $v_{\text{jet,i}}$ is the jet velocity for each respective heat sink, and *Manifold_Jet* is 30%. Without the Manifold_jet term, this equation would only represent the jet pressure drop. The *Manifold_Jet* term compensates for the pressure drop due to the fluid moving from tube to jet and is comparable with other manifolds studied in literature [79,95,96]. The K-factor is calculated similarly to the Nusselt number as shown below [76]:

$$K = 10 \wedge \left\{ \sum_{j=1}^{20} a_{\text{j}} \, \text{Re}^{b_{\text{j}}} (SD)^{c_{\text{j}}} (HD)^{d_{\text{j}}} \right\} \tag{3-35}$$

where the coefficients ($a_j$, $b_j$, $c_j$, $d_j$) to be used shown in Table 3-5 under "K-factor correlation".

A sensitivity analysis of the geometry described in Hobby et al. [79] will be performed for all the primary fluids investigated in Chapter 4. The baseline geometry however will be used to

select the primary dielectric fluids. This geometry is $D_j$ = 300 μm, *SD* = 8, *HD* = 1. Dielectrics cannot damage electrical components due to their nonconductive nature and thus, will be used in cooling configuration 3-5d. The dielectric fluids investigated were FC72, FC77, FC770, FC40, FC43, FC70, FC104 and Jet Fuel A-1. The fluid properties and results are in Table 3-6.

**Table 3-6** Dielectric test data and fluid properties for Big Chip 1 configuration 3-5d

| Fluid | FC72 | FC77 | FC770 | FC40 | FC43 | FC70 | FC104 | Jet Fuel$_{A-1}$ |
|---|---|---|---|---|---|---|---|---|
| $R_{conv}$ (K W$^{-1}$) | 0.10 | 0.10 | 0.10 | 0.10 | 0.10 | 0.10 | 0.10 | 0.10 |
| $\dot{m}$ (kg s$^{-1}$) | 0.031 | 0.043 | 0.048 | 0.070 | 0.047 | 0.047 | 0.046 | 0.012 |
| $\Delta P_{heat\ sink}$ (kPa) | 68.8 | 124.2 | 153.8 | 689+ | 689+ | 689+ | 143.8 | 201.3 |
| ρ (kg m$^{-3}$) | 1610 | 1716 | 1727 | 1801 | 1782 | 1888 | 1695 | 793 |
| μ (10$^{-3}$ kg m$^{-1}$s$^{-1}$) | 0.463 | 0.806 | 0.992 | 2.15 | 2.02 | 7.16 | 0.881 | 0.912 |
| $k_f$ (W m$^{-1}$ K$^{-1}$) | 0.055 | 0.061 | 0.060 | 0.064 | 0.063 | 0.070 | 0.061 | 0.11 |
| $c_p$ (j kg$^{-1}$ K$^{-1}$) | 1092 | 936 | 1078 | 1092 | 1107 | 1092 | 936 | 2025 |
| Prandtl | 9.3 | 12.4 | 18.8 | 36.9 | 35.6 | 112 | 13.5 | 16.6 |

The table was generated by setting the thermal resistance at 0.10 K W$^{-1}$ and solving for the flow rate and pressure drop on Big Chip 1. The pressure drop through the return jet impingement part for FC72 is the lowest at 68.8 kPa and therefore performed the best. FC72 had the lowest viscosity which aided in its success for having the lowest pressure drop. The worst fluids were not solved for at 0.10 K W$^{-1}$ because of their unreasonably high flow rate and pressure drop, requiring over 10x the pumping power of FC72. This was defined by head requirements beyond 689 kPa. Based on pressure drop, jet fuel places fifth out of the fluids considered here however, it makes up for this by requiring significantly lower overall mass flow rate. Jet Fuel A-1 and FC72 will be the primary dielectric fluids and a sensitivity analysis will be performed in the following chapter.

### 3.4.2. Radiator

This section will outline the heat exchanger modeling procedure. First, the energy equations will be presented, followed by the governing equations for the heat duty. Next, the internal heat transfer and its associated pressure drop through the radiator tubes will be discussed.

The external heat transfer will be described with its correlations and pressure drop, and finally, the air side mass flow rate available from the fans will be presented. The location of the heat exchanger in the chassis is shown in Figure 3-13 in the transparent orange box on the left.

**Figure 3-13** Keysight M9506A AXIe chassis with heat exchanger

The required heat duty of the radiator is determined from two energy balance equations at the heatsink (3-36), (3-39) and (3-40). The first equation represents the heat transferred by the working fluid for the liquid cooled chips:

$$Q_{\text{chip,i}} = UA_{\text{chip,i}} \cdot LMTD_{\text{chip,i}} / 80\% \tag{3-36}$$

where $Q_{\text{chip,i}}$ is the respective chip power, $UA_{\text{chip,i}}$ is the universal heat transfer coefficient for that heat sink, the 0.8 represents that only 80% of the heat is cooled by the method, and *LMTD* is the log mean temperature difference. The universal heat transfer coefficient for each chip is defined as:

$$UA_{\text{chip,i}} = R_{\text{cooling,i}} \tag{3-37}$$

where $R_{\text{cooling,i}}$ is the total thermal resistance between the fluid and die as previously mentioned in section 3.1.2. The log mean temperature difference for each chip is defined as:

$$LMTD = \frac{(T_s - T_{h,i}) - (T_s - T_{h,o})}{\ln\left(\frac{T_s - T_{h,i}}{T_s - T_{h,o}}\right)} \quad (3\text{-}38)$$

where $T_s$ is the surface temperature in contact with the fluid, $T_{h,i}$ is the fluid inlet temperature and $T_{h,o}$ is the fluid outlet temperature. The next equation represents the total heat transferred from the fluid as the total heat the radiator needs to cool:

$$\sum_{i=1}^{N_{chip}} Q_{chip,i} = \sum_{i=1}^{N_{chip}} \dot{m}_{chip,i} \cdot (h_{h,o} - h_{h,i}) / 80\% \quad (3\text{-}39)$$

where $\dot{m}_{chip,i}$ is the mass flow rate for each respective chip, $h_{h,i}$ is the inlet fluid enthalpy and $h_{h,,o}$ is the outlet enthalpy for each respective chip. Similarly, as mentioned in section 3.3, the enthalpy approximation for constant specific heats will be used in the place of substances with limited enthalpy data. This equation is defined as:

$$\sum_{i=1}^{N_{chip}} Q_{chip,i} = \sum_{i=1}^{N_{chip}} \dot{m}_{chip,i} \cdot c_{p,l} \cdot (T_{h,o} - T_{h,i}) / 80\% \quad (3\text{-}40)$$

where $c_{p,l}$ is the specific heat of the fluid and $T_{h,in}$ is the inlet fluid temperature and $T_{h,o}$ is the outlet temperature for each respective heat sink. The overall heat load was calculated:

$$Q_{chips,cooled} = \sum_{i=1}^{N_{chip}} N_{chip,i} Q_{chip,i} / 80\% \quad (3\text{-}41)$$

where $N_{chip,i}$ is the number repeating heat sources of a particular heat source.

Figure 3-14 [97] shows a cross flow heat exchanger with louvered fins on the air side and microchannels on the inside. This heat exchanger was modeled with the $\varepsilon$-NTU method. Equations (3-42) – (3-45) are the governing equations of a crossflow heat exchanger for one fluid unmixed.

$$Q = \varepsilon_{rad} \cdot C_{min} \cdot (T_{h,i} - T_{c,i}) \quad (3\text{-}42)$$

$$NTU = -\ln\left[1+\left(\frac{1}{C_{\mathrm{r}}}\right)\ln\left(1-\varepsilon_{\mathrm{rad}}\cdot C_{\mathrm{r}}\right)\right] \tag{3-43}$$

$$UA_{\mathrm{rad}} = NTU\cdot C_{\min} \tag{3-44}$$

where $C_{\min}$ and $C_{\mathrm{r}}$ are:

$$C_{\min} = \min\left(\dot{m}_{\mathrm{a}}c_{\mathrm{p,a}}, \dot{m}_{\mathrm{l}}c_{\mathrm{p,l}}\right) \tag{3-45}$$

$$C_{\mathrm{r}} = \frac{C_{\min}}{C_{\max}} \tag{3-46}$$

where $\dot{m}_{\mathrm{a}}$ and $\dot{m}_{\mathrm{l}}$ are the air and liquid mass flowrates and $c_{\mathrm{p,a}}$ and $c_{\mathrm{p,l}}$ are the air and liquid specific heats respectively.

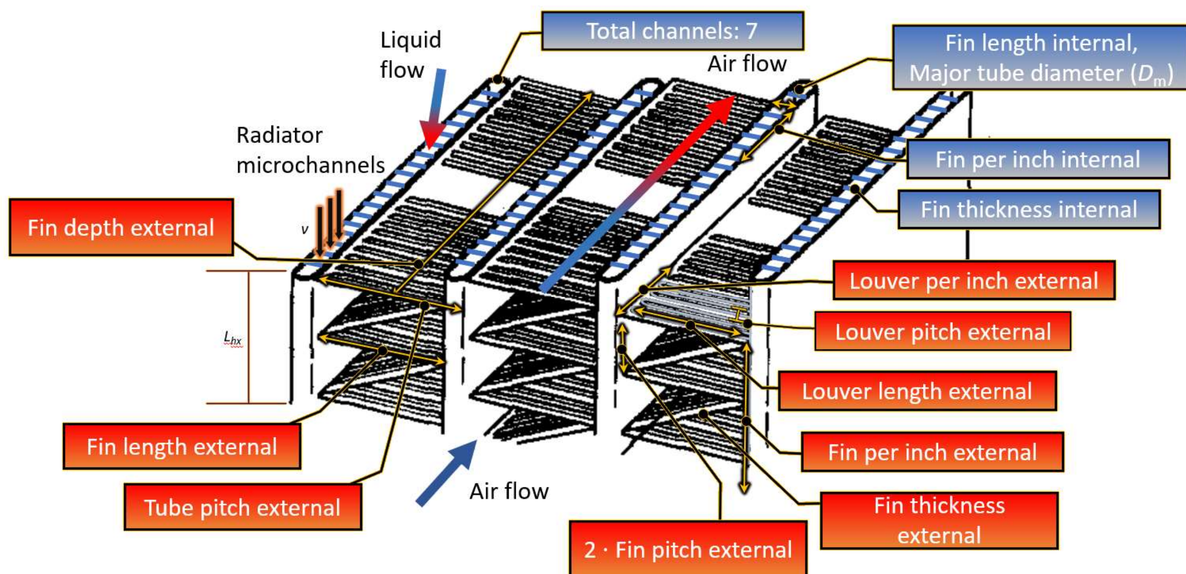


**Figure 3-14** Air side radiator geometry: corrugated louver fins in triangular arrangement [100]

There are three thermal resistances for this heat exchanger: the convective heat transfer between the liquid and microchannel, the conduction heat transfer through the wall, and the convection heat transfer between air and the louver fins. Thus, the total resistance is calculated by the sum of these three resistances and the $UA_{\mathrm{rad}}$ is calculated as shown below:

$$UA_{\text{rad}} = \frac{1}{R_{\text{inner}} + R_{\text{wall}} + R_{\text{outer}}} \tag{3-47}$$

where $R_{\text{inner}}$ and $R_{\text{outer}}$ are the internal and external convective resistances and $R_{\text{wall}}$ is the conduction resistance. Equation (3-48) is used to calculate the convection thermal resistance for both internal and external structures:

$$R = \left( \left( \frac{1}{htc \cdot A_{\text{floor}}} \right)^{-1} + \left( \frac{1}{\eta_{\text{fin}} \cdot htc \cdot A_{\text{fin}}} \right)^{-1} \right)^{-1} \tag{3-48}$$

where $htc$ is the respective heat transfer coefficient, $A_{\text{floor}}$ is the floor area exposed, $A_{\text{fin}}$ is the fin area exposed and $\eta_{\text{fin}}$ is the fin efficiency. The fin efficiency of the microchannels inside the radiator is calculated as follows:

$$\eta_{\text{fin}} = \frac{\tanh(mL_{\text{c}})}{mL_{\text{c}}} \tag{3-49}$$

where $L_{\text{c}}$ is the characteristic length of the fin and $m$ is defined as

$$m = \sqrt{\frac{2 \cdot htc}{k_{\text{rad}} \cdot th}} \tag{3-50}$$

where $htc$ is the heat transfer coefficient, $k_{\text{rad}}$ is the aluminum radiators thermal conductivity (159 W $m^{-1}$ $K^{-1}$ for aluminum), and $th$ is the fin thickness. The wall thermal resistance is calculated as shown below:

$$R_{\text{wall}} = \frac{L}{k_{\text{rad}} A_{\text{wall}}} \tag{3-51}$$

where $L$ is the wall thickness, $k_{\text{rad}}$ is the thermal conductivity of the radiator (159 W $m^{-1}$ $K^{-1}$), and $A_{\text{wall}}$ is the area of wall exposed inside the radiator. Equations (3-52) – (3-54) depict the Nusselt correlation used with Equation (3-25) to calculate the heat transfer coefficient. These correlations were developed by Shah and Bhatti [98]:

$$Nu = \left\{ {Nu_{\mathrm{lam}}}^{10} + \left\{ \frac{e^{2200-\mathrm{Re}}}{365 \cdot Nu_{\mathrm{lam}}} + \left( Nu_{\mathrm{o}} + \frac{0.079\,\mathrm{Re}\cdot \Pr(f_{\mathrm{darcy}}/8)^{0.5}}{\left(1+\Pr^{0.8}\right)^{5/6}} \right)^{-2} \right\}^{-5} \right\}^{0.1} \quad (3\text{-}52)$$

$$Nu_{\mathrm{lam}} = 8.235\left(1 - 2.0421\alpha + 3.0853\alpha^2 - 2.4765\alpha^3 + 1.5078\alpha^4 - 0.1861\alpha^5\right) \quad (3\text{-}53)$$

$$Nu_{\mathrm{o}} = 6.3 \quad (3\text{-}54)$$

where alpha is the aspect ratio and $f_{\mathrm{darcy}}$ is the Darcy friction factor. The friction factor is calculated with equations (3-55) – (3-57) depending on the Reynolds number as shown in Equation (3-29). The transition from laminar to turbulent for this correlation is Re = 2000 – 4000. Thus, if Re < 2000 then the friction factor is as follows:

$$f_{\mathrm{lam}} = \frac{96}{\mathrm{Re}}\left(1 - 1.3553\alpha + 1.9467\alpha^2 - 1.7012\alpha^3 + 0.9564\alpha^4 - 0.2537\alpha^5\right) \quad (3\text{-}55)$$

but, if 2000 ≤ Re ≤ 4000, then interpolation will be used to calculate the friction factor for the transitional flow:

$$f_{\mathrm{transistion}} = \exp\left( \frac{\ln(\mathrm{Re}) - \ln(2000)}{\ln(4000) - \ln(2000)} \cdot \left\{ \ln(f_{\mathrm{turb}}(4000) - \ln(f_{\mathrm{turb}}(2000) \right\} + \ln(f_{\mathrm{lam}}(2000)) \right) \quad (3\text{-}56)$$

and, if Re > 4000, then the friction factor is calculated as follows:

$$f_{\mathrm{turb}} = \frac{0.3164}{\mathrm{Re}^{0.25}}(1.0875 - 0.1125\alpha) \quad (3\text{-}57)$$

The Darcy friction factor calculated from the above equations is also used to calculate the microchannel heat sink pressure drop. The friction factor is used to calculate the internal pressure drop as shown below:

$$\Delta P = 0.5 f_{\mathrm{darcy}} \cdot \rho \cdot v^2 \cdot \frac{L_{\mathrm{hx}}}{D_{\mathrm{h}}} \quad (3\text{-}58)$$

where $v$ is the velocity of the fluid in the channel, and $L_{hx}$ is the length of the heat exchanger. The pressure drop due to the expansion or contraction from the radiator inlet to the microchannels is calculated as follows:

$$\Delta P_{\text{Expan/conract}} = 0.5 \cdot K_{\text{expansion/contraction}} \cdot \rho \cdot v^2 \tag{3-59}$$

where $K_{\text{expansion/contraction}}$ is the k-factor for either area expansion or contraction. This k-factor is modeled as a sudden expansion and sudden contraction based off available k-factor correlations in [99] published by Crane. The K factors are as follows

$$K_{\text{expansion}} = \frac{\left(1-\beta^2\right)^2}{\beta^4} \tag{3-60}$$

$$K_{\text{contraction}} = \frac{\left(1-\beta^2\right)}{\beta^4} \tag{3-61}$$

where $\beta$ is the ratio of diameter 1 and diameter 2. The diameter for the inlet channels is calculated by summing the total flow area and calculating its circular diameter.

The air side of the heat exchanger will now be discussed. Figure 3-14 shows the air side of the louver fins. The correlation for heat transfer and pressure drop through the louver fins used is Chang et al [100] an amendment of the original correlation by Chang and Wang [97]. The form of the Nusselt correlation used to calculate the external heat transfer coefficient is shown below:

$$Nu = j_{\text{external}} \cdot \text{Re} \cdot \text{Pr}^{1/3} \tag{3-62}$$

where $j_{\text{external}}$ is the external Colburn J friction factor which is calculated from the product of three terms:

$$j_{\text{external}} = f_1 f_2 f_3 \tag{3-63}$$

where $f_1$, $f_2$ and $f_3$ are the friction factor correlation parameters. The correlation for these depends on the Reynolds number. For $0 < \text{Re} < 130$:

$$f_1 = 14.39\,\mathrm{Re}^{-0.805 F_\mathrm{p}/F_\mathrm{l}} \cdot \left( \ln\left( 1 + \frac{F_\mathrm{p}}{L_\mathrm{p}} \right) \right)^{3.04} \quad (3\text{-}64)$$

$$f_2 = \left( \ln\left( \left( \frac{F_\mathrm{t,ext}}{F_\mathrm{p}} \right)^{0.48} + 0.9 \right) \right)^{-1.435} \cdot \left( \frac{D_\mathrm{h}}{L_\mathrm{p}} \right)^{-3.01} \left( \ln\left(0.5\,\mathrm{Re}\right) \right)^{-3.01} \quad (3\text{-}65)$$

$$f_3 = \left( \frac{F_\mathrm{p}}{L_\mathrm{i}} \right)^{-0.308} \left( \frac{F_\mathrm{d}}{L_\mathrm{i}} \right)^{-0.308} \exp^{-0.1167 \frac{T_\mathrm{p}}{D_\mathrm{m}} \cdot \theta^{0.35}} \quad (3\text{-}66)$$

For 130 < Re < 230:

$$f_\mathrm{fanning} = 0.5(1+w) \cdot f_{130} + (1-w) \cdot f_{230} \quad (3\text{-}67)$$

$$w = 3.6 - 0.02\,\mathrm{Re} \quad (3\text{-}68)$$

And for 230< Re < 5000

$$f_1 = 4.97\,\mathrm{Re}^{0.6049 - \frac{1.064}{\theta^{0.2}}} \cdot \left( \ln\left( 0.9 + \left( \frac{F_\mathrm{t,ext}}{F_\mathrm{p}} \right)^{0.5} \right) \right)^{-0.527} \quad (3\text{-}69)$$

$$f_2 = \left( \frac{D_\mathrm{h}}{L_\mathrm{p}} \ln\left(0.3\,\mathrm{Re}\right) \right)^{-2.966} \left( \frac{F_\mathrm{p}}{L_\mathrm{i}} \right)^{-0.7931 \frac{T_\mathrm{p}}{T_\mathrm{h}}} \quad (3\text{-}70)$$

$$f_3 = \left( \frac{T_\mathrm{p}}{D_\mathrm{m}} \right)^{-0.0446} \left( \ln\left( 1.2 + \left( \frac{L_\mathrm{p}}{F_\mathrm{p}} \right)^{1.4} \right) \right)^{-3.553} \cdot \theta^{-0.477} \quad (3\text{-}71)$$

where $F_\mathrm{p}$ is the fin pitch, $F_\mathrm{t,ext}$ is the external fin thickness, $F_\mathrm{d}$ is the fin depth, $\theta$ is the louver angle in degrees, $L_\mathrm{p}$ is the louver pitch, $L_\mathrm{I}$ is the louver length, $T_\mathrm{p}$ is the tube pitch, $D_\mathrm{m}$ is the major tube diameter, and $T_\mathrm{h}$ is the tube pitch minus the tube diameter. The air side pressure drop will now be calculated. The air side pressure drop can be calculated from:

$$\Delta P_\mathrm{air,hx} = 0.5 f_\mathrm{darcy} \cdot \rho \cdot v^2 \frac{F_\mathrm{d}}{D_\mathrm{h}} \quad (3\text{-}72)$$

where the Darcy friction factor is four times the Colburn J friction factor. The external geometries that will be modified during the optimization are: the $F_{t,ext}$ (fin thickness), $F_{l,ext}$ (fin length), $FPI_{ext}$ (fins per inch external), $\theta$, and $LPI_{ext}$ (louvers per inch). The initial dimensions to the model, and the dependent variables relation to the independent variables are shown in Table 3-7. By modifying the five dependent variables, all of the dimensions will be optimized. Theta will be given a base value of 28 degrees for the preliminary calculations while optimizing the other dimensions. After this is completed, Theta will then be varied to determine if changing it can offer improved performance. Similarly, the louvers per inch will also be set at 22 and will be modified after $F_{t,ext}$, $F_{l,ext}$ and $FPI_{ext}$ have been optimized. Finally, the wall thickness will set at 2 mm and will not be changed.

**Table 3-7** Louver fin dependent variables relation to independent variables

| **Variable** | **Value** |
|---|---|
| $Wall_{th}$ (Wall thickness) | 2.00 [mm] |
| $F_{t,ext}$ (fin thickness) | 0.10 [mm] |
| $F_{l,ext}$ (fin length), | 12.70 [mm] |
| $FPI_{ext}$ (fins per inch external) | 19 |
| $LPI_{ext}$ (louvers per inch) | 22 |
| $\theta$ (Louver angle) | 28 [degrees] |
| $D_m$ (Tube diameter) | $F_{l,int}$ |
| $L_p$ (Louver pitch) | 0.0254 [m] / $LPI_{ext}$ |
| $F_p$ (Fin pitch) | 0.0254 [m] / $FPI_{ext}$ |
| $F_d$ (Fin depth) | 0.05334 [m] (2.1 [in]) |
| $L_l$ (Louver length) | $0.8 \cdot F_l$ |
| $T_p$ (Tube pitch) | $F_{l,int} + Wall_{th}$ |
| $T_h$ (Tube pitch minus major tube diameter) | $T_p$ - $D_m$ |

The volumetric flow rates from the fans can be determined by solving the operating point:

$$\Delta P_{\text{fan},100} = \Delta P_{\text{air,hx}} + \Delta P_{\text{chassis}} \tag{3-73}$$

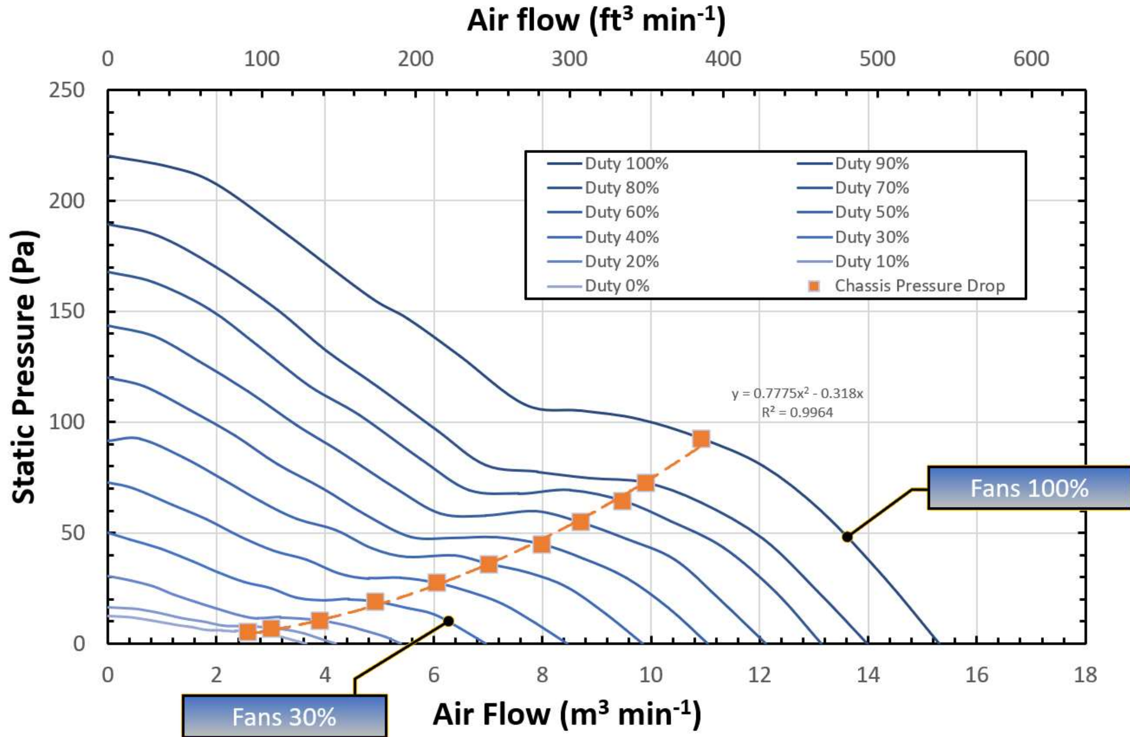


**Figure 3-15** M9506A Keysight AXIe chassis fan curves

where $\Delta P_{\text{fan,100}}$ is the fan curve of fan tray 1 at 100% duty cycle, and $\Delta P_{\text{chassis}}$ is the air side pressure drop from the chassis. The fan curves for the six fans in fan tray 1 are shown in Figure 3-15, courtesy of Keysight. The fans at 100% duty cycle in Pascals:

$$\Delta P_{\text{fan,100}} = 20.436x^6 - 147.34x^5 + 359.1x^4 - 315.06x^3 + 23.578x^2 - 25.805x + 220.39 \quad (3\text{-}74)$$

where $x$ represents the volumetric flow rate of the fans in m$^3$ min$^{-1}$. The actual flow rate at the heat exchanger can be determined:

$$\dot{V}_{\text{fan,act}} = x \cdot \frac{\rho_{\text{a,std}}}{\rho_{\text{a,hx,avg}}} \quad (3\text{-}75)$$

where $\rho_{\text{a,std}}$ is the air at standard pressure and temperature of 25°C, and $\rho_{\text{a,hx,avg}}$ is the average air density in the heat exchanger at its average air temperature and pressure. The pressure drop across the M9506A AXIe chassis was also measured in the lab

$$\Delta P_{\text{chassis}} = 0.7775x^2 - 0.318x \tag{3-76}$$

where $x$ is the volumetric flow rate.

### 3.4.3. Pump

The flow delivery device for this system will be sized based off the required head and volumetric flow rate. The head calculation for the machine:

$$H_{\text{head}} = \frac{\Lambda P_{\text{pump}}}{\rho_{\text{f}}} \tag{3-77}$$

where $\Delta P_{\text{pump}}$ is the total system pressure drop at the maximum operating point in lbf ft$^{-2}$ and $\rho_{\text{f}}$ is the density of the fluid in lbf ft$^{-3}$. This quantity reflects how high the fluid may be pumped vertically in ft based off the given pressure and density. The volumetric flow rate for the system:

$$\dot{V}_{\text{gpm}} = \frac{\dot{m}_{\text{tot}}}{\rho_{\text{f}}} \tag{3-78}$$

in gallons per minute, where $\dot{m}_{\text{tot}}$ is the total system mass flow rate in lbf s$^{-1}$. The pump will be sized with a maximum power draw of 0.5 hp to confirm the head and flow rate can be obtained with an OTS pump.

## 3.5. Acoustic Considerations

Acoustic tolerances are typically not discussed, but in real world applications remain a big problem for air-cooling. Table 3-8 [101] shows representative sound levels from different noise sources. Sound is characterized by a pressure calculation:

$$L_{\text{p,s}} = 10\log\frac{p_{rms}{}^{2}}{\left(2\cdot10^{-5}\,Pa\right)}(dB) \tag{3-79}$$

where $p_{\text{rms}}$ is the root mean square of the SPL (sound pressure level) over the broadband spectrum in Pascals and 20 μPa is the reference pressure. Typical residential and commercial limits are 68

dBa and 72 dBa, respectively. The acoustic output for the 2nd generation Keysight M9505a AXIe chassis operating at a maximum heat load of 200 W/slot is 65 dBa. The third generation M9506a chassis, however, has higher cooling capacities up to 300 W/slot and can reach the commercial acoustic limit of 72 dBa due to the increase in airflow requirements from 540 to 1080 sCFM. This seemingly small difference in decibels corresponds to a doubling in fan acoustic emissions. However, when the 3rd generation AXIe chassis is cooling 200 W/slot, the sound pressure level is 61 dBa because with the extra fan tray, each fan provides a lower pressure and flow rate compared to one fan tray. A modest gain in cooling performance can be made by doubling the flow rate, but this has fundamental limits as the commercial acoustics limit has been met. Selecting fans with sound pressure levels while operating at maximum capacity will be critical toward meeting the acoustic targets.

**Table 3-8** Noise levels referenced to real world sounds

| Noise Type | SPL (Pa) | Noise Level (dBa) |
|---|---|---|
| Hearing threshold | 0.00002 | 0 |
| Recording studio | 0.0002 | 20 |
| Bedroom at night | 0.0002 | 20 |
| Normal sleep | 0.001 | 30-35 |
| Living room | 0.002 | 40 |
| Speech interference, 4 ft | 0.04 | 65 |
| Residential limit | 0.05 | 68 |
| Commercial limit | 0.08 | 72 |
| Air compressor, 50 ft | 0.15 | 75-85 |
| OSHA 8-h limit | 1 | 90 |
| Pneumatic hammer (at Operator) | 3 | 100 |
| Airplane (Boeing 707) | 8 | 112 |
| Concorde SST | 40 | 123 |
| Threshold of pain | 180 | 140 |

As shown in literature, the sound pressure level from fans follows a linear relationship to flow rate [102–104]. This is depicted in Figure 3-16 [103] where the volumetric flow rate is plotted against the sound pressure level. To model the fans selected for this research, a linear relationship

was developed by using the minimum and maximum sound power levels and the corresponding volumetric flow rates as shown below:

$$SPL = m \cdot x + b \tag{3-80}$$

where m is the slope from point to point, x is the volumetric flow rate and b is the lower SPL limit which is a constant dependent upon the machine and its configuration. The SPL limit constant of the Keysight M9506A AXIE chassis was measured in the laboratory to be 40.2 dBa and the slope was calculated to be 17/260 where x is in CFM. This number will be used to scale the increase in acoustic output via the chassis in order to reach the cooling performance necessary to cool the proposed system.

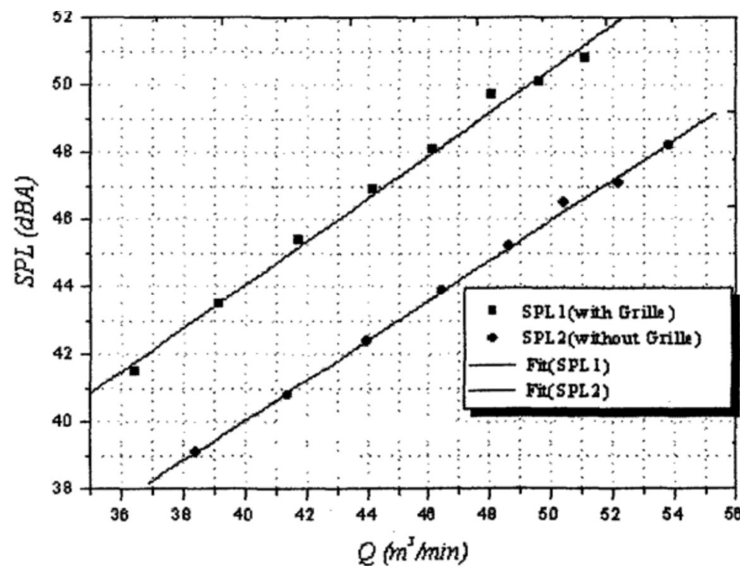


**Figure 3-16** Flow rate vs sound pressure level [103]

In this work, the equivalent air-cooled SPL of the proposed system will be predicted based off the acoustic literature presented and from previous acoustic data measured in the laboratory on the AXIe chassis. After this is calculated, it will be speculated whether it is realistic to design one of these systems with air cooling and what effect it would have on acoustics in the room. This number will be compared with OSHA (Occupational Safety and Health Administration) standards

for acoustic levels in the workplace as well as with the acoustic outputs currently in place.

# CHAPTER 4. Analysis and Discussion

In this section, the modeling results for the liquid cooled M9506A 5-slot AXIe chassis will be presented. First, the heat exchanger optimization for FC72 will be discussed, followed by the heat exchanger design and optimization for the different fluids studied, then the heat sink results, and overall heat sink performance will be presented. Next, the overall system performance will be examined to determine which configuration had the best performance. Finally, the failure rate and acoustics will be discussed to determine if a cooling method can increase the life of an electronics unit while operating at higher ambient temperatures.

## 4.1. Heat Exchanger Design

The heat exchanger for water, water glycol, FC72 and jet fuel were numerically optimized for the lowest steady state fluid operating temperature with the existing chassis fans. The ambient temperature was 50°C and the total heat load was set at 3.125 kW, where the heat exchanger rejected 2.122 kW (i.e., the liquid cooled chips absorbed heat load). The fan curves were used with the calculated pressure drop in the chassis and across the air side of the radiator to calculate the air flow rate through the chassis at 100% speed for full load. The minimum mass flow rate for the liquid side was set based off the minimum heat capacity rate provided by the fans. The allowable size of the heat exchanger was limited to fit in fan tray 2 with dimensions 2.1 in x 6.77 in x 11.5 in. The internal and external geometry optimization for FC72 in this fixed volume will now be discussed, followed by the primary fluids optimized heat exchangers geometry and performance.

The internal geometry optimization for minimizing the exit fluid temperature of the heat exchanger with FC72 as the working fluid is shown in Figure 4-1 through Figure 4-3. In Figure 4-1, the air side louver fin geometry has been set at: *total number of rows* = 19, Theta = 28 degrees, *LPI* = 22, $F_{t,ext}$ = 0.10 mm, and $FPI_{ext}$ = 19; where the internal fin length is plotted against the

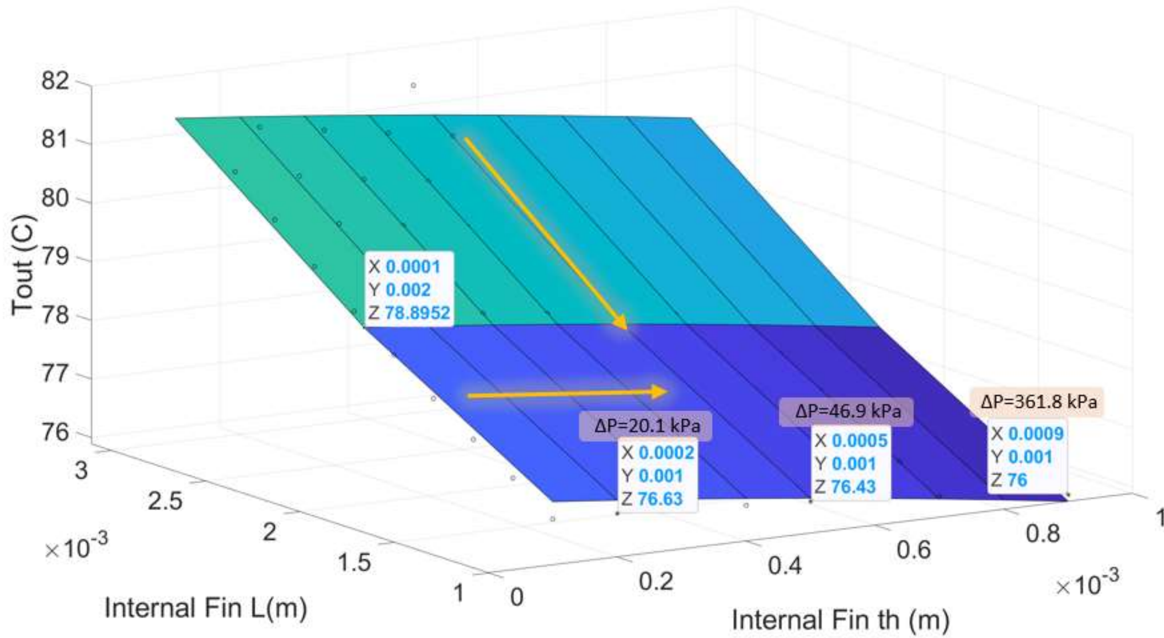


**Figure 4-1** Heat exchanger optimization for radiator outlet temperature: internal fin length vs internal fin thickness. Internal geometry: $\dot{m}_{liq}$ = 0.99 kg s$^{-1}$. External geometry: *total_rows* = 19, $\theta$ = 28 degrees, *LPI* = 22, $F_{t,ext}$ = 0.10 mm, $F_{l,ext}$ = 12.70-10.80 mm and $FPI_{ext}$ = 19.

internal fin thickness while the fluid mass flow rate is held constant at 0.99 kg s$^{-1}$, and the air side heat transfer is solved using the air flow rate that is supplied by the fans. The total number of rows is calculated as

$$total_rows = internal.rows + external.rows \tag{4-1}$$

where *internal.rows* is the total number of parallel tube rows vertically, and *external.rows* is the total number of parallel external fin rows. The air side fin length is calculated based off the internal fin length to hold the heat exchanger height constant at 171.9 mm with 10 parallel external rows and 9 parallel internal fin rows (i.e., $F_{l,ext}$ = 12.70 mm when $F_{l,int}$ = 1.00 mm and $F_{l,ext}$ = 11.2 mm when $F_{l,int}$ = 2.68 mm). The total number of tubes in the internal row is held constant at 44. It is shown that the minimal temperature will be achieved by minimizing the internal fin length to 1.0 mm and maximizing the fin thickness towards 1.0 mm. A shorter, thicker fin is more efficient by

reducing conduction resistance and the heat transfer rate increases as the internal row size decreases. Also, the area on the air side is increased through the reduction of the internal fin length. However, at high fin thickness extremes, the pressure drop rapidly increases for a small reduction in fluid temperature (e.g., $F_{th,int}$ = 0.2 mm when $\Delta P_{int}$ = 20.1 kPa and $T_2$ = 76.63°C, $F_{th,int}$ = 0.5 mm when $\Delta P_{int}$ = 46.9 kPa and $T_2$ = 76.43°C, $F_{th,int}$ = 0.9 mm when $\Delta P_{int}$ = 361.8 kPa and $T_2$ = 76.00°C). Changing the $F_{th,int}$ from 0.5 mm to 0.9 mm resulted in a pressure drop increase by a factor of eight, while the fluid temperature only reduced by 0.43°C. Due to the available pumping power (365W, 0.5 hp), which is roughly 225 kPa at 1.25 kg $s^{-1}$ for the FC72 system, the internal fin thickness cannot be increases above 0.7 mm at $FPI_{int}$ = 21. A further increase can be seen below 1.0 mm fin height; however, this has been set as the minimum height for manufacturability purposes.

In Figure 4-2, the internal fin thickness is plotted against the internal fins per inch. Again, the mass flow rate is held constant at 0.99 kg $s^{-1}$. The fluid temperature is minimized by maximizing the fins per inch to 25 and the fin thickness to 1.0 mm. There is a diminishing rate of return for outlet temperature as the pressure drop rapidly increases at extremes of these quantities. As the available pressure drop is limited, it is more beneficial to increase $FPI_{int}$ than $F_{th,int}$ as can be shown (i.e., $F_{th,int}$ = 0.5 mm and $FPI_{int}$ = 20 when $\Delta P_{int}$ = 41.8 kPa and $T_2$ = 76.49°C, $F_{th,int}$ = 0.5 mm and $FPI_{int}$ = 22 when $\Delta P_{int}$ = 52.7 kPa and $T_2$ = 76.37°C, $F_{th,int}$ = 0.6 mm and $FPI_{int}$ = 20 when $\Delta P_{int}$ = 58.6 kPa and $T_2$ = 76.40°C). When the same cooling performance is achieved from increased $FPI_{int}$ and $F_{th,int}$, the pressure drop increased by 10.9 kPa, and 16.8 kPa, respectively. Thus, it is more beneficial to increase $FPI_{int}$. The internal tube width has been set at a minimum of 0.5 mm for manufacturability purposes. This occurs at a $FPI_{int}$ of 25 and an internal fin thickness of 0.5 mm. Therefore, the optimal geometry is at $FPI_{int}$ = 25 and $F_{th,int}$ = 0.5 mm,

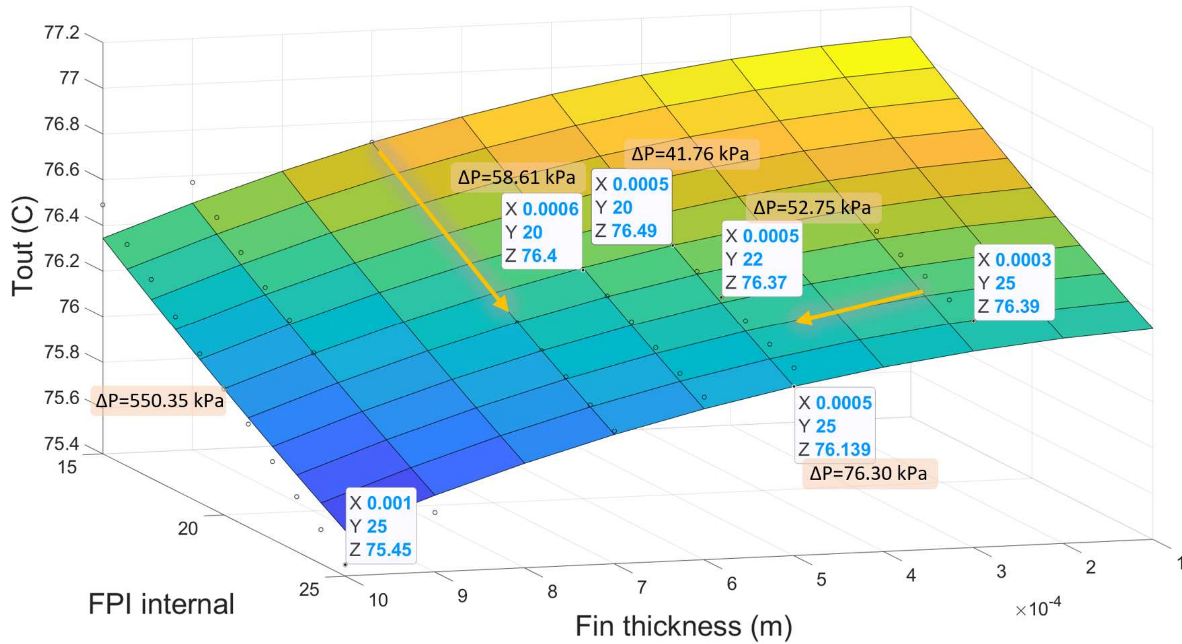


**Figure 4-2** Heat exchanger optimization for radiator outlet temperature: internal fin thickness vs internal fin per inch. Internal geometry: $\dot{m}_{liq}$=0.99 kg s$^{-1}$. External geometry: *total rows*= 19, $\theta$ = 28 degrees, *LPI* = 22, $F_{t,ext}$ = 0.10 mm, $F_{l,ext}$ = 12.70 mm and $FPI_{ext}$ = 19.

resulting in a tube width of 0.55 mm.

In Figure 4-3, the mass flow rate is varied for fins per inch 15-25, and the heat exchanger internal pressure drop is plotted. As the fins per inch is increased, the fluid temperature is reduced. For fins per inch internal increase from 21 to 25, the hydraulic diameter decreases resulting in increased heat transfer rates (4301 W m$^{-2}$ K$^{-1}$ vs 5038 W m$^{-2}$ K$^{-1}$). The internal heat transfer area also increases (0.0126 m$^2$ vs 0.0149 m$^2$), resulting in a lower internal thermal resistance (0.0108 K W$^{-1}$ vs 0.00875 K W$^{-1}$). The mass flow rate has a smaller effect on the outlet temperature. For $FPI_{internal}$ = 21, as the mass flow rate is increased from 0.96 kg s$^{-1}$ to 1.4 kg s$^{-1}$, the temperature does not change from 76.43°C, while the internal pressure drop increases from 45 kPa to 88 kPa. Thus, the optimal dimensions for the FC72 heat exchanger are 25 internal fins per inch, and roughly 0.96 kg s$^{-1}$.

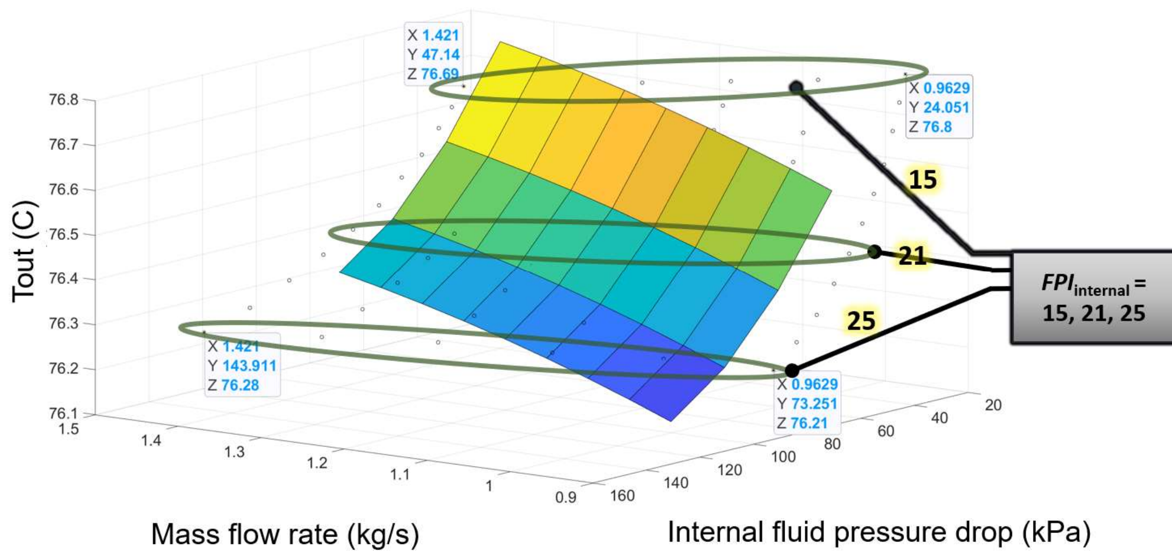


**Figure 4-3** Heat exchanger optimization for radiator outlet temperature: internal fin length vs internal fin per inch. Internal geometry: $\dot{m}_{liq}$= 0.96-1.42 kg s$^{-1}$. External geometry: *total rows* = 19, $\theta$ = 28 degrees, *LPI* = 22, $F_{t,ext}$ = 0.10 mm, $F_{l,ext}$ = 12.70 mm and $FPI_{ext}$ = 19.

The internal geometry optimization of the heat exchanger showed that as the internal fin length was minimized, fins per inch and fin thickness were maximized, resulted in the lowest steady state fluid operating temperatures. The internal fin height was set at a minimum value of 1.0 mm for manufacturability purposes, and suggests lower fin heights could further improve performance. The channel width for the internal tubes was set at a minimum of 0.50 mm for manufacturability purposes. This occurred at a fin per inch, and fin thickness, of 25, and 0.50 mm, respectively. Increasing the liquid mass flow rate for beyond 0.96 kg s$^{-1}$ did not low operating temperatures for fixed geometries, as the thermal resistance was relatively fixed. Thus, the optimal dimensions for the FC72 heat exchanger are 25 internal fins per inch, 1.0 mm fin height, 0.5 mm fin thickness and roughly 0.96 kg s$^{-1}$.

The external geometry optimization for minimizing the exit fluid temperature of the heat exchanger with FC72 as the working fluid is shown in Figure 4-4 through Figure 4-6. In Figure 4-4, the external fins per inch is plotted against the fin length while the mass flow rate of the fans is

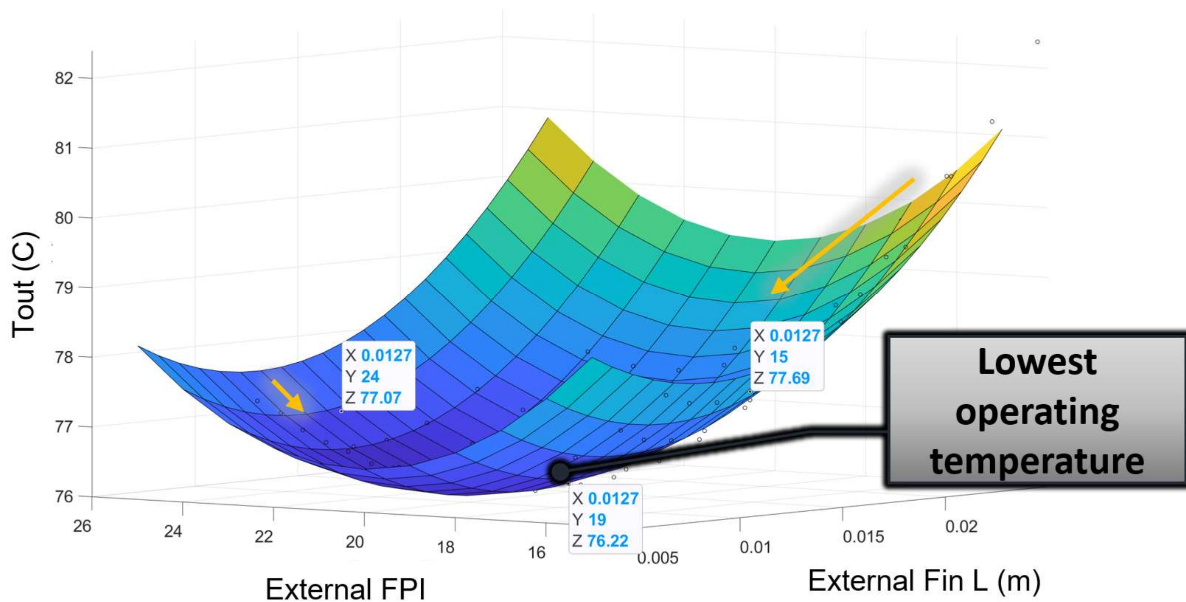


**Figure 4-4** Heat exchanger optimization for radiator outlet temperature: external fins per inch vs external fin length. Internal geometry: *total rows* = 25-11, $\dot{m}_{liq}$ = 0.96 kg s$^{-1}$, $FPI_{\text{int}}$ = 25, $F_{\text{l,int}}$ = 1.0 mm, $F_{\text{th,int}}$ = 0.5 mm. External geometry: $FPI_{\text{ext}}$ = 15-25, $F_{\text{l,ext}}$ = 8.16 – 17.2 mm, *LPI* = 22, $\theta$ = 28 degrees.

determined by balancing the pressure drop through the radiator and the chassis and the fan delivery pressure. The governing equations and fan curves used to do this are described at the end of section 3.4.2. The liquid side properties for the figures are: $\dot{m}_{\text{liq}}$ = 0.96 kg s$^{-1}$, $FPI_{\text{internal}}$ = 25, $F_{\text{th,int}}$ = 0.5 mm, and $F_{\text{l,int}}$ = 1.0 mm. The external fin length is varied by changing the total number of rows in the vertical direction from 25 to 11, where the number of external rows is always 1 more than the number of internal rows. The optimal design that results in the lowest temperature is located in the center of the grid because this yields the lowest heat exchanger outlet temperature. Here, $FPI_{\text{ext}}$ = 19 and $F_{\text{l,ext}}$ = 12.7 mm result in an air side mass flow rate of 265 sCFM. At high fins per inch, the mass flow rate decreases and does not provide enough air to reject the heat. For example, at $FPI_{\text{ext}}$ = 24 the flow rate is 212 sCFM. At low fins per inch, the air mass flow rate further increases, but the area continues to decrease which results in a higher air side thermal resistance. At high fin lengths (24 mm), the fin efficiency drops from 90% to 72%. This reduction in fin efficiency

increases the airside thermal resistance resulting in higher fluid operating temperatures (79.0°C). At low fin lengths (9 mm), the total air side surface area decreases as the total number of rows is increased to 25; with 12 internal rows for liquid and less area for the air to flow through, the air mass flow rate decreases and increases the fluid operating temperature. Thus, $FPI_{\text{ext}}$ = 19 and $F_{\text{l,ext}}$ = 12.7 mm has the lowest fluid operating temperature of 76.22°C.

The fin thickness vs external fin length is plotted in Figure 4-5. Again, the mass flow rate of the air is determined based off the air side pressure drop and the fan curve. It is clearly shown that as the external fin thickness is increased from 0.1 mm to 0.3 mm, the outlet temperature increases from 76.22°C to 78.67°C. At high fin thicknesses, the airside mass flow rate decreases from increased pressure drop (e.g., $F_{\text{th,ext}}$ = 0.10 mm, $\dot{V}_{\text{fan,act}}$ = 274 sCFM $\Delta P_{\text{air}}$ = 68.0 Pa, $F_{\text{th,ext}}$ = 0.30 mm, $\dot{V}_{\text{fan,act}}$ = 233 sCFM $\Delta P_{\text{air}}$ = 93.9 Pa). At fin thicknesses below 0.1 mm, the airside mass flow rate further increases but the outlet temperature rises because of decreased fin efficiency

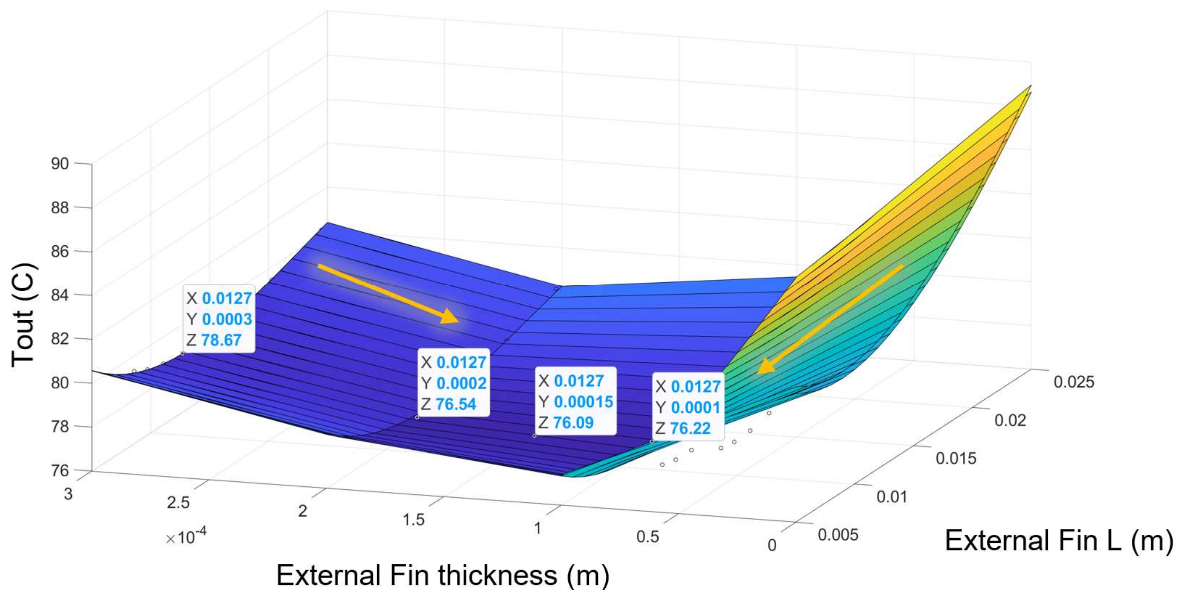


**Figure 4-5** Heat exchanger optimization for radiator outlet temperature: external fins thickness vs external fin length. Internal geometry: *total rows* = 11-25, $\dot{m}_{liq}$ = 0.96 kg s$^{-1}$, $FPI_{\text{int}}$ = 25, $F_{\text{l,int}}$ = 1.0 mm, $F_{\text{th,int}}$ = 0.5 mm. External geometry: $FPI_{\text{ext}}$ = 19, $LPI$ = 22, $\theta =$ 28 degrees.

(90% vs 80%). An external fin thickness of 0.15 mm results in the lowest operating temperature of 76.09℃ and is thus selected as the optimum value.

The louvers per inch vs. louver angle theta is plotted in Figure 4-6. Low louvers per inch result in higher air side heat transfer coefficients but at the expense of increased pressure drop, decreasing the airside mass flow rate. For example, at louvers per inch of 4, 11, and 21, the pressure drops are 109 Pa, 74 Pa, and 69 Pa, respectively. Four louvers per inch attains the highest heat transfer coefficient of 125 W $m^{-2}$ $K^{-1}$, but the increase in air side pressure drop reduces the mass flow rate and reduces its performance. 11 louvers per inch results in the lowest temperature of 75.31℃ at a heat transfer coefficient of 102 W $m^{-2}$ $K^{-1}$. The louver angle $\theta$ does not affect the operating temperature significantly, changing from 75.38℃ at 24 degrees, to 75.28℃ at 30 degrees. Higher louver angles result in lower steady state operating temperatures.

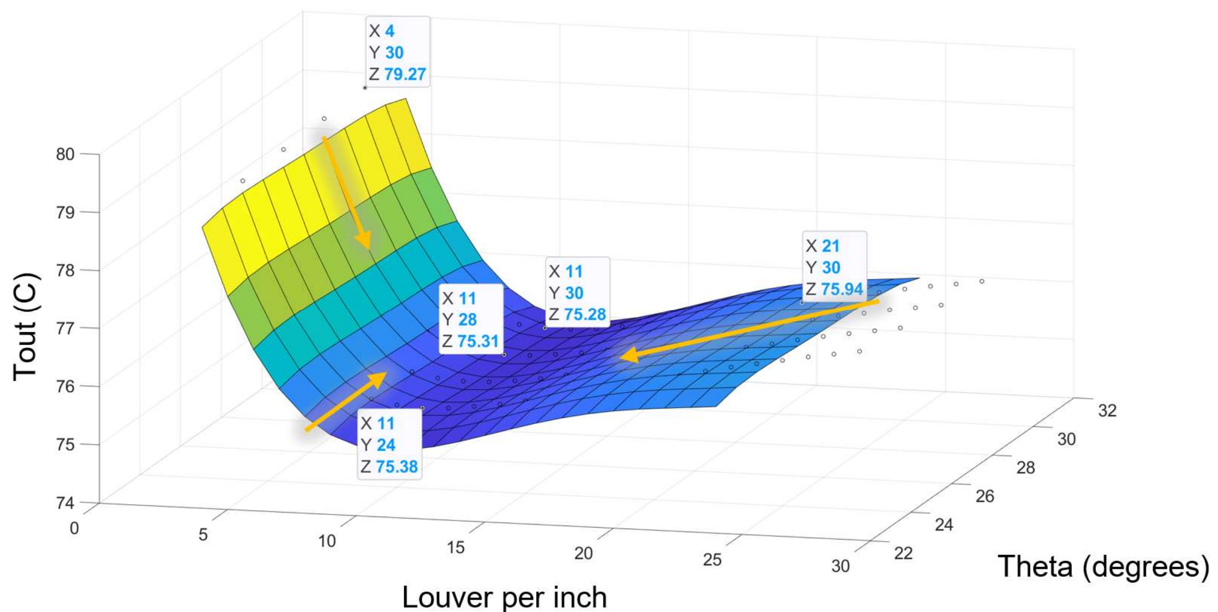


**Figure 4-6** Heat exchanger optimization for radiator outlet temperature: external louvers per inch vs theta (louver angle). Internal geometry: *total rows* = 19, $\dot{m}_{liq}$ = 0.96 kg $s^{-1}$, $F_{l,int}$ = 1.0 mm, $F_{th,int}$ = 0.5 mm. External geometry: $FPI_{ext}$ = 19, $F_{l,ext}$ = 12.7 mm.

In summary, as the external fins per inch increases, the airside mass flow rate decreases because of increased pressure drop. At low fins per inch, the thermal resistance increases from the

area reduction, increasing the steady state fluid operating temperature. At high fin lengths, the airside mass flow rate increases but the thermal resistance increases from decreased fin efficiency. At low fin lengths, the mass flow rate decreases because of increased pressure drop. At low fin thicknesses, the fin efficiency decreases but at high fin thicknesses, the mass flow rate decreases because of increased pressure drop. Low louvers per inch result in high heat transfer coefficients but increase pressure drop, lowering the airside mass flow rate. High louvers per inch result in low heat transfer coefficients but increase mass flow rate. The louver angle does not significantly change performance, but higher angles result in lower steady state fluid operating temperatures. Thus, the optimal design is 19 external fins per inch with 0.15 mm thickness, 11 louvers per inch, $\theta$ = 30 degrees, a total number of rows of 19, and a fin length of 12.70 mm.

The geometric characteristics of the four heat exchangers were optimized and resulted in very similar optimal structures and performance. These are shown in Table 4-1. All of the heat exchangers performed best at the minimum internal fin length of 1.00 mm and a fin thickness of 0.5 mm except for water which performed slightly better at 0.1 mm fin thickness. Water performed

**Table 4-1** Optimized heat exchanger dimensions for primary fluids

| Fluid | Water | FC72 | Jet Fuel | GC 50/50 |
|---|---|---|---|---|
| **Effectiveness** | 84% | 79% | 81% | 84% |
| $T_{f,2}$ (°C) | 75.35 | 75.28 | 75.30 | 75.12 |
| $F_{int, length}$ **(mm)** | 1.00 | 1.00 | 1.00 | 1.00 |
| $F_{int,th}$ **(mm)** | 0.1 | 0.5 | 0.5 | 0.5 |
| $FPI_{int}$ **(Fin/in)** | 17 | 25 | 25 | 25 |
| $F_{ext,length}$ **(mm)** | 12.70 | 12.70 | 12.70 | 12.70 |
| $F_{ext, th}$ **(mm)** | 0.15 | 0.15 | 0.15 | 0.15 |
| $FPI_{ext}$ **(Fin/in)** | 19 | 19 | 19 | 19 |
| ***LPI*** | 11 | 11 | 11 | 11 |
| $\theta$ **(degrees)** | 30 | 30 | 30 | 30 |
| **Total Rows** | 19 | 19 | 19 | 19 |
| $Re_{int}$ | 6317 | 6399 | 3573 | 2272 |
| $Nu_{int}$ | 37.92 | 69.96 | 45.54 | 29.12 |
| $k_f$ (W m$^{-1}$ K$^{-1}$) | 0.61 | 0.055 | 0.11 | 0.39 |

best at $F_{int,th}$ = 0.10 mm because all of the other fluids used the enthalpy approximation ($\Delta h \approx c_p \cdot \Delta T$). Enthalpy can be calculated with two properties, commonly temperature and pressure. As the pressure increases, additional energy needs to be rejected as heat. This was evident as the liquid side pressure drop increased, so did the total heat rejected, resulting in roughly 20-40W more heat for the radiator to cool (2143W vs 2158W). The GC50/50 (Water glycol 50/50 mixture) heat exchanger had the lowest Reynolds number and therefore the lowest Nusselt number. The Nusselt number in laminar flow region (Re < 2000) was constant at 4.337. Once the flow became transitional, the Nusselt number rapidly increased from 4.337 to 29.12 at Re = 2272. This further increases to 54.05 as the flow becomes turbulent at Re = 4190. This change in Nusselt number from 4.337 to 29.12 resulted in the internal thermal resistance decreasing from 0.01748 K $W^{-1}$ to 0.002683 K $W^{-1}$ per unit cell ($T_{f,2}$ = 76.48°C vs $T_{f,2}$ = 75.12°C). The liquid side thermal resistance represented 21% at Nusselt number = 4.337 but decreased to 4% of the overall heat exchanger thermal resistance at Nusselt number = 29.12. This phenomenon was not evident for the other fluids as GC50/50 has a much high viscosity (i.e., 2.3x that of FC72), resulting in lower Reynolds numbers for the same mass flow rate. The external geometries of the heat exchangers were the same where the maximum heat transfer occurred at an external fin thickness of 0.15 mm, fin length of 12.70 mm, 19 fins per inch, 11 louvers per inch, and a louver angle of 30 degrees. The internal geometry did not significantly matter as the internal fin height should be set to the minimum value. If the internal flow reaches transitional/turbulent, the thermal resistance becomes negligible relative to the total heat exchanger thermal resistance (<5%). After the liquid side is at these values, the air side becomes the most important to optimize and then optimizing the liquid side again.

The performance of the primary fluid heat exchangers is shown in Table 4-2. The heat exchangers achieved near the same performance resulting in a fluid outlet temperature of 75.3°C.

**Table 4-2** Radiator performance metrics

| Fluid | Water | FC72 | Jet Fuel | GC 50/50 |
|---|---|---|---|---|
| **Effectiveness** | 84% | 79% | 81% | 84% |
| $\dot{V}_{air}$ **(sCFM)** | 263.9 | 264.2 | 264.2 | 264.0 |
| $\Delta P_{air,hx}$ **(Pa)** | 73.9 | 74.7 | 73.68 | 73.8 |
| $UA$ **(W K$^{-1}$)** | 263.9 | 237.3 | 244.1 | 261.1 |
| $\dot{m}_{liq}$ **(kg s$^{-1}$)** | 0.90 | 0.99 | 0.68 | 0.84 |
| $\dot{m}_{min}$ **(kg s$^{-1}$)** | 0.034 | 0.12 | 0.064 | 0.038 |
| $\Delta P_{rad,liq}$ **(kPa)** | 18.3 | 76.1 | 77.3 | 72.2 |
| **Pr** | 2.3 | 10.1 | 11.1 | 11.6 |
| $P_{in}$ **(kPa)** | 119.5 | 298.1 | 151.0 | 142.8 |
| $T_{f,1}$ (°C) | 75.91 | 77.18 | 76.72 | 75.84 |
| $T_{f,5}$ (°C) | 75.35 | 75.28 | 75.30 | 75.12 |
| $T_{sat}$ (°C) | 100.6 | 88.5 | 176.0 | 107.0 |

The heat exchanger built for water achieved the highest effectiveness, and *UA*. It also had the lowest pressure drop of 18.3 kPa, and hence, lowest pumping power. The heat exchanger for FC72, jet fuel and GC50/50 required significantly higher pressure drop in the range of 72-77 kPa. The minimum liquid side mass flow rate was calculated based on the heat capacitance from the liquid and air flow streams. The actual minimum values should be where the Reynolds number is sufficiently transitional/turbulent, resulting the liquid side thermal resistance accounting for less than 5% of the heat exchangers total thermal resistance. The steady state operating temperature for all of the fluids was very similar, varying less than 0.20°C. Since the air side heat transfer dominated the thermal resistance, increasing liquid side heat transfer had little effect. This was evident as for the optimal water heat exchanger design, the internal and external thermal resistances were 2.5%, and 97%, respectively, of the total thermal resistance. It should also be noted that the FC72 heat exchanger needed to be pressurized to raise its saturation temperature which is 56.3°C at ambient pressure, in order to prevent cavitation in the pump. The other fluids were not at risk of boiling and did not need to be pressurized.

For all of the design cases, there is a ~25.5℃ temperature difference between ambient and the working fluid. This temperature distribution is shown in Figure 4-7 for the best cooling configuration with the fans at a maximum ambient temperature of 48℃. About 5-7℃ of this comes from the air being pre-heated before it reaches the heat exchanger because 20% of the liquid cooled heat dissipates through the back of the PCB and the miscellaneous air-cooled components dissipating through the top and bottom of the PCB. This 25.5°C temperature difference is important when operating at the maximum ambient temperature of 50℃ because the steady state fluid temperature will be a minimum of 75.5℃. Since the maximum junction temperature for Big Chip 2 is 75℃, this chip will need to be air cooled as mentioned in Chapter 3. This also leaves a small temperature budget of 9.5℃ between the maximum junction temperature and fluid operating

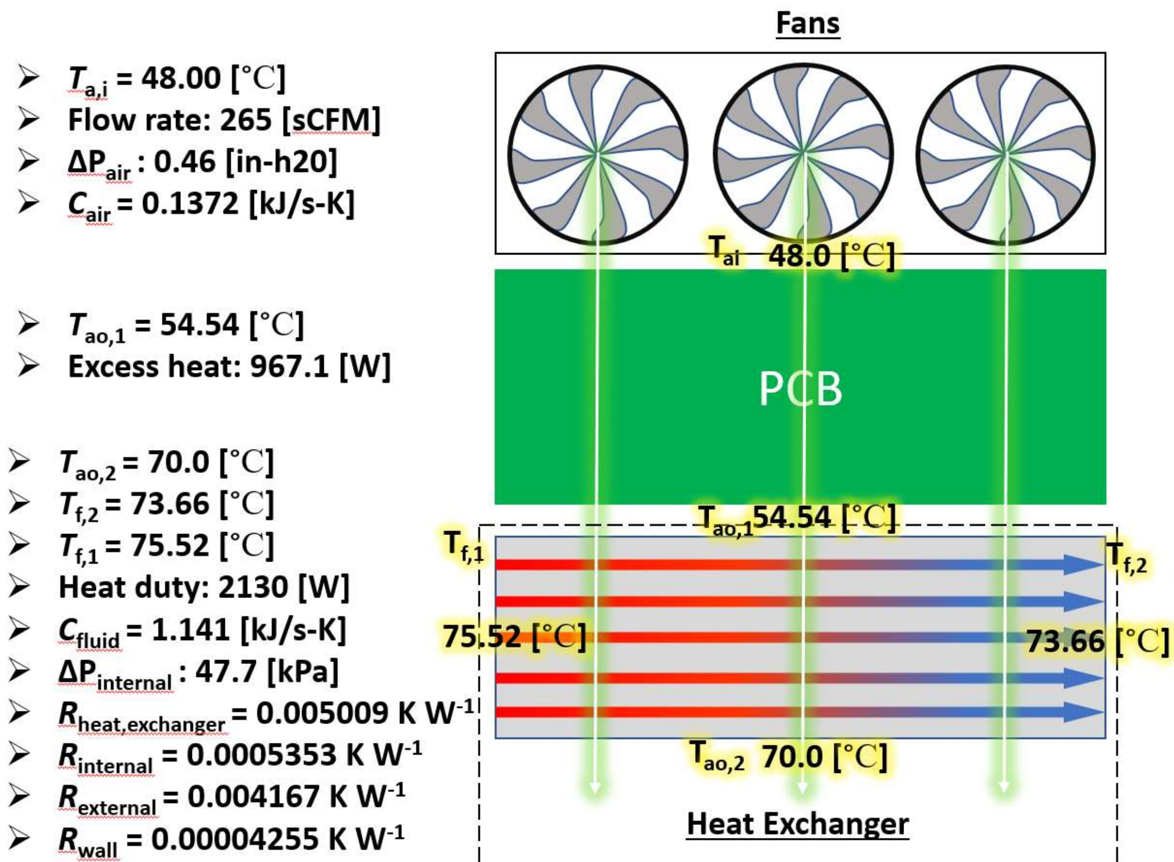


**Figure 4-7** M9506A temperature distribution

temperature for Big Chip 1. This means for the 160W Big Chip 1, a total thermal resistance between junction and fluid of 0.074 K $W^{-1}$ is required to attain the 9.5°C temperature difference. Achieving 0.074 K $W^{-1}$ is impossible in all configurations besides jet impingement on the die since the junction to lid thermal resistance is already 0.10 K $W^{-1}$ and TIM 2 adds roughly 0.03 K $W^{-1}$. This high initial temperature difference for the liquid will make it difficult to keep the electronics cool and will rely on the heat sinks to have minimum overall thermal resistance to keep the ambient to junction temperature difference within safe limits.

## 4.2. Heatsink Performance

In this section, the cooling performance of the five best testing configuration models on the M9506A will be compared. First, the total performance of the optimized cooling solutions on each chip will be discussed. In the sub sections, the total resistance will be broken down into their subcomponents to see what is preventing better cooling.

Figure 4-8 shows the total thermal resistance for the water microchannel cold plate with TIM 2, the water microchannel cold plate bypassing TIM 2, water jet impingement on the lid,

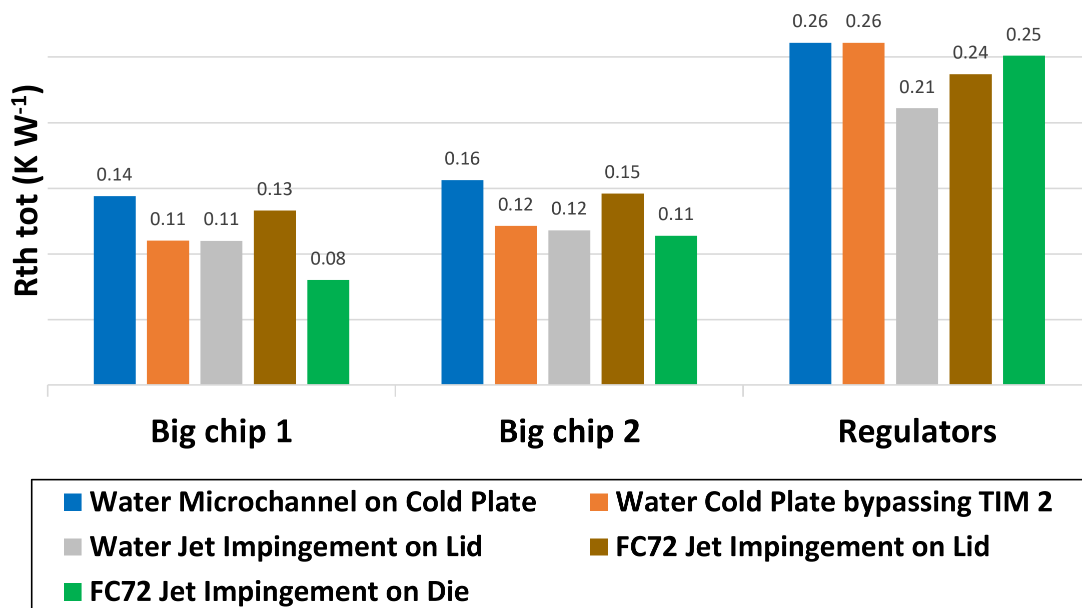


**Figure 4-8** Total thermal resistance for all chips and heat sinks

FC72 jet impingement on the lid, and FC72 jet impingement on the die for Big Chip 1, 2, and regulators, respectively. FC72 jet impingement on Big Chip 1's die achieved the lowest thermal resistance from junction to fluid of 0.080 K $W^{-1}$ and water jet impingement on the lid and the water cold plate bypassing TIM 2, tie for the second best at 0.11 K $W^{-1}$, which was roughly 37% higher. The resulting junction temperatures for these thermal resistances are shown in Figure 4-9 for an average fluid temperature of 71°C. For $TDP_{PTP}$ of 128W, these three methods correlate to a junction temperature of 85.1°C, 85.1°C, and 81.2°C, respectively for Big Chip 1. The maximum junction temperature of Big Chip 1 is 85°C meaning only FC72 can cool the chip at this fluid temperature with the subsequent cooling methods falling 0.10°C short. This means that jet impingement on the die can operate with a fluid temperature 4.9°C higher than that of water jet impingement on the lid and the water microchannels bypassing TIM 2. FC72 and water jet

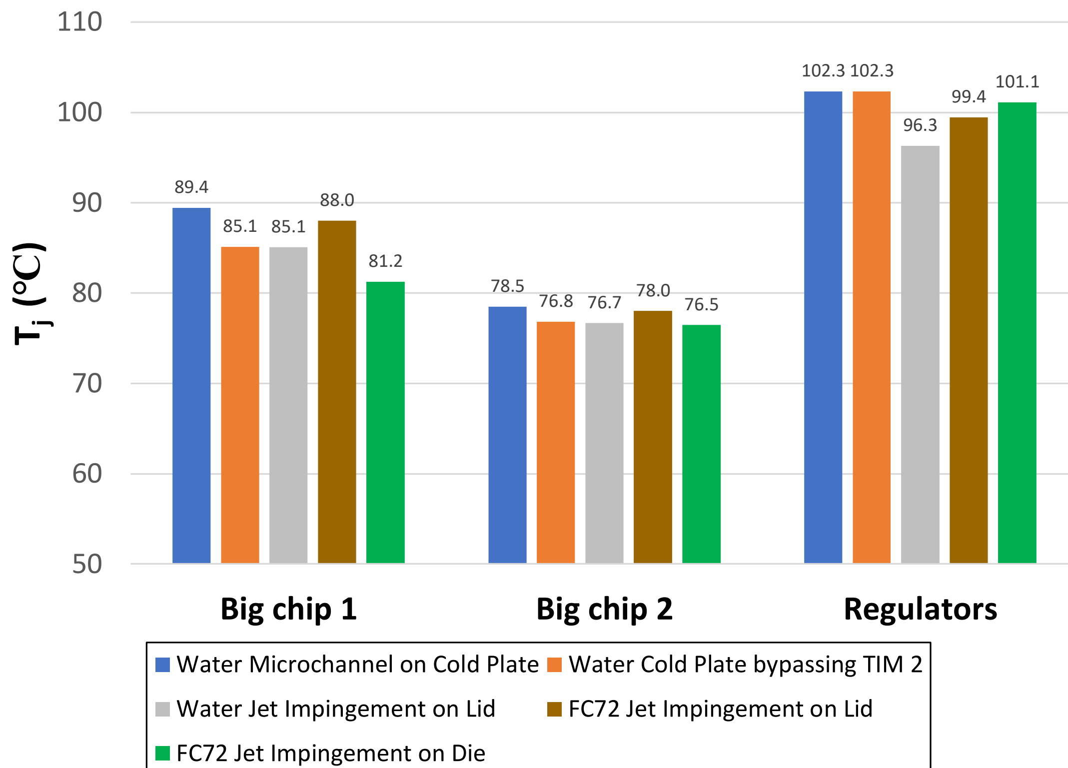


**Figure 4-9** Junction temperatures at 71°C fluid average temperature

impingement on the die and lid performed similarly on Big Chip 2 at a temperature difference around 5.7°C. This was well inside the limit as the maximum junction temperature of Big Chip 2 is 90°C. Finally, water jet impingement on the regulators achieved the lowest thermal resistance of 0.21 K $W^{-1}$ at a temperature difference of 25.3°C. With the maximum junction temperature of the regulators being 120°C, a maximum fluid temperature of 95°C could be used. Big Chip 1 has the most difficult heat removal problems for the system operating temperature as the fluid needs to be at most 75°C. Overall, FC72 jet impingement on the die performed the best allowing the highest ambient temperature.

#### 4.2.1. Microchannel cooling results

Using the optimal geometry of cold plate 1 from Table 3-3, the pressure drop breakdown was calculated at the design point of $R_{th,conv,1}$ = 0.0102 K $W^{-1}$ and is shown in Table 4-3. As the microchannel cold plate requires minimal mass flow rate to reach the thermal resistance it plateaus at, the system mass flow rate is only 0.62 kg $s^{-1}$. The heat exchanger requires the most pressure drop of the system, approximately 49%. The manifold and tubing pressure drop accounts for 35% of the system and finally the cold plate only consumes 17% of the system pressure drop. The thermal resistances were calculated for microchannel cooling as shown in Figure 4-10. The convection thermal resistance accounts for less than 7% of the

**Table 4-3** Water microchannel pressure drop breakdown

| Location | ΔP Water $Ch_{th}$ = 150 μm, $Fin_{th}$ = 254 μm $Fin_{height}$ = 4953 μm $\dot{m}_{tot}$= 0.62 kg $s^{-1}$, (kPa) |
|---|---|
| Upstream manifold 1 | 1.08 |
| Upstream manifold 2 | 2.31 |
| Main tubing | 0.59 |
| Heat sink tubing | 1.02 |
| Heat sinks | 4.07 |
| Heat exchanger | 11.8 |
| **Total pressure drop (kPa)** | 24.3 |
| **Total isentropic pumping power (W)** | 15.1 |

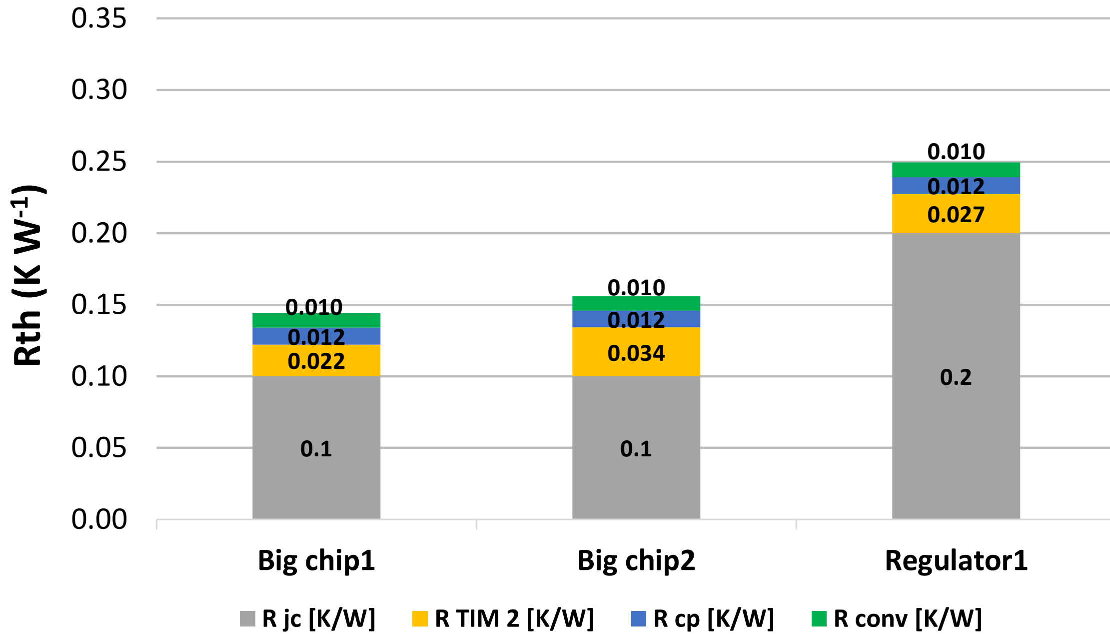


**Figure 4-10** Thermal resistance breakdown of water microchannels configuration 3-5a

overall thermal resistance in all cases. The low thermal resistance of cold plate 1 was particularly beneficial as compared to the other cold plate options which had convection resistances as high as 20%. Recalling the TDPs from Table 3-1, Big Chip 1, 2, and the regulators are 160W, 60W, and 150W, respectively, at their maximum junction temperatures. Thus, Big Chip 1 and the regulators require the most cooling. As is shown from the figure, independent of the liquid mass flow rate, the minimum attainable thermal resistance for these chips is $R_{\mathrm{jc}} + R_{\mathrm{TIM}} + R_{\mathrm{cp}}$, where the contact resistance of the TIM is lumped into $R_{\mathrm{TIM}}$. This results in a minimal thermal resistance of Big Chip 1, 0.13 K $W^{-1}$. At the heat load of 160W, this corresponds to a $\Delta T$ of 16.6°C. The actual thermal resistance and temperature difference obtained for this chip was 0.144 K $W^{-1}$ and 18.43°C at a pressure drop of 8.41 kPa. This system can only allow an ambient temperature of 41.6°C, otherwise Big Chip 1 will overheat. The regulators have a junction to case resistance of 0.20 K $W^{-1}$ caused by the cylindrical nature of regulators spreading heat to a flat cooling surface. At the obtained thermal resistance of 0.242 K $W^{-1}$, the temperature difference is 29°C. At a fluid temperature of

66.6°C (41.6+25), the junction temperature will be 95.6°C, 24.4°C from overheating ($T_{j,max}$ = 120°C). Finally, Big Chip 2 is the easiest to cool at its thermal resistance of 0.156 K W$^{-1}$, the temperature difference is 7.49°C. This results in a temperature of 75.49°C for Big Chip 2 when the fluid temperature is 68°C, 14.5°C from overheating ($T_{j,max}$ = 90°C).

The microchannel configuration bypassing TIM 2 is shown in Figure 4-11. The overall thermal resistance has been significantly reduced by bypassing the TIM. For Big Chip 1, the overall thermal resistance reduced from 0.144 K W$^{-1}$ to 0.110 K W$^{-1}$ while the effective junction thermal resistance has stayed roughly at 0.10 K W$^{-1}$. This was solved for from simulation results from the steady state conduction solver in ANSYS 2021 using $k_{TIM1}$ = 7.8 W m$^{-1}$ K$^{-1}$ with thickness 150 μm. The new temperature difference for Big Chip 1 is 14.6°C compared to 17°C. The thermal resistance on Big Chip 2 was 0.121 K W$^{-1}$ resulting in a temperature difference of 5.7°C. The

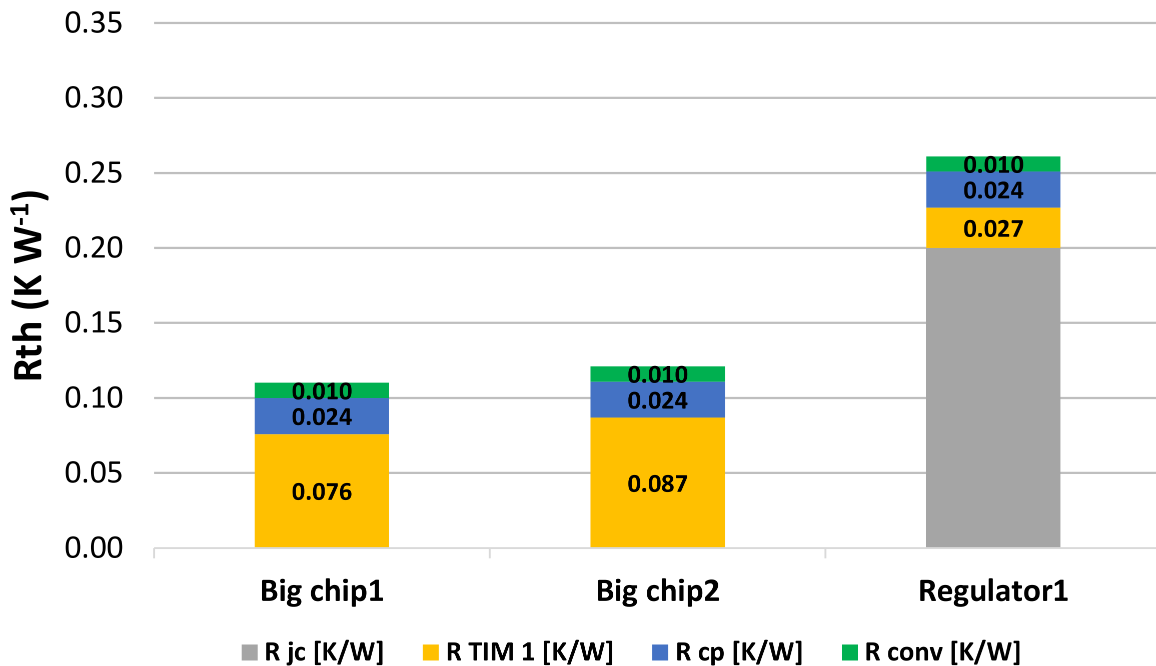


**Figure 4-11** Thermal resistance breakdown of water microchannels with TIM 2 configuration 3-5c

thermal resistance of the regulators does not change however because due to its geometry, it is not possible to remove a layer of TIM.

### 4.2.2. Jet impingement results

The thermal resistance for water jet impingement on the lid was set at 0.0080 K $W^{-1}$, and a sensitivity analysis was performed of the geometry described in Hobby et al. [79] This consisted of varying the *SD* (nondimensional spacing) at 6, 8 and 10; and varying *HD*'s (nondimensional height) of 1, 1.5, 2; and then these optimal nondimensional units were modeled at $D_j$ = 150, 200, 250, 300, and 400 μm. The results for the first portion of this data are shown in Table 4-4. As lower *SD* (nondimensional spacing) requires more mass flux, and overall flow rate to achieve a set thermal resistance, these designs have significantly higher peripheral pressure drop and overall

**Table 4-4** Pressure drop breakdown for constant 0.0080 K $W^{-1}$ varying nondimensional spacing and height Water

| Location | ΔP Water 300 μm, $\dot{m}_{tot}$= 1.76 kg $s^{-1}$, *SD* = 6, *HD* = 1.0 (kPa) | ΔP Water 300 μm, $\dot{m}_{tot}$= 1.31 kg $s^{-1}$, *SD* = 8, *HD* = 1.0 (kPa) | ΔP Water 300 μm, $\dot{m}_{tot}$= 0.90 kg $s^{-1}$, *SD* = 10, *HD* = 1.0 (kPa) | ΔP Water 300 μm, $\dot{m}_{tot}$= 1.02 kg $s^{-1}$, *SD* = 10, *HD* = 1.5 (kPa) | ΔP Water 300 μm, $\dot{m}_{tot}$= 1.07 kg $s^{-1}$, *SD* = 10, *HD* = 2.0 (kPa) |
|---|---|---|---|---|---|
| Upstream manifold 1 | 8.63 | 4.51 | 2.29 | 2.92 | 3.18 |
| Upstream manifold 2 | 18.4 | 9.65 | 4.89 | 6.24 | 6.79 |
| Main tubing | 4.71 | 2.61 | 1.24 | 1.59 | 1.74 |
| Heat sink tubing | 8.13 | 4.53 | 2.19 | 2.78 | 3.04 |
| Heat sinks | 3.78 | 7.87 | 13.5 | 18.5 | 21.4 |
| Heat exchanger | 68.7 | 40.9 | 21.4 | 26.5 | 28.7 |
| **Total pressure drop (kPa)** | **139** | **84.2** | **52.7** | **67.7** | **74.8** |
| **Total isentropic pumping power (W)** | **245** | **111** | **47.6** | **69.3** | **80.3** |

system pumping power. When the *HD* (nondimensional height) is increased for the best nondimensional spacing, more pumping power is required to achieve the same thermal resistance. The design with *SD* = 10, *HD* = 1, and $D_j$ = 300 μm, require more pressure drop at the heat sink level but reduces the overall pressure drop due to the reduction of mass flow, making it the most efficient design. Manifolds 1 and 2 represent the pressure drop through the supply fluid, of which is then multiplied by two to account for the 4 total manifolds. The manifold and tubing pressure drop accounts for roughly 36% of the pressure drop for the optimized *SD* but nearly 48% at *SD* = 6. These higher pressure drops making these lower *SD* design require more overall pumping power.

The modeling results for jet diameters $D_j$ = 150, 200, 250, 300, and 400 μm are shown in Table 4-5 at *SD* = 10 and *HD* = 1.0. The best design is at $D_j$ = 300 μm requiring only 47.6 W of

**Table 4-5** Pressure drop breakdown for constant 0.0080 K $W^{-1}$ varying jet diameter Water

| Location | ΔP Water 150 μm, $\dot{m}_{tot}$= 0.93 kg $s^{-1}$, *SD* = 10, *HD* = 1.0 (kPa) | ΔP Water 200 μm, $\dot{m}_{tot}$= 0.92 kg $s^{-1}$, *SD* = 10, *HD* = 1.0 (kPa) | ΔP Water 250 μm, $\dot{m}_{tot}$= 0.96 kg $s^{-1}$, *SD* = 10, *HD* = 1.0 (kPa) | ΔP Water 300 μm, $\dot{m}_{tot}$= 0.90 kg $s^{-1}$, *SD* = 10, *HD* = 1.0 (kPa) | ΔP Water 400 μm, $\dot{m}_{tot}$= 0.90 kg $s^{-1}$, *SD* = 10, *HD* = 1.0 (kPa) |
|---|---|---|---|---|---|
| Upstream manifold 1 | 2.45 | 2.43 | 2.61 | 2.29 | 2.28 |
| Upstream manifold 2 | 5.29 | 5.20 | 5.57 | 4.89 | 4.89 |
| Main tubing | 1.32 | 1.33 | 1.42 | 1.24 | 1.23 |
| Heat sink tubing | 2.32 | 2.34 | 2.48 | 2.19 | 2.22 |
| Heat sinks | 12.2 | 12.9 | 13.4 | 13.5 | 14.0 |
| Heat exchanger | 22.5 | 22.6 | 23.9 | 21.4 | 22.2 |
| **Total pressure drop (kPa)** | **53.8** | **54.4** | **57.6** | **52.7** | **54.0** |
| **Total isentropic pumping power (W)** | **50.2** | **50.2** | **55.5** | **47.6** | **48.7** |

isentropic pumping power to achieve 0.0080 K $W^{-1}$. This design requires the second highest heat sink pressure drop but has the lowest mass flow rate, reducing the overall pumping power. $D_j$ = 400 µm requires the second lowest pumping power followed by 150 and 200 µm, but the effect of jet diameter has small effects on the required pumping power, only varying from 47 – 56 W. Thus, the optimal design is $SD$ = 10, $HD$ = 1.0 and $D_j$ = 300 µm.

The thermal resistance breakdown for water with configuration 3-5b, return jet impingement on the lid is shown in Figure 4-12 for $SD$ = 10, $HD$ = 1.0 and $D_j$ = 300 µm. Similarly, to microchannels, the junction to case thermal resistances dominate the overall thermal resistance. However, by removing the TIM, the total thermal resistance is reduced as compared with microchannels in the same configuration. For Big Chip 1, the overall thermal resistance reduced from 0.144 K $W^{-1}$ to 0.108 K $W^{-1}$. The new temperature difference for Big Chip 1 is 13.8°C compared to 18.4°C. This new lower temperature difference allows for 71°C fluid operating

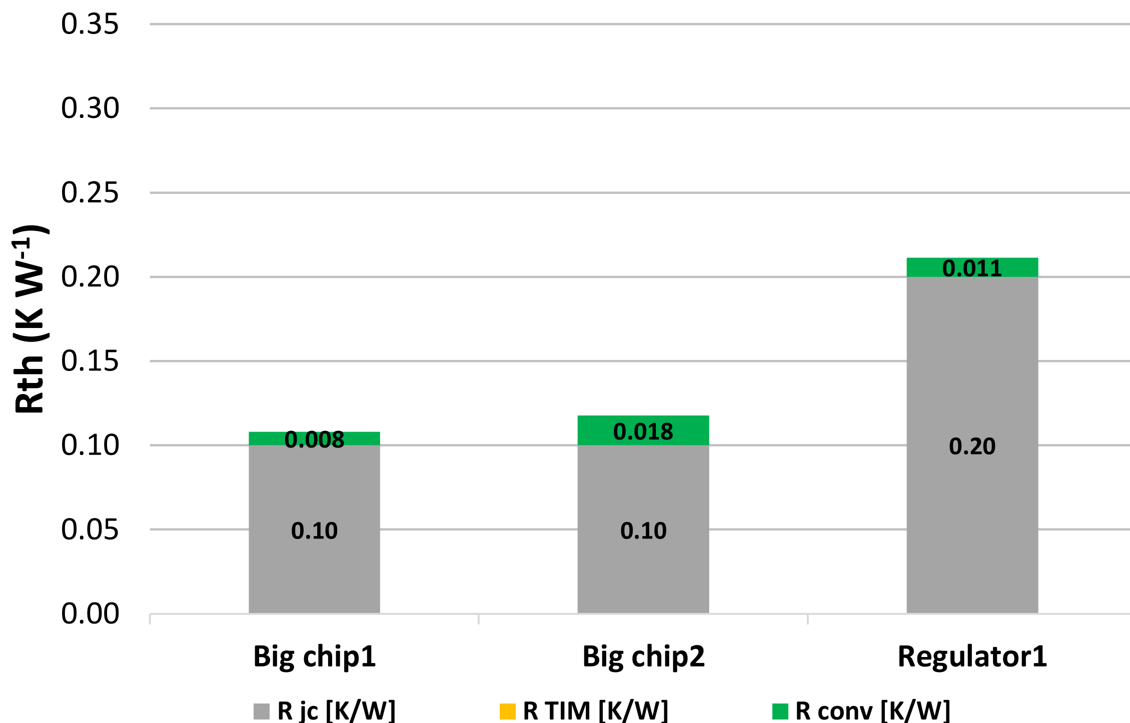


**Figure 4-12** Thermal resistance breakdown of water jet impingement on the lid config 3-5b

temperature without causing Big Chip 1 to overheat. The thermal resistance on Big Chip 2 was 0.118 K $W^{-1}$ resulting in a temperature difference of 5.7°C compared to 6.8°C of the microchannel cold plate. This chip will be able to operate with fluid up to 84°C and will not be a limiting factor. The regulators in this configuration have a total thermal resistance of 0.211 K $W^{-1}$ and result in a temperature difference of 25.3°C, 4°C lower than microchannel cold plates. Nevertheless, this is well inside the temperature limits of the regulators. The pressure drop for the jet impingement heat sink was 13.5 kPa compared to the 4.1 kPa pressure drop for the microchannel cold plate. On the system level, the isentropic pumping power and mass flow rate was 47.6W and 0.90 kg $s^{-1}$ compared to 15.1W and 0.62 kg $s^{-1}$, just over three times the pumping power but still within the operation limits of a 0.5 hp (373W) pump for the whole 5-slot chassis.

**Table 4-6** Pressure drop breakdown for constant 0.080 K $W^{-1}$ varying nondimensional spacing and height FC72

| Location | ΔP FC72 300 µm, $\dot{m}_{tot}$= 1.91 kg $s^{-1}$, *SD* = 6, *HD* = 1.0 (kPa) | ΔP FC72 300 µm, $\dot{m}_{tot}$= 1.25 kg $s^{-1}$, *SD* = 8, *HD* = 1.0 (kPa) | ΔP FC72 300 µm, $\dot{m}_{tot}$= 0.876 kg $s^{-1}$, *SD* = 10, *HD* = 1.0 (kPa) | ΔP FC72 300 µm, $\dot{m}_{tot}$= 1.44 kg $s^{-1}$, *SD* = 8, *HD* = 1.5 (kPa) | ΔP FC72 300 µm, $\dot{m}_{tot}$= 1.57 kg $s^{-1}$, *SD* = 8, *HD* = 2.0 (kPa) |
|---|---|---|---|---|---|
| Upstream manifold 1 | 6.40 | 2.74 | 1.35 | 3.65 | 4.35 |
| Upstream manifold 2 | 14.0 | 5.99 | 2.95 | 7.98 | 9.50 |
| Main tubing | 6.26 | 2.68 | 1.32 | 3.58 | 4.26 |
| Heat sink tubing | 2.54 | 1.12 | 0.53 | 1.49 | 1.77 |
| Heat sinks | 79.7 | 148 | 255 | 218 | 278 |
| Heat exchanger | 50.5 | 24.1 | 13.1 | 31.0 | 36.0 |
| **Total pressure drop (kPa)** | **180** | **193** | **279** | **277** | **348** |
| **Total isentropic pumping power (W)** | **223** | **156** | **158** | **259** | **354** |

The FC72 return jet impingement optimization will only be carried out in configuration 3-5d, jet impingement on the die due to the poor cooling potential in configuration 3-5b as will be discussed. The *SD* at 6, 8 and 10 are shown in Table 4-6 with *HD* at 1, 1.5, 2 for the best *SD*. *SD* = 8 and *HD* = 1 show the best performance at 156W of pumping power, 2W better than *SD* = 10 and *HD* = 1.0. The pressure drop for the return jet impingement design at *SD* = 10 is 72% more at the heat sink than *SD* = 8, but the reduction in mass flow rate, and effectively peripheral pressure drop makes the designs pumping power comparable. The variation in *HD* from 1.0 to 1.5, and 2.0, has a large effect on the system, requiring 66%, and 127%, increase in pumping power, respectively. The tolerance of this component will have to be kept to achieve the design heat sink performance.

The modeling results for jet diameters $D_j$ = 150, 200, 250, 300, and 400 µm are shown in Table 4-7 at *SD* = 8 and *HD* = 1.0. The best design is at $D_j$ = 400 µm requiring only 116 W of isentropic pumping power to achieve 0.080 K $W^{-1}$. This design requires the highest heat sink pressure drop but has the lowest mass flow rate, reducing the overall pumping power. $D_j$ = 250 µm requires the second lowest pumping power followed by 300 µm. The designs in this study will not investigate larger jet diameters due to their increased Reynolds number, further out of the bounds of the correlation. For instance, the Reynolds number of $D_j$ = 400 µm is 13839 at the design point and $D_j$ = 250 µm is 8383. Lowering the hydraulic diameter for jet impingement to the same as the microchannels channel width (150 µm) did not make a significant difference. In fact, the lower hydraulic diameters for jet impingement performed worse. This was because by maintaining the same *SD* ratio and decreasing jet size, the number of jets on the available surface area was dramatically increased from 5 x 5 at 400 µm to 13 x 13 at 150 µm. The reason the *SD* had to maintain the same is because if the dimensional spacing was kept, it would result in a large *SD*

**Table 4-7** Pressure drop breakdown for constant 0.080 K $W^{-1}$ varying jet diameter FC72

| Location | ΔP FC72 150 µm, $\dot{m}_{tot}$= 1.41 kg $s^{-1}$, *SD* = 8, *HD* = 1.0 (kPa) | ΔP FC72 200 µm, $\dot{m}_{tot}$= 1.31 kg $s^{-1}$, *SD* = 8, *HD* = 1.0 (kPa) | ΔP FC72 250 µm, $\dot{m}_{tot}$= 1.25 kg $s^{-1}$, *SD* = 8, *HD* = 1.0 (kPa) | ΔP FC72 300 µm, $\dot{m}_{tot}$= 1.25 kg $s^{-1}$, *SD* = 8, *HD* = 1.0 (kPa) | ΔP FC72 400 µm, $\dot{m}_{tot}$= 0.986 kg $s^{-1}$, *SD* = 8, *HD* = 1.0 (kPa) |
|---|---|---|---|---|---|
| Upstream manifold 1 | 3.51 | 3.01 | 2.74 | 2.74 | 1.71 |
| Upstream manifold 2 | 7.67 | 6.58 | 5.99 | 5.99 | 3.73 |
| Main tubing | 3.44 | 2.95 | 2.68 | 2.68 | 1.67 |
| Heat sink tubing | 1.36 | 1.16 | 1.12 | 1.12 | 0.69 |
| Heat sinks | 136 | 140 | 138 | 148 | 153 |
| Heat exchanger | 29.9 | 26.2 | 24.1 | 24.1 | 16.0 |
| **Total pressure drop (kPa)** | **193** | **189** | **183** | **193** | **182** |
| **Total isentropic pumping power (W)** | **176** | **161** | **148** | **156** | **116** |

that would effectively decrease heat transfer. The jet velocity of the 25 jets compared to the 169 jets was 9.1 m $s^{-1}$ to 8.3 m $s^{-1}$, respectively, and the Reynolds numbers were 13839 compared to 4300. Furthermore, the smaller jet sizes have higher pressure drop for the same velocities and result in greater power consumption. Thus, the optimal design is *SD* = 8, *HD* = 1.0 and $D_j$ = 400 µm.

Figure 4-13 shows modeling results obtained from using FC72 with configuration 3-5d, return jet impingement on the die. This method achieves the lowest thermal resistance on Big Chip 1 of 0.080 K $W^{-1}$. Big Chip 1 requires the most cooling and has a much larger die compared to the other chips. As mentioned earlier, larger die sizes are easier to cool as they have less conduction thermal resistance. The ΔT for Big Chip 1, and 2 are 10.2°C, and 5.1°C, respectively, at these thermal

resistances. The reason ΔT for Big Chip 1 is so much higher is due to its significantly higher TDP. The regulators do not have a die and are cooled with jet impingement on the lid. Since the

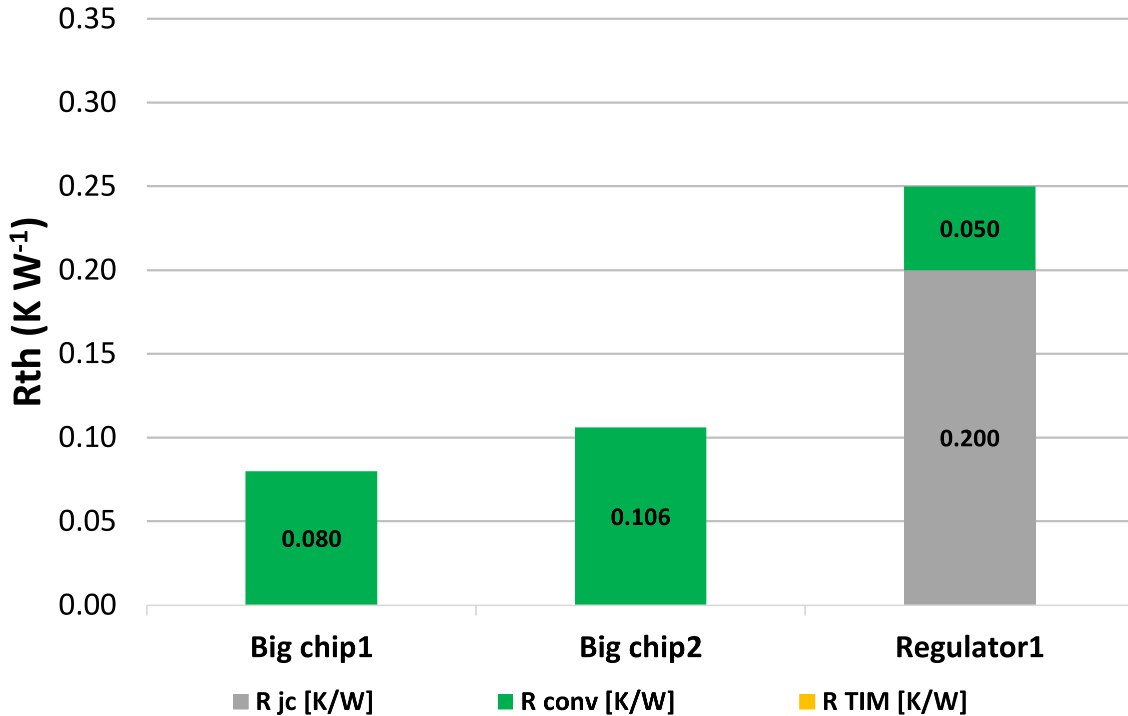


**Figure 4-13** Thermal resistance breakdown of FC72 jet impingement on the die configuration 3-5d

maximum temperature for Big Chip 1 is 85°C and the regulators are 120°C, the regulators have significantly more available thermal resistance before overheating:

$$R_{\text{th,available}} = \frac{T_{\max} - T_{\text{operating}}}{TDP} \tag{4-2}$$

where $T_{\max}$ is the maximum junction temperature, $T_{\text{operating}}$ is the device junction temperature and $TDP$ is the thermal dissipation power. The pressure drop of the heat sink for Big Chip 1 is 152 kPa where the peripheral pressure drop is 34.7 kPa. The isentropic pumping power and mass flow rate for this system are 119 W and 0.986 kg $s^{-1}$. A further decrease in thermal resistance is possible for this cooling solution by increasing the mass flow rate as the thermal resistance is 100% convection.

This is dissimilar to the other cooling configurations with higher thermal resistance as a majority (95%) of the thermal resistance was fixed.

The modeling results for FC72 return jet impingement on the lid are shown in Figure 4-14. Due to the poor heat transfer properties of dielectrics, the thermal resistance is considerably higher even at higher pumping power. The convection thermal resistance accounts for 25% of the thermal

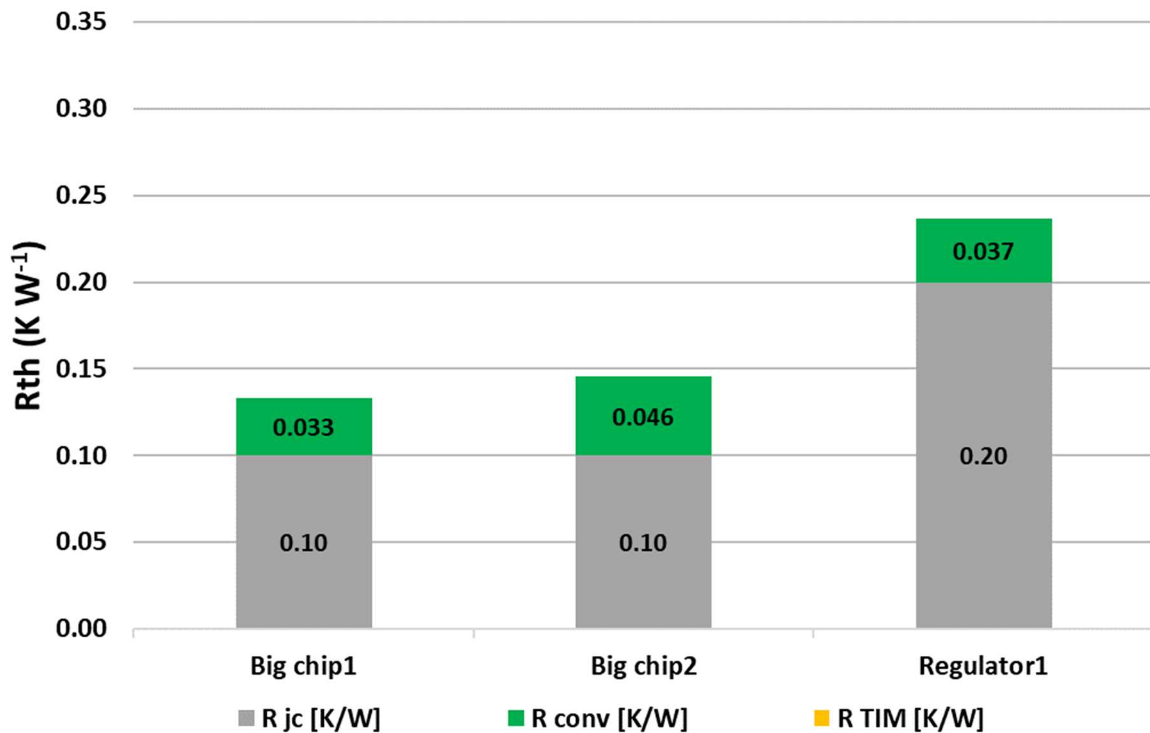


**Figure 4-14** Thermal resistance breakdown of FC72 on the lid configuration 3-5b

resistance at a pumping power of 172W, about seven times that of water. The increased surface area to jet on caused the mass flux and jet velocities to be significantly lower than FC72 jet impingement on the die and is the main reason for the poor heat transfer performance. When the mass flux is increased, there is significant pressure drop in the peripheral. The pressure drop of the heat sink for Big Chip 1 is 39.12 kPa where manifolding pressure drop accounts for around 37% of the system pressure drop at 50.10 kPa. The performance for Big Chip 2 is considerably worse compared to before. The temperature difference for these chips is still low though due to the low

chip power consumptions. The regulator is within spec at its current thermal resistance because the regulator has a maximum operating temperature 35°C greater than Big Chip 1.

### 4.2.3. Overall heat sink results

In Figure 4-15, the thermal resistance breakdown for the cooling configurations on Big Chip 1 are depicted. The first configuration 3-5a contained a microchannel cold plate attached to the lid of the chip by a TIM. Although the TIM used was high-performance, it represented a large portion (15%) of the thermal resistance to cool the chip. By removing TIM 2 and a layer of copper heat

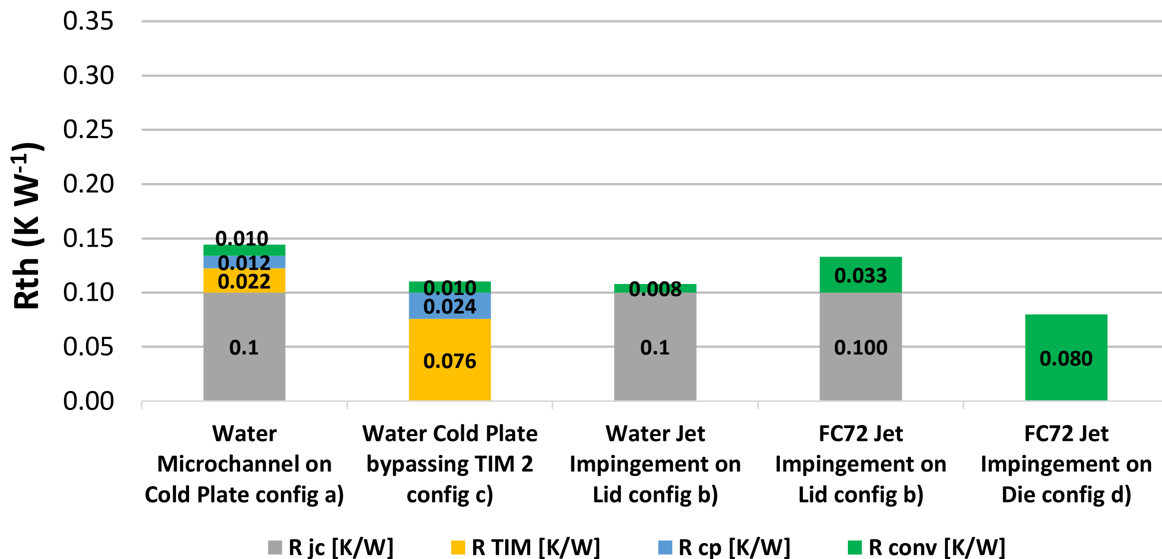


**Figure 4-15** Thermal resistance breakdown of different cooling configurations on Big Chip 1

spreading, the cold plate bypassing TIM 2 performed identically to water jet impingement on the lid. Jet impingement directly on the lid with water however showed a 15% reduction in thermal resistance for similar pumping power without requiring the removal of the lid for microchannel cooling. FC72 jet impingement on the die performed the best at a thermal resistance of 0.080 K $W^{-1}$. This came at the cost of increased pumping power due to the high dynamic viscosity of FC72 and the higher required mass flow rate. If the mass flow rate was decreased to a thermal resistance of 0.11 K $W^{-1}$ (water jet impingement on the lid), the pumping power would still be higher at

55.3W, about twice the required pumping power of water. This is very reasonable as a small pump can provide 52.2W. FC72 return jet impingement on the lid performed the fourth best of the testing configurations and performed better than its microchannel counterpart without removing the lid.

Microchannel cooling utilizes increased surface area to obtain lower convection thermal resistances per mass flow rate. Figure 4-16 compares the pressure drop and thermal resistance vs mass flow rate for microchannel and jet impingement cooling methods. Looking at these individually, the convection thermal resistance for microchannel cooling is relatively constant and approaches 0.0096 K $W^{-1}$ from its initial 0.010 K $W^{-1}$. This is because the Nusselt number only changes in the developing region and is constant for laminar flow with fixed geometry. The pressure drop of the microchannels is significantly lower but further increases in mass flow rate

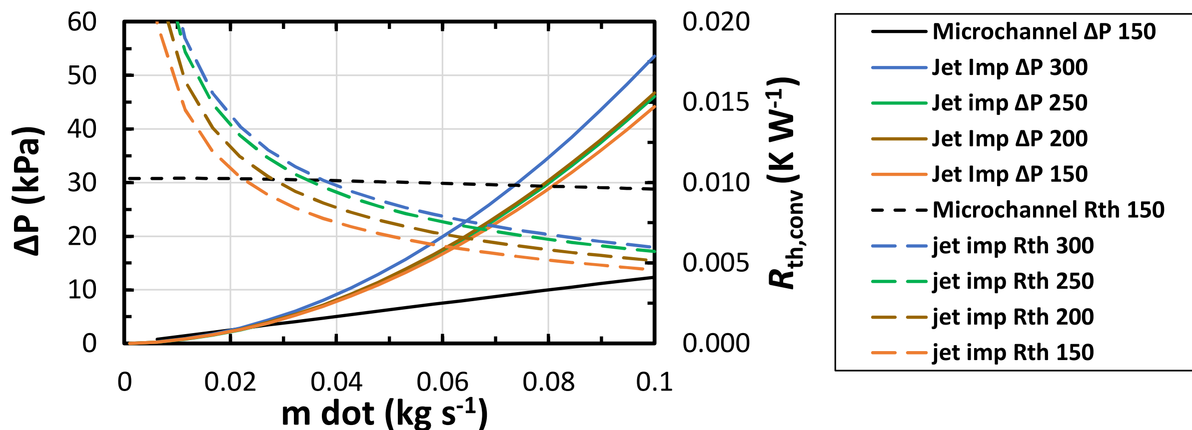


**Figure 4-16** Microchannel cooling vs return jet impingement

are limited by peripheral pressure drop. The reason the microchannel pressure drop looks somewhat linear is due to the Darcy friction factor starting out high at low flow rates and then decreasing with increased flow rates. The Reynolds numbers in the 150 µm microchannels ranged 30-500 and would need 0.30 kg $s^{-1}$ per chip to enter the transitional region. Return jet impingement out-performs microchannel cooling at roughly 0.025-0.035 kg $s^{-1}$ at a pressure drop of just under 9 kPa if TIMs are bypassed. Microchannel cooling for this configuration is better at low flow rates

but due to the Nusselt number being constant for laminar flow, microchannel cooling is limited by the manufacturable geometry. The Nusselt number for return jet impingement does not flatline as it further reduces the thermal boundary layer whether laminar or turbulent flow. In the system design perspective, this 0.0096 $K\ W^{-1}$ is only at most 7% of the total thermal resistance of the package. The primary thermal resistance is from junction to the base of the cold plate. At the cost of higher pumping power, return jet impingement can outperform microchannel cooling if TIM's are passed.

The pumping power vs junction temperature is shown in Figure 4-17 where the system mass flow rate was varied for the four configurations with 40°C ambient temperature. Water jet impingement on the lid has the best performance per the amount of pumping power required until 75W where FC72 jet impingement on the die outperforms the 78°C junction temperature attained from water with configuration 3-5b and 3-5c. Water in configuration 3-5b and 3-5c show the best performance per pumping power reaching 80°C operating temperature for ~50W pumping power. Switching fluids from water to GC50/50 for configuration 3-5b and 3-5c results in a ~3°C higher junction temperature and requires 120W+ pumping power. The microchannels in configuration 3-5c with GC50/50 however result in a slightly lower junction temperature than jet impingement in configuration 3-5b. The added layers of thermal resistance for the water microchannels in configuration 3-5a, in effect, make it perform the worst resulting in an 85°C junction temperature. FC72 jet impingement on the die with configuration 3-5d attains the lowest junction temperatures beyond 75W. Jet impingement with jet fuel A-1 requires much higher pumping power but can attain lower temperature beyond that of conventional methods. The junction temperature further decreases for jet fuel A-1 but is out of the range of pumping power available (0.5 hp, 373W) for the chassis. The total chassis load being cooled here is roughly 3000W and the fan power

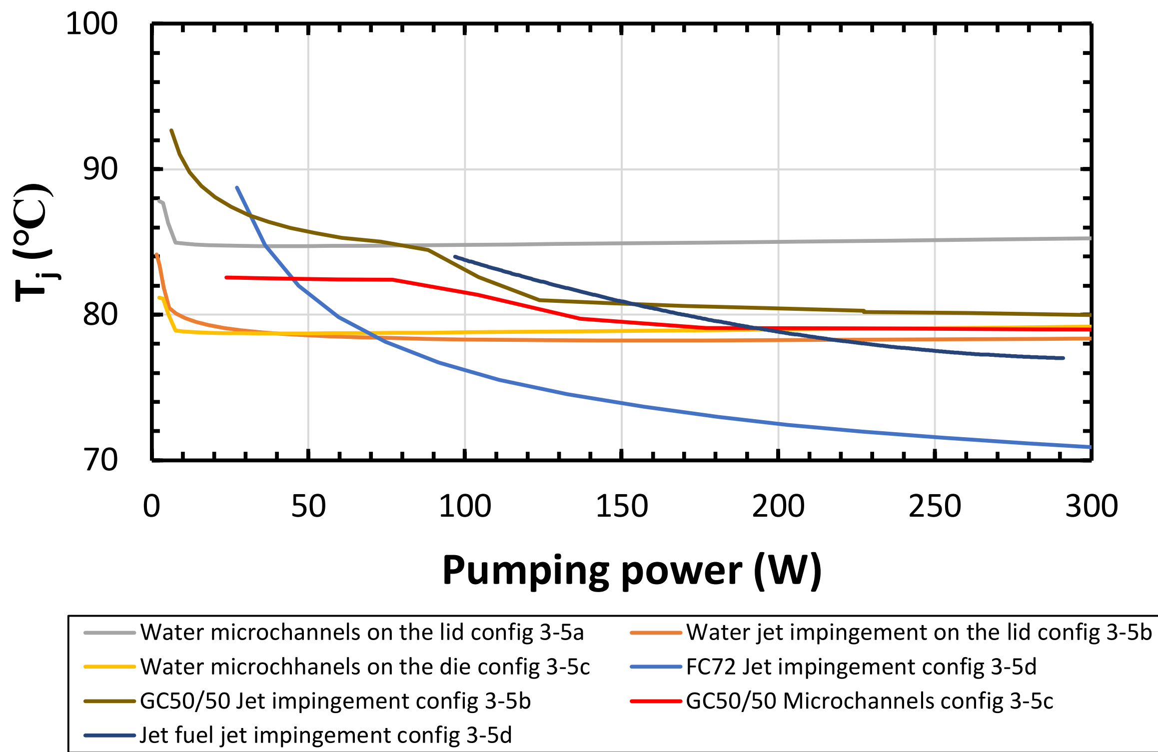


**Figure 4-17** Pumping power vs junction temperature for configurations 3-5a–d, water, GC50/50, FC72, and Jet fuel A-1

consumption is constant for all the shown cases at roughly 72W, resulting in COP of 17 for 100W pumping power.

## 4.3. System Level Performance

Four testing configuration models were developed to compare the cooling performance of the M9506A. In these configurations, different conduction paths were modeled, and the heat sinks were optimized for each cooling configuration to determine the best method. In this section, the performance of the best configurations will be expanded upon for their performance at 50°C ambient temperature. The system pressure drop for the solutions will be compared and the required pumps will be sized for the systems. The leakage current will be discussed for various ambient operating temperatures and its effect on total system power consumption. The failure rate and

acoustic performance of the systems will be discussed and finally, increased heat exchanger size and switching flow directions will be considered.

### 4.3.1. High ambient temperature operation

None of the cooling configurations could successfully cool the chassis at 50°C ambient temperature, although FC72 jet impingement on the die came close at 48.7°C. The current generation fans on the chassis were inadequate to provide the necessary flow rate to reject 3.125 kW, resulting in high operating temperatures (75.5°C). Once again, the air has become the limiting factor accounting for 76% of the total thermal resistance from junction to ambient. Thus, as the liquid cooling performance is at its maximum, there is a need to increase the airside mass flow rate beyond its current level. The addition of this makeup air would need to come from selecting new fans, or the addition of a blower in Zone 3.

The steady state conditions were solved for at 50°C ambient, and Table 4-8 was generated. Heat that was not rejected by the liquid was added to the air stream before cooling the radiator, which resulted in a roughly 7°C increase in air temperature. This increase in air temperature varied as the maximum flow rate provided by the fans was nominally 265 sCFM. The difference between

**Table 4-8** System level summary

| Method | $D_h$ (μm) | Fluid | Config | $W_{p,s}$ (W) | $\dot{V}_{air,req}$ (sCFM) | $\dot{m}_{liq}$ (kg s$^{-1}$) | $\Delta P_{liq}$ (kPa) | $T_{jc,1}$ (°C) | $R_{bigchip1}$ (K W$^{-1}$) | $R_{heat\ exchanger,req}$ (K W$^{-1}$) |
|---|---|---|---|---|---|---|---|---|---|---|
| Micro | 150 | Water | 3-5a | 14.6 | 443 | 0.62 | 23.1 | 85 | 0.145 | 0.003033 |
| Jet Imp | 300 | Water | 3-5b | 62.6 | 326 | 0.90 | 52.3 | 85 | 0.108 | 0.003469 |
| Micro | 150 | Water | 3-5c | 15.9 | 337 | 0.62 | 25.0 | 85 | 0.110 | 0.003399 |
| Jet Imp | 400 | FC72 | 3-5d | 166 | 282 | 1.01 | 223 | 85 | 0.078 | 0.004092 |

265 sCFM and the required sCFM is the makeup air needed to meet the 85°C maximum junction temperature of Big Chip 1, which results in the required thermal resistance of the heat exchanger for each configuration. For the worst configuration, 3-5a, the airside mass flow rate needs to be

nearly doubled from 265 sCFM, to 443 sCFM. This is likely not realistic and would dramatically increase acoustic output. For the best configuration, 3-5d, the airside mass flow rate needs to be increased by 17 sCFM to achieve the target conditions. Without this makeup air, the system can operate at a maximum temperature of 48°C. The second-best configurations are jetting onto the lid with water (3-5b), and the water cold plate bypassing TIM 2 (3-5c), which result in a thermal resistance of 0.108 K $W^{-1}$ and 0.110 K $W^{-1}$, respectively. This 0.002 K $W^{-1}$ increase in performance results in 3-5b requiring 11 sCFM less air mass flow rate than for configuration 3-5b to maintain the chips within safe operating limits. However, jetting directly onto the die to achieve 0.078 K $W^{-1}$ did require the highest isentropic pumping power of 166W, the maximum the selected pump can provide. By increasing the thermal resistance of FC72 on the die to be 0.110 K $W^{-1}$, the same of the second-best solutions, the isentropic pumping power is significantly reduced to 39.5W. However, this design point provides inadequate cooling.

The water microchannel cold plate in configuration 3-5a performed the worst at a thermal resistance of 0.145 K $W^{-1}$. Both water jet impingement and microchannels obtained similar pumping power and COPs by cooling 3100W with roughly 90W of cooling power ($W_{\text{fan}}$ + $W_{\text{pump}}$). Water jet impingement required more mass flow rate than the microchannels bypassing TIM 2 but obtains a slightly lower thermal resistance (0.108 K $W^{-1}$ vs 0.110 K $W^{-1}$). The heat transfer coefficient for water jet impingement was 25,224 W $m^{-2}$-$K^{-1}$. The microchannel cold plate was 17,090 W $m^{-2}$-$K^{-1}$ with 7.4 times the surface area. The microchannel cold plate in configuration 3-5a performed the worst though because it could not make up the 0.030 K $W^{-1}$ added thermal resistance from the thermal interface material and the cold plate. When these two cooling configurations switched from water to GC50/50, the heat sink thermal resistance was increased about 0.008 K $W^{-1}$ and required about 20 sCFM more air for the heat exchanger.

The maximum allowable ambient temperatures for the four primary cooling configurations are shown in Table 4-9. The FC72 system can operate with the highest allowable ambient temperature of 48.7°C. This is due to this configuration having the best cooling performance. Water jet impingement on the lid can operate with a 0.2°C higher ambient temperature than the water microchannel cold plate bypassing TIM 2. Finally, the microchannel cold plate in the conventional configuration can operate at a maximum ambient temperature of 41.7°C, 7°C lower than that of the FC72 jet impingement on the die system.

**Table 4-9** Maximum allowable ambient temperature

| Method | $D_h$ (μm) | Fluid | Config | $W_{p,s}$ (W) | T ambient (°C) | $\dot{m}_{liq}$ (kg s$^{-1}$) | $\Delta P_{liq}$ (kPa) | $T_{jc,1}$ (°C) | $R_{bigchip1}$ (K W$^{-1}$) | $R_{heat\ exchanger,req}$ (K W$^{-1}$) |
|---|---|---|---|---|---|---|---|---|---|---|
| Micro | 150 | Water | 3-5a | 14.6 | 41.7 | 0.62 | 23.1 | 85 | 0.145 | 0.003033 |
| Jet Imp | 300 | Water | 3-5b | 62.6 | 45.7 | 0.90 | 52.3 | 85 | 0.108 | 0.003469 |
| Micro | 150 | Water | 3-5c | 15.9 | 45.5 | 0.62 | 25.0 | 85 | 0.110 | 0.003399 |
| Jet Imp | 400 | FC72 | 3-5d | 166 | 48.7 | 1.01 | 223 | 85 | 0.078 | 0.004092 |

The thermal resistance for Big Chip 1, and the total heat exchanger thermal resistance from the LMTD between the four fluids are shown in Figure 4-18 for configurations 3-5a-d. The solid lines represent the total thermal resistance of the heat sink on Big Chip 1, and the dashed lines are the total heat exchanger thermal resistance. The pumping power in this graphic was generated by varying the liquid mass flow rate for the cooling configurations with a total-total pump efficiency of 50%. The three water cooling configurations, 3-5a–c, show near identical performance for the pumping power required to achieve the heat exchanger thermal resistance as it plateaus. The FC72 heat exchanger shows the best performance and plateaus at 0.004510 K W$^{-1}$. The Jet fuel A-1 heat

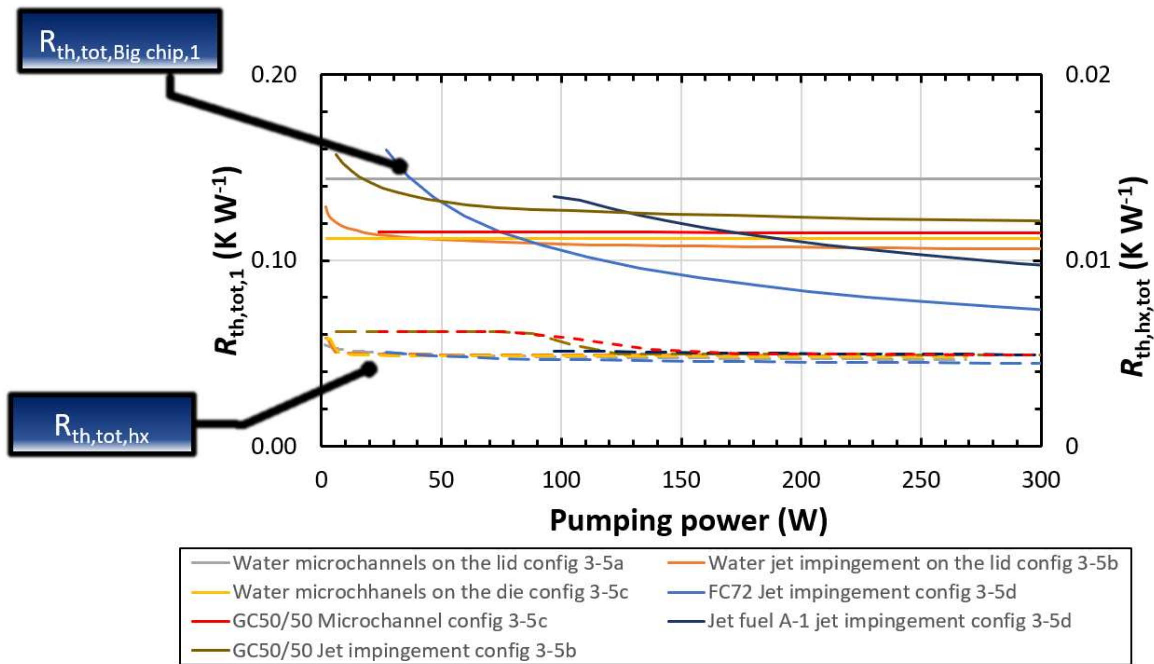


**Figure 4-18** Pumping power vs Big Chip 1 thermal resistance and heat exchanger total thermal resistance for Water, FC72, and Jet fuel A-1

exchanger plateaus at a slightly higher value, 0.004980 K W$^{-1}$. The GC 50/50 heat exchanger performs second worst and plateaus at 0.004900 K W$^{-1}$. Configuration 3-5d with FC72 achieves the lowest heat sink thermal resistance beyond 80W pumping power. This continues to further decrease beyond 150W, whereas the configurations 3-5a–c plateau at a fixed value based off the conduction path thermal resistance. Water jet impingement on the lid performs second best followed closely by the water microchannels in configuration 3-5c. Jet impingement on the lid with GC50/50 requires significantly higher pumping power when compared to water for the convection resistance to plateau for Big Chip 1 and is about 0.010 K W$^{-1}$ higher. GC50/50 microchannels with the lid on performs the worst resulting in the highest heat sink thermal resistance of 0.147 K W$^{-1}$. Switching fluid from water to GC50/50 increases the thermal resistance for the heat sink and heat exchanger. GC50/50 in configuration 3-5c attains a much lower heat sink thermal resistance when compared to 3-5b.

### 4.3.2. Pressure drop summary

The pressure drop breakdown for FC72 jet impingement on the die is shown in Figure 4-19. In this configuration, for a thermal resistance of 0.080 K $W^{-1}$, 83% of the pressure drop is in the jet impingement device, while 17% of the pressure drop is in the remaining fluid flow pathway.

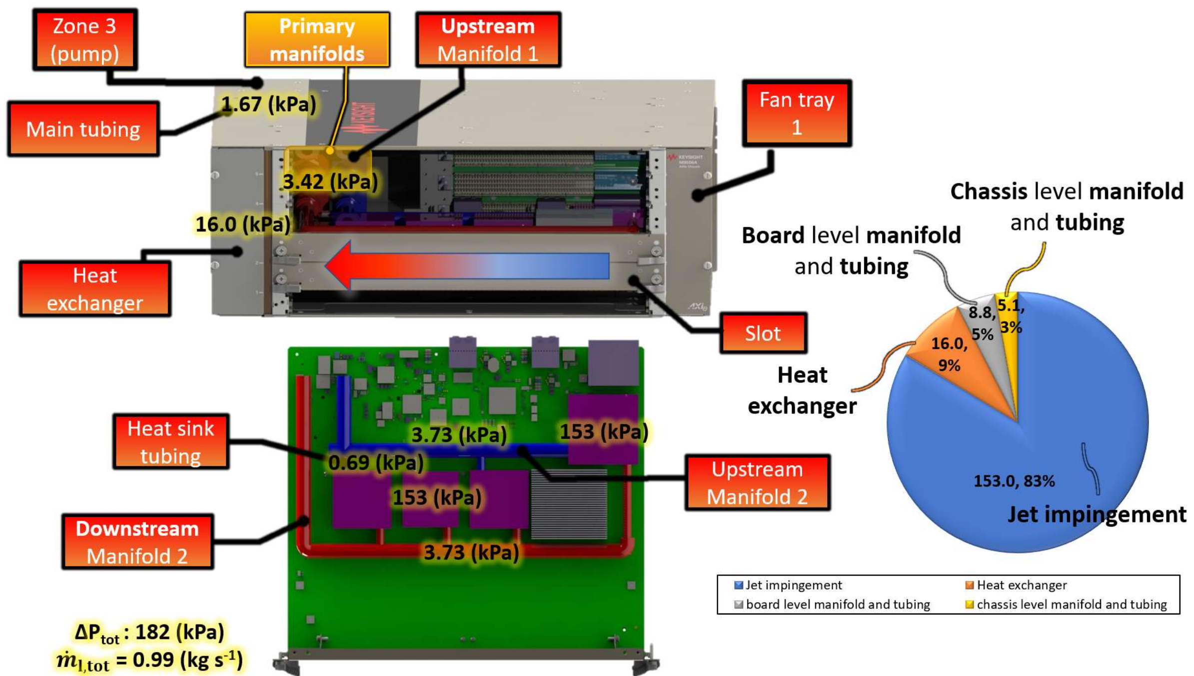


**Figure 4-19** Pressure drop breakdown of FC72 return jet impingement on the die $SD$ = 8, $D_j$ = 400 µm

This is significantly better than water jet impingement on the lid, where only 25% of the pressure drop was from the jets and 75% of the pressure drop/pumping power was being used in the peripheral as shown in Figure 4-20. The primary reason for the increased ratio of jet pressure drop to peripheral pressure drop is due to the smaller target jet area and hence higher mass flux on the chip for the FC72 impingement on the device. This smaller area achieves significantly higher jet velocities for the same mass flow rate. These higher jet velocities and mass flux increase the pressure drop for the same mass flow rate and can reduce the overall required mass flow rate by

achieving the target thermal resistance with less fluid when compared to a larger target surface.

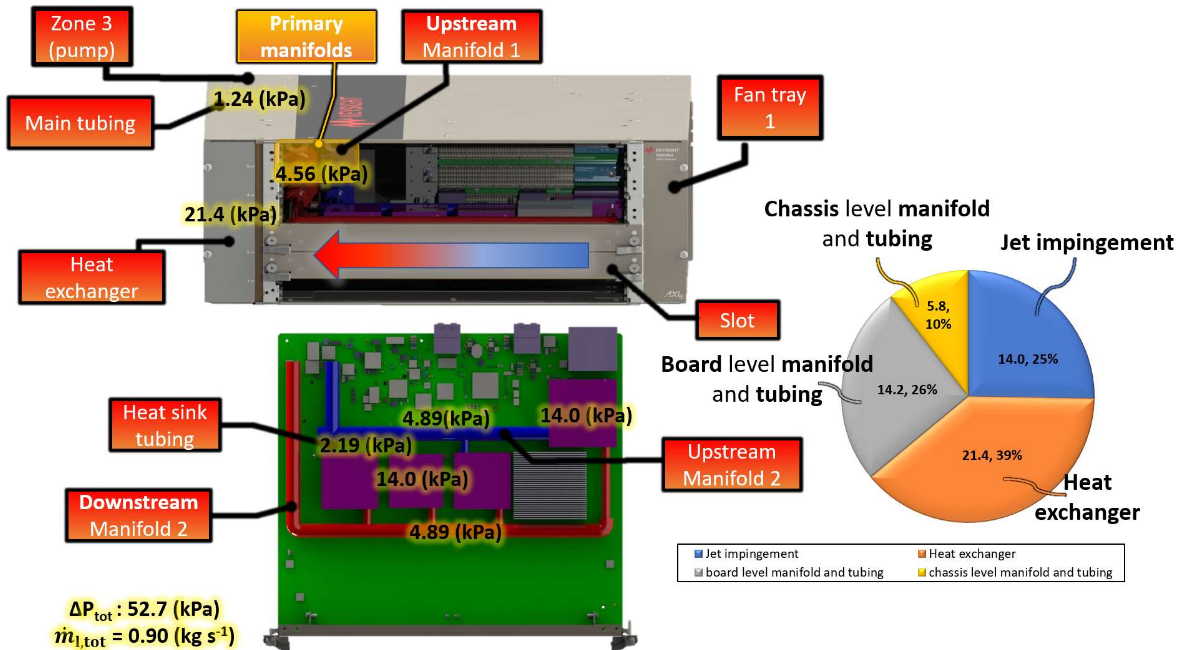


**Figure 4-20** Pressure drop break down of Water return jet impingement on the lid *SD* = 10, $D_j$ = 300 µm

The heat exchanger for water return jet impingement requires significantly more pressure drop at the design point, 21.4 kPa vs 16.0 kPa (39% vs 9%) to achieve the heat sink thermal resistance of 0.0080 K $W^{-1}$. Even though the flow rates are very similar (0.90 kg $s^{-1}$ vs 0.99 kg $s^{-1}$), the system pressure drop for water return jet impingement is roughly 1/3 that of the FC72 system even though the FC72 jet impingement system uses the pressure drop more efficiently at the heatsink level. This is because the jet velocity for FC72 is 8.8 m $s^{-1}$ and water jet impingement on the lid is 2.9 m $s^{-1}$, requiring much high jet velocities to achieve its target thermal resistance. It is important to note that only 30% of the pressure drop of heatsink for jet impingement is from the jets and 70% of the pressure drop is from the manifolding. Reducing this manifolding pressure drop could significantly reduce the pressure drop and pumping power of the FC72 system.

The pressure drop breakdown for water microchannels in configuration 3-5c is shown in Figure 4-21. As the heat transfer plateaus for microchannels, this system requires the lowest mass flow rate at 0.62 kg $s^{-1}$ to achieve its best performance. The largest portion of pressure drop comes from the heat exchanger using 49% of the system pressure drop. The microchannel cold plate consumes 17% of the pressure drop while 34% is used in the remainder of the fluid flow path. This is similar to Alkharabsheh et al. [87] where 14% of the pressure drop was at the cold plate level for a data center rack. Comparing this pressure drop to the water jet impingement method, less

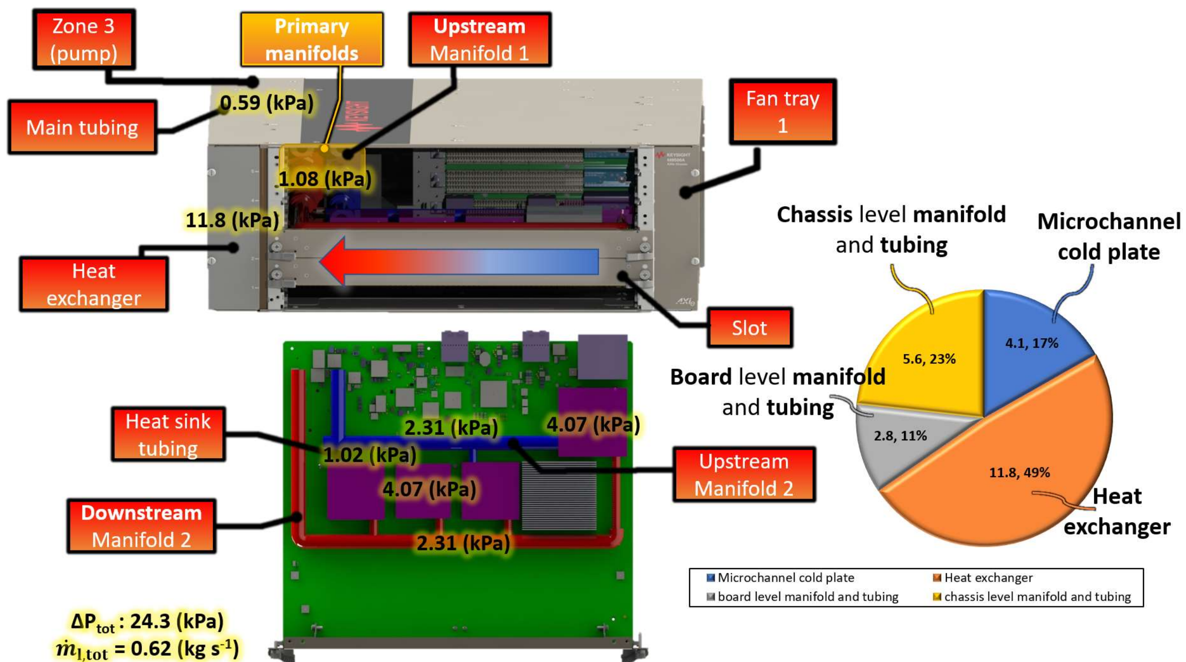


**Figure 4-21** Pressure drop breakdown of Water microchannel bypassing TIM 2

overall pressure drop is required due to the reduction in mass flow rate. This system achieves the best pressure drop performance due to the heat transfer being fixed in the laminar region for microchannel cooling.

Table 4-10 shows the required pumping power and flow rate for the four fluids investigated. The design parameters of the fluids were converted to head in ft lbf $lbm^{-1}$ and GPM to plot on Figure 4-18. Water requires the least head and flow rate from the pump and performs best with

microchannels where the minimal flow rate achieves the maximum cooling performance. GC50/50 requires more flow rate, head, and pumping power than water to achieve the same performance.

**Table 4-10** Head and flow requirements for the pumps

| Fluid | $\Delta P_{pump}$ (psi) | $\rho_{fluid}$ (kg m$^{-3}$) | Head (ft lbf lbm$^{-1}$) | Flow rate (GPM) | Isentropic pumping power (hp) |
|---|---|---|---|---|---|
| Water config a) | 3.368 | 977 | 7.94 | 10.4 | 0.0197 |
| Water config b) | 9.412 | 977 | 22.22 | 15.37 | 0.0844 |
| GC50/50 | 11.38 | 1037 | 25.31 | 17.39 | 0.1167 |
| FC72 | 26.40 | 1544 | 41.35 | 10.09 | 0.1633 |
| Jet fuel A-1 | 20.38 | 793 | 59.27 | 15.42 | 0.183 |

Jet fuel requires the most head, but its pumping power is similar to FC72, due to the lower pressure drop. The dielectrics need twice the pumping power of the other fluids but can achieve significantly better cooling. To achieve the same cooling with the other methods, additional fan power is needed which will increase the total cooling power required for those systems.

The pump selected for water and GC50/50 is a compact inline circulation pump from McMaster Carr. This pump can provide 17 GPM at 20 ft lbf lbm$^{-1}$ and is only 7.75" x 6.5" x 6". The pump selected for FC72 and Jet fuel A-1 is the 0.5 hp Sta-Rite pump [105] which can provide a maximum of 55 ft lbf lbm$^{-1}$ at 15 GPM and works for both FC72 and jet fuel A-1. The size of the pump is 9.58" x 6.6" x 15.77". The pump curve for

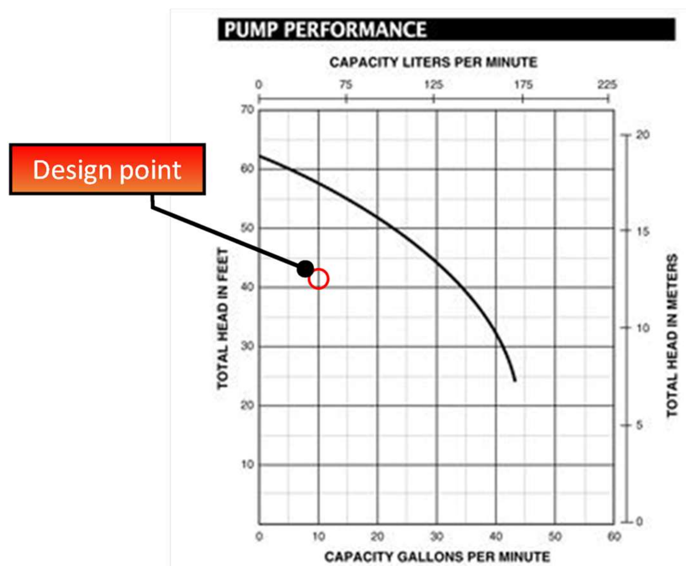


**Figure 4-22** Pump curve Sta-Rite DPC 1/2 H.P. 1/115V, Medium Head Centrifugal Pump

this is shown in Figure 4-22 where the operating point for FC72 is inside the maximum range of the pump.

### 4.3.3. Leakage current summary

As discussed in Chapter 3, IC's consume more power when they are at higher temperatures because the leakage current increases. Figure 4-23 plots the ambient temperature vs the total chassis power. The top banner includes the leakage current values and junction temperature for

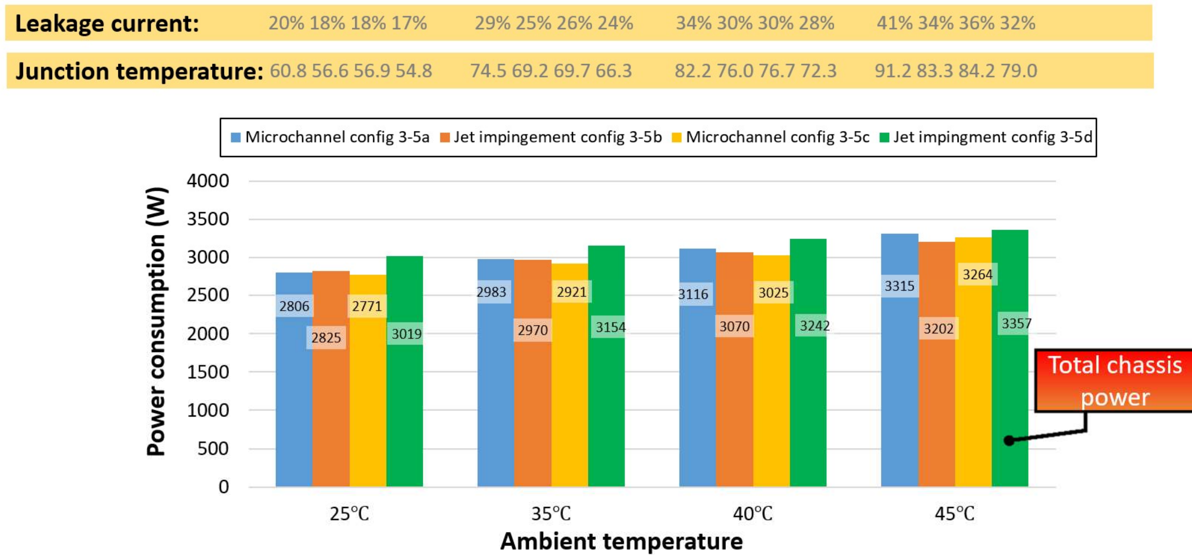


**Figure 4-23** Ambient temperature vs total power consumption due to leakage current

Big Chip 1 at each design point. For configurations 3-5b and 3-5d, the leakage current varies between 17% and 26% for ambient temperatures of 25°C and 35°C, respectively. The water microchannels bypassing TIM 2 (3-5c) performs best as the total power is the lowest for all the design points, except at 45°C ambient, where the junction temperature for water jet impingement on the lid (3-5b) is 0.9°C lower, resulting in a 2% lower leakage current. For this 2% increase in leakage current, the power consumption of Big Chip 1 increases from 157.9W to 159.4W, a 15W increase for the five-slot chassis. The total system power consumption here is 3192W and 3264W

for configuration 3-5b and 3-5c, respectively. When the ambient temperature is increased to 45℃, configuration 3-5a could not keep the chips below their maximum junction temperature, resulting in high leakage current rates (41%). For all of the design cases, FC72 jet impingement on the die (3-5d) kept the junction temperature and leakage current the lowest. However, the FC72 cooling method consumed the most power of all the configurations. The amount of additional power consumption for the FC72 system compared to configuration 3-5c at 25℃ and 45℃ ambient temperatures, were 248W and 93W, respectively. The additional total power was reduced because the leakage current was 1% lower at 25℃, but 4% lower at 45℃ ambient. The total power consumed at 45℃ ambient vs 25℃ ambient is roughly 500W more (3300W vs 2800W). Overall, it is highly beneficial to keep the whole chassis cooler as the system consumes 17% less power.

The pumping power for configurations 3-5a-d were 29W, 96W, 29W, and 332W, respectively. The fan power consumption for all of the cases was 72W. The FC72 system in configuration 3-5d consumed the most pumping power of 332W at a mass flow rate and pressure drop of 1.0 kg $s^{-1}$ and 254 kPa, respectively. Water in configuration 3-5a and 3-5c, consumed the least pumping power at 29W at a mass flow rate and pressure drop of 0.62 kg $s^{-1}$ and 25 kPa, respectively. Finally, configuration 3-5b consumed 96W at a mass flow rate and pressure drop of 0.90 kg $s^{-1}$ and 52 kPa, respectively. While the FC72 system yielded the lowest junction temperature, more pumping power is required. Thus, the designer needs to keep this in mind, and perhaps different fluids need to be considered.

#### 4.3.4. Failure rate results

The failure rate exponentially increases when an IC is operating above the 75℃ junction temperature [33]. Figure 4-24 plots the failure rates of three cooling configurations as maximum power vs ambient temperature where the red line shows the maximum allowable ambient

temperature. This figure was generated with the military handbook *Reliability Prediction of Electronic Equipment* [34]. FC72 performed the best and had the highest allowable ambient temperature for a fixed failure rate. Water microchannels have roughly a 20% higher failure rate

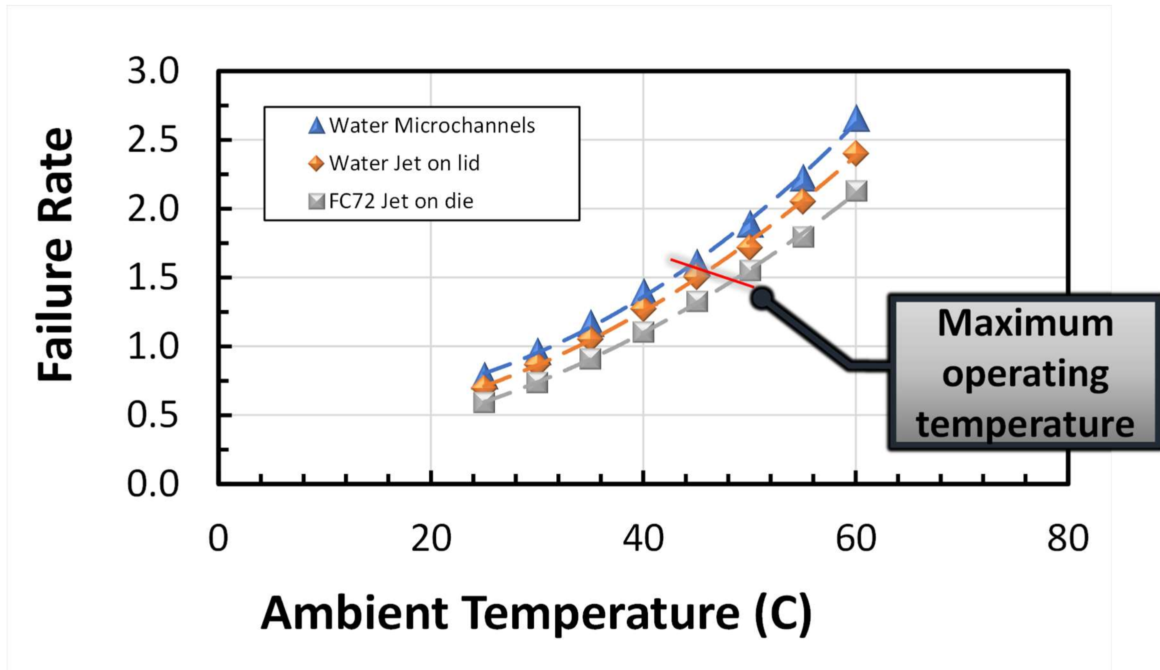


**Figure 4-24** Failure rate vs ambient operating temperature

compared to FC72 jet impingement on the die. The failure rate approaches 1 per $10^6$ hours when the fully loaded chassis ambient temperature is 32℃ for water microchannels, 35℃ for water return jet impingement on the lid and 38℃ for FC72 return jet impingement on the die. By using FC72 jet impingement on the die, the allowable ambient temperature without damaging the equipment is the highest.

#### 4.3.5. Acoustic results

The sound pressure level in dBa has been plotted against the power flux for the 2nd and 3rd generation AXIe chassis's in Figure 4-25. The increase in sound pressure level comes from the addition of a secondary fan tray and the associated increase in overall pressure and flow rate. Assuming the same rate of change in increased performance can be attained from generation to

generation, the data has been extrapolated to predict the acoustic output of the target chassis. This conservative estimate yields and acoustic output of roughly 94 dBa, although the curve is likely a

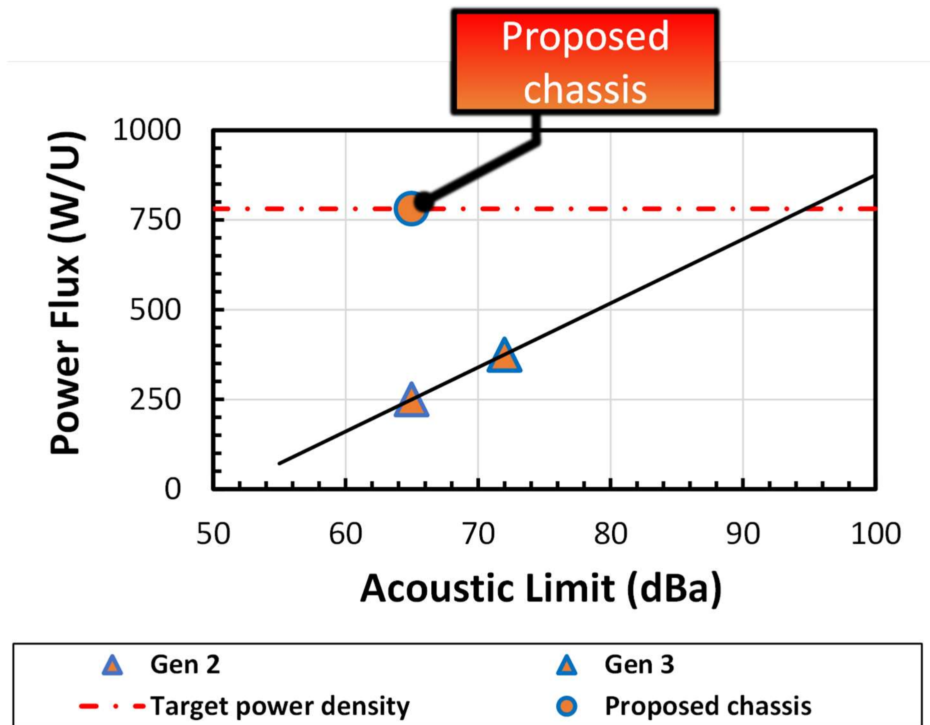


**Figure 4-25** Acoustic limit vs power flux on the M9506A Keysight AXIE chassis

power law relationship. This sound would be equivalent to a gas lawn mower from the operator position. This very high acoustic output is not acceptable for a workspace [106]. The OSHA limit for an 8-hour limit for a work shift is 90 dBa and includes industries such as construction. The acoustic output of the proposed system is 65 dBa which is twice as quiet as the 3rd generation system. Liquid cooling allows significant increases in performance for cooling high powered electronic systems without increasing the acoustic output.

#### 4.3.6. Further considerations

For all of these configurations, over 2/3 of the temperature budget, which is defined as the IC junction temperature minus the ambient temperature ($T_{jc}$-$T_{amb}$), is used by the radiator. In the best approach (3-5d), the temperature difference between the fluid and junction is 8.6°C, while the

fluid to ambient temperature difference is 21.6°C. The current size of the radiator fits in fan tray 2 with dimensions, 2.1” x 11.5” x 6.77”, and is downstream of the heat generated in the chassis. By simply switching the direction of the fan airflow, the best case can cool the maximum connector limit with 50°C ambient inlet temperature to the radiator. This is a 90% improvement from the current generation, although the outlet air temperature from the radiator is 70°C which would pass over the remaining boards in the chassis, likely too high to be feasible for the air cooled chips on legacy boards or Big Chip 3 with maximum junction temperature of 75°C. Reaching zero cold plate thermal resistance would mean the chassis could operate in 58°C environments with the current blades. Thus, improving the heat exchanger performance is much more beneficial beyond this point for increasing the maximum ambient temperature for operation.

By increasing the length of the radiator by 50% to 17 inches, the width of the chassis, the maximum ambient temperature with the 8 fans (from the increased area, more fans) improves to 56°C for FC72 configuration 3-5d. The thermal resistance of the heat exchanger, defined by the average temperature difference between the two fluids, lowers from 0.004194 K $W^{-1}$ to 0.002881 K $W^{-1}$. As shown in Figure 4-26, the airside mass flow rate increases from 264 sCFM to 371 sCFM. This results in a temperature difference of 17.5°C from the inlet air to the outlet fluid, assuming

**Heat exchanger length** | **Properties**

| Heat exchanger length | Properties |
|---|---|
| 11.5 in | $T_{a,i,max}$ = 48.7 [°C]<br>Flow rate: 264 [sCFM]<br>Fans: 6<br>$T_{f,2,liq}$ = 73.5 [°C] |
| 17 in | $T_{a,i,max}$ = 56.0 [°C]<br>Flow rate: 371 [sCFM]<br>Fans: 8<br>$T_{f,2,liq}$ = 73.5 [°C] |
| 23 in | $T_{a,i,max}$ = 60.0 [°C]<br>Flow rate: 475 [sCFM]<br>Fans: 10<br>$T_{f,2,liq}$ = 73.5 [°C] |

**Figure 4-26** Heat exchanger length effect on maximum ambient temperature

the heat from the boards is still picked up (accounting for nominally 5.5°C air temperature rise before the heat exchanger). If the heat exchanger size is doubled, and has 10 fans, the thermal resistance lowers to 0.002203 K $W^{-1}$ and can operate in 60°C ambient environments. As long as the outlet liquid temperature for the FC72 heat exchanger is a maximum of 73.5°C, jet impingement directly on the die can maintain the chips within safe operating limits.

Another configuration to consider for a liquid cooled system is attaching a cold supply line with an external heat exchanger. Fusiara et al. [57] designed a 12 slot chassis where the temperature difference between junction and the fluid was 27.6°C. This study designs a system without an external coolant supply while attaining a temperature difference between junction and fluid less-than 10°C for a higher power chip. With the use of supply fluid from an external coolant loop, the system can maintain a maximum fluid temperature of 75°C. However, at a 50°C inlet coolant temperature, the ICs would be much cooler, reducing the system power consumption. For example,

Big Chip 1 would be 60°C, reducing its power consumption for each chip from 160W to 128W, due to the reduction in leakage current.

Another possibility for increasing the maximum ambient temperature the chassis can operate in is modifying the IC being cooled, such as increasing junction temperature or die size. The allowable junction temperature for ICs has been increasing from 75°C to 100°C in recent years. New Processors of today such as an Intel i7-11700 are specified at a maximum junction temperature of 100°C [10], making higher allowable temperatures much easier to cool. Die sizes on new high-performance processors have also increased as well making these chips easier to cool. The AMD 7H12 die size is 1008 $mm^2$ [107], twice the size of the die sizes in this study. These larger die sizes would cause some reduction in thermal resistance of the heat sinks. However, as mentioned above, if the heat sink thermal resistance is zero, the maximum ambient temperature would only increase 10°C.

This study investigated several cooling configurations and the recommendation for the best cooling configuration depends upon the system requirements. As acoustics is a big priority for electronic cooling systems, the FC72 return jet impingement on the die should be used as it results in the best heat transfer performance and requires the least airside mass flow rate. This system also reduces the IC failure rate the most. If the total system power needs to be minimized, the microchannel cold plate bypassing TIM 2 configuration should be used.

# CHAPTER 5. Conclusions and Recommendations

This study considered four liquid cooling configurations for integrated circuits in a 4U high density computing box. Two cooling methods were considered (microchannel and return jet impingement cooling), each with and without a heat spreader. Liquid cooling systems were designed for the 5-slot chassis, and were modeled in Solidworks to accommodate fluid routing requirements. In each slot, four primary heat sources were cooled with liquid (ASICs, FPGA, CPU, regulators), while the rest of the components on the board were cooled with air. A full liquid cooling system was designed where heat was removed from the circuits primarily to the liquid and then subsequently transferred to the air in a radiator that was placed inside the computing box. All the configurations had the same flow loop, and their heat exchangers resulted in approximately the same performance. However, significant differences were observed among the different cooling strategies.

Microchannel cooling bypassing TIM 2 resulted in a 5°C reduction in junction temperature when compared to microchannel cooling with TIM 2 and a heat spreader. Jet impingement cooling on the lid with water and GC50/50 performed similarly to microchannels bypassing TIM 2. Jet impingement directly on the die with dielectric FC72 performed significantly better than the other configurations, resulting in a thermal resistance decrease of 30% at the package and a 4°C lower junction temperature. In addition, several system level implications were evaluated, including the impact of leakage current, total system power, failure rates, and acoustic implications.

The main results are summarized below:

- Jetting directly onto the die with FC72 resulted in the lowest obtainable thermal resistance. This was possible because all of the TIMs could be removed, thus, even though FC72 is a poor cooling fluid, this approach yielded the best performance. As a result, this system

could operate in a 49°C environment, and could reach the 50°C target with an additional 17 sCFM to the heat exchanger (i.e. 6% increase in the total flow). The failure rate of the system was lowest for FC72 jet impingement on the die as it provided the highest cooling performance.

- Removing TIM 2 in the conduction path resulted in the water microchannels being able to keep the junction temperature roughly 5°C lower for the primary chip (Big Chip 1) compared to water microchannels with TIM 2.
- Water jet impingement on the lid slightly outperforms water microchannels because it bypasses TIM 2. This improvement is 0.108 vs 0.110 K $W^{-1}$ and results in a 0.5°C lower junction temperature.
- Water microchannels bypassing TIM 2 consumed less total power when compared to water microchannels with TIM 2. The reduction in junction temperature on the IC reduced the leakage current, reducing the overall chassis power by up to 150W.
- The main barrier to improved performance was the heat rejection from the liquid to the air. The radiator in this system was undersized due to the chassis size restrictions which resulted in the radiator accounting for nominally 2/3 of the thermal resistance from ambient to the junction temperature.
- A significant result was that while increasing the total chassis power from 1.5 kW to 3.125 kW, the overall sound pressure level decreased for the liquid cooling system because one fan tray was eliminated. As a result, the sound pressure reduced to 65 dBa from 72 dBa. The sound power level did not vary between the different configurations because the radiator had a high thermal resistance, so the fans needed to run at maximum power.

- The overall system power level was found to increase from 2800W to 3300W when the ambient temperature of the system was increased from 25°C to 45°C. This 500W increase was attributed to the leakage current of the processors which operate less efficiently at high junction temperatures.

The exact number of transistors onboard an IC is a proprietary number that companies protect; however, trends have shown that there is no end in the near future for increasing the number of onboard transistors. Meanwhile, the reduction of transistor sizes (which results in more energy efficient ICs) is soon to reach fundamental limits; hence there is no end for the increase in TDP. Thermal management will remain one of the key barriers of future developments and research will continue for solutions. Removing a layer of TIM can provide further increases in performance for liquid cooling systems as this study has shown. The main barrier in liquid cooling systems is removing the heat by the cooling air through the radiator. Utilizing a higher flow delivery device such as a blower can solve this problem and lead to the highest increase in allowable ambient air temperature.

## 5.1. Recommendations for Future Research

The 3.125 kW system designed in this study allowed the chassis to operate in a maximum ambient temperature of 48°C. With the rapidly changing IC market, the design specifications for the ICs could change, making it significantly easier to cool. In order to increase the maximum ambient temperature to the target of 50°C, there are a number of future recommendations for the proposed system are as follows:

- Investigate different fans and blower options to increase the airside volumetric flow rate.
- Investigate the use of more heat exchanger volume, such as the rear of the chassis.
- The dielectric fluids investigated resulted in very high Reynolds numbers for return jet impingement that were outside of the scope of current values published in literature. A secondary analysis with CFD, or new correlations, should be completed to confirm the Nusselt number values at high Reynolds numbers for these dielectric fluids as well as investigate larger jet sizes around 300-600 μm range.
- The system also investigated die sizes of 22.5 mm x 22.5 mm. Increased package sizes could significantly increase the cooling potential of the system.
- Increasing the maximum allowable junction temperature of Big Chip 1 would result in higher allowable ambient temperatures. If possible, higher temperature ICs should be considered for this unit.
- The return jet impingement heatsink was modeled with 30% of the pressure drop at the jets and 70% of the pressure drop from the jet impingement manifold. For the dielectric fluids, 85-90% of the pressure drop was shown at heat sink. Improving the manifold structure of these heat sinks could significantly reduce the required system pumping power and further enhance their performance.

- Performing a tradeoff analysis for cost, leakage current, acoustics, and failure rates at ambient temperatures 25-40°C.
- Investigating other cooling configurations such as an external heat exchanger hookup.
- There are a few uncertainties that should be validated experimentally such as the leakage current and pumping power. The pumping power for the water cooled systems was in the range 20-100W with respect to the total chassis power consumption of ~3200W. The FC72 system consumed roughly 300W of pumping power with respect to the total chassis power of 3300W. The FC72 uncertainty would have a larger effect on the system.

# REFERENCES


[1] Bashroush, R., 2020, "Data Center Energy Use Goes up and up and Up," Uptime Inst.

[2] "Google Search Statistics" [Online]. Available: https://www.internetlivestats.com/google-search-statistics/.

[3] Bar-Cohen, A., 2017, "Gen 3 'Embedded' Cooling: Key Enabler for Energy Efficient Data Centers," IEEE Trans. Components, Packag. Manuf. Technol., **7**(8), pp. 1206–1211.

[4] Fuller, S. H., and Millett, L. I., 2011, "The Future of Computing Performance: Game Over or Next Level?," USA Natl. Acad.

[5] 2004, "Pentium® 4 Processor Extreme Edition Supporting HT Technology 3.73 GHz, 2M Cache, 1066 MHz FSB," Intel.

[6] Pedram, M., and Nazarian, S., 2006, "Thermal Modeling, Analysis, and Management in VLSI Circuits: Principles and Methods," Proc. IEEE, **94**(8), pp. 1487–1501.

[7] Jiao, J., De, X., Chen, Z., and Zhao, T., 2019, "Integrated Circuit Failure Analysis and Reliability Prediction Based on Physics of Failure," Eng. Fail. Anal., **104**(June), pp. 714–726.

[8] Garimella, S. V., Fleischer, A. S., Murthy, J. Y., Keshavarzi, A., Prasher, R., Patel, C., Bhavnani, S. H., Venkatasubramanian, R., Mahajan, R., Joshi, Y., Sammakia, B., Myers, B. A., Chorosinski, L., Baelmans, M., Sathyamurthy, P., and Raad, P. E., 2008, "Thermal Challenges in Next-Generation Electronic Systems," IEEE Trans. Components Packag. Technol., **31**(4), pp. 801–815.

[9] Corporation, I., 2019, "Intel ® Xeon ® Processor Scalable Family," (December).

[10] Processor, I.-11700, 2021, "No Title," Intel [Online]. Available: https://ark.intel.com/content/www/us/en/ark/products/212279/intel-core-i7-11700-processor-16m-cache-up-to-4-90-ghz.html. [Accessed: 05-Jun-2021].

[11] Desjardin, L., 2012, "AXIe: Time for Us to Watch Big Brother."

[12] Rubio-Jimenez, C. A., Hernandez-Guerrero, A., Cervantes, J. G., Lorenzini-Gutierrez, D., and Gonzalez-Valle, C. U., 2016, "CFD Study of Constructal Microchannel Networks for Liquid-Cooling of Electronic Devices," Appl. Therm. Eng.

[13] Gwinn, J. P., and Webb, R. L., 2003, "Performance and Testing of Thermal Interface Materials," Microelectronics J., **34**(3), pp. 215–222.

[14] Kim, N. S., Flautner, K., Blaauw, D., and Mudge, T., 2002, "Drowsy Instruction Caches Leakage Power Reduction Using Dynamic Voltage Scaling and Cache Sub-Bank Prediction," IEE Comput. Soc.

[15] Kim, N. S., Austin, T., Blaauw, D., and Mudge, T., 2003, "Leakage Current: Morre's Law Meets Static Power," IEE, (9789811049910), pp. 179–205.

[16] Wei, J., 2008, "Challenges in Cooling Design of CPU Packages for High-Performance Servers," Heat Transf. Eng., **29**(2), pp. 178–187.

[17] Krishnan, S., Garimella, S. V., Chrysler, G. M., and Mahajan, R. V., 2007, "Towards a Thermal Moore's Law," IEEE Trans. Adv. Packag., **30**(3), pp. 462–474.

[18] Garimella, S. V, Yeh, L., and Persoons, T., 2012, "Telecommunication Systems and Data Centers," IEEE Trans. Components, Packag. Manuf. Technol., **2**(8), pp. 1307–1316.

[19] Mui, M. L., Banerjee, K., and Mehrotra, A., 2004, "Power Supply Optimization in Sub-130 Nm Leakage Dominant Technologies," Proc. - 5th Int. Symp. Qual. Electron. Des. ISQUED 2004, pp. 409–414.

[20] Chung, D. D. L., 2001, "Thermal Interface Materials," J. Electron. Mater., **49**(1), pp. 268–270.

[21] Features, P., 2001, "Intel Pentium 4 Processor in the 423-Pin Package at 1.30, 1.40, 1.50, 1.60, 1.70, 1.80, 1.90 and 2 GHz," Electron. Des., **49**(11), p. 41.

[22] Number, O., 2000, "Intel ® Pentium ® 4 Processor in the 423-Pin Package Thermal Solution Functional Specification," Order A J. Theory Ordered Sets Its Appl., (November).

[23] Viswanath, Ram; Wakharkar, Vijay; Watwe, Abhay; Lebonheur, V., 2000, "Thermal Performance Challenges from Silicon to Systems," Intel Corp, pp. 1–16.

[24] Chiu, C. P., Solbrekken, G. L., and Chung, Y. D., 1997, "Thermal Modeling of Grease-Type Interface Material in PPGA Application," Annu. IEEE Semicond. Therm. Meas. Manag. Symp., pp. 57–63.

[25] Sim, L. C., Ramanan, S. R., Ismail, H., Seetharamu, K. N., and Goh, T. J., 2005, "Thermal Characterization of Al2O3 and ZnO Reinforced Silicone Rubber as Thermal Pads for Heat Dissipation Purposes," Thermochim. Acta, **430**(1–2), pp. 155–165.

[26] Koide, M., Fukuzono, K., Yosliimura, H., Sato, T., Abe, K., and Fujisaki, H., 2006, "High-Performance Flip-Chip BGA Technology Based on Thin-Core and Coreless Package Substrate," Proc. - 2006 Int. Symp. Microelectron. IMAPS 2006, **3**, pp. 1281–1286.

[27] Martindale, J., 2018, "Intels Soldered Ninth-Gen CPUs Could Give Them Even Greater Overclocking Room," Digitaltrends.

[28] Hansson, J., Nilsson, T. M. J., Ye, L., and Liu, J., 2018, "Novel Nanostructured Thermal Interface Materials: A Review," Int. Mater. Rev.

[29] Kempers, R., Kolodner, P., Lyons, A., and Robinson, A. J., 2009, "A High-Precision Apparatus for the Characterization of Thermal Interface Materials," Rev. Sci. Instrum.,

**80**(9).

[30] Zhao, Y., Strauss, D., Chen, Y. C., Liao, T., and Chen, C. L., 2012, “Experimental Study of a High Performance Aligned Graphite Thermal Interface Material,” ASME 2012 3rd Int. Conf. Micro/Nanoscale Heat Mass Transf. MNHMT 2012, pp. 283–290.

[31] Fukushima, H., Drzal, L. T., Rook, B. P., and Rich, M. J., 2006, “Thermal Conductivity of Exfoliated Graphite Nanocomposites,” J. Therm. Anal. Calorim., **85**(1), pp. 235–238.

[32] Faltstrom, L., 2014, “Graphite Sheets and Graphite Gap Pads Used as Thermal Interface Materials,” KTH Vetenskap Och Konst.

[33] Black, J. R., 1969, “Electromigration-A Brief Survey and Some Recent Results,” IEEE, (December).

[34] Defence, D. of, 1991, “Reliability Prediction of Electronic Equipment (Military Handbook),” Dep. Def. USA, p. 205.

[35] Sohel Murshed, S. M., and Nieto de Castro, C. A., 2017, “A Critical Review of Traditional and Emerging Techniques and Fluids for Electronics Cooling,” Renew. Sustain. Energy Rev., **78**, pp. 821–833.

[36] Cengel, Y. A., 2003, *Heat Transfer: A Practical Approach*, Mcgraw-Hill, New York.

[37] 2008, “Fans,” Am. Soc. Mech. Eng., p. 176.

[38] Ascierto, R., 2018, “Uptime Institute Global Data Center Survey.”

[39] Copeland, D., 2000, “Optimization of Parallel Plate Heatsinks for Forced Convection,” Annu. IEEE Semicond. Therm. Meas. Manag. Symp., pp. 266–272.

[40] Freegah, B., Hussain, A. A., Falih, A. H., and Towsyfyan, H., 2020, “CFD Analysis of Heat Transfer Enhancement in Plate-Fin Heat Sinks with Fillet Profile: Investigation of New Designs,” Therm. Sci. Eng. Prog., **17**(July 2019), p. 100458.

[41] Rodgers, P., Eveloy, V., and Pecht, M. G., 2005, “Limits of Air-Cooling: Status and Challenges,” Annu. IEEE Semicond. Therm. Meas. Manag. Symp., pp. 116–124.

[42] Al-damook, A., and Alkasmoul, F. S., 2018, “Heat Transfer and Airflow Characteristics Enhancement of Compact Plate-Pin Fins Heat Sinks – a Review,” Propuls. Power Res., **7**(2), pp. 138–146.

[43] Boukhanouf, R., Haddad, A., North, M. T., and Buffone, C., 2006, “Experimental Investigation of a Flat Plate Heat Pipe Performance Using IR Thermal Imaging Camera,” Appl. Therm. Eng., **26**(17–18), pp. 2148–2156.

[44] Abo El-Nasr, A., and El-Haggar, S. M., 1996, “Effective Thermal Conductivity of Heat Pipes,” Heat Mass Transf. und Stoffuebertragung, **32**(1–2), pp. 97–101.

[45] Wang, J. C., Huang, H. S., and Chen, S. L., 2007, "Experimental Investigations of Thermal Resistance of a Heat Sink with Horizontal Embedded Heat Pipes," Int. Commun. Heat Mass Transf., **34**(8), pp. 958–970.

[46] Xie, X. L., He, Y. L., Tao, W. Q., and Yang, H. W., 2008, "An Experimental Investigation on a Novel High-Performance Integrated Heat Pipe-Heat Sink for High-Flux Chip Cooling," Appl. Therm. Eng., **28**(5–6), pp. 433–439.

[47] Wang, Y., Wang, B., Zhu, K., Li, H., He, W., and Liu, S., 2018, "Energy Saving Potential of Using Heat Pipes for CPU Cooling," Appl. Therm. Eng., **143**(July), pp. 630–638.

[48] Mudawar, Issam. Bowers, M., 1998, "Ultra-High Critical Heat Flux (CHF) for Subcooled Water Flow Boiling -I: CHF Data and Parametric Effects for Small Diameter Tubes," Heat Mass Transf.

[49] Tuckerman, D. B., and Pease, R. F. W., 1981, "High-Performance Heat Sinking for VLSI," IEEE Electron Device Lett., **EDL-2**(5), pp. 126–129.

[50] Zhang, H. Y., Pinjala, D., Wong, T. N., Toh, K. C., and Joshi, Y. K., 2005, "Single-Phase Liquid Cooled Microchannel Heat Sink for Electronic Packages," Appl. Therm. Eng., **25**(10), pp. 1472–1487.

[51] Hung, T. C., Huang, Y. X., and Yan, W. M., 2013, "Thermal Performance of Porous Microchannel Heat Sink: Effects of Enlarging Channel Outlet," Int. Commun. Heat Mass Transf., **48**, pp. 86–92.

[52] Ramakrishnan, B., Alkharabsheh, S., Hadad, Y., Chiarot, P. R., Ghose, K., Sammakia, B., Gektin, V., and Chao, W., 2018, "Experimental Investigation of Direct Liquid Cooling of a Two-Die Package," 34th Annu. Semicond. Therm. Meas. Manag. Symp. SEMI-THERM 2018 - Proc., pp. 42–49.

[53] Ramakrishnan, B., Hadad, Y., Alkharabsheh, S., Chiarot, P. R., and Sammakia, B., 2019, "Thermal Analysis of Cold Plate for Direct Liquid Cooling of High Performance Servers," J. Electron. Packag. Trans. ASME, **141**(4), pp. 1–10.

[54] MicroSi, S.-E., 2015, "X23-7783D: Genuine Thermal Grease from Shin-Etsu Technical Data Sheet" [Online]. Available: https://www.microsi.com/wp-content/uploads/2015/06/X23-7783D-TDS-June-2015.pdf. [Accessed: 09-Aug-2020].

[55] Wei, X., Joshi, Y., and Patterson, M. K., 2007, "Experimental and Numerical Study of a Stacked Microchannel Heat Sink for Liquid Cooling of Microelectronic Devices," J. Heat Transfer, **129**(10), pp. 1432–1444.

[56] Chainer, T., Shultz, M., Parida, P., and Gaynes, M., 2013, "Improving Data Center Energy Efficiency with Advanced Thermal Management," IEEE Trans. Components Packag. Technol., **9781461419**(8), pp. 1–154.

[57] Fusiara, P., Schoonderbeek, G., and Hampson, G., 2018, "Design and Fabrication of Full

Board Direct Liquid Cooling Heat Sink for Densely Packed FPGA Processing Boards," IEEE.

[58] Lucchese, R., Varagnolo, D., and Johansson, A., 2020, "Controlled Direct Liquid Cooling of Data Servers," IEEE Trans. Control Syst. Technol., pp. 1–14.

[59] David, M. P., Iyengar, M., Parida, P., Simons, R., Schultz, M., Gaynes, M., Schmidt, R., and Chainer, T., 2012, "Experimental Characterization of an Energy Efficient Chiller-Less Data Center Test Facility with Warm Water Cooled Servers," Annu. IEEE Semicond. Therm. Meas. Manag. Symp., pp. 232–237.

[60] Kadhim, M. A., Kapur, N., Summers, J. L., and Thompson, H., 2020, "Rack Level Study of Hybrid Liquid/Air Cooled Servers: The Impact of Flow Distribution and Pumping Configuration on Central Processing Units Temperature," Heat Transf. Eng., **41**(19–20), pp. 1683–1698.

[61] Jung, K. W., Kharangate, C. R., Lee, H., Palko, J., Zhou, F., Asheghi, M., Dede, E. M., and Goodson, K. E., 2019, "Embedded Cooling with 3D Manifold for Vehicle Power Electronics Application: Single-Phase Thermal-Fluid Performance," Int. J. Heat Mass Transf., **130**, pp. 1108–1119.

[62] Chauhan, A., Sammakia, B., Ghose, K., Refai-ahmed, G., and Agonafer, D., 2011, "Single-Phase Microchannel Cooling for Stacked Single Core Chip and DRAM," pp. 1–10.

[63] Zhang, X., and Agarwal, R. K., 2020, "Numerical Simulation of Fountain Formation Due to Normal and Inclined Twin-Jet Impingement on Ground," Fluids, **5**(3), p. 132.

[64] Zuckerman, N., and Lior, N., 2006, *Jet Impingement Heat Transfer: Physics, Correlations, and Numerical Modeling*, Elsevier Masson SAS.

[65] Martin, H., 1977, "Heat and Mass Transfer Between Impinging Gas Jets and Solid Surfaces," Adv. Heat Transf., **13**, pp. 1–60.

[66] Maurel, S., and Solliec, C., 2001, "A Turbulent Plane Jet Impinging Nearby and Far from a Flat Plate," Exp. Fluids, **31**(6), pp. 687–696.

[67] Nuntadusit, C., Wae-hayee, M., Tekasakul, P., and Eiamsa-ard, S., 2012, "Local Heat Transfer Characteristics of Array Impinging Jets from Elongated Orifices," Int. Commun. Heat Mass Transf., **39**(8), pp. 1154–1164.

[68] Nuntadusit, C., Wae-hayee, M., Bunyajitradulya, A., and Eiamsa-ard, S., 2012, "Heat Transfer Enhancement by Multiple Swirling Impinging Jets with Twisted-Tape Swirl Generators," Int. Commun. Heat Mass Transf., **39**(1), pp. 102–107.

[69] Kim, B., Cho, H. H., Cho, Y., and Yu, M., 2002, "Distributions of Recovery Temperature on Flat Plate by Underexpanded Supersonic Impinging Jet," J. Thermophys. Heat Transf. - J THERMOPHYS HEAT Transf., **16**, pp. 425–431.

[70] Huber, A. M., and Viskanta, R., 1994, "Effect of Jet-Jet Spacing on Convective Heat Transfer to Confined, Impinging Arrays of Axisymmetric Air Jets," Int. J. Heat Mass Transf.

[71] Fechter, S., Terzis, A., Ott, P., Weigand, B., Von Wolfersdorf, J., and Cochet, M., 2013, "Experimental and Numerical Investigation of Narrow Impingement Cooling Channels," Int. J. Heat Mass Transf., **67**, pp. 1208–1219.

[72] Robinson, A. J., Tan, W., Kempers, R., Colenbrander, J., Bushnell, N., and Chen, R., 2017, "A New Hybrid Heat Sink with Impinging Micro-Jet Arrays and Microchannels Fabricated Using High Volume Additive Manufacturing," Annu. IEEE Semicond. Therm. Meas. Manag. Symp., pp. 179–186.

[73] Brunschwiler, T., Rothuizen, H., Fabbri, M., Kloter, U., Michel, B., Bezama, R. J., and Natarajan, G., 2006, "Direct Liquid Jet-Impingement Cooling with Micronsized Nozzle Array and Distributed Return Architecture," Thermomechanical Phenom. Electron. Syst. - Proceedings Intersoc. Conf., **2006**, pp. 196–203.

[74] Onstad, A. J., Hoberg, T. B., Elkins, C. J., Eaton, J. K., and Mall, E., 2009, "FLOW AND HEAT TRANSFER FOR JET IMPINGEMENT ARRAYS WITH LOCAL EXTRACTION," (June), pp. 22–24.

[75] Rhee, D. H., Yoon, P. H., and Cho, H. H., 2003, "Local Heat/Mass Transfer and Flow Characteristics of Array Impinging Jets with Effusion Holes Ejecting Spent Air," Int. J. Heat Mass Transf., **46**(6), pp. 1049–1061.

[76] Rattner, A. S., 2017, "General Characterization of Jet Impingement Array Heat Sinks With Interspersed Fluid Extraction Ports for Uniform High-Flux Cooling," J. Heat Transfer, **139**(8), p. 082201.

[77] Bandhauer, T. M., Hobby, D. R., Jacobsen, C., and Sherrer, D., 2018, "Thermal Performance of Micro-Jet Impingement Device with Parallel Flow, Jet-Adjacent Fluid Removal," ASME 2018 16th Int. Conf. Nanochannels, Microchannels, Minichannels.

[78] Hoberg, T. B., Onstad, A. J., and Eaton, J. K., 2010, "Heat Transfer Measurements for Jet Impingement Arrays with Local Extraction," Int. J. Heat Fluid Flow, **31**(3), pp. 460–467.

[79] Hobby, D., Walker, T., Rattner, A., Jacobsen, C., and Sherrer, D., 2020, "Comparison of Experimental and Computational Heat Transfer Characterization of Water Jet Impingement Array with Interspersed Fluid Extraction Comparison of Experimental and Computational Heat Transfer," Heat Transf. Eng., **7632**.

[80] Viskanta, R., 1993, "Nusselt-Reynolds Prize Paper Heat Transfer to Impinging Isothermal Gas and Flame Jets," Exp. Therm. Fluid Sci., **6**, pp. 111–134.

[81] Wei, T. W., Oprins, H., Cherman, V., Van der Plas, G., De Wolf, I., Beyne, E., and Baelmans, M., 2019, "Experimental Characterization and Model Validation of Liquid Jet Impingement Cooling Using a High Spatial Resolution and Programmable Thermal Test

Chip," Appl. Therm. Eng., **152**(May 2018), pp. 308–318.

[82] Wei, T., Oprins, H., Cherman, V., Yang, S., De Wolf, I., Beyne, E., and Baelmans, M., 2019, "Experimental Characterization of a Chip-Level 3-D Printed Microjet Liquid Impingement Cooler for High-Performance Systems," IEEE Trans. Components, Packag. Manuf. Technol., **9**(9), pp. 1815–1824.

[83] Han, Y., Lau, B. L., Tang, G., Chen, H., and Zhang, X., 2020, "Si Microfluid Cooler with Jet-Slot Array for Server Processor Direct Liquid Cooling," IEEE Trans. Components, Packag. Manuf. Technol., **10**(2), pp. 255–262.

[84] Han, Y., Tang, G., Lau, B. L., and Zhang, X., 2018, "Hybrid Micro-Fluid Heat Sink for High Power Dissipation of Liquid-Cooled Data Centre," 2017 IEEE 19th Electron. Packag. Technol. Conf. EPTC 2017, **2018-Febru**, pp. 1–4.

[85] El-Sheikh, H., and Garimella, S., 2000, "Enhancement of Air Jet Impingement Heat Transfer Using Pin-Fin Heat Sinks," Green Energy Technol., **23**, pp. 300–308.

[86] Ndao, S., Peles, Y., and Jensen, M. K., 2014, "Effects of Pin Fin Shape and Configuration on the Single-Phase Heat Transfer Characteristics of Jet Impingement on Micro Pin Fins," Int. J. Heat Mass Transf., **70**, pp. 856–863.

[87] Alkharabsheh, sami; Ramakrishnan, Bharath; Sammakia, B., 2017, "Pressure Drop Analysis of Direct Liquid Cooled (DLC) Rack," 16th IEEE ITHERM Conf.

[88] 2020, "M9506A AXIe High-Performance 5-Slot Chassis."

[89] Narumanchi, S. V. J., Hassani, V., and Bharathan, D., 2005, "Modeling Single-Phase and Boiling Liquid Jet Impingement Cooling in Power Electronics," (December).

[90] Gao, T., Tang, H., Cui, Y., and Luo, Z., 2018, "A Test Study of Technology Cooling Loop in a Liquid Cooling System," Proc. 17th Intersoc. Conf. Therm. Thermomechanical Phenom. Electron. Syst. ITherm 2018, pp. 740–747.

[91] Idelchik, I E;Fried, E., 1986, *Handbook of Hydraulic Resistance: Second Edition*, United States: N. p.

[92] Perry, S., Perry, R. H., Green, D. W., and Maloney, J. O., 1934, *Chemical Engineers Handbook Seventh Edition*, McGraw-Hill, New York.

[93] Berman, Theodore; Kavine, Adrienne; Incropera, Frank; Dewitt, D., 2011, *Fundementals of Heat and Mass Transfer*, Jon Wiley & Sons.

[94] Hwu, R., and Qu, W., 2010, "Heat Transfer Correlations for Thermally Developing Flow in Rectangular Micro-Channels Subject to Four-Sided and Three-Sided H1 Boundary Conditions," 2010 14th Int. Heat Transf. Conf. IHTC 14, **6**, pp. 239–244.

[95] Hobby, D., Walker, T., Rattner, A., Jacobsen, C., Sherrer, D., and Bandhauer, T., 2018,

"Comparison of Experimental and Computational Heat Transfer Characterization of Water Jet Impingement Array with Interspersed Fluid Extraction," (September), pp. 3–4.

[96] Wei, T. W., Oprins, H., Cherman, V., Beyne, E., and Baelmans, M., 2020, "Experimental and Numerical Investigation of Direct Liquid Jet Impinging Cooling Using 3D Printed Manifolds on Lidded and Lidless Packages for 2.5D Integrated Systems," Appl. Therm. Eng., **164**(October 2019), p. 114535.

[97] Chang, Y.-J., and Wang, C.-C., 1997, "A Generalized Heat Transfer Correlation for Louver Fin Geometry," **40**(3).

[98] Kakac, S., Shah, R.K., Bhatti, M. S., 1987, "Chapter 3," *Handbook of Single-Phase Convective Heat Transfer*.

[99] 1982, "Flow of Fluid through Valves, Fittings and Pipe."

[100] Chang, Y. J., Chang, W. J., Li, M. C., and Wang, C. C., 2006, "An Amendment of the Generalized Friction Correlation for Louver Fin Geometry," Int. J. Heat Mass Transf., **49**(21–22), pp. 4250–4253.

[101] Thunmann, A., 1990, *Fundamentals of Noise Control Engineering*, Fairmont Press, Atlanta.

[102] Le, N., and Filleul, S., 1966, "An Investigation of Axial Flow Fan Noise," Sound Vib., **3**, pp. 147–165.

[103] Cai-ling, J., Jiang-ping, C., Zhi-jiu, C., Jie, T., Hua, O., and Zhao-hui, D., 2007, "Experimental and Numerical Study on Aeroacoustic Sound of Axial Flow Fan in Room Air Conditioner," **68**, pp. 458–472.

[104] Krishnappa, G., 1977, *Centrifugal Blower Noise Studies Literature Survey and Noise Measurements*.

[105] Pentair, "Residential Water Systems," Centrif. Util. pumps, pp. 1–200 [Online]. Available: www.sta-rite.com.

[106] Breysse, P. N., and Lees, P. S. J., 2006, "Noise and Decibels," Johns Hopkins Univ.

[107] 2021, "AMD 7H12," X86 CPUS' Guid.

# A. APPENDIX Junction to Case Thermal Resistance

The thermal resistance from junction to case was modeled using Ansys 2021 Steady State Solver Package. The junction to case thermal resistance was set at 0.10 K $W^{-1}$ and the die size was solved for with a TIM 1 effective thermal conductivity 7.8 W $m^{-1}$ $K^{-1}$. Figure A-1 shows the inputs to the software. The boundary conditions for heat flow were set on 12 insulating surfaces, the four

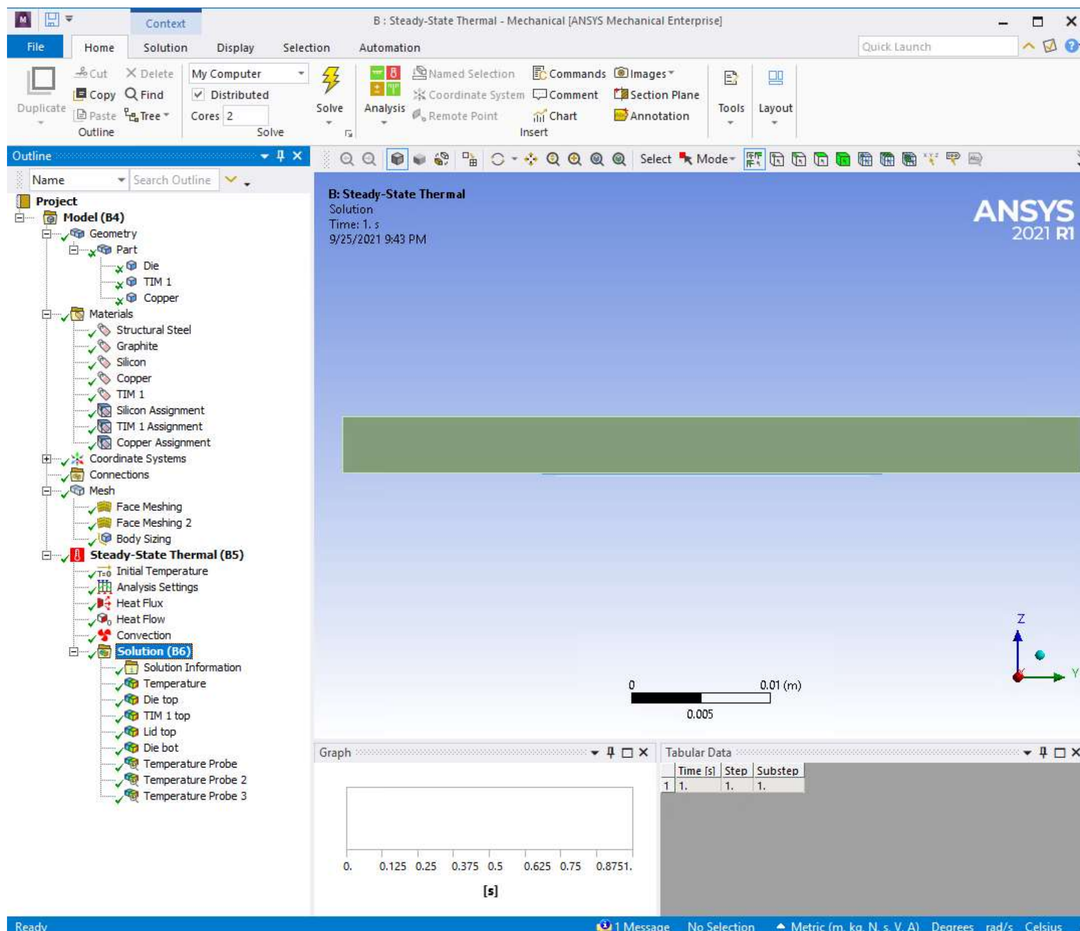


**Figure A-1** Ansys 2021 Steady State Solver boundary conditions

edges on each of the three bodies. The heat transfer coefficient applied to the lid surface was 5000 W $m^{-2}$ $K^{-1}$. A heat flux of 252840 W $m^{-2}$ $K^{-1}$ was applied on the die's body (128W). The thermal resistance was calculated as

$$R_{\mathrm{TIM},1} = \frac{T_{\mathrm{j,max}} - T_{\mathrm{TIM,1,max}}}{TDP} \quad \text{(A-1)}$$

where $T_{\mathrm{j,max}}$ is the maximum temperature on the die, $T_{\mathrm{TIM,1,max}}$ is the maximum temperature on the TIM 1, and TDP is the thermal dissipation power of 128W. Similarly, the IHS (integrated heat spreader) thermal resistance can be calculated:

$$R_{\mathrm{IHS}} = \frac{T_{\mathrm{TIM,1,max}} - T_{\mathrm{IHS,max}}}{TDP} \quad \text{(A-2)}$$

where $T_{\mathrm{IHS,max}}$ is the maximum temperature on the integrated heat spreader. The relevant dimensions and properties input to the model are shown in Table A-1. The size of the IHS is 53.1

**Table A-1** Steady state solver inputs and geometry

| **Name** | **Value** |
|---|---|
| Die width | 22.5e-03 [m] |
| Die thickness | 0.10e-03 [m] |
| Die thermal conductivity | 148 [W $m^{-1}$ $K^{-1}$] |
| TIM 1 width | 24.5e-03 [m] |
| TIM 1 thickness | 0.151e-03 [m] |
| TIM 1 thermal conductivity | 7.8 [W $m^{-1}$ $K^{-1}$] |
| IHS width | 53.1e-03 [m] |
| IHS thickness | 4.0e-03 [m] |
| IHS thermal conductivity | 400 [W $m^{-1}$ $K^{-1}$] |

x 53.1 $mm^2$ and the die size has been determined to be 22.5 x 22.5 $mm^2$. The thermal profile and maximum temperature on the three bodies for these results is shown in Figure A-2. The maximum die, TIM 1, and IHS temperatures were 66.4°C, 56.7°C and 53.4°C, respectively. Using equation

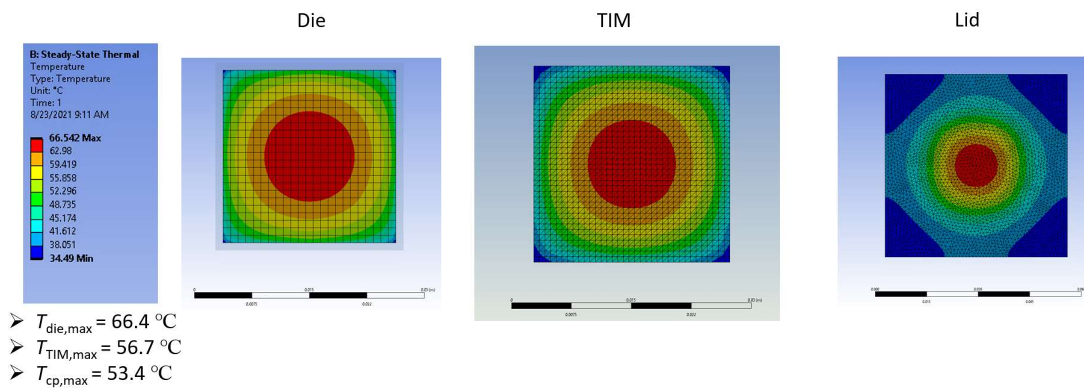


**Figure A-2** Ansys 2021 Steady State Solver results for junction to case thermal resistance

A-1 and A-2, the thermal resistances are calculated to be $R_{TIM,1}$ = 0.076 K W$^{-1}$ and $R_{IHS}$ = 0.024 K W$^{-1}$.

The geometry was created in the design modeler of Ansys and is shown in Figure A-3. Three bodies were created within 1 part, where there is no contact resistance between the bodies. The extrude features were added as frozen, and the topologies were merged. The three bodies can be seen where the die is on the bottom, TIM 1 is in the middle and the IHS is on top.

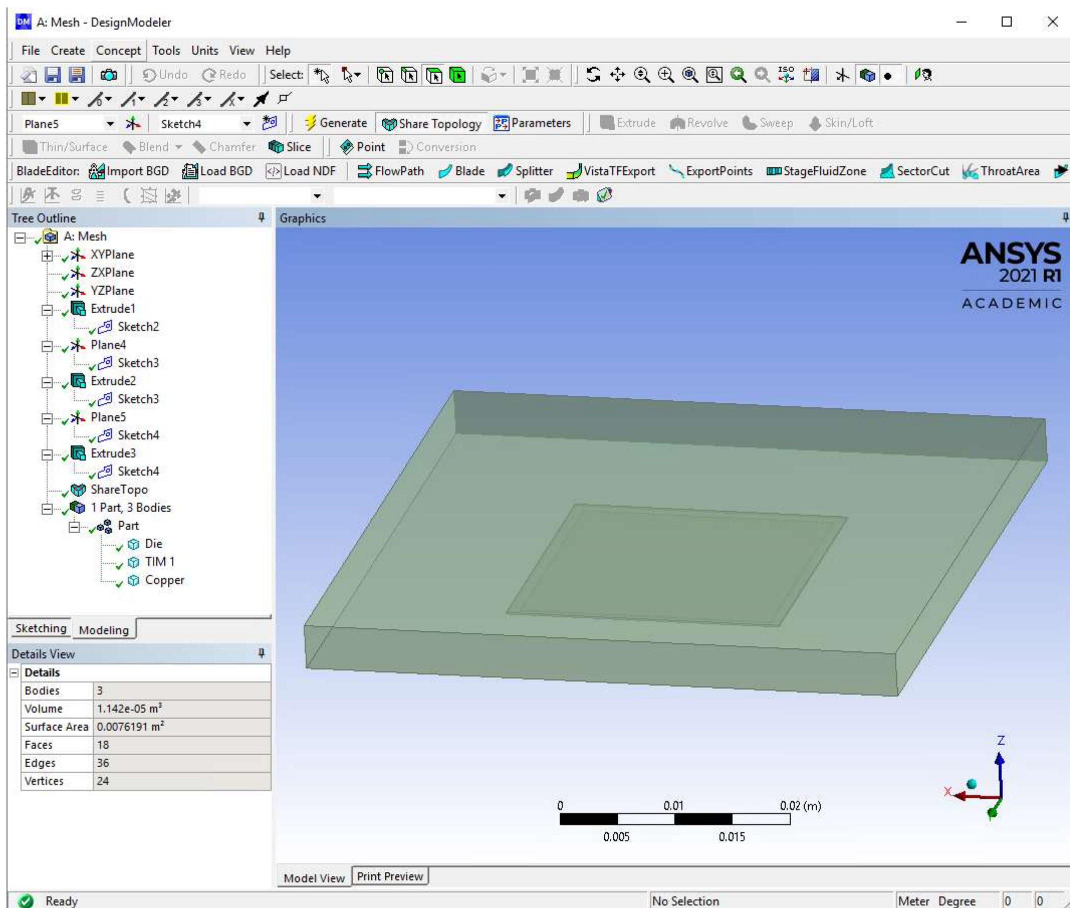

**Figure A-3** Ansys 2021 design modeler inputs

# B. APPENDIX Sample Calculations

The following appendix contains hand calculations in which validate the numerical solver, EES (Engineering Equation Solver), for the thermodynamic, heat transfer, and pressure drop calculations that were performed in this work. The state point format for the equations is displayed in Figure A-4.

## A.1 Basic Thermodynamic Calculations

The thermodynamic hand calculations performed included solving an energy balance across the heat exchanger from point 1 to 2 as depicted in the figure. The heat sink on the electronic package also used a similar energy balance between the *UA* provided by the package and the temperature in/out and at the surface.

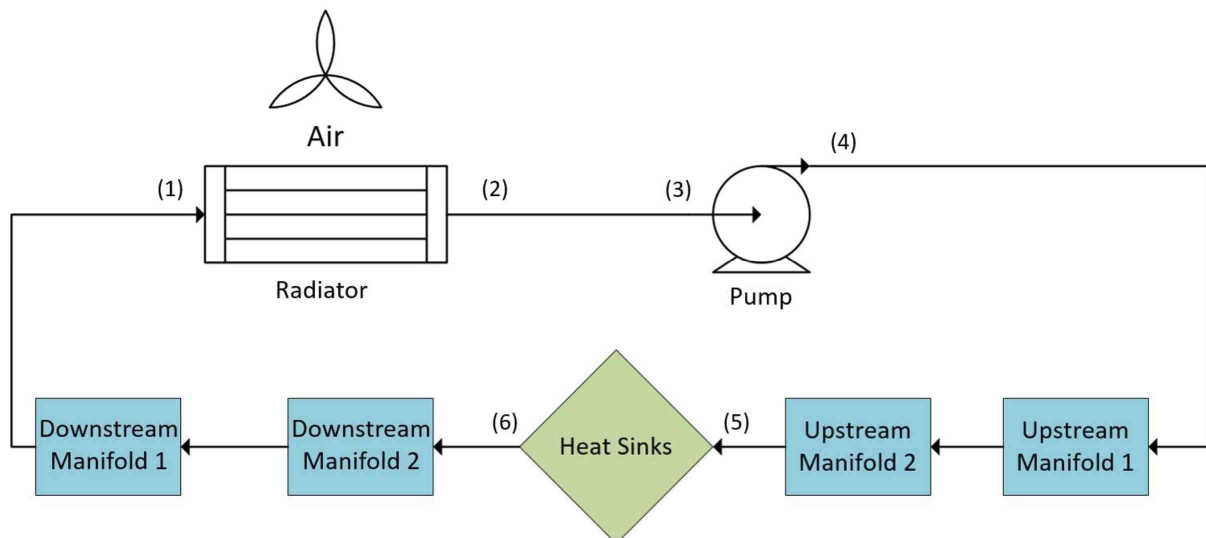


**Figure A-4** PFD of state points used for hand calculations

## A.2 Heat Exchanger Calculations

The minimum mass flow rate for the four main fluids investigated was calculated by solving the energy balance between the heat capacity rate provided by the fans and the heat capacity rate each fluid. This was independent of the of the heat sink mass flow rate optimization and there was no shown effect by optimizing the heat exchanger prior to the heat sink optimization as the air side heat capacitance was significantly lower than that of the fluids at the designed flow rates. The NTU method was used to model the heat exchanger in order to determine its effectiveness.

## A.3 Heat Exchanger UA Calculations

The heat exchanger UA was solved for by calculating the resistance of a unit cell which was half the channel height on the air and liquid side. This unit cell UA was multiplied by the number of channels to determine the heat exchangers universal heat transfer coefficient.

## A.4 Heat sink Calculations

The heat sink energy balance was solved for using the LMTD (log mean temperature difference) method. This method accounts for the fluid heating as it cools the electronics package. The LMTD was taken with respect to the inlet, outlet and surface temperature for each heat sink.

## A.5 Manifold Calculations

The manifold calculations performed in this work solve the pressure drop through a combination of frictional pressure drop in the tubing, pressure drop due to elbows, expansion/contractions, and a flow distributer pressure drop correlation discussed in Chapter 3.

## A.6 Tubing, Elbow, and other Miscellaneous Calculations

The tubing and elbow pressure drop were solved for by calculating their respective k factors. These k factors were then multiplied by the dynamic pressure to calculate the pressure loss of them.

**Table A – 2** Fluid properties

| Parameter | Value | Units |
|---|---|---|
| TDP Big Chip 1 max ($Q_{chip,1,max}$) | 102.4 | W |
| TDP Big Chip 2 max ($Q_{chip,2,max}$) | 38.4 | W |
| TDP Big Chip 3 max ($Q_{chip,2,max}$) | 12.8 | W |
| TDP regulators ($Q_{chip,4}$) | 150 | W |
| TDP memory ($Q_{chip,5,max}$) | 20 | W |
| TDP misc. ($Q_{chip,6}$) | 6.25 | W |
| Leakage $Power_4$ | 1 | Dim |
| Leakage $Power_6$ | 1 | Dim |
| $N_{chip}$ | 6 | Dim |
| Pump efficiency ($\eta_{pump}$) | 50 | % |
| Fan efficiency ($\eta_{fan}$) | 50 | % |
| Number of fans ($Z_{fans}$) | 6 | Dim |
| Total mass flow rate ($m_{dot,tot}$) | 0.60 | kg $s^{-1}$ |
| Individual fan volumetric flow rate (x) | 1.251 | $m^3$ $min^{-1}$ |
| Total fans volumetric flow rate (V dot act) | 0.1251 | $m^3$ $sec^{-1}$ |
| Ambient air temperature ($T_{amb}$) | 25,45,50,55 | °C |
| Ambient air pressure ($P_{amb}$) | 101 | kPa |
| Ambient air density ($\rho_{amb}$) | 1.085 | kg $m^{-3}$ |
| Ambient air specific heat ($C_{p,amb}$) | 1.006 | kJ $kg^{-1}$ $K^{-1}$ |
| | | |

| Parameter | Value | Units |
|---|---|---|
| Heat exchanger air temperature ($T_{air,in}$) | 48 | °C |
| Heat exchanger air pressure ($P_{amb}$) | 101 | kPa |
| Heat exchanger air density ($\rho_{hx,air}$) | 1.038 | kg $m^{-3}$ |
| Heat exchanger air thermal conductivity ($k_{hx,air}$) | 0.02902 | W $m^{-1}$ $K^{-1}$ |
| Heat exchanger air dynamic viscosity ($\mu_{hx,air}$) | 2.022e-05 | kg $m^{-1}$ $s^{-1}$ |
| Heat exchanger air specific heat ($C_{p,hx,air}$) | 1.008 | kJ $kg^{-1}$ $K^{-1}$ |
| Heat exchanger air Prandtl number ($Pr_{hx,air}$) | 0.7031 | - |
| Heat exchanger thermal conductivity ($k_{hx}$) | 158.8 | W $m^{-1}$ $K^{-1}$ |
| Heat exchanger total length ($L_{hx,tot}$) | 11.5 | in |
| Heat exchanger total width ($W_{hx,tot}$) | 2.1 | in |
| Heat exchanger total height ($H_{hx,tot}$) | 6.77 | in |
| Manifold 1 absolute roughness (assume weld steel) | 0.000045 | m |
| Manifold 2 absolute roughness (assume stretched steel) | 0.000015 | m |

| Parameter | Value | Units |
|---|---|---|
| FC72 Temperature ($T_{fluid,1}$) | 77.42 | ℃ |
| FC72 pressure ($P_{fluid,1}$) | 263 | kPa |
| FC72 density ($\rho_{fluid,1}$) | 1538 | kg $m^{-3}$ |
| FC72 thermal conductivity ($k_{fluid,1}$) | 0.05148 | W $m^{-1}$ $K^{-1}$ |
| FC72 dynamic viscosity ($\mu_{fluid,1}$) | 0.0004379 | kg $m^{-1}$ $s^{-1}$ |
| FC72 specific heat ($C_{p,fluid,1}$) | 1.134 | kJ $kg^{-1}$ $K^{-1}$ |
| FC72 Prandtl ($Pr_{fluid,1}$) | 9.647 | - |
| FC72 Temperature ($T_{fluid,5}$) | 75.12 | ℃ |
| FC72 pressure ($P_{fluid,5}$) | 371.5 | kPa |
| FC72 density ($\rho_{fluid,5}$) | 1544 | kg $m^{-3}$ |
| FC72 thermal conductivity ($k_{fluid,5}$) | 0.05174 | W $m^{-1}$ $K^{-1}$ |
| FC72 dynamic viscosity ($\mu_{fluid,5}$) | 0.0004081 | kg $m^{-1}$ $s^{-1}$ |
| FC72 specific heat ($C_{p,fluid,5}$) | 1.131 | kJ $kg^{-1}$ $K^{-1}$ |
| FC72 Prandtl ($Pr_{fluid,5}$) | 8.92 | - |
| | | |

**Table A – 3** Chip power and leakage current specifications

| Parameter | Equation | Evaluated | EES Calc. Value | Hand Calc. Value | Units |
|---|---|---|---|---|---|
| Leakage $Power_1$ | $1/\{1-(3.2251\cdot10^{-5}\cdot T_{\text{chip,1,s}}{}^2+1.9515\cdot10^{-3}\cdot T_{\text{chip,1,s}}-3.50026\cdot10^{-2})\}$ | 3.2251E-05(85)$^2$ + 1.9515E-03(85) - 3.50026E-02 | 1.573 | 1.572 | - |
| Leakage $Power_2$ | $1/\{1-(3.2251\cdot10^{-5}\cdot T_{\text{chip,2,s}}{}^2+1.9515\cdot10^{-3}\cdot T_{\text{chip,2,s}}-3.50026\cdot10^{-2})\}$ | 3.2251E-05(82.15)$^2$ + 1.9515E-03(75) - 3.50026E-02 | 1.522 | 1.522 | - |
| Leakage $Power_3$ | $1/\{1-(3.2251\cdot10^{-5}\cdot T_{\text{chip,3,s}}{}^2+1.9515\cdot10^{-3}\cdot T_{\text{chip,3,s}}-3.50026\cdot10^{-2})\}$ | 3.2251E-05(75)$^2$ + 1.9515E-03(75) - 3.50026E-02 | 1.414 | 1.414 | - |
| Leakage $Power_5$ | $1/\{1-(3.2251\cdot10^{-5}\cdot T_{\text{chip,5,s}}{}^2+1.9515\cdot10^{-3}\cdot T_{\text{chip,5,s}}-3.50026\cdot10^{-2})\}$ | 3.2251E-05(75)$^2$ + 1.9515E-03(75) - 3.50026E-02 | 1.433 | 1.414 | - |
| $Q_{\text{chip,act,i}}$ | $Q_{\text{chip,act,i}}=\sum_{i=1}^{N_{\text{chip}}} Q_{\text{chip,i}}\cdot Leakage\ Power_{\text{i}}$ | $Q_{\text{chip,act,1}}=(102.4)1.572$<br>$Q_{\text{chip,act,2}}=(38.4)1.522$<br>$Q_{\text{chip,act,3}}=(12.8)1.414$<br>$Q_{\text{chip,act,4}}=(150)$<br>$Q_{\text{chip,act,5}}=(20)1.414$<br>$Q_{\text{chip,act,6}}=(6.25)$ | 160.8<br>58.4<br>18.1<br>150<br>28.3<br>6.25 | 161.0<br>58.4<br>18.1<br>150<br>28.3<br>6.25 | W |

**Table A - 4** System thermal variables and heat exchanger inlet air temperature

| Parameter | Equation | Evaluated | EES Calc. Value | Hand Calc. Value | Units |
|---|---|---|---|---|---|
| $T_{\text{air,in}}$ | $T_{\text{air,in}}=T_{\text{amb}}+\frac{Q_{\text{chip,back}}+Q_{\text{chip,air}}}{\dot{m}_{\text{air}}c_{\text{p,air}}}$ | $T_{\text{air,in}}=48+\frac{530.4+436}{0.1357\cdot1007}$ | 55.07 | 55.07 | °C |
| $Q_{\text{chip,back}}$ | $Q_{\text{chip,back}}=Q_{\text{liq}}\cdot(1-Percent.back)$ | $Q_{\text{chip,back}}=2652\cdot(1-80\%)$ | 533.7 | 530.4 | W |

| Parameter | Equation | Evaluated | EES Calc. Value | Hand Calc. Value | Units |
|---|---|---|---|---|---|
| $Q_{\text{chip,total}}$ | $Q_{\text{chip,total}} = N_{\text{blades}} \sum_{i=1}^{N_{\text{chip}}} N_{\text{chip,i}} Q_{\text{chip,act}}$ | $Q_{\text{chip,total}} = 5(2 \cdot 161 + 1 \cdot 58.4 + 1 \cdot 18.1 + 1 \cdot 150 + 2 \cdot 28.3 + 2 \cdot 6.25)$ | 3089 | 3088 | W |
| $Q_{\text{chip,liq}}$ | $Q_{\text{chip,liq}} = N_{\text{blades}} \sum_{i=1}^{1,2,4} N_{\text{chip,i}} Q_{\text{chip,act}}$ | $Q_{\text{chip,liq}} = 5(2 \cdot 161 + 1 \cdot 58.4 + 1 \cdot 150)$ | 2653 | 2652 | W |
| $Q_{\text{chip,air}}$ | $Q_{\text{chip,air}} = N_{\text{blades}} \sum_{i=1}^{3,5,6} N_{\text{chip,i}} Q_{\text{chip,act}}$ | $Q_{\text{chip,total}} = 5(1 \cdot 18.1 + 2 \cdot 28.3 + 2 \cdot 6.25)$ | 435.8 | 436 | W |
| System Q | $Q_{\text{sys}} = Q_{\text{liq}} \cdot Percent.back$ | $Q_{\text{sys}} = 2652 \cdot 80\%$ | 2129 | 2121.6 | W |
| $\dot{m}_{air}$ | $\dot{m}_{air} = \dot{V}_{\text{sCMPS}} \cdot \rho_{\text{amb}}$ | $\dot{m}_{\text{air}} = 0.1251 \cdot 1.085$ | 0.1358 | 0.1357 | kg $s^{-1}$ |
| $C_{\text{air}}$ | $C_{\text{air}} = \dot{m}_{\text{a}} c_{\text{p,air,hx}}$ | $C_{\text{air}} = 0.1357 \cdot 1.008$ | 0.1369 | 0.1368 | kJ $s^{-1}$ $K^{-1}$ |
| $C_{\text{liq}}$ | $C_{\text{liq}} = \dot{m}_{\text{liq,tot}} c_{\text{p,f,1}}$ | $C_{\text{liq}} = 1.286 \cdot 1.132$ | | | kJ $s^{-1}$ $K^{-1}$ |
| Liquid mass flow min | $C_{\text{air}} = \dot{m}_{\text{liq,tot}} c_{\text{p,f,1}}$ | $0.1368 = \dot{m}_{\text{liq,tot}} \cdot 1.132$ | | 0.1208 | |
| $C_{\text{ratio}}$ | $C_{\text{ratio}} = \frac{C_{\text{min}}}{C_{\text{max}}}$ | $C_{\text{ratio}} = \frac{0.1368}{}$ | | | |
| $C_{\text{min}}$ | $C_{\text{ratio}} = \min(C_{\text{air}}, C_{\text{liq}})$ | $C_{\text{ratio}} = \min(,)$ | 0.1369 | 0.1368 | kJ $s^{-1}$ $K^{-1}$ |
| Air outlet temperature | $T_{\text{air,out}} = T_{\text{air,in}} + \frac{Q_{\text{liq}} + Q_{\text{chip,air}}}{\dot{m}_{\text{air}} c_{\text{p,air}}}$ | $T_{\text{air,out}} = 55.08 + \frac{2653}{0.1357 \cdot 1007}$ | | 74.49 | °C |

**Table A-5** Heat exchanger external Nusselt number and pressure drop

| Parameter | Equation | Evaluated | EES Calc. Value | Hand Calc. Value | Units |
|---|---|---|---|---|---|
| Nusselt number external | $Nu_{\text{ext}} = j_{\text{external}} \cdot Re_{\text{ext}} \cdot Pr^{1/3}$ | $Nu_{\text{ext}} = 0.01780 \cdot 440.2 \cdot 0.7031^{1/3}$ | 6.964 | 6.967 | - |
| Coluburn j friction factor external | $j_{\text{external}} = Re_{\text{ext}}{}^{-0.49} \cdot \theta^{0.27} \cdot \frac{Fin_{\text{p,ext}}}{L_{\text{p,ext}}}^{-0.14} \frac{Fin_{\text{L,ext}}}{L_{\text{p,ext}}}^{-0.29} \frac{F_{\text{d,ext}}}{L_{\text{p,ext}}}^{-0.23} \frac{L_{\text{L,ext}}}{L_{\text{p,ext}}}^{0.68} \frac{T_{\text{p,ext}}}{L_{\text{p,ext}}}^{-0.28} \frac{wall_{th}}{L_{\text{p,ext}}}^{-0.05}$ | $j_{\text{external}} = 440.2^{-0.49} \cdot 28/90^{0.27} \cdot \frac{1.337}{1.20}^{-0.14} \frac{14.28}{1.20}^{-0.29} \frac{53.34}{1.20}^{-0.23} \frac{11.42}{1.20}^{0.68} \frac{11.42}{1.20}^{-0.28} \frac{2.0}{1.20}^{-0.05}$ | 0.01782 | 0.01780 | - |
| Fan Speed 10 | $\Delta P_{\text{fan,10}} = 20.436 \cdot x^6 - 147.34 \cdot x^5 + 359.10 \cdot x^4 - 315.06 \cdot x^3 + 23.58 \cdot x^2 - 25.81 \cdot x + 220.4$ | $\Delta P_{\text{fan,10}} = 20.436 \cdot 1.251^6 - 147.34 \cdot 1.251^5 + 359.10 \cdot 1.251^4 - 315.06 \cdot 1.251^3 + 23.58 \cdot 1.251^2 - 25.81 \cdot 1.251 + 220.4$ | 114.60 | 114.59 | Pa |
| $\Delta P_{fan}$ | $\Delta P_{\text{fan}} = \Delta P_{\text{chassis,air}} + \Delta P_{\text{rad,air}}$ | $\Delta P_{\text{fan}} = 41.42 + 73.02$ | 114.60 | 114.44 | Pa |
| $\Delta P_{chassis,air}$ | $\Delta P_{\text{chassis,air}} = 27.990 \cdot x^2 - 1.908 \cdot x + 0$ | $\Delta P_{\text{chassis,air}} = 27.990 \cdot 1.251^2 - 1.908 \cdot 1.251$ | 41.43 | 41.42 | Pa |
| $\Delta P_{hx,air}$ | $\Delta P_{\text{hx,air}} = f_{\text{darcy}} \frac{1}{2} \rho_{\text{hx,air}} v_{\text{hx,air}}{}^2 \left(\frac{Fin_{\text{d,ext}}}{D_{\text{h,ext}}}\right)$ | $\Delta P_{\text{hx,air}} = 0.4235 \frac{1}{2} 1.038 \cdot 3.766^2 \left(\frac{0.05334}{0.002277}\right)$ | 73.13 | 73.02 | Pa |

| Parameter | Equation | Evaluated | EES Calc. Value | Hand Calc. Value | Units |
|---|---|---|---|---|---|
| $f_{darcy,ext}$ | $if\ 0 < Re < 130, then\ f_{\text{darcy}} = 4f_{\text{fanning,lam}}$ $if\ 130 < Re < 260, then\ f_{\text{darcy}} = 4f_{\text{fanning,trans}}$ $if\ 260 < Re < 5000, then\ f_{\text{darcy}} = 4f_{\text{fanning,turb}}$ | $f_{\text{darcy,ext}} = 4 \cdot 0.1059$ | 0.4241 | 0.4235 | - |
| Reynolds number | $Re_{\text{ext}} = \frac{\rho_{\text{rad,air}} D_{\text{h,ext}} v_{\text{rad,air}}}{\mu_{\text{rad,air}}}$ | $Re_{\text{ext}} = \frac{1.038 \cdot 0.002277 \cdot 3.766}{2.022 \cdot 10^{-5}}$ | 440.1 | 440.2 | - |
| Air velocity | $v_{\text{hx,air}} = \frac{\dot{V}_{\text{sCMPS}}}{Area_{\text{ext,tot}}} \frac{\rho_{\text{std,air}}}{\rho_{\text{rad,air}}}$ | $v_{\text{hx,air}} = \frac{0.1251}{0.03473} \frac{1.085}{1.038}$ | 3.766 | 3.766 | m $s^{-1}$ |
| Air hydraulic diameter | $D_{\text{h,ext}} = \frac{4A_{\text{c,ext}}}{P_{\text{w,ext}}}$ | $D_{\text{h,ext}} = \frac{4 \cdot 1.766 \cdot 10^{-5}}{3.103 \cdot 10^{-2}}$ | 2.277e -03 | 2.277e-03 | m |
| Air cross section area | $A_{\text{c,ext}} = \left(Fin_{\text{p,ext}} - Fin_{\text{th,ext}}\right) \cdot Fin_{\text{l,ext}}$ | $A_{\text{c,ext}} = (1.337 - 0.100) \cdot 14.28 \cdot 10^{-6}$ | 1.766e -05 | 1.766e-05 | $m^2$ |
| Air wetted perimeter | $P_{\text{w,ext}} = 2 \cdot (Fin_{\text{l,ext}} + Fin_{\text{p,ext}} - Fin_{\text{th,ext}})$ | $P_{\text{w,ext}} = 2 \cdot (14.28 + 1.337 - 0.1) \cdot 10^{-3}$ | 3.103e -02 | 3.103e-02 | m |
| Air area flow area | $\text{A}_{\text{ext,tot}} = \text{A}_{\text{c,ext}} \cdot (L_{\text{hx,tot}} \cdot FPI_{\text{ext}} \cdot Ch_{\text{ext}})$ | $\text{A}_{\text{ext,tot}} = 1.766 \cdot 10^{-5} \cdot (11.5 \cdot 19 \cdot 9)$ | 3.473e -02 | 3.473e-02 | $m^2$ |
| Friction factor air laminar | $f_{\text{fanning,lam}} = f_{1,\text{lam}} f_{2,\text{lam}} f_{3,\text{lam}}$ | $f_{\text{fanning,lam}} = 18.64 \cdot 0.0096029 \cdot 0.5915$ | 0.1060 | 0.1058 | - |
| Friction factor air turbulent | $f_{\text{fanning,turb}} = f_{1,\text{turb}} f_{2,\text{turb}} f_{3,\text{turb}}$ | $f_{\text{fanning,turb}} = 18.64 \cdot 0.009602 \cdot 0.5915$ | 0.1060 | 0.1059 | - |
| Fins in one channel ext | $fins_{1\text{chan,ext}} = round\left(FPI_{\text{ext}} \cdot\ L_{\text{hx,tot}}\right) - 1$ | $fins_{1\text{chan,ext}} = round(19 \cdot\ 11.5) - 1$ | 217 | 217 | - |

| Parameter | Equation | Evaluated | EES Calc. Value | Hand Calc. Value | Units |
|---|---|---|---|---|---|
| Floor area external | $A_{\text{floor,ext}} = \left(L_{\text{hx,tot}} - Fin_{\text{th.ext}} \cdot fins_{\text{1chan,ext}}\right) \cdot W_{\text{hx,tot}}$ | $A_{\text{floor,ext}} = (0.2921 - 0.0001 \cdot 217) \cdot 0.05334$ | 0.01442 | 0.01442 | m$^2$ |
| Fin area external | $A_{\text{fins,ext}} = 2 \cdot Fin_{\text{L,ext}} \cdot Fin_{\text{d,ext}} \cdot fins_{\text{1chan,ext}} \cdot \frac{1}{2}$ | $A_{\text{fins,ext}} = 2 \cdot 0.01428 \cdot 0.05334 \cdot 217 \cdot \frac{1}{2}$ | 0.1653 | 0.1653 | m$^2$ |
| Wall area | $A_{\text{wall}} = L_{\text{hx,tot}} W_{\text{hx,tot}}$ | $A_{\text{wall}} = 0.2921 \cdot 0.05334$ | 0.01558 | 0.01558 | m$^2$ |
| Air friction factor 1 | $f_{1,\text{lam}} = 4.97 Re_{\text{ext,ch}}^{\;0.6049 - \frac{1.064}{\theta^{0.2}}} \cdot \left( ln\left( 0.9 + \left( \frac{Fin_{\text{th,ext}}}{Fin_{\text{p,ext}}} \right)^{0.5} \right) \right)^{-0.527}$ | $f_{1,\text{lam}} = 4.97 \cdot 440.2^{0.6049 \;\; \frac{1.064}{28^{0.2}}} \cdot \left( ln\left( 0.9 + \left( \frac{0.100}{1.337} \right)^{0.5} \right) \right)^{-0.527}$ | 18.64 | 18.64 | - |
| Air friction factor 2 | $f_{2,\text{lam}} = \left( \frac{D_{\text{h,ext}}}{L_{\text{p,ext}}} \ln\left(0.3 Re_{\text{ext,ch}}\right) \right)^{-2.966} \left( \frac{Fin_{\text{p,ext}}}{L_{\text{i,ext}}} \right)^{-0.7931 \frac{T_{\text{p,ext}}}{T_{\text{h,ext}}}}$ | $f_{2,\text{lam}} = \left( \frac{2.277}{1.200} \ln(0.3 \cdot 440.2) \right)^{-2.966} \left( \frac{1.337}{11.42} \right)^{-0.7931 \frac{11.42}{9.924}}$ | 0.009620 | 0.009602 | - |
| Air friction factor 3 | $f_{3,\text{lam}} = \left( \frac{T_{\text{p,ext}}}{D_{\text{m,ext}}} \right)^{-0.0446} \left( ln\left( 1.2 + \left( \frac{L_{\text{p,ext}}}{Fin_{\text{p,ext}}} \right)^{1.4} \right) \right)^{-3.553} \cdot \theta^{-0.477}$ | $f_{3,\text{lam}} = \left( \frac{11.42}{1.500} \right)^{-0.0446} \left( ln\left( 1.2 + \left( \frac{1.200}{1.337} \right)^{1.4} \right) \right)^{-3.553} \cdot 28^{-0.477}$ | 0.5913 | 0.5915 | - |

**Table A - 6** Thermodynamic cycle

| Parameter | Equation | Evaluated | EES Calc. Value | Hand Calc. Value | Units |
|---|---|---|---|---|---|
| Hot inlet temperature | $Q_{hx} = \varepsilon_{hx} \cdot C_{min} \cdot (T_{h.i} - T_{c,i})$ | $2121.6 = 0.7002 \cdot 136.8 \cdot (T_{h.i} - 55.07)$ | 77.30 | 77.22 | °C |
| Hot outlet temperature | $Q_{hx} = \dot{m}_{liq,tot} \cdot cp_{f,1} \cdot (T_{h.i} - T_{c,o})$ | $2121.6 = 1.286 \cdot 1132 \cdot (77.22 - T_{h,o})$ | 75.12 | 75.05 | °C |
| Number of transfer units | $NTU = \frac{UA_{hx,tot}}{C_{min}}$ | $NTU = \frac{189.0}{136.8}$ | 1.382 | 1.382 | - |
| Heat exchanger UA tot | $UA_{hx,tot} = UA_{hx,ch} \cdot channels_{int} \cdot 2$ | $UA_{hx,tot} = 11.81 \cdot 8 \cdot 2$ | 189 | 189.0 | W K$^{-1}$ |
| 1 channel UA | $UA_{hx,ch} = \frac{1}{R_{hx,tot}}$ | $UA_{hx,ch} = \frac{1}{0.08439}$ | 11.81 | 11.81 | W K$^{-1}$ |
| 1 channel thermal resistance | $R_{hx,tot} = R_{internal} + R_{wall} + R_{external}$ | $R_{hx,tot} = 0.01037 + 0.0008084 + 0.07321$ | 0.0846 5 | 0.0843 9 | K W$^{-1}$ |
| Wall thermal resistance | $R_{wall} = \frac{wall_{th}}{k_{rad}A_{wall}}$ | $R_{wall} = \frac{0.002}{158.8 \cdot 0.01558}$ | 8.084e -04 | 8.084e- 04 | K W$^{-1}$ |
| Total thermal resistance int | $R_{internal} = \left(R_{int,floor}{}^{-1} + R_{int,fins}{}^{-1}\right)^{-1}$ | $R_{internal} = (0.02440^{-1} + 0.01803^{-1})^{-1}$ | 0.0103 6 | 0.0103 7 | K W$^{-1}$ |
| Total thermal resistance ext | $R_{external} = \left(R_{ext,floor}{}^{-1} + R_{ext,fins}{}^{-1}\right)^{-1}$ | $R_{external} = (0.7810^{-1} + 0.08078^{-1})^{-1}$ | 0.0732 3 | 0.0732 1 | K W$^{-1}$ |
| Floor thermal resistance int | $R_{int,floor} = \frac{1}{h_{hx,int}A_{floor,int}}$ | $R_{int,floor} = \frac{1}{3914 \cdot 0.01047}$ | 0.0244 1 | 0.0244 0 | K W$^{-1}$ |
| Fin thermal resistance int | $R_{int,fins} = \frac{1}{\eta_{fins,int}h_{hx,int}A_{fins,int}}$ | $R_{int,fins} = \frac{1}{0.970 \cdot 3914 \cdot 0.01461}$ | 0.0180 1 | 0.0180 3 | K W$^{-1}$ |
| Floor thermal resistance ext | $R_{ext,floor} = \frac{1}{h_{hx,ext}A_{floor,ext}}$ | $R_{ext,floor} == \frac{1}{88.79 \cdot 0.01442}$ | 0.7811 | 0.7810 | K W$^{-1}$ |

| Parameter | Equation | Evaluated | EES Calc. Value | Hand Calc. Value | Units |
|---|---|---|---|---|---|
| Fin thermal resistance ext | $R_{\text{ext,fins}} = \frac{1}{\eta_{\text{fins,ext}} h_{\text{hx,ext}} A_{\text{fins,ext}}}$ | $R_{\text{ext,fins}} = \frac{1}{0.8434 \cdot 88.79 \cdot 0.1653}$ | 0.08081 | 0.08078 | K W$^{-1}$ |
| Heat transfer coefficient internal | $h_{\text{hx,int}} = \frac{Nu_{\text{int}} k_{\text{f,1}}}{D_{\text{h,int}}}$ | $h_{\text{hx,int}} = \frac{90.24 \cdot 0.05175}{0.001193}$ | 3913 | 3914 | W m$^{-2}$ K$^{-1}$ |
| Fin efficiency internal | $\eta_{\text{fins,int}} = \frac{\tanh(mL_{c,hx,int})}{mL_{c,hx,int}}$ | $\eta_{\text{fins,int}} = \frac{\tanh(313.99 \cdot 0.000965)}{313.99 \cdot 0.000965}$ | 0.971 | 0.970 | - |
| Fin efficiency constant internal | $m_{\text{hx,int}} = \sqrt{\frac{2h_{\text{hx,int}}}{k_{\text{alum}} fin_{\text{th}}}}$ | $m_{\text{hx,int}} = \sqrt{\frac{2 \cdot 3914}{158.8 \cdot 0.0005}}$ | 313.99 | 313.99 | m |
| Fin characteristic length internal | $L_{c,\text{hx,int}} = L/2 + fin_{\text{th,int}}/2$ | $L_{c,\text{hx,int}} = 0.00143/2 + 0.0005/2$ | 0.000965 | 0.000965 | m |
| Heat transfer coefficient external | $h_{\text{hx,ext}} = \frac{Nu_{ext} k_{\text{air}}}{D_{\text{h,ext}}}$ | $h_{\text{hx,ext}} = \frac{6.967 \cdot 0.02902}{0.002277}$ | 88.77 | 88.79 | W m$^{-2}$ K$^{-1}$ |
| Fin efficiency external | $\eta_{\text{fins,ext}} = \frac{\tanh(mL_{c,hx,ext})}{mL_{c,hx,ext}}$ | $\eta_{\text{fins,ext}} = \frac{\tanh(105.75 \cdot 0.00719)}{105.75 \cdot 0.00719}$ | 0.8434 | 0.8434 | - |
| Fin efficiency constant external | $m_{\text{hx,ext}} = \sqrt{\frac{2h_{\text{hx,int}}}{k_{\text{alum}} fin_{\text{th}}}}$ | $m_{\text{hx,ext}} = \sqrt{\frac{2 \cdot 88.79}{158.8 \cdot 0.0001}}$ | 105.75 | 105.75 | m |
| Fin characteristic length external | $L_{c,\text{hx,ext}} = L/2 + fin_{\text{th,ext}}/2$ | $L_{c,\text{hx,ext}} = 0.01428/2 + 0.0001/2$ | 0.00719 | 0.00719 | m |

| Parameter | Equation | Evaluated | EES Calc. Value | Hand Calc. Value | Units |
|---|---|---|---|---|---|
| Nusselt number internal | $Nu_{\text{int}} = \left\{ Nu_{\text{lam}}{}^{10} + \left\{ \frac{e^{2200- \quad \text{int}}}{365 \cdot Nu_{\text{lam}}} + \left( Nu_{\text{o}} + \frac{0.079 Re_{\text{int}} \cdot Pr_{\text{HEXI}} (f_{\text{darcy}}/8)^{1/2}}{(1 + Pr_{\text{HEXI}}{}^{0.8})^{5/6}} \right)^{-2} \right\}^{-5} \right\}^{0.1}$ | $Nu_{\text{int}} = \left\{ 4.709^{10} + \left\{ \frac{e^{2200-5761}}{365 \cdot 4.709} + \left( 6.3 + \frac{0.079 \cdot 5761 \cdot 9.679 (0.03689/8)^{1}}{(1 + 9.603^{0.8})^{5/6}} \right. \right. \right.$ | 90.24 | 90.24 | - |
| Laminar Nusselt Number | $Nu_{\text{lam}} = 8.235(1 - 2.0421 \cdot \alpha_{\text{int}} + 3.0853 \cdot \alpha_{\text{int}}{}^{2} - 2.4765 \cdot \alpha_{\text{int}}{}^{3} + 1.5078 \cdot \alpha_{\text{int}}{}^{4} - 0.1861 \cdot \alpha_{\text{int}}{}^{5})$ | $Nu_{\text{lam}} = 8.235(1 - 2.0421 \cdot 0.7161 + 3.0853 \cdot 0.7161^{2} - 2.4765 \cdot 0.7161^{3} + 1.5078 \cdot 0.7161^{4} - 0.1861 \cdot 0.7161^{5})$ | 4.709 | 4.709 | - |
| Nusselt number constant 0 | $Nu_{o} = 6.3$ | $Nu_{o} = 6.3$ | 6.3 | 6.3 | - |
| Darcy friction factor internal | $f_{\text{darcy,int}} = f_{\text{turb}}$ $\frac{0.3164}{Re_{\text{int}}{}^{0.25}} (1.0875 - 0.1125 \cdot \alpha_{\text{int}})$ | $f_{\text{darcy,int}} = \frac{0.3164}{9194^{0.25}} (1.0875 - 0.1125 \cdot 0.7161)$ | 0.0325 4 | 0.0332 54 | - |
| Reynolds number internal | $Re_{\text{int}} = \frac{\rho_{\text{f,1}} v_{\text{f,1}} D_{\text{h,int}}}{\mu_{\text{f,1}}}$ | $Re_{\text{int}} = \frac{1538 \cdot 2.040 \cdot 1.193 \cdot 10^{-3}}{0.0004071}$ | 9193 | 9194 | - |

| Parameter | Equation | Evaluated | EES Calc. Value | Hand Calc. Value | Units |
|---|---|---|---|---|---|
| Fluid Velocity internal | $v_{\text{HEXI}} = \frac{\dot{m}_{\text{liq,tot}}}{\rho_{\text{f,1}} \cdot A_{\text{flow,int}}}$ | $v_{\text{HEXI}} = \frac{1.286}{1538 \cdot 4.099 \cdot 10^{-4}}$ | 2.031 | 2.040 | m $s^{-1}$ |
| Flow area internal | $A_{\text{flow,int}} = A_{\text{c,int}} \cdot fins_{\text{1chan,int}} \cdot Int_{\text{chans}}$ | $A_{\text{flow,int}} = 1.464 \cdot 10^{-6} \cdot 35 \cdot 8$ | 4.1e-04 | 4.099e-04 | $m^2$ |
| Aspect ratio internal | $\alpha_{\text{int}} = \frac{H_{\text{hx,1,int}}}{W_{\text{hx,1,int}}}$ | $\alpha_{\text{int}} = \frac{1.024}{1.43}$ | 0.7161 | 0.7161 | - |
| Hydraulic diameter internal | $D_{\text{h,int}} = \frac{4A_{\text{c,int}}}{P_{\text{wet}}} = \frac{4 \cdot (W_{\text{hx,1,int}} \cdot H_{\text{hx,1,int}})}{2 \cdot (W_{\text{hx,1,int}} + H_{\text{hx,1,int}})}$ | $D_{\text{h,int}} = \frac{4 \cdot (1.464 \cdot 10^{-6})}{2 \cdot (1.024 + 1.43) \cdot 10^{-3}}$ | 1.193e-03 | 1.193e-03 | m |
| Cross sectional flow area internal | $A_{\text{c,int}} = (W_{\text{hx,1,int}} \cdot H_{\text{hx,1,int}})$ | $A_{\text{c,int}} = (1.024 \cdot 1.43 \cdot 10^{-6})$ | 1.464e-06 | 1.464e-06 | $m^2$ |
| Floor area area (1 chan) internal | $A_{\text{floor,int}} = W_{\text{hx,1,int}} \cdot L_{\text{hx,tot}} \cdot fins_{\text{1chan,int}}$ | $A_{\text{floor,int}} = 1.024 \cdot 10^{-3} \cdot 0.2921 \cdot 35$ | 0.01047 | 0.01047 | $m^2$ |
| Fin area (1 chan) internal | $A_{\text{fins,int}} = 2 \cdot H_{\text{hx,1,int}} \cdot L_{\text{hx,tot}} \cdot fins_{\text{1chan,int}} \cdot \frac{1}{2}$ | $A_{\text{fins,int}} = 2 \cdot 1.43 \cdot 10^{-3} \cdot 0.2921 \cdot 35 \cdot \frac{1}{2}$ | 0.01462 | 0.01461 | $m^2$ |
| Width single box internal | $W_{\text{hx,1,int}} = \left(W_{\text{hx,tot}} - fins_{\text{1chan,int}} \cdot Fin_{\text{th,int}}\right)/fins_{\text{1chan,int}}$ | $W_{\text{hx,1,int}} = (0.05334 - 35 \cdot 0.0005)/35$ | 1.024e-03 | 1.024e-03 | m |
| Hieght single box internal | $H_{\text{hx,1,int}} = fin_{\text{l,int}}$ | $H_{\text{hx,1,int}} = 1.43 \cdot 10^{-3}$ | 1.43e-03 | 1.43e-03 | m |
| Fins in one channel | $fins_{\text{1chan,int}} = round\left(FPI_{\text{int}} \cdot W_{\text{hx,tot}}\right) - 1$ | $fins_{\text{1chan,int}} = round(17 \cdot 2.1) - 1$ | 35 | 35 | - |
| Temp fluid statepoint 6 | $Q_{\text{sys}} = \dot{m}_{\text{liq,tot}} \cdot cp_{f,5} \cdot \left(T_{\text{f,6}} - T_{\text{f,5}}\right)$ | $2121.6 = 1.286 \cdot 1131 \cdot \left(T_{\text{f,6}} - 73.56\right)$ | 75.02 | 75.02 | °C |

**Table A - 7** Heat sink performance, FC72 configuration d)

| Parameter | Equation | Evaluated | EES Calc. Value | Hand Calc. Value | Units |
|---|---|---|---|---|---|
| Temp fluid 6, 1 | $Q_{\text{chip,act,1}} \cdot Percent.back = \dot{m}_{\text{chip,1}} \cdot cp_{f,5} \cdot (T_{\text{f,5}} - T_{\text{f,6,1}})$ | $161.0 \cdot 80\% = 0.05273 \cdot 1131(T_{\text{f,6,1}} - 73.56)$ | 75.73 | 75.73 | ℃ |
| Temp fluid 6, 2 | $Q_{\text{chip,act,2}} \cdot Percent.back = \dot{m}_{\text{chip,2}} \cdot cp_{f,5} \cdot (T_{\text{f,5}} - T_{\text{f,6,2}})$ | $58.4 \cdot 80\% = 0.04168 \cdot 1131(T_{\text{f,6,1}} - 73.56)$ | 74.52 | 74.52 | ℃ |
| Temp fluid 6, 4 | $Q_{\text{chip,act,4}} \cdot Percent.back = \dot{m}_{\text{chip,4}} \cdot cp_{f,5} \cdot (T_{\text{f,5}} - T_{\text{f,6,4}})$ | $150 \cdot 80\% = 0.110 \cdot 1131(T_{\text{f,6,1}} - 73.56)$ | 74.53 | 74.53 | ℃ |
| $T_s$ chip 1 | $LMTD_1 = \frac{(T_{\text{chip,s,1}} - T_{f,5}) - (T_{\text{chip,s,1}} - T_{\text{f,6,1}})}{ln\left(\frac{(T_{\text{chip,s,1}} - T_{\text{f,5}})}{(T_{\text{chip,s,1}} - T_{\text{f,6,1}})}\right)}$ | $10.32 = \frac{(T_{\text{chip,s,1}} - 73.56) - (T_{\text{chip,s,1}} - 75}{ln\left(\frac{(T_{\text{chip,s,1}} - 73.56)}{(T_{\text{chip,s,1}} - 75.73)}\right)}$ | 84.96 | 85.00 | K |
| $T_s$ chip 2 | $LMTD_2 = \frac{(T_{\text{chip,s,2}} - T_{f,5}) - (T_{\text{chip,s,2}} - T_{\text{f,6,2}})}{ln\left(\frac{(T_{\text{chip,s,2}} - T_{\text{f,5}})}{(T_{\text{chip,s,2}} - T_{\text{f,6,2}})}\right)}$ | $4.91 = \frac{(T_{\text{chip,s,2}} - 73.56) - (T_{\text{chip,s,2}} - 74}{ln\left(\frac{(T_{\text{chip,s,2}} - 73.56)}{(T_{\text{chip,s,2}} - 74.52)}\right)}$ | 78.79 | 78.97 | K |
| $T_s$ chip 4 | $LMTD_4 = \frac{(T_{\text{chip,s,4}} - T_{f,5}) - (T_{\text{chip,s,4}} - T_{\text{f,6,4}})}{ln\left(\frac{(T_{\text{chip,s,4}} - T_{\text{f,5}})}{(T_{\text{chip,s,4}} - T_{\text{f,6,4}})}\right)}$ | $29.94 = \frac{(T_{\text{chip,s,4}} - 73.56) - (T_{\text{chip,s,4}} - 74}{ln\left(\frac{(T_{\text{chip,s,4}} - 73.56)}{(T_{\text{chip,s,4}} - 74.53)}\right)}$ | 104 | 104.0 | K |
| LMTD chip 1 | $Q_{\text{chip,act,1}} \cdot Percent.back = UA_{\text{hs,1}} \cdot LMTD_1$ | $161.0 \cdot 80\% = 12.48 \cdot LMTD_1$ | 10.28 | 10.32 | K |
| LMTD chip 2 | $Q_{\text{chip,act,2}} \cdot Percent.back = UA_{\text{hs,2}} \cdot LMTD_2$ | $58.4 \cdot 80\% = 9.515 \cdot LMTD_2$ | 4.73 | 4.91 | K |

| Parameter | Equation | Evaluated | EES Calc. Value | Hand Calc. Value | Units |
|---|---|---|---|---|---|
| LMTD chip 4 | $Q_{\mathrm{chip,act,4}} \cdot Percent.back = UA_{\mathrm{hs,4}} \cdot LMTD_4$ | $150 \cdot 80\% = 4.008 \cdot LMTD_4$ | 29.92 | 29.94 | K |
| UA chip 1 | $UA_{\mathrm{hs,1}} = \frac{1}{R_{\mathrm{tot,1}}}$ | $UA_{\mathrm{hs,1}} = \frac{1}{0.0801}$ | 12.52 | 12.48 | W K$^{-1}$ |
| UA chip 2 | $UA_{\mathrm{hs,2}} = \frac{1}{R_{\mathrm{tot,2}}}$ | $UA_{\mathrm{hs,2}} = \frac{1}{0.1051}$ | 9.542 | 9.515 | W K$^{-1}$ |
| UA chip 4 | $UA_{\mathrm{hs,4}} = \frac{1}{R_{\mathrm{tot,4}}}$ | $UA_{\mathrm{hs,4}} = \frac{1}{0.2495}$ | 4.011 | 4.008 | W K$^{-1}$ |
| Thermal resistance chip 1 | $R_{\mathrm{tot,1}} = \frac{1}{h_{\mathrm{hs,1}} A_{\mathrm{die,1}}}$ | $R_{\mathrm{tot,1}} = \frac{1}{25787 \cdot 0.000484}$ | 0.0798 5 | 0.0801 | K W$^{-1}$ |
| Thermal resistance chip 2 | $R_{\mathrm{tot,2}} = \frac{1}{h_{\mathrm{hs,2}} A_{\mathrm{die,2}}}$ | $R_{\mathrm{tot,2}} = \frac{1}{25808 \cdot 0.00036864}$ | 0.1048 | 0.1051 | K W$^{-1}$ |
| Thermal resistance chip 4 | $R_{\mathrm{tot,4}} = \frac{1}{h_{\mathrm{hs,4}} A_{\mathrm{die,2}}} + R_{\mathrm{jc,4}}$ | $R_{\mathrm{tot,4}} = \frac{1}{25787 \cdot 0.000784} + 0.20$ | 0.2493 | 0.2495 | K W$^{-1}$ |
| Heat transfer coefficient 1 | $h_{\mathrm{hs,1}} = \frac{Nu_{\mathrm{j,1}} k_{\mathrm{f,5}}}{D_{j,1}}$ | $h_{\mathrm{hs,1}} = \frac{124.6 \cdot 0.05174}{0.000250}$ | 25876 | 25787 | W m$^{-2}$ K$^{-1}$ |
| Heat transfer coefficient 2 | $h_{\mathrm{hs,2}} = \frac{Nu_{\mathrm{j,2}} k_{\mathrm{f,5}}}{D_{\mathrm{j,2}}}$ | $h_{\mathrm{hs,2}} = \frac{124.7 \cdot 0.05174}{0.000250}$ | 25886 | 25808 | W m$^{-2}$ K$^{-1}$ |
| Heat transfer coefficient 4 | $h_{\mathrm{hs,4}} = \frac{Nu_{\mathrm{j,4}} k_{\mathrm{f,5}}}{D_{\mathrm{j,4}}}$ | $h_{\mathrm{hs,4}} = \frac{124.6 \cdot 0.05174}{0.000250}$ | 25875 | 25787 | W m$^{-2}$ K$^{-1}$ |

| Parameter | Equation | Evaluated | EES Calc. Value | Hand Calc. Value | Units |
|---|---|---|---|---|---|
| Nusselt number chip 1 | $Nu_{\text{chip},1} = {Pr_{\text{Impi}}}^{0.29} \cdot 10\char`^ \left\{ \sum_{j=1}^{20} a_j {Re_{j,1}}^{b_j} (SD)^{c_j} (HD)^{d_j} \right\}$ | $Nu_{\text{chip},1} = 8.92^{0.29} \cdot 10\char`^ \left\{ \sum_{j=1}^{20} a_j 11284^{b_j} (10)^{c_j} (1)^{d_j} \right\}$ | 124.6 | 124.6 | - |
| Nusselt number chip 2 | $Nu_{\text{chip},2} = {Pr_{\text{Impi}}}^{0.29} \cdot 10\char`^ \left\{ \sum_{j=1}^{20} a_j {Re_{j,2}}^{b_j} (SD)^{c_j} (HD)^{d_j} \right\}$ | $Nu_{\text{chip},2} = 8.92^{0.29} \cdot 10\char`^ \left\{ \sum_{j=1}^{20} a_j 7279^{b_j} (10)^{c_j} (1)^{d_j} \right\}$ | 124.7 | 124.7 | - |
| Nusselt number chip 4 | $Nu_{\text{chip},4} = {Pr_{\text{Impi}}}^{0.29} \cdot 10\char`^ \left\{ \sum_{j=1}^{20} a_j {Re_{j,4}}^{b_j} (SD)^{c_j} (HD)^{d_j} \right\}$ | $Nu_{\text{chip},4} = 8.92^{0.29} \cdot 10\char`^ \left\{ \sum_{j=1}^{20} a_j 7862^{b_j} (10)^{c_j} (1)^{d_j} \right\}$ | 124.6 | 124.6 | - |
| Reynolds number jet 1 | $Re_{\text{j},1} = \frac{\rho_{\text{fluid},5} v_{\text{j},1} D_{\text{j},1}}{\mu_{\text{fluid},5}}$ | $Re_{\text{j},1} = \frac{1544 \cdot 8.589 \cdot 250 \cdot 10^{-6}}{0.0003943}$ | 8407 | 8408 | - |
| Reynolds number jet 2 | $Re_{\text{j},2} = \frac{\rho_{\text{fluid},5} v_{\text{j},2} D_{\text{j},2}}{\mu_{\text{fluid},5}}$ | $Re_{\text{j},2} = \frac{1544 \cdot 8.591 \cdot 250 \cdot 10^{-6}}{0.0003943}$ | 8410 | 8410 | - |
| Reynolds number jet 4 | $Re_{\text{j},4} = \frac{\rho_{\text{fluid},5} v_{\text{j},4} D_{\text{j},4}}{\mu_{\text{fluid},5}}$ | $Re_{\text{j},4} = \frac{1544 \cdot 8.588 \cdot 250 \cdot 10^{-6}}{0.0003943}$ | 8406 | 8407 | - |
| Jet velocity 1 | $v_{\text{j},1} = \frac{\dot{V}_{\text{chip},1}}{\pi/4 \cdot {D_{\text{j},1}}^2} \frac{1}{N_{\text{jets},1}}$ | $v_{\text{j},1} = \frac{3.415 \cdot 10^{-5}}{\pi/4 \cdot 0.000250^2} \frac{1}{81}$ | 8.566 | 8.589 | $\text{m s}^{-1}$ |
| Jet velocity 2 | $v_{\text{j},2} = \frac{\dot{V}_{\text{chip},2}}{\pi/4 \cdot {D_{\text{j},2}}^2} \frac{1}{N_{\text{jets},2}}$ | $v_{\text{j},2} = \frac{2.699 \cdot 10^{-5}}{\pi/4 \cdot 0.000250^2} \frac{1}{64}$ | 8.569 | 8.591 | $\text{m s}^{-1}$ |

| Parameter | Equation | Evaluated | EES Calc. Value | Hand Calc. Value | Units |
|---|---|---|---|---|---|
| Nusselt number chip 1 | $Nu_{\text{chip,1}} = {Pr_{\text{Impi}}}^{0.29} \cdot 10^\wedge \left\{ \sum_{j=1}^{20} a_j {Re_{j,1}}^{b_j} (SD)^{c_j} (HD)^{d_j} \right\}$ | $Nu_{\text{chip,1}} = 8.92^{0.29} \cdot 10^\wedge \left\{ \sum_{j=1}^{20} a_j 11284^{b_j} (10)^{c_j} (1)^{d_j} \right\}$ | 124.6 | 124.6 | - |
| Nusselt number chip 2 | $Nu_{\text{chip,2}} = {Pr_{\text{Impi}}}^{0.29} \cdot 10^\wedge \left\{ \sum_{j=1}^{20} a_j {Re_{j,2}}^{b_j} (SD)^{c_j} (HD)^{d_j} \right\}$ | $Nu_{\text{chip,2}} = 8.92^{0.29} \cdot 10^\wedge \left\{ \sum_{j=1}^{20} a_j 7279^{b_j} (10)^{c_j} (1)^{d_j} \right\}$ | 124.7 | 124.7 | - |
| Nusselt number chip 4 | $Nu_{\text{chip,4}} = {Pr_{\text{Impi}}}^{0.29} \cdot 10^\wedge \left\{ \sum_{j=1}^{20} a_j {Re_{j,4}}^{b_j} (SD)^{c_j} (HD)^{d_j} \right\}$ | $Nu_{\text{chip,4}} = 8.92^{0.29} \cdot 10^\wedge \left\{ \sum_{j=1}^{20} a_j 7862^{b_j} (10)^{c_j} (1)^{d_j} \right\}$ | 124.6 | 124.6 | - |
| Reynolds number jet 1 | $Re_{\text{j,1}} = \frac{\rho_{\text{fluid,5}} v_{\text{j,1}} D_{\text{j,1}}}{\mu_{\text{fluid,5}}}$ | $Re_{\text{j,1}} = \frac{1544 \cdot 8.589 \cdot 250 \cdot 10^{-6}}{0.0003943}$ | 8407 | 8408 | - |
| Reynolds number jet 2 | $Re_{\text{j,2}} = \frac{\rho_{\text{fluid,5}} v_{\text{j,2}} D_{\text{j,2}}}{\mu_{\text{fluid,5}}}$ | $Re_{\text{j,2}} = \frac{1544 \cdot 8.591 \cdot 250 \cdot 10^{-6}}{0.0003943}$ | 8410 | 8410 | - |
| Reynolds number jet 4 | $Re_{\text{j,4}} = \frac{\rho_{\text{fluid,5}} v_{\text{j,4}} D_{\text{j,4}}}{\mu_{\text{fluid,5}}}$ | $Re_{\text{j,4}} = \frac{1544 \cdot 8.588 \cdot 250 \cdot 10^{-6}}{0.0003943}$ | 8406 | 8407 | - |
| Jet velocity 1 | $v_{\text{j,1}} = \frac{\dot{V}_{\text{chip,1}}}{\pi/4 \cdot {D_{\text{j,1}}}^2} \frac{1}{N_{\text{jets,1}}}$ | $v_{\text{j,1}} = \frac{3.415 \cdot 10^{-5}}{\pi/4 \cdot 0.000250^2} \frac{1}{81}$ | 8.566 | 8.589 | m s$^{-1}$ |
| Jet velocity 2 | $v_{\text{j,2}} = \frac{\dot{V}_{\text{chip,2}}}{\pi/4 \cdot {D_{\text{j,2}}}^2} \frac{1}{N_{\text{jets,2}}}$ | $v_{\text{j,2}} = \frac{2.699 \cdot 10^{-5}}{\pi/4 \cdot 0.000250^2} \frac{1}{64}$ | 8.569 | 8.591 | m s$^{-1}$ |

**Table A-8** Microchannel cooling heat transfer and thermodynamic calculations configuration 3-5a

| Parameter | Equation | Evaluated | EES Calc. Value | Hand Calc. Value | Units |
|---|---|---|---|---|---|
| $T_s$ chip cold plate | Cannot be calculated because the chip temperature will overheat with the current fans at 50°C ambient | | | | |
| LMTD chip 1 cold plate | $Q_{\text{chip,act,1}} \cdot Percent.back = UA_{\text{cp}} \cdot LMTD_{1,\text{cp}}$ | $160 \cdot 80\% = 7.547 \cdot LMTD_4$ | 16.98 | 16.96 | K |
| UA chip 1 cold plate | $UA_{\text{cp}} = \frac{1}{R_{\text{tot,cp}}}$ | $UA_{\text{cp}} = \frac{1}{0.1325}$ | 7.558 | 7.547 | $W\,K^{-1}$ |
| Total thermal resistance cp | $R_{\text{tot,cp}} = R_{\text{jc,1}} + R_{\text{TIM,2}} + R_{\text{conv,cp}}$ | $R_{\text{tot,cp}} = 0.10 + 0.02217 + 0.01033$ | 0.1397 | 0.1325 | $K\,W^{-1}$ |
| TIM 2 thermal resistance | $R_{\text{TIM,2}} = \frac{th_{\text{TIM,2}}}{k_{\text{TIM,2}} A_{\text{TIM,2}}}$ | $R_{\text{TIM,2}} = \frac{150 \cdot 10^{-6}}{2 \cdot (53.1 \cdot 10^{-3})^2}$ | 0.02217 | 0.02217 | $K\,W^{-1}$ |
| Cp conduction Rth | $R_{\text{cond,cp}} = \frac{th_{\text{cp}}}{k_{\text{cp}} A_{\text{cp}}}$ | $R_{\text{cond,cp}} = \frac{3000 \cdot 10^{-6}}{395 \cdot (25.4 \cdot 10^{-3})^2}$ | 0.01177 | 0.01177 | $K\,W^{-1}$ |
| Cp convection Rth | $R_{\text{conv,cp}} = \frac{1}{h_{\text{micro,avg}} A_{\text{s,hs}}}$ | $R_{\text{conv,cp}} = \frac{1}{17435 \cdot 0.005551}$ | 0.01049 | 0.01033 | $K\,W^{-1}$ |
| Surface area cold plate | $A_{\text{s,cp}} = \eta_{\text{cp}} \cdot A_{\text{s,fin,cp}} + A_{\text{s,floor,cp}}$ | $A_{\text{s,cp}} = 0.3322 \cdot 2 \cdot 62(0.00508 \cdot 0.0254) + 62(0.000150 \cdot 0.0254)$ | 0.005641 | 0.005551 | $m^2$ |
| Fin efficiency cold plate | $\eta_{\text{cp}} = \frac{\tanh(mL_{c,\text{hs}})}{mL_{c,\text{hs}}}$ | $\eta_{\text{cp}} = \frac{\tanh(589.54 \cdot 0.00508)}{589.54 \cdot 0.00508}$ | 0.3378 | 0.3322 | - |
| Fin efficiency constant cold plate | $m_{\text{cp}} = \sqrt{\frac{2h_{\text{micro,avg}}}{k_{\text{copper}} th_{\text{fin,hs}}}}$ | $m_{\text{cp}} = \sqrt{\frac{2 \cdot 17435}{395 \cdot 0.000254}}$ | 580.37 | 589.54 | m |
| Fin char length cp | $L_{c,\text{cp}} = H_{\text{ch,hs}} + th_{\text{fin,hs}}/2$ | $L_{c,\text{cp}} = 0.004953 + 0.000254/2$ | 0.00508 | 0.00508 | m |

| Parameter | Equation | Evaluated | EES Calc. Value | Hand Calc. Value | Units |
|---|---|---|---|---|---|
| Htc average cp | $h_{\text{cp,avg}} = \frac{Nu_{3,\text{avg}} \cdot k_{\text{f},5}}{D_{\text{h,ch,hs}}}$ | $h_{\text{cp,avg}} = \frac{8.050 \cdot 0.6307}{0.0002912}$ | 16897 | 17435 | W m^-1 K^-1 |
| Developing 3 channel Nu | $Nu_{3,\text{avg}} = Nu_{3,\text{ch,fd}} + \frac{1}{L_{\text{fin}}} \int_0^{L_{\text{fin}}} 8.68 \left(1000 \cdot \frac{z}{Re_{\text{ch}} D_{\text{h,ch,hs}} Pr_5}\right)^{-0.506} exp\left[(-9.427\alpha - 23.472) \cdot \frac{z}{Re_{\text{ch}} D_{\text{h,ch,hs}} Pr_5}\right] dz$ | $Nu_{3,\text{avg}} = 7.793 + \frac{1}{0.0254} \int_0^{0.0254} 8.68 \left(1000 \cdot \frac{z}{Re_{\text{ch}} D_{\text{h,ch,hs}} Pr_5}\right)^{-0.506} exp\left[(-9.427\alpha - 23.472) \cdot \frac{z}{Re_{\text{ch}} D_{\text{h,ch,hs}} Pr_5}\right] dz$ | 7.861 | 8.050 | - |
| Fully dev 3 channel Nu | $Nu_{3,\text{ch,fd}} = 8.235(1 - 1.883 \cdot \alpha + 3.767 \cdot \alpha^2 - 5.814 \cdot \alpha^3 + 5.361 \cdot \alpha^4 - 2.0 \cdot \alpha^5)$ | $Nu_{3,\text{ch,fd}} = 8.235(1 - 1.883 \cdot 0.03028 + 3.767 \cdot 0.03028^2 - 5.814 \cdot 0.03028^3 + 5.361 \cdot 0.03028^4 - 2.0 \cdot 0.03028^5)$ | 7.793 | 7.793 | - |
| Aspect ratio | $\alpha = \frac{th_{\text{ch,hs}}}{H_{\text{ch,hs}}}$ | $\alpha = \frac{150}{4953}$ | 0.03028 | 0.03028 | - |
| Reynolds number ch | $Re_{\text{ch}} = \frac{\rho_{\text{fluid},5} v_{\text{ch}} D_{\text{h,ch,hs}}}{\mu_{\text{fluid},5}}$ | $Re_{\text{ch}} = \frac{992 \cdot 0.4377 \cdot 0.0002912}{0.0004053}$ | 306.6 | 312.0 | - |
| Wall velocity | $v_{\text{ch}} = \frac{\dot{V}_{\text{chip},1}}{H_{\text{ch,hs}} \cdot th_{\text{ch,hs}}} \frac{1}{N_{\text{ch},1}}$ | $v_{\text{ch}} = \frac{2.016 \cdot 10^{-5}}{4953 \cdot 150 \cdot 10^{-12}} \frac{1}{62}$ | 0.4377 | 0.4377 | m s^-1 |
| Volumetric flow rate 1 | $\dot{V}_{\text{chip}} = \frac{\dot{m}_{\text{chip},1}}{\rho_{\text{fluid},5}}$ | $\dot{V}_{\text{chip}} = \frac{0.020}{992}$ | 2.016e-05 | 2.016e-05 | m^3 s^-1 |

| Parameter | Equation | Evaluated | EES Calc. Value | Hand Calc. Value | Units |
|---|---|---|---|---|---|
| Number of channels | $N_{\mathrm{ch}} = trunc\left(\frac{W_{\mathrm{micro}} - th_{\mathrm{fin,hs}}}{th_{\mathrm{fin,hs}} + th_{\mathrm{ch,hs}}}\right)$ | $N_{\mathrm{ch}} = trunc\left(\frac{25.4 - 0.254}{0.254 + 0.150}\right)$ | 62 | 62 | - |
| Cold plate hydraulic diameter | $D_{\mathrm{ch}} = \frac{4 \cdot A_{\mathrm{ch}}}{P_{\mathrm{w,ch}}}$ | $D_{\mathrm{ch}} = \frac{4 \cdot (4953 \cdot 150 \cdot 10^{-12})}{2 \cdot (4953 + 150) \cdot 10^{-6}}$ | 0.0002 912 | 0.0002 912 | m |

**Table A-9** FC72 Pressure drop configuration 3-5d

| Parameter | Equation | Evaluated | EES Calc. Value | Hand Calc. Value | Units |
|---|---|---|---|---|---|
| Manifolding total $\Delta P$ | $\Delta P_{\mathrm{mani,tot}} = \Delta P_{\frac{\mathrm{in}}{\mathrm{out}},\mathrm{tot}} + 2 \cdot \Delta P_{\mathrm{mani,1}} + 2 \cdot \Delta P_{\mathrm{mani,2}} + 2 \cdot \Delta P_{\mathrm{tube,chip,tot}}$ | $\Delta P_{\mathrm{mani,tot}} = 2.879 + +2 \cdot 2.753 + 2 \cdot 6.88 + 1.139$ | 23.57 (3.42) | 24.42 (3.54) | kPa (psi) |
| Total jet $\Delta P$ | $\Delta P_{\mathrm{j,tot}} = \frac{1}{\dot{m}_{\mathrm{tot}}}(\sum_{i=1}^{2} N_{\mathrm{chip,i}} \cdot \Delta P_{\mathrm{j,i}} \cdot \dot{m}_{\mathrm{chip,i}} + \sum_{i=4}^{4} N_{\mathrm{chip,i}} \cdot \Delta P_{\mathrm{j,i}} \cdot \dot{m}_{\mathrm{chip,i}})$ | $\Delta P_{\mathrm{j,tot}} = \frac{1}{1.256}(\sum_{i=1}^{2} N_{\mathrm{chip,i}} \cdot \Delta P_{\mathrm{j,i}} \cdot \dot{m}_{\mathrm{chip,i}} + \sum_{i=4}^{4} N_{\mathrm{chip,i}} \cdot \Delta P_{\mathrm{j,i}} \cdot \dot{m}_{\mathrm{chip,i}})$ | 146.0 (21.18 ) | 154.5 (22.41) | kPa (psi) |
| Chip 1 $\Delta P$ | $\Delta P_{\mathrm{j,1}} = k_{j,1} \frac{1}{2} \rho_{\mathrm{f,1}} v_{\mathrm{j,1}}{}^2 / 30\%$ | $\Delta P_{\mathrm{j,1}} = 0.8139 \frac{1}{2} 1544 \cdot 8.451^2 / (0.3 \cdot 1000)$ | 141.4 (20.51 ) | 149.6 (21.70) | kPa (psi) |
| Chip 2 $\Delta P$ | $\Delta P_{\mathrm{j,2}} = k_{j,2} \frac{1}{2} \rho_{\mathrm{f,1}} v_{\mathrm{j,2}}{}^2 / 30\%$ | $\Delta P_{\mathrm{j,1}} = 0.8139 \frac{1}{2} 1544 \cdot 8.454^2 / (0.3 \cdot 1000)$ | 141.5 (20.52 ) | 149.7 (21.71) | kPa (psi) |
| Chip 4 $\Delta P$ | $\Delta P_{\mathrm{j,4}} = k_{j,4} \frac{1}{2} \rho_{\mathrm{f,1}} v_{\mathrm{j,4}}{}^2 / 30\%$ | $\Delta P_{\mathrm{j,1}} = 0.8139 \frac{1}{2} 1544 \cdot 8.448^2 / (0.3 \cdot 1000)$ | 141.4 (20.51 ) | 149.5 (21.68) | kPa (psi) |

| Parameter | Equation | Evaluated | EES Calc. Value | Hand Calc. Value | Units |
|---|---|---|---|---|---|
| Jet k factor Chip 1 | $k_{\text{j,1}} = 10\text{^}\left\{\sum_{j=1}^{20} a_j {Re_{j,1}}^{b_j}(SD)^{c_j}(HD)^{d_j}\right\}$ | $k_{\text{j,1}} = 10\text{^}\left\{\sum_{j=1}^{20} a_j 8290^{b_j}(8)^{c_j}(1)^{d_j}\right\}$ | 0.7715 | 0.8139 | - |
| Jet k factor Chip 2 | $k_{\text{j,2}} = 10\text{^}\left\{\sum_{j=1}^{20} a_j {Re_{j,2}}^{b_j}(SD)^{c_j}(HD)^{d_j}\right\}$ | $k_{\text{j,2}} = 10\text{^}\left\{\sum_{j=1}^{20} a_j 8293^{b_j}(8)^{c_j}(1)^{d_j}\right\}$ | 0.7715 | 0.8139 | - |
| Jet k factor Chip 4 | $k_{\text{j,4}} = 10\text{^}\left\{\sum_{j=1}^{20} a_j {Re_{j,4}}^{b_j}(SD)^{c_j}(HD)^{d_j}\right\}$ | $k_{\text{j,4}} = 10\text{^}\left\{\sum_{j=1}^{20} a_j 8289^{b_j}(8)^{c_j}(1)^{d_j}\right\}$ | 0.7715 | 0.8139 | - |
| Hx internal $\Delta P$ (11.5”) | $\Delta P_{\text{hx,int}} = f_{\text{darcy,int}}\frac{1}{2}\rho_{\text{f,1}}{v_{\text{schd,1}}}^2\left(\frac{L_{\text{hx,tot}}}{D_{\text{h,int}}}\right)$ | $\Delta P_{\text{hx,int}} = 0.03254\frac{1}{2}1538 \cdot 2.031^2\left(\frac{0.2921}{0.001193}\right)/1000$ | 25.353 (3.677 ) | 25.27 (3.665) | kPa (psi) |
| Hx out expansion $\Delta P$ | $\Delta P_{\text{expan,1}} = 0.5 \cdot K_{\text{expan,1}} \cdot \rho_{\text{f,1}} \cdot {v_{\text{schd,1}}}^2$ | $\Delta P_{\text{expan,1}} = 0.5 \cdot 0.0556 \cdot 1538 \cdot 2.031^2/1000$ | 0.177 | 0.176 | kPa |
| Hx out expansion k factor | $K_{\text{expan,1}} = \frac{\left(1-\left(\frac{D_{\text{mani,1}}}{D_{\text{rad,equiv}}}\right)^2\right)^2}{\left(\frac{D_{\text{mani,1}}}{D_{\text{rad,equiv}}}\right)^4}$ | $K_{\text{expan,1}} = \frac{\left(1-\left(\frac{0.02614}{0.02285}\right)^2\right)^2}{\left(\frac{0.02614}{0.02285}\right)^4}$ | 0.0556 | 0.0556 | - |
| Hx equivielent radi | $D_{\text{hx,equiv}} = \sqrt{\frac{4 \cdot A_{\text{flow,int}}}{\pi}}$ | $D_{\text{rad,equiv}} = \sqrt{\frac{4 \cdot 4.099 \cdot 10^{-4}}{\pi}}$ | 0.0228 5 | 0.0228 5 | m |

| Parameter | Equation | Evaluated | EES Calc. Value | Hand Calc. Value | Units |
|---|---|---|---|---|---|
| Hx in contraction $\Delta P$ | $\Delta P_{\text{contr},1} = 0.5 \cdot K_{\text{contr},1} \cdot \rho_{\text{f},1} \cdot {v_{\text{schd},1}}^2$ | $\Delta P_{\text{contr},1} = 0.5 \cdot 0.0953 \cdot 1538 \cdot 1.558^2/1000$ | 0.219 | 0.178 | kPa |
| Hx in contraction k factor | $K_{\text{contr},1} = \frac{\left(1-\left(\frac{D_{\text{rad,equiv}}}{D_{\text{mani},1}}\right)^2\right)^2}{\left(\frac{D_{\text{rad,equiv}}}{D_{\text{mani},1}}\right)^4}$ | $K_{\text{contr},1} = \frac{\left(1-\left(\frac{0.02285}{0.02614}\right)^2\right)^2}{\left(\frac{0.02285}{0.02614}\right)^4}$ | 0.1179 | 0.0953 | - |
| Velocity sched 40 (1") | $v_{\text{schd},1} = \frac{\dot{m}_{\text{liq,tot}}}{\rho_{\text{f},1} \cdot A_{\text{schd},1}}$ | $v_{\text{schd},1} = \frac{1.286}{1538 \cdot \frac{\pi}{4} 0.02614^2}$ | 1.548 | 1.558 | m s$^{-1}$ |
| Inlet/outlet $\Delta P$ | $\Delta P_{\frac{\text{in}}{\text{out}},\text{tot}} = \Delta P_{\text{tube,main,cold}} + \Delta P_{\text{main,elbow}}$ | $\Delta P_{\frac{\text{in}}{\text{out}},\text{tot}} = 336.3 + 2543$ | 2842 (0.412 ) | 2879 (0.418) | Pa (psi) |
| Main cold/hot tubing $\Delta P$ (6.7"+1.12") | $\Delta P_{\text{tube,main,cold}} = f_{\text{darcy,tube},1} \frac{1}{2} \rho_{\text{f},1} {v_{\text{schd},1}}^2 \left(\frac{L_{\text{tube,1,c}}}{D_{\text{mani},1}}\right)$ | $\Delta P_{\text{tube,main,cold}} = \frac{1}{2} 0.02392 \cdot 1544 \cdot 1.548^2 \left(\frac{0.1702 + 0.02845}{0.02614}\right)$ | 337.1 (0.048 9) | 336.3 (0.0489 ) | Pa (psi) |
| Main hot/cold elbows $\Delta P$ (2) | $\Delta P_{\text{main,elbow}} = K_{\text{elbow,main}} \frac{1}{2} \rho_{\text{f},1} {v_{\text{schd},1}}^2$ | $\Delta P_{\text{main,elbow}} = 1.38 \frac{1}{2} 1538 \cdot 1.548^2$ | 2505 (0.363 ) | 2543 (0.369) | Pa (psi) |
| Main hot/cold elbow k factor | $K_{\text{elbow,main}} = N_{\text{elbow},1} \cdot f_{\text{T}(0.015/0.02614)} \cdot 30$ | $K_{\text{elbow,main}} = 2 \cdot 0.023 \cdot 30$ | 1.351 | 1.38 | - |
| Reynolds number main tube 1 | $Re_{\text{main},1} = \frac{\rho_{\text{fluid},5} v_{\text{schd},1} D_{\text{mani},1}}{\mu_{\text{fluid},5}}$ | $Re_{\text{main},1} = \frac{1544 \cdot 1.045 \cdot 0.02614}{0.0004093}$ | 10270 5 | 103045 | - |
| Relative roughness tube main | $eD_{\text{main}.1} = \frac{Absolute\ rough_{\text{schd},1}}{D_{\text{schd},1}}$ | $eD_{\text{main}.1} = \frac{0.000045}{0.02614}$ | 0.0017 22 | 0.0017 21 | m |

| Parameter | Equation | Evaluated | EES Calc. Value | Hand Calc. Value | Units |
|---|---|---|---|---|---|
| Relative roughness mani 1 | $eD_{\text{mani.1}} = \frac{Absolute\ rough_{\text{mani,1}}}{D_{\text{mani,1}}}$ | $eD_{\text{main.1}} = \frac{0.000015}{0.02950}$ | | 0.0050 85 | m |
| Total chip tubing $\Delta P$ | $\Delta P_{\text{tube,chip,tot}} = \frac{1}{\dot{m}_{\text{blade}}} (\sum_{i=1}^{2} N_{\text{chip,i}} \cdot \Delta P_{\text{tube,chip,i}} \cdot \dot{m}_{\text{chip,i}} + N_{\text{chip,i}} \cdot \Delta P_{\text{tube,chip,i}} \cdot \dot{m}_{\text{chip,i}})$ | $\Delta P_{\text{tube,chip,tot}} = \frac{1}{0.2571} (\sum_{i=1}^{2} N_{\text{chip,i}} \cdot \Delta P_{\text{tube,chip,i}} \cdot \dot{m}_{\text{chip,i}} + \sum_{i=4}^{4} N_{\text{chip,i}} \cdot \Delta P_{\text{tube,chip,i}} \cdot \dot{m}_{\text{chip,i}})$ | 1.128 | 1.139 | kPa |
| Main mani cold/hot $\Delta P$ | $\Delta P_{\text{mani,1}} = \zeta_{\text{mani,1}} \cdot \frac{1}{2} \rho \cdot v_{\text{mani,1,in}}{}^{2}$ | $\Delta P_{\text{mani,1}} = 2.38 \cdot \frac{1}{2} 1544 \cdot 1.224^{2}/1000$ | 2.947 | 2.753 | kPa (psi) |
| Mani 2 cold/hot $\Delta P$ | $\Delta P_{\text{mani,2}} = \zeta_{\text{mani,2}} \cdot \frac{1}{2} \rho \cdot v_{\text{mani,2,in}}{}^{2}$ | $\Delta P_{\text{mani,2}} = 1.437 \cdot \frac{1}{2} 1544 \cdot 2.491^{2}/1000$ | 6.272 | 6.88 | kPa (psi) |
| Other main mani $\Delta P$ | $\Delta P_{\text{app section,1}} = \Delta P_{\text{turns,1}} + \Delta P_{\text{friction,1}} = K_{\text{elbow,mani,1}} \frac{1}{2} \rho_{\text{f,1}} v_{\text{mani,1}}{}^{2} + f_{\text{darcy,tube,1}} \frac{1}{2} \rho_{\text{f,1}} v_{\text{mani,1}}{}^{2} \left( \frac{L_{\text{tube,1,c}}}{D_{\text{mani,1}}} \right)$ | $\Delta P_{\text{app section,1}} = 1.38 \frac{1}{2} 1538 \cdot 1.224^{2} + \frac{1}{2} 0.02473 \cdot 1544 \cdot 1.224^{2} \left( \frac{0.1433}{0.02614} \right)$ | 1697 | 1747 | Pa |
| Other mani 2 $\Delta P$ | $\Delta P_{\text{app section,2}} = \Delta P_{\text{turns,2}} + \Delta P_{\text{friction,2}} = K_{\text{elbow,mani,2}} \frac{1}{2} \rho_{\text{f,1}} v_{\text{mani,2}}{}^{2} + f_{\text{darcy,tube,2}} \frac{1}{2} \rho_{\text{f,1}} v_{\text{mani,2}}{}^{2} \left( \frac{L_{\text{tube,2,c}}}{D_{\text{mani,2}}} \right)$ | $\Delta P_{\text{app section,2}} = 0.69 \frac{1}{2} 1538 \cdot 2.491^{2} + \frac{1}{2} 0.02545 \cdot 1544 \cdot 2.491^{2} \left( \frac{0.3829}{0.009246} \right)$ | 7972 | 8341 | Pa |

| Parameter | Equation | Evaluated | EES Calc. Value | Hand Calc. Value | Units |
|---|---|---|---|---|---|
| Main mani elbow k factor | $K_{\mathrm{elbow,mani,1}} = N_{\mathrm{elbow,mani,1}} \cdot f_{\mathrm{T(0.015/0.02614)}} \cdot 30$ | $K_{\mathrm{elbow,mani,1}} = 2 \cdot 0.023 \cdot 30$ | 1.351 | 1.38 | - |
| Mani 2 elbow k factor | $K_{\mathrm{elbow,mani,2}} = N_{\mathrm{elbow,mani,2}} \cdot f_{\mathrm{T(0.015/0.02614)}} \cdot 30$ | $K_{\mathrm{elbow,mani,2}} = 1 \cdot 0.023 \cdot 30$ | 0.6649 | 0.69 | - |
| Mani 1 pressure factor | $\zeta_{\mathrm{mani,1}} = 2.63 - 0.54\bar{A}_{\mathrm{mani,1}}$ | $\zeta_{\mathrm{mani,1}} = 2.63 - 0.54 \cdot 0.463$ | | 2.38 | - |
| Mani 1 side branch factor | $\bar{A}_{\mathrm{mani,1}} = \bar{f}_{\mathrm{mani,1}} \left(0.6 + \left(\frac{A_{\mathrm{s,1,in}}}{A_{\mathrm{s,out,1}}}\right)^2 + \zeta_{\mathrm{mani,1,app}}\right)^{-0.5}$ | $\bar{A}_{\mathrm{mani,1}} = 0.4913 \left(0.6 + \left(\frac{6.714 \cdot 10^{-5}}{4 \cdot 3.167 \cdot 10^{-5}}\right)^2 + 0.2434\right)^{-0.5}$ | | 0.463 | - |
| Dynamic pressure app 1 | $\zeta_{\mathrm{mani,1,app}} = \frac{2 \cdot \Delta P_{\mathrm{app\ section,1}}}{\rho(\bar{f}_{\mathrm{mani,1}} \cdot v_{\mathrm{mani,1,in}})^2}$ | $\zeta_{\mathrm{mani,1,app}} = \frac{2 \cdot 1747}{1544(0.4913 \cdot 1.224)^2}$ | | 0.2434 | - |
| Mani 2 pressure factor | $\zeta_{\mathrm{mani,2}} = 2.63 - 0.54\bar{A}_{\mathrm{mani,2}}$ | $\zeta_{\mathrm{mani,2}} = 2.63 - 0.54 \cdot 2.212$ | | 1.437 | - |
| Mani 2 side branch factor | $\bar{A}_{\mathrm{mani,2}} = \bar{f}_{\mathrm{mani,2}} \left(0.6 + \left(\frac{A_{\mathrm{s,in,2}}}{A_{\mathrm{s,out,2}}}\right)^2 + \zeta_{\mathrm{mani,2,app}}\right)^{-0.5}$ | $\bar{A}_{\mathrm{mani,2}} = 2.358 \left(0.6 + \left(\frac{3.167 \cdot 10^{-5}}{6.714 \cdot 10^{-5}}\right)^2 + 0.3132\right)^{-0.5}$ | | 2.212 | - |

| Parameter | Equation | Evaluated | EES Calc. Value | Hand Calc. Value | Units |
|---|---|---|---|---|---|
| Dynamic pressure app 2 | $\zeta_{mani,2,app} = \frac{2 \cdot \Delta P_{app\ section,2}}{\rho(\bar{f}_{mani,2} \cdot v_{mani,2,in})^2}$ | $\zeta_{mani,2,app} = \frac{2 \cdot 8341}{1544(2.358 \cdot 2.491)^2}$ | | 0.3132 | - |
| Mani 1 inlet/outlet ratio | $\bar{f}_{mani,1} = n_{s,1} \frac{A_{s,1,in}}{A_{mani,1}}$ | $\bar{f}_{mani,1} = 5 \cdot \frac{\frac{\pi}{4} 0.009246^2}{0.02614^2}$ | | 0.4913 | - |
| Mani 2 inlet/outlet ratio | $\bar{f}_{mani,2} = n_{s,2} \frac{A_{s,2,in}}{A_{in,2}}$ | $\bar{f}_{mani,2} = 4 \cdot \frac{\frac{\pi}{4} 0.00635^2}{\frac{\pi}{4} 0.009246^2}$ | | 2.358 | - |
| Reynolds number main tube 1 | $Re_{mani,1} = \frac{\rho_{fluid,5} v_{mani,1} D_{h,mani,1}}{\mu_{fluid,5}}$ | $Re_{mani,1} = \frac{1544 \cdot 1.224 \cdot 0.02614}{0.0004093}$ | 12473 9 | 120696 | - |
| Velocity in mani 1 | $v_{mani,1} = \frac{\dot{m}_{liq,tot}}{\rho_{f,1} \cdot A_{mani,1}}$ | $v_{mani,1} = \frac{1.286}{1538 \cdot 0.02614^2}$ | 1.216 | 1.224 | m $s^{-1}$ |
| Reynolds number main tube 2 | $Re_{mani,2} = \frac{\rho_{fluid,5} v_{mani,2} D_{h,mani,2}}{\mu_{fluid,5}}$ | $Re_{mani,2} = \frac{1544 \cdot 2.491 \cdot 0.009246}{0.0004093}$ | 89796 | 86883 | - |
| Velocity in mani 2 | $v_{mani,2} = \frac{\dot{m}_{liq,tot}}{N_{blades} \cdot \rho_{f,1} \cdot A_{mani,2}}$ | $v_{mani,2} = \frac{1.286}{5 \cdot 1544 \cdot \frac{\pi}{4} 0.009246^2}$ | 2.474 | 2.491 | m $s^{-1}$ |
| Relative roughness mani 1 | $eD_{mani,1} = \frac{absroughness}{D_{h,mani,1}}$ | $eD_{mani,1} = \frac{0.000045}{0.02614}$ | 0.0017 22 | 0.0017 21 | - |
| Relative roughness mani 2 | $eD_{mani,2} = \frac{absroughness}{D_{h,mani,2}}$ | $eD_{mani,2} = \frac{0.000015}{0.009246}$ | 0.0016 22 | 0.0016 22 | - |
| Length diameter ratio mani 1(5.64") | $LD_{r,m,1} = \frac{L_{tube,1,c}}{D_{h,mani,1}}$ | $LD_{r,m,1} = \frac{0.1433}{0.02614}$ | 5.491 | 5.482 | - |

| Parameter | Equation | Evaluated | EES Calc. Value | Hand Calc. Value | Units |
|---|---|---|---|---|---|
| Length diameter ratio mani 2 (0.5*30.25”) | $LD_{\mathrm{r,m,2}} = \frac{L_{\mathrm{tube,2,c}}}{D_{\mathrm{h,mani,2}}}$ | $LD_{\mathrm{r,m,2}} = \frac{0.3829}{0.009246}$ | 41.55 | 41.41 | - |
| Mani 1 K factor | $K_{\mathrm{mani,1}} = 1 - \frac{A_{\mathrm{final,manifold,1}}}{A_{\mathrm{inlet,manifold,1}}}$ | $K_{\mathrm{mani,1}} = 1 - \frac{0.02614^2}{0.02614^2}$ | 0 | 0 | - |
| Mani 2 K factor | $K_{\mathrm{mani,2}} = 1 - \frac{A_{\mathrm{final,manifold,2}}}{A_{\mathrm{inlet,manifold,2}}}$ | $K_{\mathrm{mani,2}} = 1 - \frac{\frac{\pi}{4}0.00635^2}{\frac{\pi}{4}0.00635^2}$ | 0 | 0 | - |
| Chip cold/hot tubing $\Delta P$ (0.88”) | $\Delta P_{\mathrm{tube,chip,1}} = (f_{\mathrm{darcy,tube,chip,1}}\left(\frac{L_{\mathrm{tube,1,c}}}{D_{\mathrm{h,chip,tube}}}\right) + K_{\mathrm{elbow,1}})\frac{1}{2}\rho_{\mathrm{f,5}}v_{\mathrm{chip,tube,1}}{}^2$ | $\Delta P_{\mathrm{tube,chip,1}} = (0.03696\left(\frac{0.022352}{0.00635}\right) + 1.015)\frac{1}{2}1544 \cdot 1.082^2$ | 1025 (0.149 ) | 1035 (0.150) | Pa (psi) |
| Chip cold/hot tubing $\Delta P$ (0.88”) | $\Delta P_{\mathrm{tube,chip,2}} = (f_{\mathrm{darcy,tube,chip,2}}\left(\frac{L_{\mathrm{tube,2,c}}}{D_{\mathrm{h,chip,tube}}}\right) + K_{\mathrm{elbow,2}})\frac{1}{2}\rho_{\mathrm{f,5}}v_{\mathrm{chip,tube,2}}{}^2$ | $\Delta P_{\mathrm{tube,chip,2}} = (0.03764\left(\frac{0.022352}{0.00635}\right) + 1.015)\frac{1}{2}1544 \cdot 0.855^2$ | 642 (0.093 1) | 648 (0.0940 ) | Pa (psi) |
| Regs cold/hot tubing $\Delta P$ (2.55”) | $\Delta P_{\mathrm{tube,regs}} = (f_{\mathrm{darcy,tube,chip,4}}\left(\frac{L_{\mathrm{tube,4,c}}}{D_{\mathrm{h,chip,tube}}}\right) + K_{\mathrm{elbow,4}})\frac{1}{2}\rho_{\mathrm{f,5}}v_{\mathrm{chip,tube,4}}{}^2$ | $\Delta P_{\mathrm{tube,regs}} = 0.0355\frac{1}{2}1544 \cdot 2.256^2\left(\frac{0.06477}{0.00635}\right)$ | 1411 (0.205 ) | 1423 (0.206) | Pa (psi) |
| Reynolds number chip tube 1 | $Re_{\mathrm{chip,tube,1}} = \frac{\rho_{\mathrm{fluid,5}}v_{\mathrm{mani,1}}D_{\mathrm{h,chip,tube}}}{\mu_{\mathrm{fluid,5}}}$ | $Re_{\mathrm{chip,tube,1}} = \frac{1544 \cdot 1.082 \cdot 0.00635}{0.0004093}$ | 26810 | 25918 | - |
| Velocity in mani 1 | $v_{\mathrm{chip,tube,1}} = \frac{\dot{m}_{\mathrm{liq,chip,1}}}{\rho_{\mathrm{f,1}} \cdot A_{\mathrm{chip,tube}}}$ | $v_{\mathrm{chip,tube,1}} = \frac{0.05273}{1538 \cdot 0.0000317}$ | 1.075 | 1.082 | m $s^{-1}$ |

| Parameter | Equation | Evaluated | EES Calc. Value | Hand Calc. Value | Units |
|---|---|---|---|---|---|
| Reynolds number chip tube 2 | $Re_{\text{chip,tube,2}} = \frac{\rho_{\text{fluid,5}} v_{\text{mani,1}} D_{\text{h,chip,tube}}}{\mu_{\text{fluid,5}}}$ | $Re_{\text{chip,tube,2}} = \frac{1544 \cdot 0.855 \cdot 0.00635}{0.0004093}$ | 21191 | 20481 | - |
| Velocity in mani 2 | $v_{\text{chip,tube,2}} = \frac{\dot{m}_{\text{liq,chip,2}}}{\rho_{\text{f,1}} \cdot A_{\text{chip,tube}}}$ | $v_{\text{mani,1}} = \frac{0.04168}{1538 \cdot 0.0000317}$ | 0.850 | 0.855 | m s$^{-1}$ |
| Reynolds number chip tube 4 | $Re_{\text{chip,tube,4}} = \frac{\rho_{\text{fluid,5}} v_{\text{mani,1}} D_{\text{h,chip,tube}}}{\mu_{\text{fluid,5}}}$ | $Re_{\text{chip,tube,4}} = \frac{1544 \cdot 2.256 \cdot 0.00635}{0.0004093}$ | 55933 | 54040 | - |
| Velocity in mani 4 | $v_{\text{chip,tube,1}} = \frac{\dot{m}_{\text{liq,chip,4}}}{\rho_{\text{f,1}} \cdot A_{\text{chip,tube}}}$ | $v_{\text{mani,1}} = \frac{0.11}{1538 \cdot 0.0000317}$ | 2.244 | 2.256 | m s$^{-1}$ |

| Parameter | | Equation | | | | |
|---|---|---|---|---|---|---|
| Friction factor main tube cold | Equation | $f_{\text{darcy,tube,1}} = 8 \cdot \left(\left(\frac{8}{Re_{\text{main,1}}}\right)^{12} + \left(\left(-2.457 \cdot \ln\left(\left(\frac{7}{Re_{\text{main,1}}}\right)^{0.9} + 0.27eD_{\text{main,1}}\right)\right)^{16} + \left(\frac{37530}{Re_{\text{main,1}}}\right)^{16}\right)^{-1.5}\right)^{\frac{1}{12}}$ | | | | |
| | Evaluated | $f_{\text{darcy,tube,1}} = 8 \cdot \left(\left(\frac{8}{103045}\right)^{12} + \left(\left(-2.457 \cdot \ln\left(\left(\frac{7}{103045}\right)^{0.9} + 0.27 \cdot 0.001721\right)\right)^{16} + \left(\frac{37530}{103045}\right)^{16}\right)^{-1.5}\right)^{\frac{1}{12}}$ | | | | |
| **EES Calc. Value** | | 0.02453 | **Hand Calc. Value** | 0.02452 | **Units** | - |
| Friction factor chip tubing | Equation | $f_{\text{darcy,chip,tube}} = 8 \cdot \left(\left(\frac{8}{Re_{\text{chip,tube,1}}}\right)^{12} + \left(\left(-2.457 \cdot \ln\left(\left(\frac{7}{Re_{\text{chip,tube,1}}}\right)^{0.9} + 0.27eD_{\text{chip,tube}}\right)\right)^{16} + \left(\frac{37530}{Re_{\text{chip,tube,1}}}\right)^{16}\right)^{-1.5}\right)^{\frac{1}{12}}$ | | | | |
| | Evaluated | $f_{\text{darcy,chip,tube}} = 8 \cdot \left(\left(\frac{8}{25918}\right)^{12} + \left(\left(-2.457 \cdot \ln\left(\left(\frac{7}{25918}\right)^{0.9} + 0.27 \cdot 0.007087\right)\right)^{16} + \left(\frac{37530}{25918}\right)^{16}\right)^{-1.5}\right)^{\frac{1}{12}}$ | | | | |
| **EES Calc. Value** | | 0.03696 | **Hand Calc. Value** | 0.03694 | **Units** | - |

<table>
<tr><th>Parameter</th><th></th><th colspan="4">Equation</th></tr>
<tr><td rowspan="2">Friction factor manifold 1</td><td>Equation</td><td colspan="4">$$f_{\text{darcy,mani,1}} = 8 \cdot \left( \left(\frac{8}{Re_{\text{mani,1}}}\right)^{12} + \left( \left(-2.457 \cdot \ln\left(\left(\frac{7}{Re_{\text{mani,1}}}\right)^{0.9} + 0.27eD_{\text{mani,1}}\right)\right)^{16} + \left(\frac{37530}{Re_{\text{mani,1}}}\right)^{16}\right)^{-1.5}\right)^{\frac{1}{12}}$$</td></tr>
<tr><td>Evaluated</td><td colspan="4">$$f_{\text{darcy,mani,1}} = 8 \cdot \left( \left(\frac{8}{91374}\right)^{12} + \left( \left(-2.457 \cdot \ln\left(\left(\frac{7}{91374}\right)^{0.9} + 0.27 \cdot 0.001721\right)\right)^{16} + \left(\frac{37530}{91374}\right)^{16}\right)^{-1.5}\right)^{\frac{1}{12}}$$</td></tr>
<tr><td colspan="2">EES Calc. Value</td><td>0.02497</td><td>Hand Calc. Value</td><td>0.02473</td><td>Units | -</td></tr>
<tr><td rowspan="2">Friction factor manifold 2</td><td>Equation</td><td colspan="4">$$f_{\text{darcy,mani,2}} = 8 \cdot \left( \left(\frac{8}{Re_{\text{mani,2}}}\right)^{12} + \left( \left(-2.457 \cdot \ln\left(\left(\frac{7}{Re_{\text{mani,2}}}\right)^{0.9} + 0.27eD_{\text{mani,2}}\right)\right)^{16} + \left(\frac{37530}{Re_{\text{mani,2}}}\right)^{16}\right)^{-1.5}\right)^{\frac{1}{12}}$$</td></tr>
<tr><td>Evaluated</td><td colspan="4">$$f_{\text{darcy,mani,2}} = 8 \cdot \left( \left(\frac{8}{58073}\right)^{12} + \left( \left(-2.457 \cdot \ln\left(\left(\frac{7}{58073}\right)^{0.9} + 0.27 \cdot 0.001622\right)\right)^{16} + \left(\frac{37530}{58073}\right)^{16}\right)^{-1.5}\right)^{\frac{1}{12}}$$</td></tr>
<tr><td colspan="2">EES Calc. Value</td><td>0.02545</td><td>Hand Calc. Value</td><td>0.02545</td><td>Units | -</td></tr>
</table>

**Table A - 10** Microchannel cold plate pressure drop configuration 3-5a

| Parameter | Equation | Evaluated | EES Calc. Value | Hand Calc. Value | Units |
|---|---|---|---|---|---|
| Micro channel $\Delta P$ | $\Delta P_{\mathrm{tube,chip,1}} = f_{\mathrm{darcy,cp}} \left(\frac{L_{\mathrm{cp}}}{D_{\mathrm{ch}}}\right) \frac{1}{2} \rho_{\mathrm{f,5}} \cdot v_{\mathrm{ch}}{}^2$ | $\Delta P_{\mathrm{tube,chip,1}} = 0.296 \left(\frac{0.0254}{0.0002912}\right) \frac{1}{2} 992 \cdot 0.4437^2/1000$ | 2.53 (0.367) | 2.52 (0.365) | kPa (psi) |
| Microchannel friction factor | $f_{\mathrm{lam,darcy,cp}} = \frac{96}{Re_{\mathrm{ch}}}(1 - 1.3553 \cdot \alpha + 1.9467 \cdot \alpha^2 - 1.7012 \cdot \alpha^3 + 0.9564 \cdot \alpha^4 - 0.2537 \cdot \alpha^5)$ | $f_{\mathrm{lam,darcy,cp}} = \frac{96}{306.6}(1 - 1.3553 \cdot 0.03028 + 1.9467 \cdot 0.03028^2 - 1.7012 \cdot 0.03028^3 + 0.9564 \cdot 0.03028^4 - 0.2537 \cdot 0.03028^5)$ | 0.3006 | 0.296 | - |

**Table A - 11** Head and flow rate calculation for pumps

| Parameter | Equation | Evaluated | EES Calc. Value | Hand Calc. Value | Units |
|---|---|---|---|---|---|
| Pump head required FC72 | $H_{\mathrm{FC72}} = \frac{\Delta P_{\mathrm{FC72,tot}}}{\rho_{\mathrm{FC72}}}$ | $H_{\mathrm{FC72}} = \frac{28.33 \cdot 144}{1544 \cdot 0.0623705}$ | 44.22 | 42.36 | ft lbf $lbm^{-1}$ |
| Pump head required Jet fuel | $H_{\mathrm{Jet\ fuel}} = \frac{\Delta P_{\mathrm{Jet\ fuel,tot}}}{\rho_{\mathrm{Jet\ fuel}}}$ | $H_{\mathrm{Jet\ fuel}} = \frac{20.38 \cdot 144}{793 \cdot 0.0623705}$ | 59.33 | 59.27 | ft lbf $lbm^{-1}$ |
| Pump head required Water | $H_{\mathrm{Water}} = \frac{\Delta P_{\mathrm{Water,tot}}}{\rho_{\mathrm{Water}}}$ | $H_{\mathrm{Water}} = \frac{9.412 \cdot 144}{989.5 \cdot 0.0623705}$ | 22.22 | 21.96 | ft lbf $lbm^{-1}$ |
| Pump head required GC5050 | $H_{\mathrm{GC5050}} = \frac{\Delta P_{\mathrm{GC5050,tot}}}{\rho_{\mathrm{GC5050}}}$ | $H_{\mathrm{GC5050}} = \frac{11.38 \cdot 144}{1048 \cdot 0.0623705}$ | 25.07 | 25.31 | ft lbf $lbm^{-1}$ |
| Volumetric flow rate FC72 | $\dot{V}_{\mathrm{FC72,gpm}} = \frac{\dot{m}_{\mathrm{tot,FC72}}}{\rho_{\mathrm{FC72}}}$ | $\dot{V}_{\mathrm{FC72,gpm}} = \frac{1.286}{1544} \cdot 15850.32$ | 13.16 | 13.20 | GPM |
| Volumetric flow rate Jet Fuel | $\dot{V}_{\mathrm{Jet\ fuel,gpm}} = \frac{\dot{m}_{\mathrm{tot,Jet\ Fuel}}}{\rho_{Jet\ Fuel}}$ | $\dot{V}_{\mathrm{Jet\ fuel,gpm}} = \frac{0.77}{793} \cdot 15850.32$ | 15.40 | 15.42 | GPM |
| Volumetric flow rate Water | $\dot{V}_{\mathrm{Water,gpm}} = \frac{\dot{m}_{\mathrm{tot,Water}}}{\rho_{\mathrm{Water}}}$ | $\dot{V}_{\mathrm{Water,gpm}} = \frac{0.9477}{989.5} \cdot 15850.32$ | 15.37 | 15.18 | GPM |
| Volumetric flow rate GC5050 | $\dot{V}_{\mathrm{GC5050,gpm}} = \frac{\dot{m}_{\mathrm{tot,GC5050}}}{\rho_{\mathrm{GC5050}}}$ | $\dot{V}_{\mathrm{GC5050,gpm}} = \frac{1.14}{1048} \cdot 15850.32$ | 17.35 | 17.39 | GPM |